Gold and Gold-Palladium Catalysts Synthesized by a Modified Sol-Immobilisation Method for Thermal and Plasmonic Glycerol Oxidation

Thesis submitted in accordance with the requirement of Cardiff University
for the degree of Doctor of Philosophy

Laura Abis

School of Chemistry

Cardiff University

March 2018

DECLARATION

This work has not been submitted in substance for any other degree or award at this or any other university or place of learning, nor is being submitted concurrently in candidature for any degree or other award.

Signed ……………………………………… (candidate)   Date ……………………………………………

STATEMENT 1

This thesis is being submitted in partial fulfilment of the requirements for the degree of PhD

Signed ……………………………………… (candidate)   Date ……………………………………………

STATEMENT 2

This thesis is the result of my own independent work/investigation, except where otherwise stated, and the thesis has not been edited by a third party beyond what is permitted by Cardiff University's Policy on the Use of Third Party Editors by Research Degree Students. Other sources are acknowledged by explicit references. The views expressed are my own.

Signed ……………………………………… (candidate)   Date ……………………………………………

STATEMENT 3

I hereby give consent for my thesis, if accepted, to be available online in the University's Open Access repository and for inter-library loan, and for the title and summary to be made available to outside organisations.

Signed ……………………………………… (candidate)   Date ……………………………………………

STATEMENT 4: PREVIOUSLY APPROVED BAR ON ACCESS

I hereby give consent for my thesis, if accepted, to be available online in the University's Open Access repository and for inter-library loans **after expiry of a bar on access previously approved by the Academic Standards & Quality Committee.**

Signed ……………………………………… (candidate)   Date ……………………………………………

Summary

A novel sol-immobilisation methodology, where the use of the stabilising agent was omitted, has been employed for the synthesis of supported noble metal nanoparticles. The main idea behind this approach is the observation that the presence of a stabiliser layer around the nanoparticles is often related to limited catalytic performances. However, despite the existence of other synthetic methods where stabilisers are not required, the sol-immobilisation presents several advantages in terms of controlling the colloid prior to the deposition, besides being quick, easy and rather inexpensive.

The new materials (1% wt Au/TiO$_2$ and 1% wt AuPd/TiO$_2$) were extensively characterised, and showed very similar features when compared to the traditional samples synthesized by PVA or PVP, also confirmed by catalytic testing. However, although as active, investigation into glycerol oxidation in basic conditions revealed that the selectivity towards main products tartronate and glycerate depends on the presence and nature of the stabilising agent. Further insight on the reaction mechanism also evidenced that the tartronate is produced as a primary product, in contrast to the main reaction pathways proposed in the literature.

Plasmonic (photocatalytic) glycerol oxidation under neutral conditions was also investigated using a series of sol-immobilised catalysts, proving that these materials show plasmonic response. The role of parameters such as irradiation time and wavelength, absence of stabilising polymer and nature of stabilising polymer were also investigated in order to determine their effect on the plasmonic response. Bimetallic catalysts with different Au:Pd ratios were also investigated, and showed a plasmonic enhancement increasing accordingly with the Au content.

The work showed that active sol-immobilised catalysts can be successfully synthesized without the addition of any stabilising polymer, exhibiting characteristics and catalytic activity comparable to the traditional samples. It was demonstrated that the presence and nature of the stabilising agent might influence the selectivity. Furthermore, for the first time, mono and bimetallic sol-immobilised materials were successfully employed for plasmonic-enhanced reactions.

Abstract

The common thread of this PhD Thesis is the use of sol-immobilised noble metal nanoparticles prepared by a novel synthetic route, where the addition of the stabilising agent has been avoided.

The first part of the Thesis presents the development of a novel sol-immobilisation route without the addition of stabilisers (e.g., PVA, PVP). A monometallic 1% wt Au/TiO_2 and a bimetallic 1% wt $AuPd/TiO_2$ catalysts were prepared and extensively characterised by different techniques in order to gain information including metal loading, nanoparticles morphology and oxidation state of the metals. It has been shown that despite the stabilisers absence, is still possible to obtain materials exhibiting very similar characteristics with respect to the traditional catalysts prepared by PVA and PVP addition. The catalytic activity of the monometallic sample was firstly evaluated for the oxidation of CO (gas-phase) and glycerol (liquid-phase under basic conditions), whereas the bimetallic was employed for the solvent-free oxidation of benzyl alcohol. It has been shown that for the liquid phase reactions, samples behave in a very similar manner to the traditional ones. However, the stabiliser-free catalyst was not active as expected for CO oxidation: reasons for this behaviour might be related to the nanoparticles size or to the presence of poisoning species (i.e., chloride) on the catalyst's surface.

The second part is focused on the study of glycerol oxidation in basic conditions by using the novel mono and bimetallic catalysts synthesized stabiliser-free and their comparison in terms of activity and selectivity to the traditional catalysts synthesized by common stabilising agents PVA and PVP. It has been shown on the first instance that the selectivity towards the main products tartronate and glycerate follows a trend depending on the presence and nature of the stabiliser, with the stabiliser-free samples being more selective towards the former, followed by PVA and PVP. Experiments at short time and using glyceric acid as starting material revealed that the tartronate cannot only arise as product of secondary oxidation of glycerate. Finally, experiments where selected aliquots of PVA and PVP were added during reaction showed that the nature of the polymer affects the conversion and selectivity. However, the mechanisms involved have not been fully understood yet.

The third part presents the catalytic activity of a series of Au and AuPd sol-immobilised catalysts for the plasmonic oxidation of glycerol under neutral conditions. It has been shown that the catalysts prepared by sol-immobilisation are active under plasmonic conditions. The effect of the presence and nature of the stabilising polymer, the wavelength and time of illumination and of calcination have also been investigated. The catalytic activity was proven to be related to the plasmonic effect by performing reactions using different wavelengths of illumination; the nature of the polymer was proven to affect the plasmonic response of the catalyst; stabiliser-free samples activity significantly improved after calcination, likely due to a stronger nanoparticle/support interaction. The plasmonic effect has also been observed for a series of 1% wt $AuPd/TiO_2$ catalysts prepared with different Au:Pd ratios, with enhancement in the conversion increasing with the increase in the gold content.

Acknowledgements

Ringraziamenti

Glossary

IEP	Isoelectric point
DP	Deposition-precipitation
SF	Stabiliser-free
PVA	Polyvinyl alcohol
PVP	Polyvinyl pyrrolidone
LSPR	Localised Surface Plasmon Resonance
CMB	Carbon Mass Balance
TiO$_2$	Titania
H$_2$O$_2$	Hydrogen peroxide
CO$_2$	Carbon dioxide
CO	Carbon monoxide
GLY	Glycerol
GA	Glyceric acid / glycerate
TA	Tartronic acid / tartronate
GLYA	Glycolic acid / Glycolate
DHA	Dihydroxyacetone
OXA	Oxalic acid / Oxalate
LA	Lactic acid / Lactate
FA	Formic acid / Formate
PA	Pyruvic acid / Pyruvate
ACA	Acetic acid / Acetate
TEM	Transmission Electron Microscopy
AC-STEM	Aberration Corrected-Scanning Transmission Electron Microscopy

vi

DRIFTS	Diffuse Reflectance Infrared Fourier Transform Spectroscopy
DR-UV Vis	Diffuse Reflectance UV-Visible
XPS	X-ray Photoelectron Spectroscopy
XRD	X-ray Diffraction
TGA	Thermogravimetric Analysis
ICP-MS	Inductively Coupled Plasma – Mass Spectrometry
MP-AES	Microwave Plasma – Atomic Emission Spectroscopy
HPLC	High Pressure Liquid Chromatography
GC	Gas Chromatography
nm	Nanometer (10^{-9} m)
cm^{-1}	Wavenumber
mol	moles
M	Molar, concentration mol/L

LIST OF FIGURES

CHAPTER 1

CHAPTER 2

CHAPTER 3

CHAPTER 4

CHAPTER 5

TABLE OF CONTENTS

Page

Chapter 1

Introduction

1.1 Catalysis

1.1.1 General principles

The common definition of a catalyst is a substance that increases the rate at which a chemical equilibrium is attained without itself undergoing a chemical change or being consumed during the reaction [1]. The catalyst is a species that does not change the thermodynamics of the chemical reaction (i.e., the ΔG), but only influences the barriers to reaction, the *activation energy* (E_a), and therefore the kinetics (rate). This concept is displayed in Scheme 1.1.
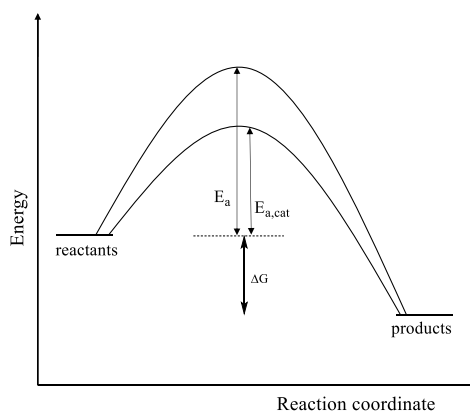
Scheme 1.1 – Scheme of a catalysed process *vs* an uncatalysed process. E_a is the activation energy barrier, lower for a catalysed reaction ($E_{a,cat}$) and ΔG is Gibbs free energy

The rate of a reaction depends on the composition and temperature of the system, according to the following relationships (Eq. 1.1-1.3). For a generic reaction:

$$aA + bB \rightarrow cC + dD \quad \text{(Eq. 1.1)}$$
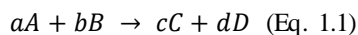
in a simple way, the reaction rate can be expressed as:

$$r = k * [A]^m [B]^n \quad \text{(Eq. 1.2)}$$

where [A] and [B] are the concentration of the reactants, m and n are exponential factors that represent the order of the reaction with respect to [A] and [B] and they are not necessarily equal to stoichiometric factors a and b in Eq. 1.1. Their sum represents the so-called global order of the reaction and k is the kinetic constant, expressed by the Arrhenius' law:

$$k = A * e^{-Ea/RT} \quad \text{(Eq. 1.3)}$$

where A is a pre-exponential factor, E_a is the activation energy (J/mol), R the gas constant (J/mol·K) and T the temperature (K). As displayed in Scheme 1.1, the Ea represent the amount of energy required for the reactants to overcome the barrier to reaction and react to form products. This is an intrinsic parameter of the reaction, and the role of the catalyst is to lower its value. From Equation 1.3 it is clear that the dependence of the reaction rate on temperature and E_a: the bigger the activation energy the smaller the factor k and consequently the slower the reaction rate. Increasing the temperature will result in a decrease of the exponential value ($-E_a/RT$), resulting in a bigger value of k and faster reaction rate.

Catalytic reactions can be classified into two main categories: homogeneous and heterogeneous. The former identifies catalytic processes where the catalyst is in the same phase as the reactants and products (e.g., liquid): typical example of homogeneous catalysts are enzymes. The main advantage of these processes is their specificity and ability to work at mild conditions; however, a common drawback is the difficulty in separating the catalyst from the liquid phase post reaction. In heterogeneous catalysis, the catalyst is in a different phase (usually solid) with respect to the reactants and products and activity is determined by several parameters that are typical of surface processes and interface phenomena. The main advantage of heterogeneous catalysts is that they can be easily separated by the products.

1.1.2   Heterogeneous catalysis

Heterogeneous catalysis is at the heart of the world's economy, since the 90% of the industrial production of medicines, food, pharmaceutical, fuels, are obtained *via* heterogeneous catalytic processes [2]. In the past three decades, the increasing awareness of urgent problems such as the global warming and the depletion of fossil fuels has led to the necessity of developing sustainable processes in a *Green Chemistry* perspective [3], which includes not only chemical synthesis but also clean energy production. Therefore, many efforts are being made in order to develop adequate catalysts and to improve existing processes [1,2]. Heterogeneous catalysis is crucial in addressing the production of chemicals *via* safer and more sustainable routes. These include the development of catalytic processes for the conversion of bio-derived feedstocks into useful chemicals [4-6] where the CO_2 cycle can be virtually closed, to the development of catalysts able to promote chemical reactions with sunlight (photocatalysts), in an attempt to exploit this timeless renewable energy source [7-10]. An ideal heterogeneous catalyst should possess high activity and long-term stability. Also, even more desirable is high selectivity, that reflects the ability of the catalyst to convert the reactant(s) along one specific pathway, and minimise the production of undesired byproducts [1,2].

The phenomenon of *adsorption* can be considered the core of the catalytic process. It completely differs from *absorption* (a bulk phenomenon), since it involves the preferential accumulation of material at the surface. A simple experiment to distinguish between the two is given by the observation of the amount of gas taken up by a solid at a fixed pressure and temperature: if it is proportional to its surface area, and not to its volume, then adsorption predominates, not absorption [2]. However, adsorption can be classified into two processes depending on the respective enthalpy: physical and chemical. The former (physisorption) involves the forces of molecular interaction (Van der Waals) and is characterised by small changes in enthalpy, typically in the range 10-40 kJ/mol. The latter (chemisorption) occurs at particular locations in the solid surface (the active sites), and involves the rearrangement of the electrons of the interacting gas (or liquid) and solid, with consequential formation and rupture of chemical bonds (associated heats between 80 kJ/mol and 400 kJ/mol [2]), and is largely responsible for the catalytic process. The nature of the active sites strongly depends on the solid, which is usually crystalline, and different active sites can be present at the same time due to the crystalline

anisotropy [1]. The crystalline defects such as kinks, edges, steps and vacancies are of fundamental importance for the catalytic activity and selectivity, as these high-energy sites are often the sites for adsorption.

The interface phenomena that characterise heterogeneous catalysis are conventionally summarised as follows and in Scheme 1.2:

1) External diffusion: the reactant diffuse through a boundary layer surrounding the catalyst particle;

2) Internal diffusion: intra-particle diffusion of the reactants into the catalyst pores;

3) Adsorption of the reactants onto active sites;

4) Reaction;

5) Desorption of products;

6) Internal diffusion: intra-particle diffusion of the products;

7) External diffusion of the products.

The overall rate of a catalytic reaction is therefore dependent on different parameters, including **1)** film diffusion control (steps 1 and 7); **2)** pore diffusion control (steps 2 and 6) **3)** intrinsic kinetic reaction control (steps 3-5). In addition to *mass* transfer effects (steps 1, 2, 6, 7) also *heat* transfer effects can occur in heterogeneous catalysis for highly exothermic or endothermic reactions [1].
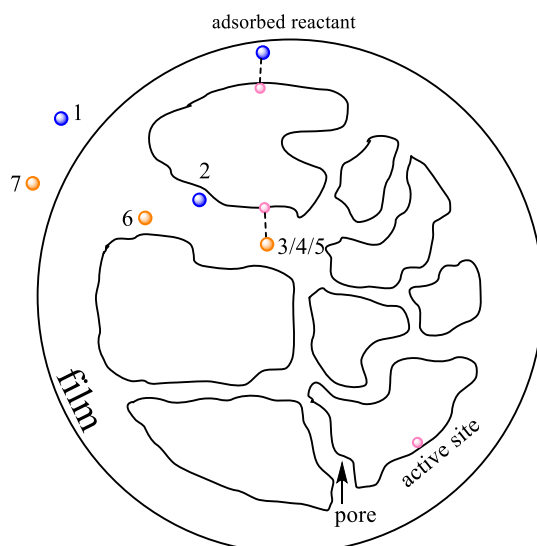
Scheme 1.2 – Scheme of heterogeneous catalysis steps occurring on a catalyst particle

Generally, working at high temperatures ensures higher reaction rate, therefore the rate-determining step is represented by the diffusion processes [11]. In order to avoid diffusion problems and to make sure that the reaction is not mass-transfer limited, the size of the catalyst should be very small and the diffusion coefficient very large [11], conditions that can be achieved by finely dispersing the material and increasing the stirring speed (or the space velocity in flow reactors) respectively.

In general, the desirable features of a heterogeneous catalyst should be:

- good selectivity to target products with a minimal generation of by-products;

- reasonable rate of reaction at the reaction conditions;

- stability over time and conditions.

The catalyst activity at a given temperature is often expressed in terms of reactant converted per unit of time. However, this definition does not account for the catalyst itself (i.e., of its active sites), being therefore inappropriate when the activities of different catalysts need to be compared. A more appropriate definition of the catalyst activity is given by the turnover number (TON), originally used to describe the activity of enzymatic reactions and defined as the maximum number of reactant molecules converted per catalytic site per unit of time [11]. In heterogeneous catalysis, the TON is dimensionless and defined as the moles of reactant converted per moles of active sites. However, according to Boudart [12], this appellation is rather unfortunate and generates confusion, besides not providing any information about the catalyst lifetime; therefore, a better measure of the catalytic activity on surfaces is given by turnover frequency (TOF) or turnover rate (TOR), which define the number of catalytic cycles of the active site per unit of time [1, 12].

Since the catalytic activity of a solid catalyst is usually proportional to the active surface area per unit volume of catalyst, a high activity per unit volume requires small particles [13, 14]. The surfaces of these nano-sized particles contains a large number of defects such as edges, kinks, terraces and vacancies, which give rise to reactivity. Therefore, the discovery and investigation of their properties is of fundamental importance in the catalysis field.

1.2 Nanoparticles

1.2.1   Introduction and definition

Nanoparticles (particles with one dimension between 1-100 nm) [15] are considered to be intermediate between the bulk and molecular state of the matter. Investigation of nanoparticles has received considerable attention due to many potential innovative applications such as biomedicine [16-19], catalysis [20-22], fuel cell [23], magnetic data storage [24], agriculture [25], and solar cells [26].

Synthetic approaches for the preparation of nanoparticles can be gathered into two broad classes: top-down and bottom up [27-29], illustrated in Figure 1.1. The idea behind the top down approach is to break down the bulk material to form the nanoparticles (e.g. by mechanical milling), but these syntheses are limited by the difficulty in controlling the size uniformity of the nanoparticles produced. Conversely, in the bottom-up approach, the synthesis proceeds from metal precursor molecules, generally *via* wet-chemistry synthetic routes (e.g., colloidal methods) or in the gas-phase (e.g. chemical vapour deposition). The main advantage of this approach is the better control of nanoparticles properties and the versatility, as syntheses can be carried out in polar and non-polar solvents or solvent-free environment.
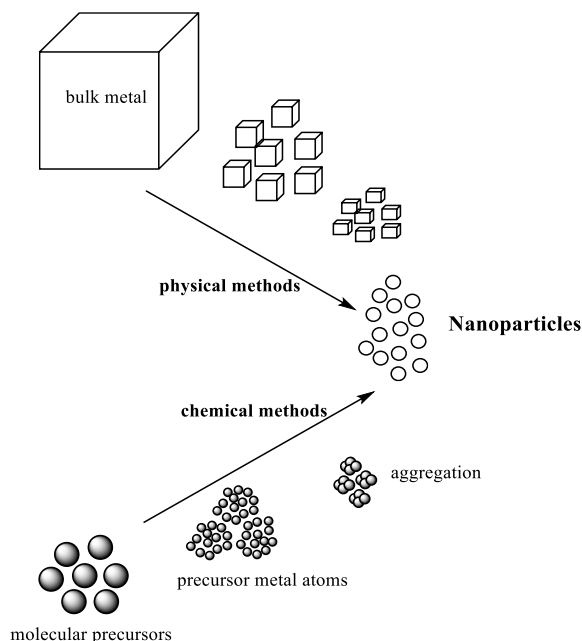
Figure 1.1 – Top-down and bottom-up approaches (adapted from ref. [30])

There are different perspectives and theories regarding the formation of nanoparticles *via* bottom-up methodologies, and discussion about the detailed mechanisms of nucleation and colloidal theory is out of the scope of this introduction. However, complete and exhaustive reviews can be found e.g. in references [31-33]. Theories agree that the formation of nanoparticles is a multi-step process and involves: 1) nucleation 2) formation of seeds 3) growth of seeds into nanocrystals, which are briefly explained in the following sections.

1) Nucleation

Nucleation is the first step to the formation of a nanocrystal, and occurs when a metal precursor is brought to the zero-valent state by decomposition (e.g., thermal) or by chemical reduction. In the first case the nucleation process is believed to start when the concentration of zero-valent atom in the solution reaches a point of supersaturation [34]; in the second case, it is still unclear if the nucleation starts before or after the precursors' reduction [31]. In both cases, the formation of new nuclei is a kinetically controlled step, since they are less stable than bigger nanoparticles. The process stops when their concentration drops below the level of supersaturation and the growth proceeds as long as the solution is oversaturated [32].

2) Formation of seeds

In the following step, seeds (stable aggregation of atoms with a well-defined structure) are formed when structural fluctuations become energetically expensive. The shape of the seeds is of fundamental importance to determine the final shape of the nanocrystals, and control over shape can be achieved by taking into account kinetic and thermodynamic factors [31, 32]. For example, at the very beginning of the growth the seeds are spherical due to the rapid deposition of atoms on the nucleus (kinetic control), but at a later stage the slower reaction rate and dissolving/deposition equilibrium drive the formation of the most stable facets (thermodynamic control).

3) Growth of seeds into nanocrystals

Once the seeds are formed, the growth into nanocrystals can proceed ideally *via* attachment of atoms onto already formed nanoparticles or through aggregation of the latter [32]. In the former case, the final nanocrystal is expected to present a regular shape, while in the latter it is expected to be mostly spherical and

polycrystalline [35]. In the reality, these processes happen together, and the prevailing route will determine the shape and the degree of polycristallinity of the final particles.

1.2.1.1 Control over size and shape of nanoparticles

The final size of nanoparticles is strongly influenced by the nature of the reducing agent; for example, the use of a stronger reducing agent leads to the formation of smaller nanoparticles, whereas larger nanoparticles are generally obtained through the generation of a small number of nuclei that grow at the expenses of the remaining metal in solution [35]. In both cases, the aggregation of nanoparticles must be controlled in order to obtain stable dispersions. This can be achieved by electrostatic, hydration/solvation, steric and electrosteric control. The hydration repulsion dominates in well-solvated surfaces in water [36, 37]; the presence of anions and cations from the precursors remain in the solvation shell of the nanoparticles and form an electrical double layer, which give rise to electrostatic repulsion. However, since this mechanism relies on the distance r between the nanoparticles as displayed in Figure 1.2, it is inefficient in concentrated systems, where at some point the Van der Waals attractive forces prevail and the nanoparticles will aggregate to form bulk metal particles.
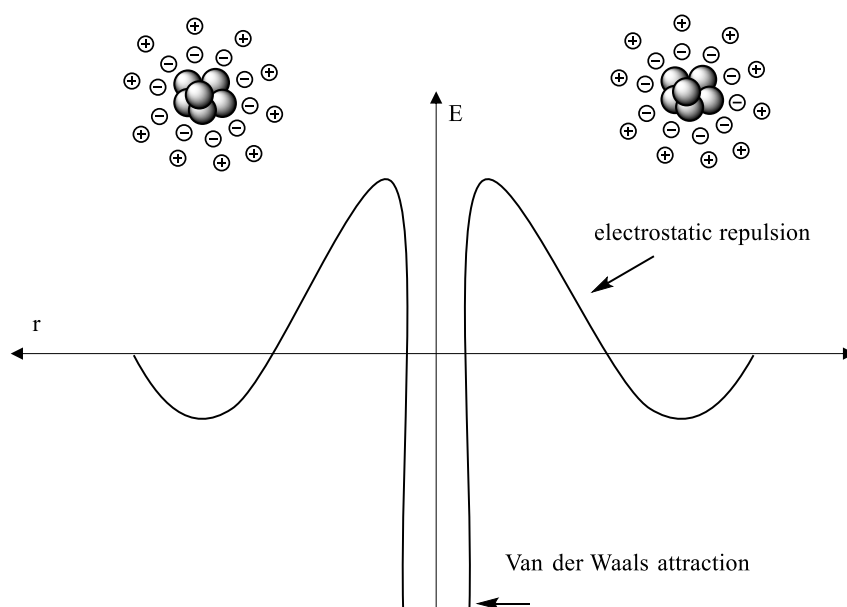
Figure 1.2 – Electrostatic stabilisation (adapted from ref. [38]). The system is stabilised only at determined distance r

Steric and electrosteric control can be achieved by using macromolecules such as polymers, dendrimers and surfactants and they are based on steric hindrance (Figure 1.3) and unbalanced attractive Van der Waals forces [35]. Finally, stabilisation can also be achieved by depositing the nanoparticles onto a support [38,39].
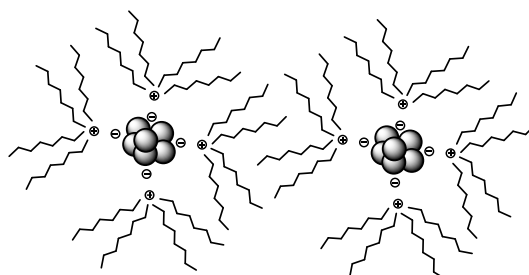
Figure 1.3 – Steric stabilisation (adapted from ref. [38])

In addition to their role in preventing aggregation, ligands or surfactants can be also employed as capping agents to supress the growth of nanocrystals by modulating the stability of their facets. The most used capping agents can be either a by-product generated during the synthesis (e.g. CO) or added (e.g. polymers such as PVA and PVP, or ionic surfactants like cetyltrimethylammonium bromide, CTAB), in addition to ions such as Br^- which derive from the reductant and/or ligand (e.g. $NaBH_4$, CTAB).

The role of the capping agents can be regarded from both a thermodynamic and a kinetic perspective: in the former case, the passivation of growing facets stabilises some crystal faces therefore further growth cannot proceed; in the latter case, the growth rate at the unstable facets is faster than at the stable facets because the energy barrier is lower. Of course, the mechanisms involved in the facet stabilisation processes are complex and interdependent, meaning that it is challenging to make such a distinction between the thermodynamic and kinetic effects [32]. However, understanding the principles at the basis of facet stabilisation is fundamental to achieve a better control on the synthesis of nanoparticles of different and complex shape, in particular when some degree of anisotropy is desired.

1.2.1.2   Colloidal methods for nanoparticles preparation

Among the most commonly used wet-chemistry bottom-up approaches in nanoparticles synthesis, colloidal methods are relatively synthetically simple and ensure a good control of the reaction parameters. The most widely used are chemical reduction, electrochemical synthesis and thermal decomposition.

In the *chemical reduction synthesis*, firstly reported by Michael Faraday, the basis of the whole process is the reduction (by e.g. borohydrides, hydrazine, citric and oxalic acid, polyols) which involves nucleation and growth of nanoparticles as earlier described. When these two take place in the same process, it is called *in situ* synthesis, and it generally leads to nanoparticles of spherical shape, whereas if it happens separately it is called *seed-growth* method and it is mostly used for preparing non-spherical nanoparticles with some degree of anisotropy such as e.g. nanorods, nanostars, nanocubes. In this method, several factors such as reducing and stabilising agents, metal precursor, solvent, concentration, temperature and reaction time [38] control the size and shape of the nanoparticles.

In *electrochemical synthesis*, developed by Reetz *et al.* in 1990s [40], the synthesis proceeds by the oxidative dissolution of the sacrificial bulk anode, followed by the migration of the ions M^+ to the cathode, where zero-valent metal atoms (M^0) are formed. Thereafter, metal nanoparticles form by nucleation and growth in an environment with stabilisers, until the precipitation of the metallic colloids. Conversely to the previous method, the absence of chemical reductant here avoids any contamination with by-products of the reducing agents. Furthermore, tuning the current density and the distance between the electrodes, the reaction time, temperature and polarity of the solution allow control of the nanoparticles size.

Thermal decomposition of organometallic compounds and metal-surfactant complexes are typically performed in hot surfactant solutions to synthesize monodisperse nanoparticles of various materials. Starting from low-valency metal complexes, the ligands are typically reduced with H_2, or carbon monoxide. The reduced ligands leave the M^0 centre, allowing the clustering of metal atoms.

The so-prepared nanoparticles dissolved in the form of organosols or hydrosols can be directly used for quasi-homogeneous catalytic reactions, or, if supported, they can be employed in heterogeneous catalytic processes [23]. For consistency with the main topic of the present Thesis, only the latter case will be covered extensively. The following section presents the main synthetic methodologies for the preparation of supported nanoparticles for heterogeneous catalytic applications.

1.2.2   Supported nanoparticles for heterogeneous catalysis

Nanoparticles can be directly employed for "quasi-homogeneous" catalytic processes [23]. However, for heterogeneous catalytic applications where high temperature and pressure are often required, their deposition on a supporting material becomes essential in order to achieve active and stable catalyst. The support, besides supplying the shape, mechanical strength and porous structure to the catalyst [13], may also be crucial in determining its activity and selectivity by providing acidity/basicity or by tuning the electronic density of the nanoparticles [41, 42]. Even though nowadays several methodologies [43] are available for the preparation of supported nanoparticles, the most used are impregnation, co-precipitation and deposition-precipitation, briefly introduced in the following paragraphs (more complete description can be found in references [43-45]).

- *Impregnation*

This synthesis method involves filling the pore space of the support material with a metal precursor solution, the choice of which is very important in determining the final nanoparticle dispersion [44]. The dispersion is also determined by the interaction of the precursors with the support [44]. When the volume of the solution exceeds the pore volume of the support, the method is known as *wet-impregnation*; otherwise, it is termed *incipient wetness*. The characteristics of the catalyst depend on the supporting material and on the post treatment conditions [15, 46]. Typically, drying is necessary in order to remove the solvent from the pores: this process would lead to supersaturation and subsequent precipitation of the precursor; additionally, precipitation of the precursor can also be caused by any chemical changes of the precursor induced by temperature, dehydration or gas atmosphere. The main advantage of this method relies on its relative ease and low waste streams.

- *Co-precipitation*

In this synthetic approach, generally carried out at a constant pH, the salt precursors of the support and metal (generally nitrates) are dissolved and mixed in an alkaline solution (K_2CO_3, Na_2CO_3 or NaOH), such that a combined nucleation and growth of support and active metal is obtained in the form of hydroxide or carbonates. Subsequently, the precipitate is filtered, washed, dried and thermally treated [46]. A number of factors influence these preparations: for example, the choice of the base has to be carefully selected according to the nature of the metal cation; also the anions of the metallic precursors must be taken into consideration in order to avoid

the deposition of poisoning species. Additional factors and a description of their effects can be found in reference [44]. With this method is possible to achieve high metal loadings while keeping small nanoparticle size.

- *Deposition-Precipitation*

In this synthesis, the metal precursors are dissolved in water and the pH adjusted to achieve the complete deposition of the metal hydroxide onto the support. The obtained material is then filtered, washed dried and generally calcined. Since the optimum pH is determined by the isoelectric point (IEP) of the support, the synthesis is not commonly used for acidic oxide materials with IEP < 5, e.g. SiO_2 (IEP=2) [46]. The main advantage of this technique is that allows to achieve high metal loading ensuring that all the metal is deposited onto the surface and not buried into the support [47]. However, the main drawback of these synthesis methodologies is the poor control of the distribution of the size and shape of nanoparticles, which determine the nature of the surface sites [48].

- *Sol-immobilisation*

The traditional sol-immobilisation method was firstly reported by Prati and Martra in 1999 [49] for the synthesis of spherical Au nanoparticles supported on carbon. This technique, which originates from previous studies on Au colloids generation [50] and supporting [51], involves the preparation of a nanoparticles sol by reduction (with $NaBH_4$) of the precursor in presence of a stabilising agent (polymer, surfactant, polar molecules) and its immobilisation onto a support. The crucial step is the immobilisation, since a good metal dispersion depends on surface properties (i.e., IEP and surface area) and morphology of the support. Moreover, the nature and the relative amount of the protective agent are additional factors influencing the metal dispersion [52]. The main advantage of this method is the size, shape and composition control of the colloidal nanoparticles prior to the immobilisation on the support [43, 46, 53, 54]. The basic steps for the colloid preparation are displayed in Figure 1.4. However, the main drawback of this synthetic methodology is the stabilising agent presence, since it can affect the catalytic performances [55, 56] by e.g., blocking the access to the active site. Removal of stabiliser by post-synthesis treatments such as calcination often results in sintering and morphological changes of nanoparticles, with consequent loss in catalytic activity [43, 57, 58]. In this perspective, the development of a method in which the use of stabiliser is avoided would be desirable.
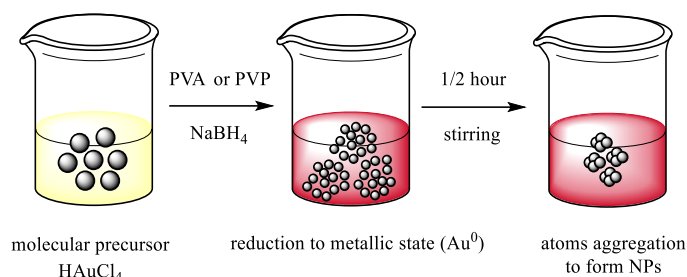
Figure 1.4 – Colloid formation during the sol-immobilisation procedure for the preparation of Au nanoparticles

The literature reports a variety of catalysts prepared by this method, ranging from monometallic (e.g., Au [59, 60], Pd [61]) to bimetallic (e.g., Au-Pd , Pd-Pt) and trimetallic (e.g., Au-Pd-Pt [62-64]) nanoparticles, supported on different materials such as e.g., various oxides, carbon [59, 61, 65-67]. The method allows achieving metal loadings up to 5% wt, without significantly changing the morphology or the dispersion of nanoparticles. For the multimetallic nanostructures, their morphology was found to be likely homogeneous alloy [62, 68]. These catalysts were employed for a wide range of oxidation and reduction reactions [49, 59, 69-74].

1.2.3 Noble metal nanoparticles

1.2.3.1 Au nanoparticles

Gold nanoparticles have be investigated since ancient times and used for a large range of applications, from colouring, as witnessed by the famous Lycurgus cup (4th-5th century B.C.), to medicine [21]. The birth of the modern gold colloidal science can be traced to 1857, when Faraday reported the synthesis of colloidal gold by reduction of a chloroaurate solution with phosphorus in CS_2 [75]. In the 20th century, the increasing interest in the subject, led to the development of other important synthetic methods, which allowed better control in the stabilisation and dispersion of nanoparticles size [21, 76-78]. The considerable interest in Au nanoparticles arises from their potential application in catalysis (in quasi-homogeneous or heterogeneous processes) [20], biology [18] and optics [79-81], since they are the most stable to oxidation, better electron conductors and offer unique surface chemistry that allows them to be used as a platform for organic molecule assembly [82]. Moreover, biocompatibility, availability and easy recovery make gold a very promising material from a green chemistry perspective [83]. One of the most fascinating properties of Au nanoparticles is that they exhibit the *localised*

surface plasmon resonance (LSPR) in the visible region of the spectrum. This, as will be further discussed, represents one of the most interesting phenomena that can be used for a wide range of applications.

Historically, the two most popular methods for the preparation of colloidal gold nanoparticles are the citrate-reduction, introduced by Turkevich [76] in 1951, and the two-phase Brust-Schiffrin method [77,84] developed in 1990s. The former involves the reduction in water of $HAuCl_4$ with citrate, which also works as a stabiliser, and leads to the formation of spherical Au nanoparticles sized ca. 20 nm. The latter involves the transfer of an aqueous solution of $HAuCl_4$ in alkanethiol in toluene by using tetraoctylammonium bromide (TOAB, $(octyl)_4$ N^+Br^-) as a phase transfer reagent, followed by reduction with $NaBH_4$ under vigorous stirring. This method allows homogenously sized nanoparticles with a maximum size distribution at 2-2.5 nm. Both these methodologies provided the basis for the development of other synthetic routes, e.g., use of different ligands and/or reductants [21].

Catalytic activity on gold surfaces has long been considered impossible: because of its high reduction potential, gold has long been regarded as an "inert" surface [21, 85], until Bond and co-workers firstly demonstrated that very small Au nanoparticles supported on silica could give interesting catalytic activity for hydrogenation of alkenes [86]. The field of gold catalysis began to accelerate in the 1980s with the pioneering work of Haruta [87, 88] on CO oxidation at low temperature, and Hutchings [89] on ethyne hydrochlorination, which clearly demonstrated that gold had unique catalytic properties, that seem to be highly dependent on the size and shape of nanoparticles. Supported gold nanoparticles have been and are currently being investigated for a large number of reactions of industrial interest, including selective oxidation (e.g., alcohols and polyols [49, 59, 83, 90-96]), production of hydrogen peroxide (H_2O_2) starting from H_2 and O_2 [97-99], hydrogenations [100-103] and C-C couplings [20, 104]. However, it was found that their activity strongly depends on the synthesis route, especially when employed in structure-sensitive reactions such as e.g. CO oxidation and propylene epoxidation. According to Haruta [105, 106], in these cases, both rate and selectivity markedly depend on the size of Au nanoparticles, the selection of the support and the contact structure of the Au nanoparticles with the support. Since the preparation method affects the morphology of the nanoparticles and the metal/support interaction, a

lot of efforts have been made in order to assess as much as possible the relationship between the support/preparation and characteristics of the produced materials [46, 56].

In general, the synthetic procedures for preparing supported gold nanoparticles follow the methods described in Section 1.2.2. Amongst these, the sol-immobilisation method has been largely employed. The group of Prati was the first to employ and investigate such catalysts for oxidation of ethylene glycol [49, 107, 108] and glucose [91]. Since the method presents important advantages in terms of control of the size and distribution of the nanoparticles, investigation was also extended to other important reactions such as benzyl alcohol [59] and glycerol oxidation [73, 90, 92]. All these studies highlighted how the nature of the sol (i.e., of the stabilising agent) and of the support play a fundamental role in determining the size and distribution of the nanoparticles [107]; also heat treatment [59] was proven to have an important effect on the size and hence, ultimately, on the catalytic activity.

As previously mentioned, the possibility of controlling the size and shape of nanoparticles is very important for catalyst design, since it leads to the modification of the properties of the material by introducing defects (e.g., kinks, edges, vacancies), thereby determining its catalytic activity. In the case of Au nanoparticles, the possibility of controlling their size and shape is even more interesting since it would allow to tune the LSPR response, as will be covered more in detail in the present chapter. Amongst the synthetic routes for controlling the nanoparticles shape, one of the most employed is the seed-growth method [109-114], which involves the preparation of spherical nanoparticles (seeds) and their growth in a micellar environment achieved by the introduction of surfactants, and leading to different shapes (e.g., nanorods). This method allows fine control of the nanoparticles shape [112], but major limitations in the use of such nanostructures for heterogeneous catalytic applications are again due to the presence of a surfactant layer which might interfere with the catalytic activity, and to the loss of the anisotropy when supported.

1.2.3.2 *Noble metal alloys*

The investigation on Au nanoparticles is not only limited to the monometallic materials: indeed, their properties can be enhanced by alloying with other metals, opening a complete new field where great efforts have been and are currently made in order to understand and valorise the synergistic effects. As remarked by

Gilroy *et al.* [115], one of the most important features of using multimetallic nanocrystals is the possibility of combining the different physicochemical properties of the two metals: for example, Au, Ag and Cu are important for their plasmonic properties, Pd, Pt, Ir, Ru, Rh for catalysis and Ni, Co, Fe for magnetism. Nanoalloys are often described in terms of "composition" only. However, this definition is rather reductive, since their properties are quite sensitive to the architecture: they can indeed differ in terms of atomic ordering (alloy or intermetallic), crystal structure, internal structure (with different types of defects), shape or type of facets, configuration (dimeric, dendritic, core-shell) [115,116]. All these features contribute to the determination of the final properties of the nanoalloys [115]; for example, catalytic properties, depending on the surface, are widely affected by the presence of another metal [117]. A general classification of the nanoalloys can be made in terms of atomic ordering and geometry, as reported by Ferrando *et al.* [118] (Figure 1.5).

core-shell   segregated   mixed   three - shell
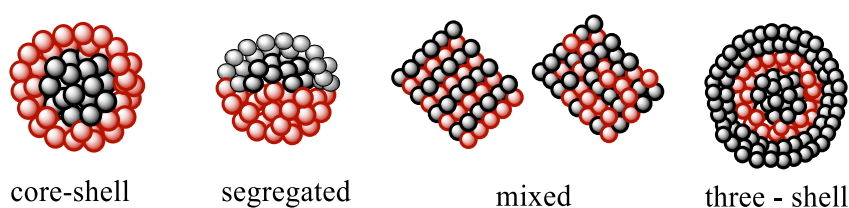
Figure 1.5 – Possible mixing patterns for a bimetallic nanoalloy (adapted from ref. [118])

The possibility of forming a thermodynamically stable alloy or intermetallic compound relies on several parameters. In general, the mixing of two metals (M and N) is favoured when (i) the M-N bond is stronger than the M-M or N-N bond; (ii) the two metals have similar lattice parameters (e.g., crystal structure); (iii) the two metals have similar surface energy [118]. The synthesis of (supported) bimetallic and trimetallic nanoparticles of Au alloyed with other metals (e.g., Pt, Pd) for heterogeneous catalytic applications has been reported in a wide number of studies, were references can be found in complete reviews [30,115].

The synthetic strategies that allow preparation of nanoalloys include co-reduction, thermal decomposition and seed mediated growth [116]. Depending on the route followed, parameters such as the difference in the reduction potential of the metals or the rate of decomposition of their precursors must be taken into account for the aforementioned reasons. The presence of ligands or coordination ions has also a crucial importance since the reduction potential changes depending on their nature [115], and these properties might be useful when

preparing core/shell structures. Also capping agents which are effective for the synthesis of monometallic nanoparticles, might not have the same outcome in the synthesis of multimetallic nanoparticles.

1.3 Nanoparticles for photocatalytic applications

1.3.1 Classic photocatalysis

Photocatalysis and photocatalytic processes have been attracting tremendous attention during the last years due to the necessity to overcome problems such as environmental pollution and finding energy sources alternative to fossil fuels. The investigation of the photocatalysis field started in the early 1920s, when Renz at the University of Lugano (Switzerland) observed that titania (TiO_2) is partially reduced in presence of light and an organic compound [119, 120], and similar behaviour was found in other materials such as Ta_2O_5, CeO_2, and Nb_2O_5. Later, it was proposed that these materials act as photocatalysts since they accelerate the degradation of organic compounds under illumination, and the origin of their activity relies on their semiconductor nature.

A semiconductor, according to the band theory [121], shows a valence band (VB) and a conduction band (CB) separated by a band gap of energy E_g. In order to promote an electron from the VB to the CB an appropriate amount of energy is required to overcome the band gap [122]. This energy can be supplied by a light of determined frequency ($h\nu \geq E_g$), and results in the generation of an electron in the CB and a correspondent hole left in the VB (Figure 1.6).
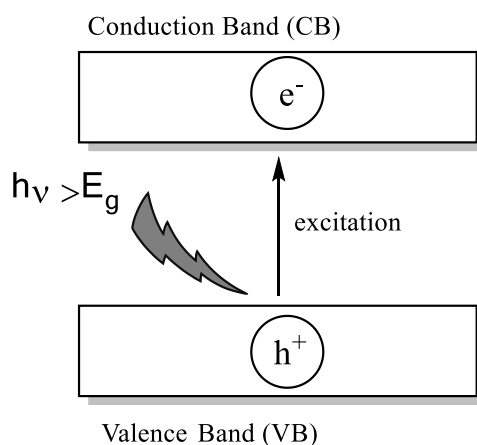
Figure 1.6 – Charge separation induced by light of energy $h\nu \geq E_g$

Electrons and holes are named *charge carriers* and can subsequently migrate to the surface of the semiconductor and promote reduction and oxidation reactions respectively [123], as displayed in Figure 1.7. Therefore, an efficient separation and consequent enhancement in the life-time of the charge carriers is of crucial importance for an effective photocatalyst.
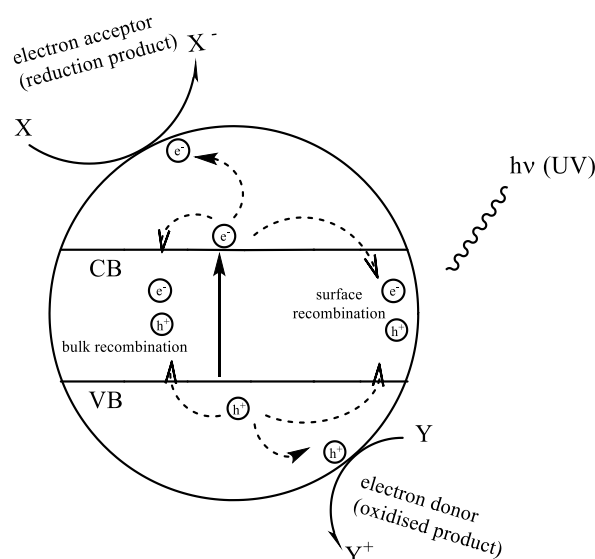
Figure 1.7 – Photocatalytic mechanism on a semiconductor particle, involving the separation of the charge carriers electrons (e^-) and holes (h^+) and their migration on the surface to promote reactions or their recombination with consequent energy dissipation (adapted from ref. [124])

Since the very early discoveries, among the semiconductors, TiO_2-based materials have been the most extensively used photocatalysts in applications such as environmental cleaning [122] and hydrogen energy generation [125] due to high stability, nontoxicity and high reactivity [123]. However, the short lifetime of the generated charge carriers and the photo-absorption limited to the UV region only (4% of the solar spectrum) [126, 127] due to the wide band gap (for TiO_2, 3.0-3.2 eV [128]), forced the development of new photocatalytic materials. Many strategies including metal and non-metal doping [123] have been widely investigated and applied in order to reduce the band gap of the semiconductors, but unfortunately, these materials typically suffer from thermal instability, photocorrosion and fast h^+/e^- recombination rates [126].

Since classic photocatalysis suffers from these inherent drawbacks, the development of efficient future generation of photocatalysts could involve the use of nanoparticles able to harvest the visible portion of the

light through the localised surface plasmon resonance (LSPR), such as Ag, Cu and Au, which have been successfully applied to many fields and proven to be very promising [129]. These materials are of great interest because they can potentially catalyse reactions at lower temperatures, leading to the possibility of decreasing operating costs and reducing the formation of unwanted side products [130]. In addition, many of them already show good activity for "thermal" catalytic processes (e.g., Au nanoparticles).

1.3.2 Origin of the LSPR

The LSPR is defined by Mie theory as a resonant photoinduced coherent oscillation of the free electrons at the metal-dielectric interface that is established when the photon frequency of an incident wavelength bigger than the nanoparticle size, matches the natural frequency of the metal surface electrons oscillating against the restoring force of their positive nuclei [10, 81, 127, 131-133] (Figure 1.8). Mie solved the Maxwell equations for a homogeneous sphere irradiated by an electromagnetic plane wave; assuming that the incident wavelength is much bigger than the nanoparticle size [10], the optical interaction depends on the radius of the nanoparticle (r), the wavelength of the incident light (λ), the dielectric constant of the surrounding medium (ε_m) and the real and imaginary parts of the particle's dielectric constant, ε_r and ε_i respectively. The extinction cross section C_{ext} is given by:

$$C_{ext} = \frac{24\pi^2 r^3 \varepsilon_m^{3/2}}{\lambda} \frac{\varepsilon_i}{(\varepsilon_r + 2\varepsilon_m)^2 + \varepsilon_i^2} \quad \text{(Eq. 1.4)}$$
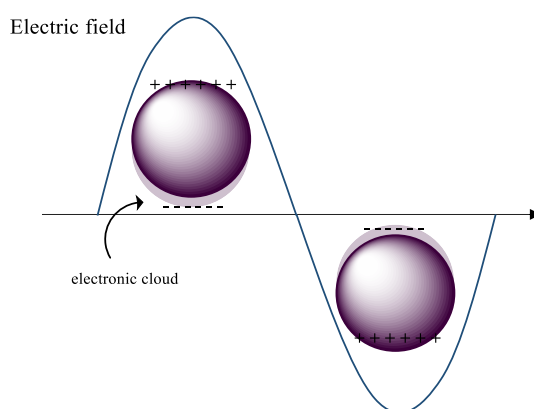
Figure 1.8 – Schematic representation of the LSPR in a nanoparticles irradiated by light

From this equation, C_{ext} has a maximum when the denominator is minimised, and this is ultimately determined by the dielectric constant. Since this is generally considered to be invariant with respect to the nanoparticles size and shape, by simply knowing the dielectric constant of the material is possible to calculate the resonation wavelength (C_{ext} maximum), given when the condition $\varepsilon_r = -2\,\varepsilon_m$ [115] (Eq. 1.4) is verified. It also follows, from Eq. 1.4, that the LSPR can be tuned by modifying the dielectric constant of the surrounding (as demonstrated, e.g., by Ghosh *et al.* [134]), and the size and shape of the nanoparticle [9]: an increase in the size of a spherical nanoparticle results in a more intense and red-shifted LSPR absorption signal, due to a low frequency of the collective oscillation of electrons [135,136]; a different shape results in the modification of the LSPR signal, as displayed in Figure 1.9 for Ag nanoparticles. The presence of any degree of anisotropy, such as in e.g. nanorods, results in two LSPR signals correspondent to longitudinal and transversal resonance, which is very sensitive to the aspect ratio (length/width): e.g., higher aspect ratio results in a red-shift of the LSPR signal [16,131,133,137,138] as displayed in Figure 1.10.
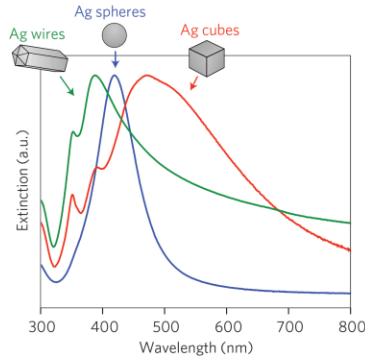
Figure 1.9 – LSPR wavelengths for Ag nanoparticles of different shape (from ref. [9])
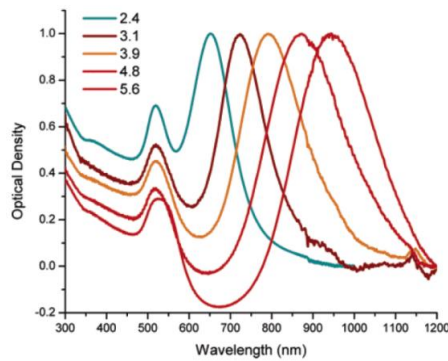
Figure 1.10 – LSPR wavelengths for Au nanorods of different aspect ratio (from ref. [16])

Finally yet important, the LSPR can also be tuned by controlling the composition, electron density and configuration (e.g., core-shell) of the nanocrystals. Indeed, the formation of an alloy or intermetallic compounds of two plasmonic metals that show a LSPR in the visible region (e.g., Au-Cu, Au-Ag, Ag-Cu) give rise to structure where the LSPR position varies linearly with the stoichiometry of the nanocrystal [115]. However, alloying with any of the UV-resonant metal such as Pd or Pt leads to a quenching of the LSPR signal, attributed to a different electronic structure that modifies the intrinsic optical properties of the material and/or to the presence of inhomogeneous doping/alloying [139, 140].

1.3.3 Photochemistry

LSPR is a complex phenomenon that gives rise to a number of interdependent physical effects such as optical near field enhancement, heat generation and excitation of highly energetic electrons (the so-called "hot electrons") [81]. The optical field enhancement is due to the light-induced oscillation of the electronic cloud, which behaves as a dipole and re-emits the light coherently at the same frequency of the incident light; a part of this light is scattered, whereas another is concentrated at the metal surface, thereby increasing the available number of photons per unit volume [81]. These optical "hot spots" are expected to increase the yield of photochemical reactions in the proximity of the metal surface by the generation of hot electrons [81, 127], and is an area of great interest for applications where an enhanced light-matter interaction is required [133] (e.g., solar cells and some spectroscopic techniques). The generation and relaxation of the hot electrons following the plasmon excitation are responsible for the cascade processes leading to the redistribution of energy from the metal to the nearby acceptors, through heating of the nanoparticles or excitation of charge carriers. These processes are rather complex and not fully understood, but current theories also supported by experimental data propose that hot electrons, which remain in the excited state in a timescale of tens femtoseconds [133], undergo relaxation mechanisms through radiative photon re-emission or non-radiative excitation of charge-carriers (absorption) [131, 133]. This latter mechanism is responsible for the energy transfer to the adsorbate, thereby inducing chemical reactions. In their complete and exhaustive review, Linic *et al.* [133] propose that the non-radiative relaxation occurs *via* two mechanisms:

1) heating of the nanoparticles induced by the interaction of the energetic charge carriers with other charge carriers and the vibrational modes of the nanoparticles;

2) formation of transient ions or excited states through charge carrier energy transfer to the energetically accessible orbitals of the adsorbed molecules.

Figure 1.11 illustrates the mechanism for the thermal (a) and electron-driven (b) dissociation of a diatomic molecule: the thermal energy (a) causes the molecule to dissociate by exciting the vibrational levels in the ground state; in the charge-carrier mechanism (b), the injection of an electron promotes the excitation of the molecule to a charged state, and when the system relaxes, the molecule moves back to the ground state at higher energy (i.e., higher vibrational levels). This charge-carrier mechanism can potentially drive the selectivity to certain chemical pathways that are forbidden in the thermal reaction mechanism, as illustrated in Figure 1.12. However, despite this distinction between the mechanisms, it is likely that they occur and contribute together during the plasmonic-enhanced chemical transformations.
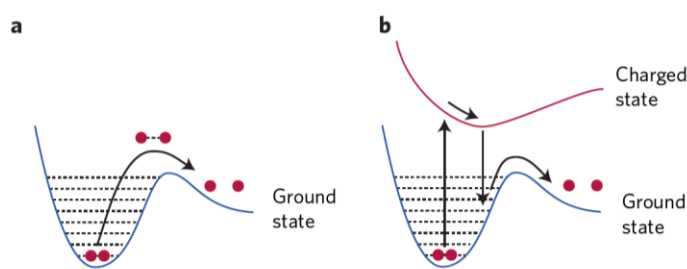
Figure 1.11 – Mechanism of a diatomic molecule dissociation induced by thermal energy (a) and charge carriers (b) (from ref [133])
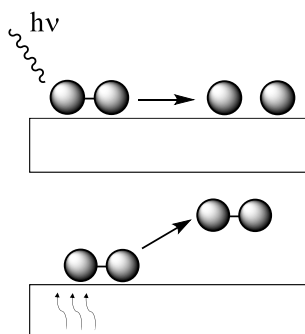
Figure 1.12 – Difference in the reaction pathways for charge carrier (top) and thermal (bottom) mechanism (adapted from ref [133])

The energy transfer to the adsorbate induced by the charge carriers can occur indirectly or directly, as illustrated in Figure 1.13. In the former (Figure 1.13 a), plasmon relaxation results in an electron distribution characterised by low-energy charge carriers, that can be transferred to the lowest unoccupied orbitals of the adsorbate, potentially inducing chemical transformations. In the latter mechanism, depicted in Figure 1.13 b the hot electrons are directly injected to the adsorbate orbitals causing the excitation of electrons to the lowest unoccupied adsorbate state. However, despite the distinctions made between the mechanisms (heat and charge carriers), it is likely that they occur and contribute together to the plasmonic-enhanced chemical transformations.
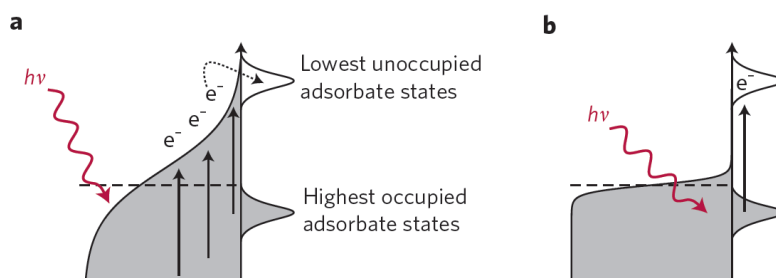
Figure 1.13 - Indirect and direct mechanism of charge transfer in plasmonic nanostructures (from ref. [133])

In the case of heterogeneous photocatalysts, where plasmonic nanoparticles are often combined with a semiconductor material (e.g., TiO_2, ZrO_2, CeO_2), the energy transfer from the nanoparticles to the adjacent semiconductor plays a fundamental role in the photocatalytic functions [127, 131].

As reported by Linic and co-workers in their remarkable review [9], experimental measurements on such catalysts evidenced a photocatalytic rate enhancement as a function of irradiation wavelength, confirming the fundamental role of LSPR; as expected, irradiation wavelengths corresponding to the metal LSPR resulted in the highest rate enhancements, and same conclusion were found after manipulation of size, shape and composition of the nanostructure. These results demonstrated the existence of a positive relationship between SPR intensity and the rate enhancement, and led to the hypothesis that the plasmonic nanostructures enhance rates of photocatalytic reactions on nearby semiconductors by energy transfer. There are three proposed mechanisms through which this happens: direct injection of charge carriers into semiconductor surface, localised electromagnetic field and scattering of resonant photons.

The former mechanism is found effective for nanoparticles in direct contact with semiconductor, and presents analogies to a dye-sensitisation mechanism: the plasmonic nanostructure behaves similar to a dye molecule, absorbing visible light and transferring energetic charge carriers to semiconductor. In this sense, noble metal plasmonic nanoparticles represent a very promising sensitizers, being characterised by an excellent mobility of charge carriers, high absorption cross sections and the possibility to tune the LSPR by modifying their shape and size. In this mechanism [141, 142], the LSPR excitation of conduction electrons of the noble metal nanoparticles can be transferred to the conduction band of the semiconductor, leaving the nanoparticles positively charged and therefore able to accept electrons from a donor (i.e., the substrate), as illustrated in Figure 1.14.
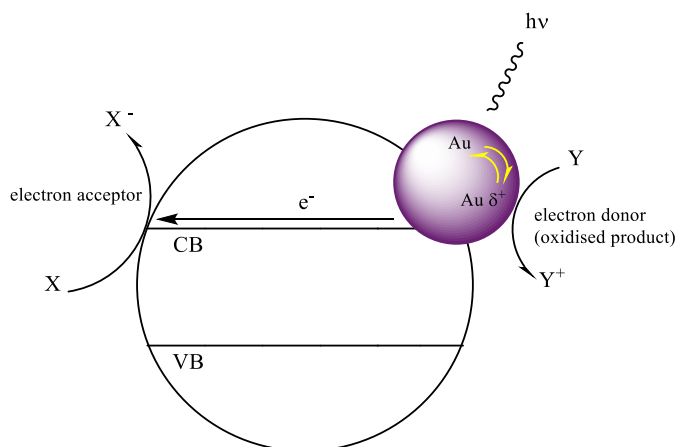
Figure 1.14 – Proposed mechanism for plasmonic electron transfer from an Au nanoparticles deposited on a semiconductor (adapted from ref. [142])

Therefore, it is easily understandable how the presence of any obstacle at the interface, such as a layer of stabiliser, will hinder this mechanism or dramatically decrease the intensity of the LSPR-induced electromagnetic field close to the semiconductor, as this exponentially decays with distance [143]. Conversely, when nanoparticles are supported on insulators, the photocatalytic activity is expected to be determined by the enhancement of the optical field and by direct interaction of the hot electrons generated by the LSPR with the reactants [127].

In these cases plasmonic enhanced chemical transformations occur according to the second and third charge transfer possibilities, which involve radiative energy transfer from the metal LSPR to the semiconductor

via near-field electromagnetic and resonant photon-scattering [9]. The former is based on the interaction of the semiconductor with the strong LSPR-induced electric fields of the plasmonic nanostructure. These fields present the highest intensity at the surface of nanostructures and decrease exponentially with distance from the surface within ~20-30 nm, and linearly further away, therefore when a semiconductor is in the proximity of a photo-excited plasmonic nanostructure it experiences these strong fields. Since the rate of electron-hole formation in a semiconductor is proportional to the local intensity of the electric field, the rate of electron-hole formation in some regions (i.e., near the surface) of the semiconductor is enhanced. The second and last mechanism of photon-scattering is predominant in larger nanoparticles (diameter ~50 nm) and increases the average path length of photons, causing an increased rate of electron-hole pair formation in the semiconductor.

The synthesis of plasmonic nanostructures follows the synthetic procedures of nanoparticles already reviewed in the present chapter, but more detailed descriptions along with the catalytic applications are available in references [115, 116, 127, 131, 135, 138, 144]. Amongst the heterogeneous catalysed reactions, plasmonic nanoparticles have been successfully employed for the oxidation of glycerol.

1.4 Glycerol oxidation using supported noble metal nanoparticles

Since the late 1940s glycerol, which finds a wide range of industrial applications, ranging from food to pharmaceutical and cosmetics, was exclusively produced from epichlorydrin, obtained from propylene (i.e., fossil resources). However, nowadays its availability has increased since the development of green routes to obtain so-called bio-fuels, e.g. bio-ethanol. In this process, based on the transesterification reaction of animal or vegetable waste fats, the glycerol is left as an inevitable by-product. However, the low purity of the glycerol obtained in this way makes it unsuitable for the pharmaceutical or cosmetic industry, therefore its immediate application is in the production of large volume of commodities (Scheme 1.3). For example, among the processes already commercialised there are:

- chlorination to epichlorydrin, developed by Dow and Solvay in 2007, an important intermediate for epoxy resins [145];

- esterification to monoacyl and diacyl esters, which find applications in food and cosmetics where they are used as emulsifiers, supports for flavourings and essences, plasticisers, solvents and many others.
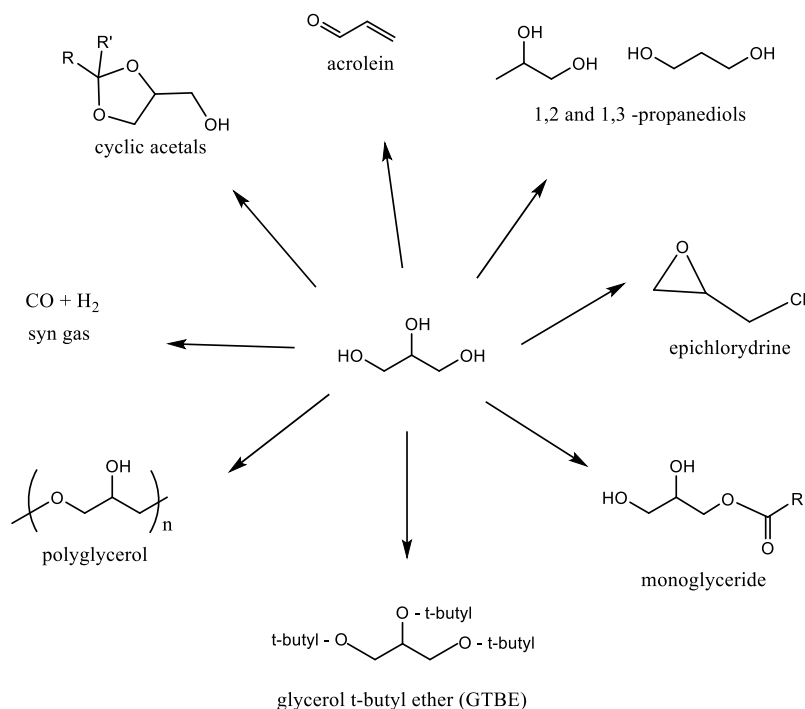
Scheme 1.3 – Possible glycerol valorisation products

Intensive investigation is currently ongoing on other potential applications such as: etherification to glycerol tert-butyl ether (GTBE), a gasoline additive for increasing the number of octane [145, 146]; selective reduction to 1,2 and 1,3-propanediol [147], which would find application in the polymer industry [145]; dehydration to acrolein, used in the synthesis of agrochemicals like methionine, fragrances and dyes [145, 148].

However, one of the most promising routes for the valorisation of the glycerol is selective oxidation (see Scheme 1.4), since its high level of functionalisation makes it a very promising building block for obtaining high alue fine chemicals. Thanks to the presence of two primary and one secondary hydroxyl groups, selective oxidation would potentially lead to a large number of valuable products, for example:

- dihydroxyacetone (DHA), used as active ingredients in self-tanners [145]; its dimeric structure easily dissociates to the monomer in water, and the carbonyl group is responsible for the aforementioned function as a tanning agent, based on the Maillard reaction with amino group of human skin and hair [149];

- glyceric acid, would find application in the production of bioplastics, pharmaceuticals, and is an important intermediate for further oxidation products such as tartronic acid and mesoxalic acid;

- glycolic acid, used in personal care products;

- tartronic acid, used in the pharmaceutical industry for the treatment of osteoporosis and obesity but is also used as an anticorrosive protective agent for high temperature applications in which steam has to be handled. Its anti-corrosive properties are ascribed to its role as an oxygen scavenger, which also are of interest in the third commercial application of TA as an oxygen absorber in the food industry;

- mesoxalic (or ketomalonic) acid in its hydrate form is a fine chemical used in the pharmaceutical industry for the treatment of diabetes;

- formic acid might find applications as hydrogen storage molecule, capable to catalytically release H_2 on demand [150,151].
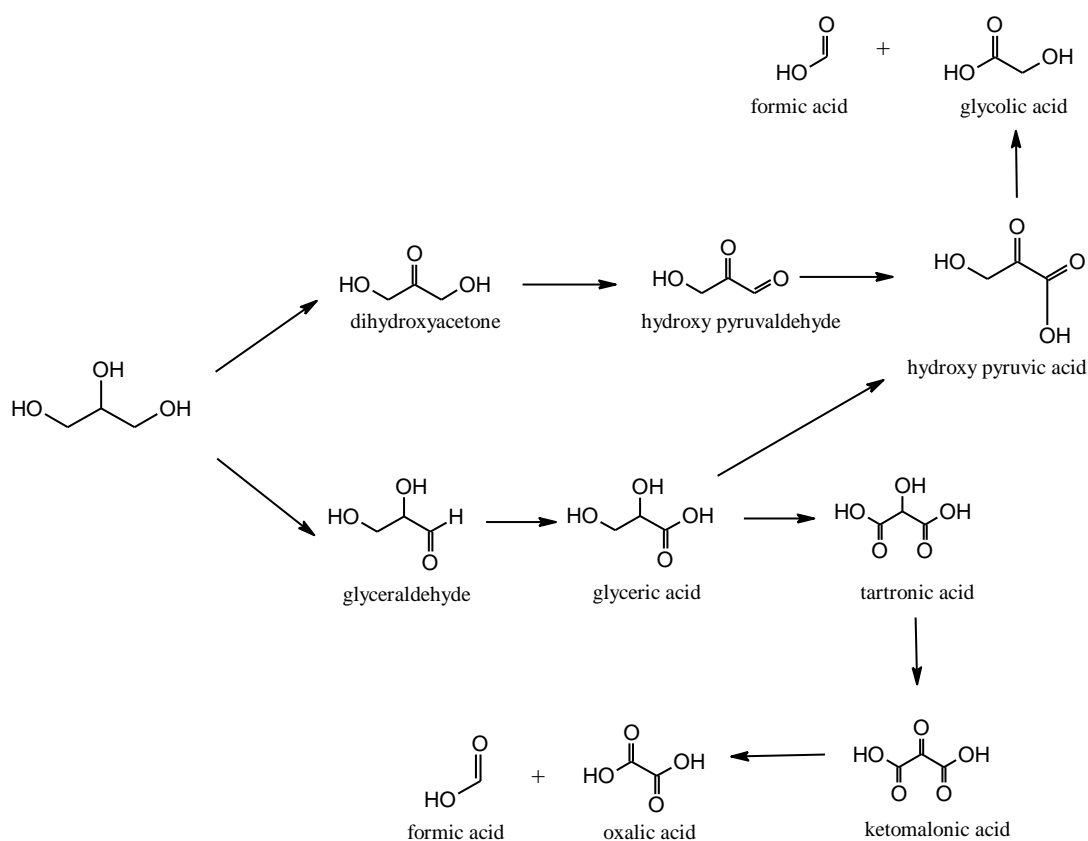
Scheme 1.4 – Selective glycerol oxidation pathways and products

The real challenge is to keep the catalytic processes selective, and this implies the design of new, effective heterogeneous catalysts to control the chemoselectivity to desired products. An increasing number of studies

have been published concerning this topic, and they are mainly based on the use of supported noble metal nanoparticles [6] for catalytic processes either under "thermal" and photocatalytic (plasmonic) conditions, as it is reviewed in the following paragraphs.

Rossi and Prati [91, 107], followed by Hutchings [152-155] firstly demonstrated that supported Au nanoparticles were active in the selective catalytic oxidation of glycerol with O_2. These studies showed that Au nanoparticles based catalysts were less prone to deactivation and O_2 poisoning when compared to traditional catalysts based on Pt or Pd. However, when working with monometallic Au nanoparticles-based catalysts, basic conditions are required in order to achieve an effective catalysis, with the drawback that the products are in the form of salt, therefore need further purification [6, 156]. It is believed that the high pH is necessary in order to promote the formation of the alkoxide by hydrogen abstraction, as first step of catalytic reaction [152, 154, 157].

The preparation method and the nature of the support were of fundamental importance for achieving high catalytic activity and selectivity [60, 92, 93, 158, 159]. One of the most employed methodologies for the synthesis of catalysts for glycerol oxidation is the sol-immobilisation, that allowed to deposit the metallic nanoparticles on a wide range of supports (e.g., carbon and oxides such as e.g., Al_2O_3, TiO_2, MgO [66]) as described in Section 1.2.2. The main drawback of this method, however, is the presence of stabilising agents such as polymers or surfactants, needed to achieve a good control on the nanoparticles size, which might have an influence on the catalytic activity and selectivity [55, 160, 161]. Therefore, a lot of effort were made to assess the influence of the different stabilisers and methodology for removal without changing the nanoparticles morphology [52, 57].

A large number of studies [54, 73, 108, 162] have been carried out in order to determine the influence of the nanoparticles size on the catalytic performances. In general, smaller Au nanoparticles (2-6 nm), because of the large surface area and edge exposure, were found to be more active than larger nanoparticles (10-30 nm), but these latter showed an increased selectivity towards the glycerate [149]. Conversely, smaller nanoparticles leaded to an increased selectivity towards C_2 (mainly glycolate) and C_1 products, as a consequence of the increased hydrogen peroxide production and subsequent C-C cleavage, as demonstrated by Davis' group [157, 162-164].

Moreover, it seems that the formation of hydrogen peroxide is favoured by the (111) facets of the Au nanoparticles [165].

In addition to the size, also the influence of the location of Au nanoparticles have been investigated. In their study, the group of Prati [159] compared the catalytic response of two monometallic catalysts based on Au nanoparticles supported on nitrogen-doped carbon nanofibers (N-CNF). The sol-immobilisation method was employed to deposit the Au nanoparticles on the N-CNF surface, whereas the incipient wetness impregnation led to the deposition of the Au nanoparticles inside the tubular structure of the N-CNF. The so-synthesized nanoparticles showed a mean diameter of 3.2-3.4 nm. Studies on glycerol oxidation evidenced that the nanoparticles location plays a fundamental role in determining the catalytic activity of the sample: indeed, at *iso-conversion*, the catalyst prepared *via* wet-impregnation led to an increased activity and selectivity to tartronic acid. They concluded that the preferential orientation of the glycerol due to its confinement inside the CNF tubes probably causes a different adsorption mode which favours the oxidation to tartronate.

It has been shown that alloying the Au with other metals such as Pd, Pt with acidic or basic supports improves the activity under neutral conditions [95, 156, 158], and the use of such multi-metallic nanoparticles based catalysts has been shown to be very promising in terms of improvement of catalytic stability, activity and selectivity [68, 74, 152, 166, 167]. For example, it has been shown that alloying Au with Pd or Pt resulted in higher selectivity to C_3 products (tartronate and glycerate) [94]; as proposed by Davis' group [168], the presence of Pd is beneficial since promotes a faster decomposition of hydrogen peroxide.

Photocatalysis (plasmonic) was also proven to be effective for the aerobic oxidation of glycerol under neutral conditions. The group of Tüysüz investigated this reaction using Au nanoparticles supported on TiO_2 [169] and Au and AuCu on mesoporous SiO_2 [170]. In both cases, they showed that an improvement in the conversion, compared to dark conditions, can be achieved when the reaction is conducted under visible light, confirming the plasmonic response of the catalysts. For the Au/TiO$_2$ catalysts, it was shown that the activity increase with the increase in the metal loading, reaching 50% conversion under illumination vs 30% conversion in dark (thermal) conditions. However, after a given value, no further increase was observed (Figure 1.15 a). Figure 1.15 b reports the selectivity to the oxidation products, with the highest value to DHA.

The lower carbon mass balance and the increase glycolic acid production detected for the reaction under illumination conditions were ascribed to an increased production of hydrogen peroxide, which leads to the C-C cleavage as already observed by other groups (and aforementioned) on Au/TiO$_2$ catalysts. They proposed an oxidation mechanism similar to the one proposed by Tsukamoto et $al.$ [142] (Figure 1.14).

The catalysts supported on mesoporous silica spheres tested for the same reaction were proven to show a visible-light plasmonic response, and it was observed that the mesoporous structure of the support plays an important role in the stability of the Au nanoparticles, leading to higher activity. The alloying with Cu resulted in an increased glycerol conversion of a 2.5 factor due to the synergistic effect.
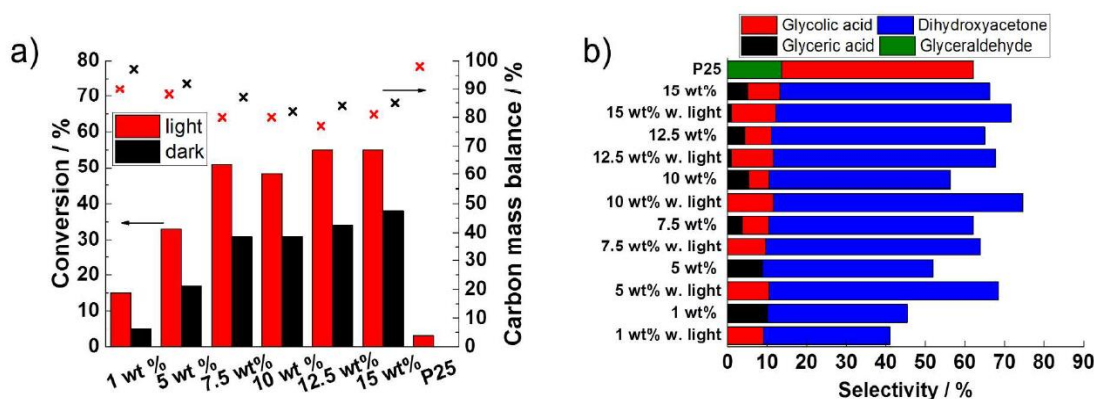
Figure 1.15 – Glycerol conversion and selectivity under dark conditions and illumination on Au/TiO$_2$ (from ref. [169])

1.5 Aim of the work

The aim of the present Thesis is to show that active 1% wt Au and AuPd supported on TiO$_2$ can be successfully synthesized by the sol-immobilisation method without any stabilising agent control. The activity of these catalysts was evaluated and compared with the activity of the analogous counterparts synthesized via the traditional sol-immobilisation method using PVA or PVP.

The catalysts were tested for the gas phase CO oxidation (monometallic only), solvent-free benzyl alcohol oxidation (bimetallic only) and glycerol oxidation under basic conditions (both). For this latter, it will be demonstrated how the presence and the nature of the polymer can affect the selectivity towards major products, while not influencing the conversion.

Higher loading monometallic catalysts (1-7 nominal wt %) were also synthesized *via* stabiliser-free and traditional sol-immobilisation methods and employed, for the first time, for the oxidation of glycerol in neutral and plasmonic conditions. It will be shown that, conversely to the "thermal" catalysis, the absence of the stabiliser has a major effect on the catalytic activity, perhaps due to the crucial role of the metal/support interface.

Finally, for the first time, bimetallic 1% wt AuPd/TiO$_2$ (with different Au:Pd ratio) catalysts prepared *via* sol-immobilisation were employed for the oxidation of glycerol under plasmonic conditions. It will be shown how the catalytic activity under illumination depends on the content of the plasmonic metal Au, confirming the existence of a visible light response also in bimetallic structures.

Bibliography

1. J. A. Dumesic, G. W. Huber and M. Boudart, *in Handbook of Heterogeneous Catalysis,* Wiley and Sons, **1999-2014**, pp. 1-15.

2. J. M. Thomas and J. W. Thomas, *Principles and Practice of Heterogeneous Catalysis,* Wiley-VCH, **1997**.

3. P. Anastas and N. Eghbali, *Chemical Society Reviews*, **2010**, *39*, 301-312.

4. N. Dimitratos, J. A. Lopez-Sanchez and G. J. Hutchings, *Topics in Catalysis*, **2009**, *52*, 258-268.

5. G. W. Huber and A. Corma, *Angewandte Chemie Int. Ed.*, **2007**, *46*, 7184-7201.

6. C. H. Zhou, J. N. Beltramini, Y. X. Fan and G. Q. Lu, *Chemical Society Reviews*, **2008**, *37*, 527-549.

7. M. A. Fox and M. T. Dulay, *Chemical Reviews*, **1993**, *93*, 341-357.

8. A. Ibhadon and P. Fitzpatrick, *Catalysts*, **2013**, *3*, 189-218.

9. S. Linic, P. Christopher and D. B. Ingram, *Nature materials*, **2011**, *10*, 911-921.

10. X. Zhang, Y. L. Chen, R. S. Liu and D. P. Tsai, *Reports on Progress in Physics. Physical Society*, **2013**, *76*, 046401 (41pp).

11. B. C. Gates, *Catalytic Chemistry,* Wiley & Sons, **1992**.

12. M. Boudart, *Chemical Reviews*, **1995**, *95*, 661-666.

13. J. W. Geus and A. J. van Dillen, *in Handbook of Heterogeneous Catalysis,* Wiley and Sons, **1999-2014**, pp. 428-467.

14. J. K. Norskov, T. Bligaard, B. Hvolbaek, F. Abild-Pedersen, I. Chorkendorff and C. H. Christensen, *Chemical Society Reviews*, **2008**, *37*, 2163-2171.

15. J. M. Campelo, D. Luna, R. Luque, J. M. Marinas and A. A. Romero, *ChemSusChem*, **2009**, *2*, 18-45.

16. X. Huang, I. H. El-Sayed, W. Qian and M. A. El Sayed, *Journal of the American Chemical Society*, **2006**, *128*, 2115-2120.

17. X. Huang and M. A. El-Sayed, *Journal of Advanced Research*, **2010**, *1*, 13-28.

18. P. K. Jain, K. S. Lee and M. El-Sayed, *The Journal of Physical Chemistry B*, **2006**, *110*, 7238-7248.

19. R. Mout, D. F. Moyano, S. Rana and V. M. Rotello, *Chemical Society Reviews*, **2012**, *41*, 2539-2544.

20. M. Stratakis and H. Garcia, *Chemical Reviews*, **2012**, *112*, 4469-4506.

21. M. C. Daniel and D. Astruc, *Chemical Reviews*, **2004**, *104*, 293-346.

22. A. Corma and H. Garcia, *Chemical Society Reviews*, **2008**, *37*, 2096-3126.

23. H. Bönnemann and R. M. Richards, *European Journal of Inorganic Chemistry*, **2001**, *2001*, 2455-2480.

24. T. Hyeon, *Chemical Communications*, **2003**, *0*, 927-934.

25. N. Sozer and J. L. Kokini, *Trends in Biotechnology*, **2009**, *27*, 82-89.

26. S. Anandan, X. Wen and S. Yang, *Materials Chemistry and Physics*, **2005**, *93*, 35-40.

27.   C. J. Jia and F. Schuth, *Physical Chemistry Chemical Physics: PCCP*, **2011**, *13*, 2457-2487.

28.   M. Brust and C. J. Kiely, *Colloids and Surfaces A: Physicochemical and Engineering Aspects*, **2002**, *202*, 175-186.

29.   P. Zhao, N. Li and D. Astruc, *Coordination Chemistry Reviews*, **2013**, *257*, 638-665.

30.   N. Toshima and T. Yonezawa, *New Journal of Chemistry*, **1998**, *22*, 1179-1201.

31.   Y. Xia, Y. Xiong, B. Lim and S. E. Skrabalak, *Angewandte Chemie Int. Ed.*, **2009**, *48*, 60-103.

32.   Y. Wang, J. He, C. Liu, W. H. Chong and H. Chen, *Angewandte Chemie Int. Ed.*, **2015**, *54*, 2022-2051.

33.   N. T. Thanh, N. Maclean and S. Mahiddine, *Chemical Reviews*, **2014**, *114*, 7610-7630.

34.   V. K. LaMer and R. H. Dinegar, *Journal of the American Chemical Society*, **1950**, *72*, 4847-4854.

35.   D. V. Goia and E. Matijevic, *New Journal of Chemistry*, **1998**, *22*, 1203-1215.

36.   I. J. and H. Wennerstrom, *Nature Photonics*, **1996**, *379*, 219-225.

37.   H. Chen, J. R. Cox, H. Ow, R. Shi and A. Z. Panagiotopoulos, *Scientific Reports*, **2016**, *6*, 28553.

38.   L. D. Pachón and G. Rothenberg, *Applied Organometallic Chemistry*, **2008**, *22*, 288-299.

39.   R. G. Finke, *Metal Nanoparticles: Synthesis, Characterisation and Applications,* Marcel Dekker, New York, **2002**, 17.

40.   M. T. Reetz and W. Helbig, *Journal of the American Chemical Society*, **1994**, *116*, 7401-7402.

41.   S. Navalon and H. Garcia, *Nanomaterials*, **2016**, *6*, 123.

42.   M. Comotti, C. Della Pina, R. Matarrese and M. Rossi, *Angewandte Chemie Int. Ed.*, **2004**, *43*, 5812-5815.

43.   P. Munnik, P. E. de Jongh and K. P. de Jong, *Chemical Reviews*, **2015**, *115*, 6687-6718.

44.   G. J. Hutchings and J. C. Védrine, in *Basic Principles in Applied Catalysis*, Springer, **2004**, pp. 215-258.

45.   J. A. Schwarz, C. Contescu and A. Contescu, *Chemical Reviews*, **1995**, *95*, 477-510.

46.   L. Prati and A. Villa, *Catalysts*, **2011**, *2*, 24-37.

47.   G. C. Bond and D. T. Thompson, *Catalysis Reviews*, **1999**, *41*, 319-388.

48.   S. Linic, P. Christopher, H. Xin and A. Marimuthu, *Accounts of Chemical Research*, **2012**, *46*, 1890-1899.

49.   L. Prati and G. Martra, *Gold Bulletin*, **1999**, *32*, 96-101.

50.   R. G. DiScipio, *Analytical Biochemistry*, **1996**, *236*, 168-170.

51.   J.-D. Grunwaldt, C. Kiener, C. Wogerbauer and A. Baiker, *Journal of Catalysis*, **1999**, *181*, 223-232.

52.   A. Villa, D. Wang, G. M. Veith, F. Vindigni and L. Prati, *Catalysis Science & Technology*, **2013**, *3*, 3036-3041.

53.   D. G. Duff, A. Baiker and P. P. Edwards, *Chemical Communications*, **1993**, *0*, 96-98.

54. S. M. Rogers, C. R. A. Catlow, C. E. Chan-Thaw, D. Gianolio, E. K. Gibson, A. L. Gould, N. Jian, A. J. Logsdail, R. E. Palmer, L. Prati, N. Dimitratos, A. Villa and P. P. Wells, *ACS Catalysis*, **2015**, *5*, 4377-4384.

55. S. Campisi, M. Schiavoni, C. Chan-Thaw and A. Villa, *Catalysts*, **2016**, *6*, 185

56. L. Prati and A. Villa, *Accounts of Chemical Research*, **2013**, *47*, 855-863.

57. J. A. Lopez-Sanchez, N. Dimitratos, C. Hammond, G. L. Brett, L. Kesavan, S. White, P. Miedziak, R. Tiruvalam, R. L. Jenkins, A. F. Carley, D. Knight, C. J. Kiely and G. J. Hutchings, *Nature Chemistry*, **2011**, *3*, 551-556.

58. A. R. Tao, S. Habas and P. Yang, *Small*, **2008**, *4*, 310-325.

59. N. Dimitratos, J. A. Lopez-Sanchez, D. Morgan, A. Carley, L. Prati and G. J. Hutchings, *Catalysis Today*, **2007**, *122*, 317-324.

60. N. Dimitratos, A. Villa, C. L. Bianchi, L. Prati and M. Makkee, *Applied Catalysis A: General*, **2006**, *311*, 185-192.

61. A. Villa, D. Wang, N. Dimitratos, D. Su, V. Trevisan and L. Prati, *Catalysis Today*, **2010**, *150*, 8-15.

62. Q. He, P. J. Miedziak, L. Kesavan, N. Dimitratos, M. Sankar, J. A. Lopez-Sanchez, M. M. Forde, J. K. Edwards, D. W. Knight, S. H. Taylor, C. J. Kiely and G. J. Hutchings, *Faraday Discussions*, **2013**, *162*, 365-378.

63. G. J. Hutchings, *Catalysis Today*, **2014**, *238*, 69-73.

64. S. A. Kondrat, P. Miedziak, M. Douthwaite, G. L. Brett, T. E. Davies, D. J. Morgan, J. K. Edwards, D. W. Knight, C. J. Kiely, S. H. Taylor and G. J. Hutchings, *Chem Sus Chem*, **2014**, *7*, 1326-1334.

65. J. Pritchard, M. Piccinini, R. Tiruvalam, Q. He, N. Dimitratos, J. A. Lopez-Sanchez, D. J. Morgan, A. F. Carley, J. K. Edwards, C. J. Kiely and G. J. Hutchings, *Catalysis Science & Technology*, **2013**, *3*, 308-317.

66. G. Dodekatos, L. Abis, S. Freakley, H. Tüysüz and G. J. Hutchings, *ChemCatChem*, **2018**, *10*, 1-10.

67. H. Bahruji, M. Bowker, G. Hutchings, N. Dimitratos, P. Wells, E. Gibson, W. Jones, C. Brookes, D. Morgan and G. Lalev, *Journal of Catalysis*, **2016**, *343*, 133-146.

68. N. Dimitratos, J. A. Lopez-Sanchez, J. M. Anthonykutty, G. Brett, A. F. Carley, R. C. Tiruvalam, A. A. Herzing, C. J. Kiely, D. W. Knight and G. J. Hutchings, *Physical Chemistry Chemical Physics : PCCP*, **2009**, *11*, 4952-4961.

69. N. Dimitratos, J. A. Lopez-Sanchez, D. Morgan, A. F. Carley, R. Tiruvalam, C. J. Kiely, D. Bethell and G. J. Hutchings, *Physical Chemistry Chemical Physics : PCCP*, **2009**, *11*, 5142-5153.

70. J. A. Lopez-Sanchez, N. Dimitratos, P. Miedziak, E. Ntainjua, J. K. Edwards, D. Morgan, A. F. Carley, R. Tiruvalam, C. J. Kiely and G. J. Hutchings, *Physical Chemistry Chemical Physics : PCCP*, **2008**, *10*, 1921-1930.

71. P. Miedziak, M. Sankar, N. Dimitratos, J. A. Lopez-Sanchez, A. F. Carley, D. W. Knight, S. H. Taylor, C. J. Kiely and G. J. Hutchings, *Catalysis Today*, **2011**, *164*, 315-319.

72. V. Peneau, Q. He, G. Shaw, S. A. Kondrat, T. E. Davies, P. Miedziak, M. Forde, N. Dimitratos, C. J. Kiely and G. J. Hutchings, *Physical Chemistry Chemical Physics : PCCP*, **2013**, *15*, 10636-10644.

73. N. Dimitratos, J. A. Lopez-Sanchez, D. Lennon, F. Porta, L. Prati and A. Villa, *Catalysis Letters*, **2006**, *108*, 147-153.

74. G. L. Brett, Q. He, C. Hammond, P. J. Miedziak, N. Dimitratos, M. Sankar, A. A. Herzing, M. Conte, J. A. Lopez-Sanchez, C. J. Kiely, D. W. Knight, S. H. Taylor and G. J. Hutchings, *Angewandte Chemie Int. Ed.*, **2011**, *50*, 10136-10139.

75. M. Faraday, *Philosophical Transactions of the Royal Society of London*, **1857**, *147*, 145-181.

76. J. Turkevich, P. C. Stevenson and J. Hillier, *Discussion of the Faraday Society*, **1951**, *11*, 55-75.

77. M. Brust, M. Walker, D. Bethell, D. J. Schiffrin and R. Whyman, *Chemical Communications*, **1994,** *0*, 801-802.

78. G. Schmid, R. Pfeil, R. Boese, F. Bandermann, S. Meyer, G. H. M. Gijs. H. M. Calis and J. W. A. Van der Velden, *European journal of inorganic chemistry,* **1981**, *114*, 3634-3642

79. Y. Xia and N. J. Halas, *MRS Bulletin*, **2011**, *30*, 338-348.

80. R. Elghanian, J. J. Storhoff, R. Mucic, C., R. L. Letsinger and C. A. Mirkin, *Science*, **1997**, *277*, 1078-1081.

81. G. Baffou and R. Quidant, *Chemical Society Reviews*, **2014**, *43*, 3898-3907.

82. J. Shan and H. Tenhu, *Chemical Communications*, **2007**, 4580-4598.

83. C. Della Pina, E. Falletta, L. Prati and M. Rossi, *Chemical Society Reviews*, **2008**, *37*, 2077-2095.

84. M. Brust, J. Fink, D. Bethell, D. J. Schiffrin and C. Kiely, *Chemical Communications*, **1995**, *0*, 1655-1656.

85. R. Meyer, C. Lemire, S. Shaikhutdinov and H. J. Freund, *Gold Bulletin*, **2004**, *37*, 72-124.

86. P. A. Sermon, G. C. Bond and P. B. Wells, *Journal of the Chemical Society, Faraday Transactions 1: Physical Chemistry in Condensed Phases*, **1979**, *75*, 385-394.

87. M. Haruta, T. Kobayashi, H. Sano and N. Yamada, *Chemistry Letters*, **1987**, *16*, 405-408.

88. M. Haruta, S. Tsubota, T. Kobayashi, H. Kageyama, M. Genet and B. Delmon, *Journal of Catalysis*, **1993**, *144*, 175-192.

89. G. J. Hutchings, *Journal of Catalysis*, **1985**, *96*, 292-295.

90. C. L. Bianchi, P. Canton, N. Dimitratos, F. Porta and L. Prati, *Catalysis Today*, **2005**, *102-103*, 203-212.

91. S. Biella, G. L. Castiglioni, C. Fumagalli, L. Prati and M. Rossi, *Catalysis Today*, **2002**, *72*, 43-49.

92. F. Porta and L. Prati, *Journal of Catalysis*, **2004**, *224*, 397-403.

93.   L. Prati, A. Villa, C. E. Chan-Thaw, R. Arrigo, D. Wang and D. S. Su, *Faraday Discussions*, **2011**, *152*, 353-365.

94.   A. Villa, N. Dimitratos, C. E. Chan-Thaw, C. Hammond, L. Prati and G. J. Hutchings, *Accounts of Chemical Research*, **2015**, *48*, 1403-1412.

95.   A. Villa, G. M. Veith and L. Prati, *Angewandte Chemie Int. Ed.*, **2010**, *49*, 4499-4502.

96.   L. Prati, P. Spontoni and A. Gaiassi, *Topics in Catalysis*, **2009**, *52*, 288-296.

97.   P. Landon, P. J. Collier, A. J. Papworth, C. J. Kiely and G. J. Hutchings, *Chemical Communications*, **2002**, *0*, 2058-2059.

98.   G. J. Hutchings, *Chemical Communications*, **2007**, *0*, 1148-1164.

99.   J. K. Edwards, B. Solsona, E. Ntainjua, A. F. Carley, A. A. Herzing, C. J. Kiely and G. J. Hutchings, *Science*, **2009**, *323*, 1037-1041.

100.   J. Bailie and G. J. Hutchings, *Chemical Communications*, **1999**, *0*, 2151-2152.

101.   M. Boronat, A. Corma and P. Serna, *Journal of the American Chemical Society*, **2007**, *129*, 16230-16237.

102.   A. Corma and P. Serna, *Science*, **2006**, *313*, 332-334v.

103.   H. Chen, D. A. Cullen and J. Z. Larese, *The Journal of Physical Chemistry C*, **2015**, *119*, 28885-28894.

104.   S. Carrettin, J. Guzman and A. Corma, *Angewandte Chemie Int. Ed.*, **2005**, *44*, 2242-2245.

105.   M. Haruta, *Journal of New Materials for Electrochemical Systems*, **2004**, *7*, 163-172.

106.   M. Haruta, *Catalysis Today*, **1997**, *36*, 153-166.

107.   F. Porta, L. Prati, M. Rossi, S. Coluccia and G. Martra, *Catalysis Today*, **2000**, *61*, 165-172.

108.   C. L. Bianchi, F. Porta, L. Prati and M. Rossi, *Topics in Catalysis*, **2000**, *13*, 231-236.

109.   B. D. Busbee, S. O. Obare and C. J. Murphy, *Advanced Materials*, **2003**, *15*, 414-416.

110.   C. J. Murphy, *Advanced Materials*, **2001**, *13*, 1389-1393.

111.   C. J. Murphy and T. Li, *The Journal of Physical Chemistry B*, **2005**, *109*, 13857-13870.

112.   T. K. Sau and C. J. Murphy, *Journal of the American Chemical Society*, **2004**, *126*, 8648-8649.

113.   T. K. Sau and C. J. Murphy, *Langmuir:the ACS Journal of Surfaces and Colloids*, **2004**, *20*, 6414-6420.

114.   B. Nikoobakht and M. El-Sayed, *Chemistry of Materials*, **2003**, *15*, 1957-1962.

115.   K. D. Gilroy, A. Ruditskiy, H. C. Peng, D. Qin and Y. Xia, *Chemical Reviews*, **2016**, *116*, 10414-10472.

116.   M. B. Cortie and A. M. McDonagh, *Chemical Reviews*, **2011**, *111*, 3713-3735.

117.   M. Laskar and S. E. Skrabalak, *Journal of Materials Chemistry A*, **2016**, *4*, 6911-6918.

118.   R. Ferrando, J. Jellinek and R. L. Johnston, *Chemical Reviews*, **2008**, *108*, 845-910.

119.   A. Fujishima and J. Honda, *Nature*, **1972**, *238*, 37-38.

120. A. Fujishima, X. Zhang and D. Tryk, *Surface Science Reports*, **2008**, *63*, 515-582.

121. G. L. Miessler, P. J. Fischer and D. A. Tarr, *Inorganic Chemistry*, Pearson, **1991**.

122. M. Hoffmann and W. Bahnemann, *Chemical Reviews*, **1995**, *95*, 69-96.

123. J. Schneider, M. Matsuoka, M. Takeuchi, J. Zhang, Y. Horiuchi, M. Anpo and D. W. Bahnemann, *Chemical Reviews*, **2014**, *114*, 9919-9986.

124. A. Zielińska-Jurek, *Journal of Nanomaterials*, **2014**, *214*, 1-17.

125. M. Ni, M. K. H. Leung, D. Y. C. Leung and K. Sumathy, *Renewable and Sustainable Energy Reviews*, **2007**, *11*, 401-425.

126. L. Liu, S. Ouyang and J. Ye, *Angewandte Chemie Int. Ed.*, **2013**, *52*, 6689-6693.

127. S. Sarina, E. R. Waclawik and H. Zhu, *Green Chemistry*, **2013**, *15*, 1814-8133.

128. A. L. Linsebigler, G. Lu and J. T. J. Yates, *Chemical Reviews*, **1995**, *95*, 735-758.

129. P. Wang, B. Huang, Y. Dai and M. H. Whangbo, *Physical Chemistry Chemical Physics: PCCP*, **2012**, *14*, 9813-9825.

130. S. Sarina, H. Y. Zhu, Q. Xiao, E. Jaatinen, J. Jia, Y. Huang, Z. Zheng and H. Wu, *Angewandte Chemie Int. Ed.*, **2014**, *53*, 2935-2940.

131. C. Wang and D. Astruc, *Chemical Society Reviews*, **2014**, *43*, 7188-7216.

132. C. Clavero, *Nature Photonics*, **2014**, *8*, 95-103.

133. S. Linic, U. Aslam, C. Boerigter and M. Morabito, *Nature Materials*, **2015**, *14*, 567-576.

134. S. K. Ghosh, S. Nath, S. Kundu, K. Esumi and T. Pal, *The Journal of Physical Chemistry B*, **2004**, *108*, 13963-13971.

135. M. Rycenga, C. M. Cobley, J. Zeng, W. Li, C. H. Moran, Q. Zhang, D. Qin and Y. Xia, *Chemical Reviews*, **2011**, *111*, 3669-3712.

136. S. Link and M. El-Sayed, *International Reviews in Physical Chemistry*, **2000**, *19*, 409-453.

137. G. Baffou and R. Quidant, *Laser & Photonics Reviews*, **2013**, *7*, 171-187.

138. X. Lu, M. Rycenga, S. E. Skrabalak, B. Wiley and Y. Xia, *Annual Review of Physical Chemistry*, **2009**, *60*, 167-192.

139. S. Sarina, S. Bai, Y. Huang, C. Chen, J. Jia, E. Jaatinen, G. A. Ayoko, Z. Bao and H. Zhu, *Green Chemistry*, **2014**, *16*, 331-341.

140. S. Sarina, H. Zhu, E. Jaatinen, Q. Xiao, H. Liu, J. Jia, C. Chen and J. Zhao, *Journal of the American Chemical Society*, **2013**, *135*, 5793-5801.

141. Y. Tian and T. Tatsuma, *Journal of the American Chemical Society*, **2005**, *127*, 7632-7637.

142. D. Tsukamoto, Y. Shiraishi, Y. Sugano, S. Ichikawa, S. Tanaka and T. Hirai, *Journal of the American Chemical Society*, **2012**, *134*, 6309-6315.

143. E. A. Coronado, E. R. Encina and F. D. Stefani, *Nanoscale*, **2011**, *3*, 4042-4059.

144. F. Kretschmer, S. Mühlig, S. Hoeppener, A. Winter, M. D. Hager, C. Rockstuhl, T. Pertsch and U. S. Schubert, *Particle & Particle Systems Characterization*, **2014**, *31*, 721-744.

145. M. Pagliaro, R. Ciriminna, H. Kimura, M. Rossi and C. Della Pina, *Angewandte Chemie Int. Ed.*, **2007**, *46*, 4434-4440.

146. M. Di Serio, L. Casale, R. Tesser and E. Santacesaria, *Energy & Fuels*, **2010**, *24*, 4668-4672.

147. Y. Wang, J. Zhou and X. Guo, *RSC Advances*, **2015**, *5*, 74611-74628.

148. G. D. Yadav, R. V. Sharma and S. O. Katole, *Industrial & Engineering Chemistry Research*, **2013**, *52*, 10133-10144.

149. B. Katryniok, H. Kimura, E. Skrzyńska, J.-S. Girardon, P. Fongarland, M. Capron, R. Ducoulombier, N. Mimura, S. Paul and F. Dumeignil, *Green Chemistry*, **2011**, *13*, 1960.

150. J. Reichert, B. Brunner, A. Jess, P. Wasserscheid and J. Albert, *Energy & Environmental Science*, **2015**, *8*, 2985-2990.

151. M. Zacharska, L. G. Bulusheva, A. S. Lisitsyn, S. Beloshapkin, Y. Guo, A. L. Chuvilin, E. V. Shlyakhova, O. Y. Podyacheva, J. J. Leahy, A. V. Okotrub and D. A. Bulushev, *ChemSusChem*, **2017**, *10*, 720-730.

152. S. Carrettin, P. McMorn, P. Johnston, K. Griffin and G. J. Hutchings, *Chemical Communications*, **2002**, *0*, 696-697.

153. S. Carrettin, P. McMorn, P. Johnston, K. Griffin, C. J. Kiely and G. J. Hutchings, *Physical Chemistry Chemical Physics: PCCP*, **2003**, *5*, 1329-1336.

154. S. Carrettin, P. McMorn, P. Johnston, K. Griffin, C. J. Kiely, G. A. Attard and G. J. Hutchings, *Topics in Catalysis*, **2004**, *27*, 131-136.

155. D. I. Enache, J. K. Edwards, P. Landon, B. Solsona-Espriu, A. F. Carley, A. A. Herzing, M. Watanabe, C. J. Kiely, D. Knight and G. J. Hutchings, *Science*, **2006**, *311*, 362-365.

156. A. Villa, N. Dimitratos, C. E. Chan-Thaw, C. Hammond, L. Prati and G. J. Hutchings, *Accounts of Chemical Research*, **2015**, *48*, 1403-1412.

157. B. N. Zope, D. D. Hibbitts, M. Neurock and R. J. Davis, *Science*, **2010**, *330*, 74-78.

158. A. Villa, S. Campisi, K. M. H. Mohammed, N. Dimitratos, F. Vindigni, M. Manzoli, W. Jones, M. Bowker, G. J. Hutchings and L. Prati, *Catalysis Science & Technology*, **2015**, *5*, 1126-1132.

159. A. Villa, D. Wang, C. E. Chan-Thaw, S. Campisi, G. M. Veith and L. Prati, *Catalysis Science & Technology*, **2016**, *6*, 598-601.

160. A. Villa, D. Wang, D. S. Su and L. Prati, *ChemCatChem*, **2009**, *1*, 510-514.

161. S. Campisi, C. E. Chan-Thaw, D. Wang, A. Villa and L. Prati, *Catalysis Today*, **2016**, *278*, 91-96.

162. W. Ketchie, Y. Fang, M. Wong, M. Murayama and R. Davis, *Journal of Catalysis*, **2007**, *250*, 94-101.

163. S. E. Davis, M. S. Ide and R. J. Davis, *Green Chemistry*, **2013**, *15*, 17-45.

164. W. C. Ketchie, M. Murayama and R. J. Davis, *Topics in Catalysis*, **2007**, *44*, 307-317.

165. D. Wang, A. Villa, D. Su, L. Prati and R. Schlögl, *ChemCatChem*, **2013**, *5*, 2717-2723.

166. S. A. Kondrat, P. J. Miedziak, M. Douthwaite, G. L. Brett, T. E. Davies, D. J. Morgan, J. K. Edwards, D. W. Knight, C. J. Kiely, S. H. Taylor and G. J. Hutchings, *ChemSusChem*, **2014**, *7*, 1326-1334.

167. A. Villa, C. Campione and L. Prati, *Catalysis Letters*, **2007**, *115*, 133-136.

168. W. Ketchie, M. Murayama and R. Davis, *Journal of Catalysis*, **2007**, *250*, 264-273.

169. G. Dodekatos and H. Tüysüz, *Catalysis Science & Technology*, **2016**, *6*, 7307-7315.

170. S. Schünemann, G. Dodekatos and H. Tüysüz, *Chemistry of Materials*, **2015**, *27*, 7743-7750.

Chapter 2

Experimental

Materials Used

HAuCl$_4$·3H$_2$O- Sigma Aldrich, metal content ≥49.0%

PdCl$_2$ – Sigma Aldrich Reagent Plus® 99%

Poly vinyl alcohol (PVA) average molecular weight (chain) M_W = 9000-10000 g/mol, 80% hydrolysed - Sigma Aldrich

Poly vinyl pirrolydone (PVP) average molecular weight (chain) M_W = 10000 g/mol – Sigma Aldrich

NaBH$_4$ ≥ 99.99%– Sigma Aldrich

TiO$_2$ P25 – Aeroxide®, Evonik

Cerium (IV) oxide nanopowder - Aldrich

Benzyl alcohol – Sigma Aldrich 99.9%

Benzaldehyde – Sigma Aldrich 98%

Toluene – Sigma Aldrich 99%

Mesitylene – Sigma Aldrich 98%

CO 5000 ppm in synthetic air – BOC gases

Glycerol – Sigma Aldrich 98% pure

Glyceric Acid – 20 % wt solution, TCI

Sodium hydroxide, pellets, anhydrous - Sigma Aldrich BioXtra, >98%,

Water HPLC grade - Fisher

Definitions

$$\text{Carbon Conversion \%} = \frac{\text{moles of reactant converted (carbon)}}{\text{moles of fed reactant (carbon)}} * 100 \qquad (2.1)$$

$$\text{Carbon Selectivity \%} = \frac{\text{moles of product (carbon)}}{\text{moles of reactant converted (carbon)}} * 100$$

$$(2.2)$$

$$\text{Yield \%} = \frac{\text{moles of product (carbon)}}{\text{moles of fed reactant (carbon)}} * 100 \qquad (2.3)$$

$$\text{Carbon Mass Balance \%} = \frac{\sum \text{moles of carbon of products}}{\text{moles of carbon of fed reactant}} * 100 \qquad (2.4)$$

Moles of carbon are calculated by multiplying the moles of product/reactant by the number of carbons in the product/reactant (e.g., 2 moles of a C_3 product/reactant contains 6 moles of carbon).

Unless otherwise stated, the results showed in the present Thesis are expressed as average of three experiments, and the associated error bars represent the standard deviation of each value. Where repeatability experiments were not carried out, the associated error bars on the displayed values represent the errors calculated for same catalysts on standard experiments.

2.1 Catalyst Preparation

2.1.1   Traditional and modified sol-immobilisation method

2.1.1.1   Synthesis of 1% wt Au/TiO$_2$ and 1% wt AuPd/TiO$_2$

Monometallic (1% wt Au/TiO$_2$) and bimetallic (1% wt AuPd/TiO$_2$ (molar ratio Au:Pd 1:1)) samples were prepared by sol-immobilisation using PVA and PVP as stabilizing polymer ligands, as well as without any addition of stabilizer (the latter being denoted SF). In a typical synthesis of 1 g of monometallic sample, an aqueous solution of HAuCl$_4$·3H$_2$O (0.8 mL, 12.5 mg Au/mL Sigma Aldrich, metal content ≥49.0%) was added to 400 mL of deionised water under vigorous stirring conditions, followed by the addition of a polymer stabilizer (polymer/Au wt/wt = 0.65). This was either a 1 wt% aqueous solution of PVA (average molecular weight M_W = 9000-10000 g/mol, 80% hydrolysed), or a 1 wt% aqueous solution of PVP (Sigma Aldrich, average molecular weight M_W = 10000 g/mol). Subsequently, a 0.1 M freshly prepared solution of NaBH$_4$ (≥99.99%, Aldrich) was added (mol NaBH$_4$/mol Au = 5) to form a red sol. After 30 min of sol generation, the colloid was immobilised by adding 0.99 g of TiO$_2$ (P25 Aeroxide®, Evonik) and 8 drops of concentrated H$_2$SO$_4$. After 1 h of continuous stirring, the slurry was filtered, the catalyst washed thoroughly with deionised water and dried at 110 °C for 16 h. Syntheses for the bimetallic AuPd sample proceeded in the same way, but with the further addition of PdCl$_2$ (Sigma Aldrich, Reagent Plus® 99%) in aqueous solution (6 mg Pd/mL). In this case, the stabilizer-to-metals ratio was 1.2 (wt/wt). The immobilisation steps were carried out in the same manner as previously described [1,2]. For the stabilizer free (SF) variants, both monometallic and bimetallic analogues were prepared as described above but the addition of stabilizer to the preparation was omitted. The SF sample was immobilised on TiO$_2$ after 30 min of sol generation. It was observed that the SF colloids start to collapse between 24 and 36 hours after reduction.

2.1.1.2   Synthesis of 3-7% wt Au/TiO$_2$

Monometallic catalysts with higher metal loading (3, 5, 7 nominal wt %) were prepared by sol-immobilisation using PVA as stabilising agent as well as without any stabiliser addition. An additional 3% wt Au/TiO$_2$ catalyst was prepared by sol-immobilisation using PVP as a stabilising polymer (M_W

=1300000 g/mol). The synthesis procedure is the same described for the preparation of 1 g of catalyst, and the amount of TiO_2 added was appropriately scaled down in order to obtain the desired metal loading, as reported in Table 2.1.

Selected samples were calcined for 3 hours at 500 °C in static air, with heating rate of 10 °C/min. Reduction was performed in the same conditions under H_2 flow.

Table 2.1 - Higher loaded Au catalysts and correspondent TiO_2 amount

Metal loading / wt %	TiO_2 amount / g
3	0.33
5	0.20
7	0.14

2.1.1.3 Synthesis 1% wt AuPd/TiO₂ at different Au:Pd molar ratio

A series of 1% wt AuPd/TiO_2 catalysts with different Au:Pd molar ratios as reported in Table 2.2 were prepared by sol-immobilisation using PVA as stabilising agent. Synthesis procedure was the same as reported for the preparation of a standard 1% wt AuPd/TiO_2 Au:Pd molar ratio 1:1, with the only difference the relative metals amount.

Table 2.2 - 1%wt AuPd/TiO₂ catalysts and correspondent Au:Pd molar ratio

	Catalyst	Au:Pd molar ratio
	Au1Pd9	1:9
Au<Pd	Au1Pd4	1:4
	Au1Pd3	1:3
	Au1Pd2	1:2
	Au1.5Pd1	1.5:1
	Au2Pd1	2:1
Au>Pd	Au3Pd1	3:1
	Au5Pd1	5:1
	Au9Pd1	9:1

For the preparation of 1 g of catalyst 1% wt metals loading (corresponding to 0.01 g of metal), the following relationships were used (Eq. 2.1 and 2.2):

$$X_{Au}\,(mol) * MW_{Au}\,(g\,mol^{-1}) + X_{Pd}\,(mol) * MW_{Pd}\,(g\,mol^{-1}) \;=\; 0.01\;g \quad \text{(Eq. 2.1)}$$

$$X_{Au} \;=\; Y\,X_{Pd} \quad \text{(Eq. 2.2)}$$

Where X_{Au} and X_{Pd} are the moles of Au and Pd respectively, and MW_{Au} and MW_{Pd} their molar mass. Y in Eq. 2.2 represents the relationship between the moles of the two metals (e.g., for the synthesis of Au9Pd1, Y = 9).

2.1.2 Impregnation-reduction method

A 3% wt Au/CeO$_2$ catalyst was prepared by an impregnation-reduction method, slightly modified from the procedure reported by Ke *et al.* [3]. In a typical synthesis, 0.97 g of CeO$_2$, 2.45 mL of HAuCl$_4$ (12.25 mg Au/mL) and 1.95 mL of PVA solution (0.1 g/10 mL) were added to 100 mL deionised water. Subsequently, 10 mL of a NaBH$_4$ solution 0.15 M were added dropwise. The final pH was 9.15. The slurry was left stirring for one hour and aged for 24 hours. The solid washed three times with deionised water and separated from the liquid by centrifugation. Finally, it was dried at 60 °C for 16 hours.

2.2 Catalyst Testing

2.2.1 Glycerol oxidation in basic conditions and related experiments

Glycerol Oxidation - Glycerol oxidation under basic conditions was performed in a glass reactor (Colaver®) positioned in a thermostatically controlled oil bath at 60 °C and at 3 bar O$_2$ pressure, under continuous stirring (1200 rpm). Glycerol (5 mL, 0.6 M, Sigma Aldrich, anhydrous, >99.5 %) and NaOH (5 mL, 1.2 M, Sigma Aldrich BioXtra >98%, pellets, anhydrous) were added to the reactor to give a total reaction volume of 10 mL. The glycerol/metal(s) molar ratio was 500:1. The total reaction time employed was 240 min, with sampling performed after 30, 60, 120 and 240 min of reaction. Samples were quenched and diluted 1:10 in deionised water before analysis by HPLC. Product analysis was carried out using an Agilent 1260 Infinity HPLC with a Metacarb 67H column with a 0.1% wt solution of phosphoric acid as mobile phase. Re-usability

tests were performed by halving the catalyst amount (fresh and used) and using reactant concentrations of 2.5 mL of glycerol solution 0.6 M, 2.5 mL NaOH 1.2 M and 5 mL of deionised water. Catalysts were recovered for stability testing by washing and centrifugation cycles in deionized water and acetone followed by drying in air at room temperature.

Glyceric Acid - Experiments on glyceric acid (TCI, 20% wt aqueous solution ca. 2 M) as substrate were performed in the same conditions as the glycerol oxidation test, using 5 mL of solution, 0.6 M.

Short reaction time oxidation – Short reaction time experiments were carried out using the conditions described above. The reaction mixtures prior to the reaction were sonicated at room temperature and purged three times with N_2 in order to remove the oxygen to prevent reaction during heating to reaction temperature. The reactors were then sealed and allowed to reach thermal equilibrium for 15 minutes under N_2 atmosphere (3 bar) and stirring (1200 rpm). Thereafter gas was switched to O_2 and samples were collected after 5, 10, 15 and 20 minutes.

Polymer Influence - Experiments to investigate the effect of polymer presence (PVA and PVP) were performed using the monometallic SF sample in the presence of PVA or PVP in defined weight ratios with respect to the Au mass (0.3, 0.65, 1.3), starting from solutions 0.1 g/10 mL. Experiments were carried out at the same conditions as standard glycerol oxidation. Each reactor was charged with the Au/ TiO$_2$ SF catalyst, glycerol and NaOH and a certain aliquots of PVA or PVP solution, correspondent to stabiliser/Au (weight ratio) 0.325, 0.65 and 1.3 respectively. The required amount of PVA and PVP solutions (0.1 g / 10 mL) were 38.4 µL, 76.8 µL and 0.154 mL respectively. The weight ratios were determined considering stabiliser/Au ratio 0.65 which is used in the standard catalyst synthesis, with 0.325 and 1.3 being respectively the half and the double of this quantity.

2.2.2   Solvent - free benzyl alcohol oxidation

In a typical test, 2 g of benzyl alcohol (Sigma-Aldrich, 99-100%) and 0.02 g of catalyst were added to a Radleys® round bottom flask reactor. The reactions were carried out at a pressure of 1 bar O_2, a temperature of 120 °C and with stirring at 1200 rpm. Time-on-line measurements were carried out by running 5 equivalent reactions in parallel that were quenched after 30, 60, 90, 120 and 180 min respectively by cooling in ice. The

resultant slurry was centrifuged in order to separate out the catalyst, and then analysed by GC (Varian Star 450, with a CP-Sil 5CB column) using mesitylene as an external standard.

2.2.3 CO oxidation

CO oxidation tests were performed in a quartz microreactor with internal diameter of 0.4 cm (0.1 cm wall), schematically shown in Figure 2.1.
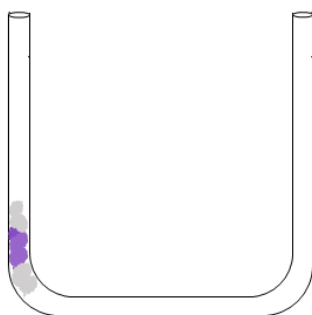
Figure 2.1 – Representation of the quartz microreactor loaded with the catalyst and the glass wool

In a typical test, 50 mg of catalyst were packed between two small pieces of glass wool to secure the catalyst in place. The length of the catalyst bed was 0.5 cm. The reactor was fixed inside a thermostatic water bath with temperature kept at 25 °C for all the experiment duration. The gas feed, 5000 ppm of CO in synthetic air, was passed through the catalyst bed with a flow of 25 mL/min (GHSV = 24000 h^{-1}) controlled by a mass flow controller. The reaction products were analysed every 5 minutes by an online GC.

2.2.4 Plasmonic photocatalysis for the oxidation of glycerol under neutral conditions

Plasmonic photocatalytic reactions were performed in a stainless steel custom designed autoclave reactor and built by DG Innovation. The reactor consist of two parts: a top, with a borosilicate window, equipped with inlet, outlet, thermocouple inlet, pressure gauge and pressure release valve; and a vessel where the reaction liner is located. Originally the reactor was equipped with a Teflon liner of 30 mL internal volume, converted afterwards to a glass vial of 15 mL placed in a Teflon jacket of 2.5 cm width, and wrapped in aluminium foil to ensure both thermal contact and light reflection inside the reaction bath. The reactor's maximum operating pressure, determined by the presence of the window, is 11 bar. The maximum operating volume is 7.5 mL. Heating is provided by a heating mantle designed, connected to a control box (K39 Ascon Tecnologic,

assembled by Elmatic, Cardiff). The light source is a 300 W lamp (USHIO) positioned inside a case and connected to a control box (ORIEL OPL-500). Prior to the experiments, the lamp was focused and aligned to ensure the maximum operative efficiency.

For all the experiments, unless otherwise stated, the IR radiation was removed from the output light by a water filter, and wavelengths below 420 nm were eliminated through a cut-off filter (Newport Stablife® Technology). The filtered light was focused on the top of the reactor through a 90° mirror placed at the end of the filters, as shown in Figure 2.2.

Experimental

Plasmonic photocatalytic glycerol oxidation in neutral conditions was performed by loading the autoclave with 5 mg of catalyst and 5 mL glycerol (Sigma-Aldrich, 98% pure) 0.05 M. Prior to the experiment, the liner was weighed and wrapped in aluminium foil. The reactor was sealed, flushed with 5 bar O_2 for five times and finally pressurised with O_2 (continuously supplied). Temperature was set to 90 °C for the reaction under dark conditions and at 86 °C for the reactions under illumination due to the small amount of thermal energy introduced by the illumination. The temperature was kept at this value throughout all the duration of the experiment. The experiment started when temperature in the heating mantle reached the selected value. Total reaction time was initially 5 hours for the first experiments, reduced to 3 hours later.

After reaction, the reactor was rapidly quenched in an ice bath, the liner weighed and the slurry collected, filtered through a micropore PTFE filter (Fisherbrand® or Sartorius®, 0.25 μm) and directly injected to HPLC for analysis.
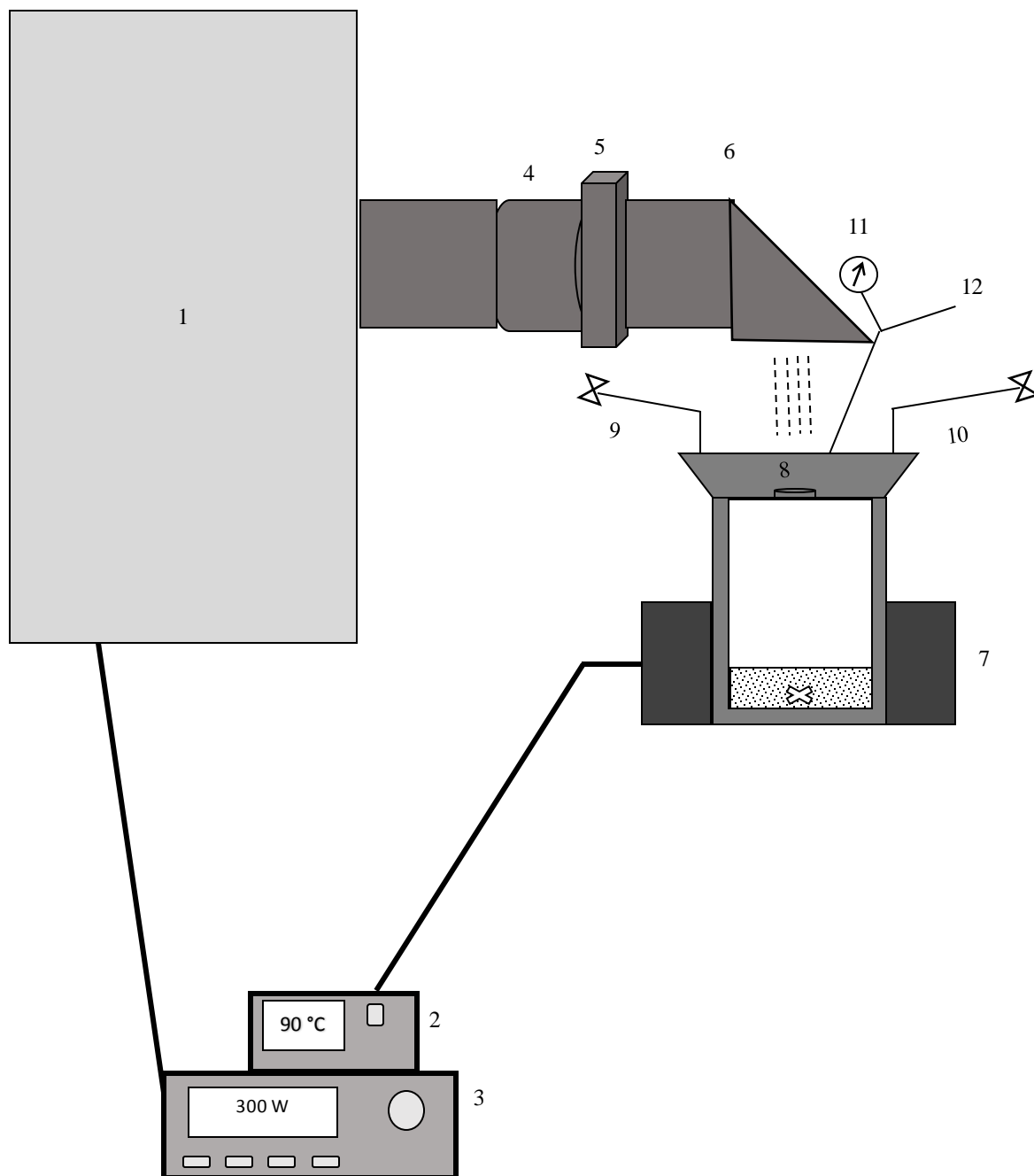
Figure 2.2 - Scheme of the photoreactor set up. 1. Lamp case 2. Temperature controller 3. Light power control 4. IR-water filter 5. Wavelength cut-off filter 6. 90 o mirror block 7. Heating mantle 8. Borosilicate window 9. Inlet valve 10. Outlet valve 11. Pressure gauge 12. Safe vent

2.3 Analytical Techniques

2.3.1 Gas-Chromatography

Gas chromatography (GC) is a widely used technique for separation and quantification of chemical mixtures. As in all chromatographic techniques, the separation is determined by the affinity of the substances with two phases, the stationary phase and mobile phase (in GC the mobile phase it is a gas often named *carrier gas*). The GC is typically composed by the injector, the column (placed in an oven) and the detector, as schematically illustrated in Figure 2.3.
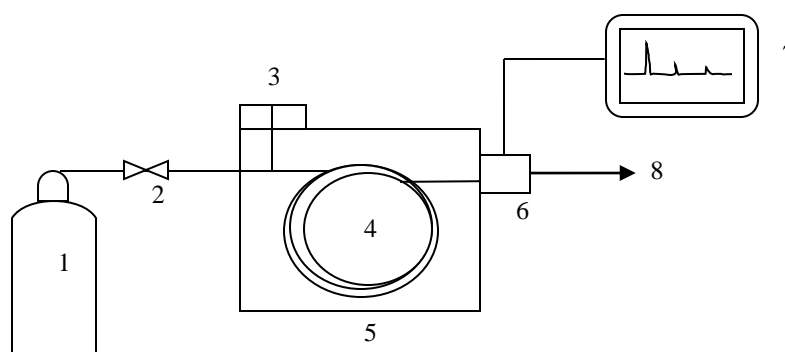
Figure 2.3 - Schematic diagram of the GC used for analysing the reaction products. 1. Carrier Gas 2. Flow controller 3. Injector 4. Column 5. Column Oven 6. Detector 7. Software 8. Waste

The analysis starts when a small quantity of sample is introduced as either liquid or gas into the injector, which has a duel function of vaporising the sample and mixing it with the carrier gas. The injector can operate in splitting mode, i.e. it separates the injected flow into two fractions, venting the largest portion, helping to prevent column saturation from concentrated samples. The injected sample passes through a coiled temperature-controlled column, where the separation between the different analytes occurs. At the end of the column, the carrier gas passes through a detector before exiting to the atmosphere. High purity helium, hydrogen or nitrogen are often used as carrier gas, and their nature has no influence upon the partition coefficients of the compounds. On the other hand, the diffusion and dispersion of the analytes is influenced by the viscosity and the flow rate of the gas, affecting the detection. Commonly employed GC detectors are:

- *Thermal Conductivity Detector (TCD)*. It is used for the identification of a large range of compounds since it is based on the principle that each compound has a different thermal conductivity with respect to the

carrier. It is composed by two thermistors located within the path of the carrier gas and maintained at a temperature above that of the column. One thermistor is exposed to the carrier gas, the other one to the gas evolving from the column containing the eluted species. In the steady state, a thermal equilibrium is established between the thermal conductivity of the carrier gas and electrical current of the thermistor. When a solute elutes, the composition in the carrier changes, resulting in a modification of its thermal conductivity and consequently in the thermal equilibrium of the thermistor, and this variation is proportional to the concentration of the compound in the carrier gas [4,5].

- *Flame Ionisation Detector (FID).* Consists of a hydrogen flame in excess oxygen, and it is used for the identification of hydrocarbon compounds. Carrier gas from the column enters at the bottom of the detector and is mixed with hydrogen in the area below the flame jet. This mixture is then combined with air and burned just above the jet tip, ionising the combustible species in the sample. A negative polarizing voltage is applied between the jet tip and a collector electrode; as electrons are generated, they are accelerated across the jet tip–collector gap by the electric field and sent to an electrometer. The current across the collector is proportional to the rate of ionisation that depends on the hydrocarbon concentration in the sample.

Experimental

GC setup for analysis of benzyl alcohol oxidation

Benzyl alcohol reaction samples were analysed by a Varian 450 GC equipped with a CP 3800 autosampler and a CP-Sil 5CB column and fitted with a flame ionisation detector. The method used for the analysis is schematically shown in Figure 2.4. The GC was calibrated in the range of interest (0-100% benzyl alcohol conversion) for benzyl alcohol, benzaldehyde and toluene concentrations, each signal was normalised to the signal of the external standard, mesitylene. The concentration of each compound ($Conc_x$) was calculated according to Equation 2.3, where RF is the slope (response factor) of the calibration curve for the compound

x, $Conc_s$ and $Area_s$ the concentration and the area of the standard respectively and $Area_x$ the area of the compound. Finally, the conversion of benzyl alcohol was calculated according to Definition 2.1.

$$Conc_x = \frac{Area_x}{Area_s} * \frac{Conc_s}{RF} \text{ (Eq. 2.3)}$$
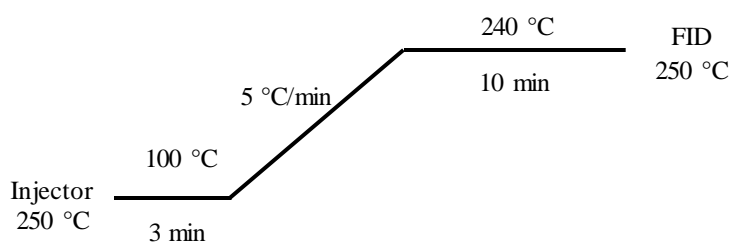
Figure 2.4 - Schematic representation of the GC method used for the analysis of benzyl alcohol reaction effluents

GC setup for analysis of CO oxidation

Gas samples from CO oxidation was analysed by a Varian 3800 GC fitted with a TCD detector every 5 minutes by automatic injection into a 1.5 m carbosieve column held at 195 °C. Retention times of the species involved in the reaction are listed in Table 2.3. CO_2 was calibrated in the range 0-5000 ppm.
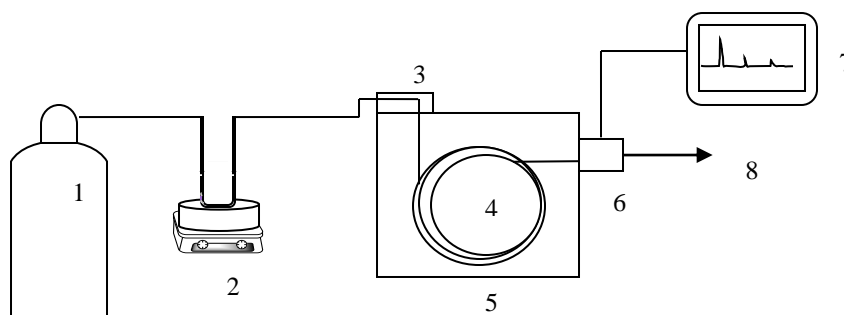
Figure 2.5 - Schematic diagram of reaction set up. 1. CO cylinder 2. Thermostated reactor 3. Injector 4. Column 5. Oven 6. Detector 7. Software 8. Waste

Table 2.3 – Retention times of the reaction components

Compound	Retention time / min
CO + synthetic air	0.4
CO_2	1.4
Moisture	3.0

The conversion was calculated dividing the area of the CO_2 peak by the area of the CO_2 peak correspondent to 5000 ppm (100% CO conversion), according to Equation 2.4.

$$Conversion\ \% = \frac{area\ CO_2}{area\ CO_2\ corresponding\ to\ full\ CO\ conversion} * 100 \quad \text{(Eq. 2.4)}$$

2.3.2   High Performance Liquid Chromatography

High performance liquid chromatography (HPLC) represents another widely used chromatographic technique complementary to GC, as approximately the 85% of compounds are not sufficiently volatile or stable to be separated by GC.

The HPLC apparatus consists of four parts: the mobile phase supply system, which contains the pump to provide the high pressure required; the sample injector; the column (stationary phase); the detector. A scheme of this is illustrated in Figure 2.6.
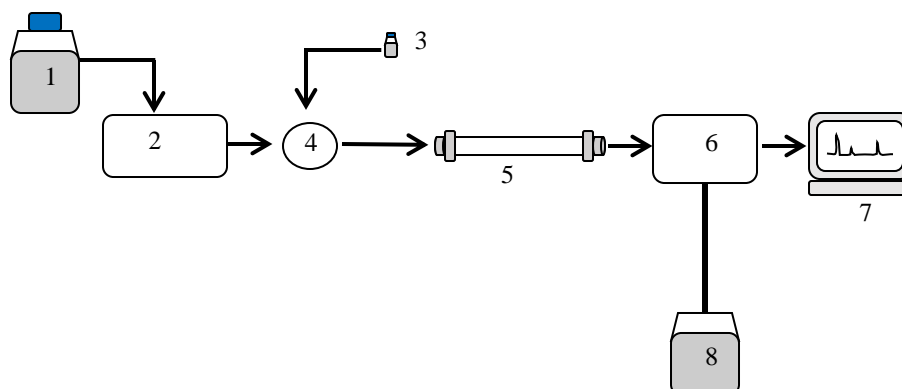
Figure 2.6 - Schematic diagram of the HPLC used for analysing the reaction products. 1. Solvent reservoir 2. Pump 3. Autosampler 4. Injection valve 5. Column 6. Detectors (RID, DAD) 7. Software 8. Waste

The column and the mobile phase represent the core of the separation process. The interaction between the column and the mobile phase must be very efficient in order to minimise the diffusion time: in order to achieve this, the column must be finely divided and homogeneously packed. The high packing density necessitates the use of a high pressure pump to ensure the mobile phase can pass through the column.

HPLC can operate in two modes: normal phase and reverse phase, which refer to the relationship between the mobile and stationary phase. In normal phase chromatography, the stationary phase is polar (e.g. silica gel) and the mobile phase is less polar: the separation relies on the adsorption coefficient, i.e. the accumulation of the compound at the interface between stationary and mobile phase. In the reverse phase chromatography, the stationary phase is non polar (e.g. silica gel bonded with organic molecules) and the mobile phase is polar (usually water with solvents such as acetonitrile or methanol). In this case, the separation process does not rely anymore on the adsorption coefficient but on the partition coefficient: by changing the composition of the mobile phase and then its polarity, this affects the distribution coefficients therefore the retention factors of the analytes [5].

At the column exit, the flow is analysed by the detector(s). The commonly used detectors are:

- refractive index detector (RID), which measures changes in the refractive index of eluent and it is highly sensitive to temperature changes;

- spectrophotometric detectors, where detection is based upon the Lambert-Beer law (the intensity of absorption depends upon the molar absorption coefficient of the species detected). These detectors include UV and diode array detectors (DAD). The first one is not temperature sensitive and is useful for a large number of organic compounds; the second one is equipped with a polychromator to disperse the radiation which passes through the sample and the light is allowed to hit the diode array, this last acting as a sort of monochromator. This detector is very useful for analysis of mixtures of absorbing species whose spectra overlap (Figure 2.7).

The HPLC used is equipped with both the detectors. The DAD was used to detect compounds with carbonyl groups whereas the RID to detect the compounds with hydroxyl groups, as further explained in the experimental section below.

W lamp

flow cell

diffraction grating

the light from the two
sources is merged and shines
into the flow cell

photodiode array
the light is converted
into electric signal

D$_2$ lamp
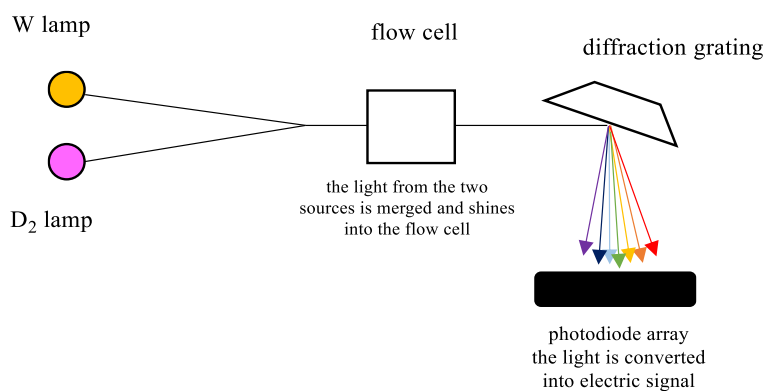
Figure 2.7 - Schematic representation of the HPLC detector system

Experimental

The glycerol oxidation reaction products (thermal and photocatalytic process) were analysed by HPLC chromatography. The analysis was carried out using an Agilent 1200 series with refractive index (RID) and ultraviolet (DAD) detectors. The signals in the DAD were analysed at λ=210 nm. Reactants and products were separated using a MetaCarb 67 H column. The eluent was an aqueous solution of H$_3$PO$_4$ (0.01 M) and the flow was 0.800 mL/min.

For the quantification of the amounts of reactants consumed and products generated, an external calibration method was used. Calibration solutions for each potential compound were prepared at concentration 0.15 M, 0.6 M, 0.03 M and 0.0075 M. Some of them, however, were rarely observed under experimental conditions (e.g., mesoxalic acid, β-hydroxypyruvate, glyoxylic acid, glycolaldehyde). Retention times for the compounds as well as the detector at which they are revealed are listed in Table 2.4.

Table 2.4 - Reactant and products detector and retention times

Compound / name	Detector	Retention Time / min
Glycerol	RID	7.5
Oxalic Acid	DAD	3.4
Mesoxalic Acid	DAD	3.6
Tartronic Acid	DAD	4.1
β-Hydroxypyruvate	DAD	4.3
Pyruvic Acid	DAD	4.8

Compound / name	Detector	Retention Time / min
Glyoxylic Acid	DAD	5.2
Glyceric Acid	DAD	5.9
Glyceraldehyde	DAD	6.16
Glycolaldehyde	DAD	6.7
Glycolic Acid	DAD	6.71
Lactic Acid	DAD	6.97
DHA	DAD/RID	7.37
Formic Acid	DAD	7.5
Acetic Acid	DAD	8.22

The calculation of the conversion for the glycerol oxidation reaction in neutral conditions was not straightforward. A first complication is given by the overlap of the DHA signal with the glycerol signal in RID detector of the HPLC chromatogram, resulting in a higher final glycerol concentration (*apparent final glycerol concentration*). The problem was solved by subtracting the apparent final glycerol concentration to the DHA concentration calculated from its signal in the DAD (for which was calibrated), in order to obtain the *actual final glycerol concentration*. The second problem is the evaporation and condensation of liquid on the reactor's top. Assuming that this is composed by water only, the final glycerol concentration was adjusted taking into account the mass loss (determined by weighing the liner before and after reaction) and the consequent variation in concentration. These two steps allowed the conversion values for the experiments to be calculated using the photocatalytic set-up. This data treatment allowed reproducible results to be obtained. In most instances the catalytic conversion and selectivity reported are the average of duplicate experiments and the standard deviation is denoted using the reported error bars. In the cases where not duplicate experiments were carried out (e.g., Figures 5.7, 5.13-14, 5.19 (off)) the error displayed is the typical error associated with repeat tests of the same catalyst sample at standard conditions.

2.3.3 Spectroscopic techniques

Spectroscopy comprises a large range of techniques that allow information to be obtained on the samples by means of light-matter interaction. The energy of the light is responsible for the different interactions that occurs with the matter, e.g. visible light (λ=400-700 nm) affects electronic levels, while IR (700-1100 nm) vibrational levels.

2.3.3.1 UV-Vis Spectroscopy

In UV-visible (UV-Vis) spectroscopy, the portion of the electromagnetic radiation employed is the visible region, conventionally divided into three sub-domains: near UV (185-400 nm), visible (400-700 nm) and very near infrared (700-1100 nm). The origin of absorption is the interaction of photons with ions or molecules of the sample, which involves excitation of rotational, vibrational, and electronic levels. Since each of this energy transitions is quantised, they will occur only at defined wavelengths. When there is a modification in the electronic energy, this affects rotational and vibrational levels as well, resulting in a collection of possible transitions obtained in all three cases.

All spectrophotometers are composed by a source of continuous radiation over the wavelengths of interest, a monochromator (prisms, diffraction gratings, optical filters) for the selection of a narrow wavelength band, and a detector for converting the radiant energy into electric energy. The output of the spectrometer is a plot representing the transmittance (or the absorbance) as a function of wavelength, usually given in nanometers. Transmittance (T) and absorbance (A) are interdependent, the first one being a measure of the attenuation of a beam of a monochromatic light and expressed by the relationship (Eq. 2.5):

$$T = \frac{I}{I_0} \quad \text{(Eq. 2.5)}$$

where I and I_0 are the intensities of the transmitted and the incident light respectively, and the second one related to this by the following equation (2.6):

$$A = -logT \quad \text{(Eq. 2.6)}$$

The absorbance (or transmittance) is directly proportional to the concentration as described by the Lambert-Beer equation (2.7):

$$A = \varepsilon * l * C \quad \text{(Eq. 2.7)}$$

Where ε is the molar absorptivity (L/cm·g), l the cell path way (cm) and C the concentration in g/L [4,5].

For the characterisation of solid samples, diffuse reflection (DR) spectroscopy is widely employed. In DR the spectra result from the radiation incident on a powdered sample that is absorbed as it refracts through each particle, and is scattered by the combined process of reflection, refraction, and diffraction.

Experimental

In the present work UV-Vis analysis has been performed on colloidal solutions to qualitatively confirm the formation of metallic nanoparticles. In the case of gold, this was evaluated by the appearance of the plasmonic peak at around 520 nm. Spectra were recorded in the range 200-800 nm using a Cary UV-Vis 60 Spectrophotometer.

Diffuse reflectance UV-Vis spectra were recorded in the range 200-800 nm on catalysts after the nanoparticles deposition by using a Cary UV 4000 Spectrophotometer. Prior to the analysis, the baseline was recorded using a PTFE disc.

2.3.3.2   CO – Diffuse Reflectance Infra-Red Spectroscopy (CO-DRIFTS)

In IR spectroscopy the interaction of IR-light with the matter excites the electric dipole of molecules (i.e., vibrational levels), which oscillates with a specific quantised frequency. As in UV-Vis, the technique is quite versatile, allowing analysis of gaseous, liquid and solid samples (diffuse reflectance).

IR spectrometers are fairly similar for construction to UV-vis spectrometers, except for the presence of an interferometer which acts as a monochromator for IR radiation. The interferometer is composed by a moving and a fixed mirror and a beam splitter, which splits the polychromatic radiation from the source into two beams, one directed to the fixed mirror, and the other one to the moving mirror. These beams recombine before passing through the sample and reach the detector (Figure 2.8).
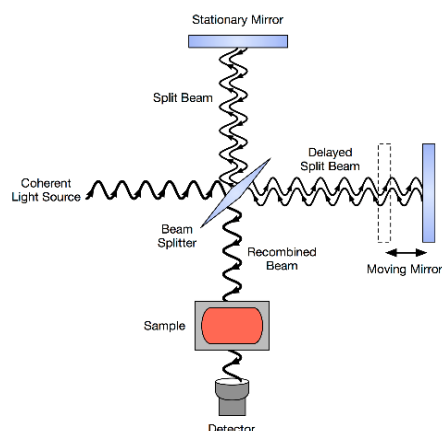
Figure 2.8 – Schematic representation of the interferometer

This system is controlled electronically and the data obtained from the interference of the radiation with the sample are converted (Fourier transform, FT) leading to the amplitude of each wavelength of the spectral band studied. Infrared spectra are usually plotted as transmittance or absorbance in function of frequency expressed in wavenumbers (cm^{-1}).

As in the UV-Vis spectroscopy, also IR can be performed on solids (DRIFTS, acronym for *Diffuse Reflectance Infra-Red Fourier Transform Spectroscopy*), making this technique even more useful for catalyst characterisation. Indeed, not only it is possible to obtain information about the nature and the structure of surface or the adsorbed species [6], but also on the catalytic active site. This is achieved by studying the interaction of the surface with probe molecules *in situ*: CO is one of the most used probe molecules because the position of its vibrational bands can give information on coordination and electrophilic properties of active sites, especially precious metals [7]. A typical CO-DRIFTS cell is illustrated in Figure 2.9. The cell consist of an inlet and outlet for the gas and a connection for the temperature control.
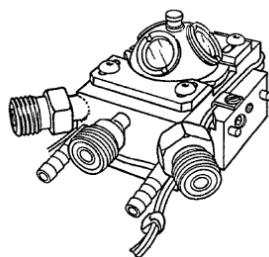
Figure 2.9 - A typical DRIFTS cell

Experimental

CO-DRIFTS measurements were taken on a Bruker Tensor 27 spectrometer fitted with a mercury cadmium telluride (MCT) detector and a ZnSe windows. Before starting the experiment, the background was recorded using KBr under experimental conditions (gases flow rate CO 0.40 mL/min and N_2 19.60 mL/min) until the complete saturation with CO. Each sample was then introduced in the cell and analysed at room temperature until the saturation point was reached.

2.3.3.3   Atomic Emission Spectroscopy (AES)

Atomic emission spectroscopy (AES) techniques are widely used for obtaining quantitative and qualitative analysis of sample composition. The principle of atomic emission is relatively simple and is based on the quantum theory: it predicts that each atom or ion possesses definite energy states in which the various electrons can exist, and in the normal or ground state the electrons have the lowest energy. Upon the application of sufficient energy by light, thermal or other means, one or more electrons may be removed to a higher energy state further from the nucleus: these energised electrons tend to relax and return to the ground state, and in doing so they emit the extra energy as a photon of radiant energy ($h\nu$) (Figure 2.10).

$$E_2 - E_1 = \Delta E = h\nu$$
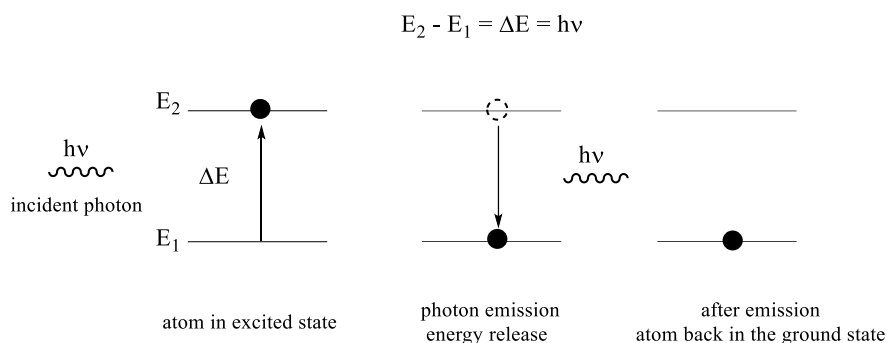
Figure 2.10 – Schematic representation of the principle of atomic emission spectroscopy

Since there are definite energy states and since only certain changes are possible according to the quantum theory, there are a limited number of wavelengths possible in the emission spectrum which are element specific. The greater the energy of the exciting source, the higher the energy of the excited electrons, hence the greater the number of lines that may appear. Qualitative analysis is possible since the lines in the spectrum from any

element always occur in the same position relative to each other. The intensity of the spectral lines is related to the probability of the transition to take place. Quantitative analysis can be performed by keeping the excitation conditions constant and varying the sample composition. The atomising sources used in an AES instrument are flame, arc, sparkle and plasma.

In this latter, the atoms of the samples are excited by the plasma, which might be defined as a cloud of highly ionised gas (usually argon), composed of ions, electrons and neutral particles. The ionisation is achieved through the influence of a strong electrical field by microwave or radiofrequency, producing the Microwave Plasma (MP) or the inductively coupled plasma (ICP) respectively. Plasma sources operate at high temperatures, between 7000 and 15000 K. A nebuliser carries the sample into the hot plasma, where the elements are atomised and excited.

Experimental

Microwave Plasma – Atomic Emission Spectroscopy (MP-AES)

The analysis on 1% wt Au/TiO_2 and 1% wt $AuPd/TiO_2$ samples was carried out using an Agilent 4100 MP-AES. Au content was analysed using two emission wavelengths. A known mass of sample in a volumetric flask was digested overnight in aqua regia in order to dissolve all the metal. Subsequently, the digested catalyst was diluted up to the desired volume with water in order to give metal concentrations in the calibrated range. The sample was filtered using a PTFE micropore filter (Fisherbrand®, 0.45 μm) and introduced into a stream of argon plasma. The instrument was calibrated with Au and Pd standard solution at concentration 5, 10 and 15 ppm. Each sample was injected three times and the average value was taken.

Inductively Coupled Plasma – Mass Spectrometry (ICP-MS)

The determination of the actual metal content on 1% wt Au/TiO_2 and 1% wt $AuPd/TiO_2$ samples was carried out by the Analytical Department in Cardiff University using an Agilent 7900 ICP-MS. The procedure followed for the sample preparation was the same described before for MP-AES analysis.

Determination of the metal leaching in the reaction effluent was carried out using a sample of solution after glycerol oxidation reaction, appropriately diluted by the operator if required.

2.3.3.4 X-Ray Photoelectron Spectroscopy (XPS)

The X-ray photoelectron spectroscopy (XPS) is a surface analytical technique which is employed to obtain information about oxidation state and composition of the sample surface [8]. It is based on the photoelectric effect: when a sample is irradiated with light of a sufficiently small wavelength, it emits electrons from the K shell. This process is illustrated in Figure 2.11.
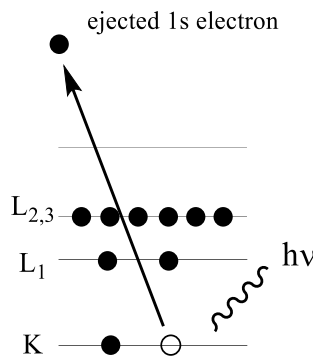
Figure 2.11 – Schematic representation of the photoelectric effect on 1s electron

where an electron from the K shell of the atom (1s) is excited by the incident X-rays and is emitted, according to the equation (2.8):

$$E_k = h\upsilon - E_b - \varphi \text{ (Eq. 2.8)}$$

Where E_k and E_b are respectively the kinetic and binding energy of the electrons in the material, $h\upsilon$ the energy of the source and φ the work function of the spectrometer.

The electrons which escape without energy loss contribute to the characteristic peaks in the spectrum. Since the photoexcitation produces ionised atoms, they must relax in some way. One of the typical relaxation, besides the X-ray fluorescence, is the decadence of an electron from a higher energy level (e.g. L1) to fill the hole left by the first photoemitted electron (e.g. K). This process causes the photoemission of another electron (Auger electron) for the energy conservation law, which can be collected and analysed to obtain further information [9].

X rays source are usually Mg Kα (1253.6 eV) and Al Kα (1486.3 eV). The kinetic energy of the electron is the experimental quantity measured by the instrument, but it is dependent on the photon energy of the X-rays

employed (see equation 2.6) and therefore is not an intrinsic property of the material. The binding energy is the parameter which identifies the electrons specifically, in terms of its parent element and atomic energy level. The XPS spectra are usually plotted as intensity in function of binding energy.

Experimental

XPS analysis was performed by Dr. David Morgan in Cardiff University using a Kratos Axis Ultra DLD XPS spectrometer, equipped with a 300W Al Kα X-ray source. The binding energies were standardised against a C 1s reference (284.7 eV). The data treatment was carried out using Casa XPS software.

2.3.3.5 Transmission Electron Microscopy (TEM)

Transmission Electron Microscopy (TEM) is one of the most useful characterisation technique in the catalysis field to study metal nanoparticles. The electron microscope works, in principle, as an optic microscope with the difference that the radiation source is an electron beam. Electrons present the double nature of wave and particles, so they can be treated as a radiation. By employing the electrons as a light source is possible to obtain higher resolution images, particularly useful when investigating the nano-world: in fact, the maximum resolution *d* that can be obtained from a microscope is dependent from the radiation wavelength λ and from the numerical aperture of the system, NA, according to the equation (2.9):

$$d = \frac{\lambda}{2n sin\theta} \approx \frac{\lambda}{2NA} \text{ (Eq 2.9)}$$

Where n is the refractive index. Moreover, the wavelength λ of electrons is inversely proportional to the kinetic energy, so the higher the kinetic energy, the lower the wavelength. In a TEM, a beam of collimated electrons is accelerated by a difference of potential on the sample. The interaction of the electrons with the material produces not only the image (given by the transmitted electrons), but also other phenomena like X-rays, Auger electrons, diffracted electrons, and so forth, which can give additional information on the composition and internal structure of the particles (Figure 2.12). When analysing samples in the TEM, the corresponding images can be given in the so-called bright field (response of the transmitted electrons) or dark-field (response of the diffracted electrons) [8].

The basis of the X-ray Energy Dispersive Spectroscopy (XEDS) relies on the analysis of the X-ray emitted during the process of relaxation of an atom whose core electrons have been ejected after the interaction with the electronic beam. The X-rays emitted are analysed by an energy-dispersive X-ray detector, which consists of a nitrogen-cooled semiconductor crystal (typically Si(Li)), located at a fixed position respect to the sample. The EDX spectrum represents the intensity of the signal detected in function of the wavelength of the generated X-rays. Since to each element corresponds a characteristic wavelength attributed to the energy difference between the core electrons and higher levels, this allows to obtain qualitative and quantitative information on the elements.
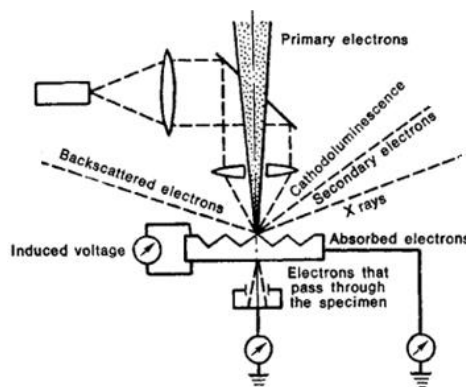
Figure 2.12 – Schematic representation of the effects of the electronic beam interaction with the sample

Experimental

TEM analysis was performed in Cardiff using a JEOL 2100 microscope with a LaB_6 filament operating at 200 kV. Samples were prepared by dispersing the catalyst in ethanol and allowing a drop of suspension to evaporate on a lacey carbon film supported over a 300 mesh copper TEM grid.

Scanning Transmission Electron Microscopy (STEM) was carried out by Dr. Qian He in Lehigh University using a using an aberration corrected JEM ARM-200CF microscope operating at 200 kV. The instrument was also equipped with a JEOL Centurio silicon drift detector for X-ray energy dispersive spectroscopy (XEDS).

The software ImageJ was used for measuring the diameter of 100 nanoparticles, from which the size distribution was generated.

2.3.3.6 X-ray Diffraction (XRD)

A useful technique available to understand the spatial arrangement of atoms in bulk materials is X-ray diffraction (XRD). In a diffraction experiment, an incident X-ray wave is directed into a material and a detector is typically moved about to scan the intensity of the diffracted radiation as a function of the angle. The diffraction phenomenon arises from the coherent interference of the scattered waves, i.e. they have the same phase (Figure 2.13) [10].

There is a profound geometrical relationship between the direction of waves that interfere constructively, which comprise the "diffraction pattern" and the crystal structure of material [10]. This relationship is summarised by the Bragg's Law (Eq. 2.10):

$$n\lambda = 2dsin\theta \text{ (Eq 2.10)}$$

Where λ is the wavelength of X-rays, d is the distance between two lattice planes, θ is the angle between the incoming X-rays and the normal to the reflecting lattice plane, n is the integer number called the order of the reflection. From this relationship it is possible, given the 2θ angles from the experiment, to relate these to the lattice distances d, which are characteristic of specific crystalline phase. From the diffraction data it is also possible to estimate the crystallite size L by the Scherrer equation (2.11):

$$L = \frac{K\lambda}{Bcos\theta} \text{ (Eq. 2.11)}$$

Where K is a dimensionless shape factor often close to unit, λ is the source wavelength, B (radians) is the full width at half maximum of the peak, and θ is the angle (in degrees).

A conventional XRD source consists of a target (usually Cu) that is bombarded with high energy electrons. The resultant high energy electrons (X-rays) are emitted at discrete energy typical of the elements in the source, which give rise to the characteristic lines in the spectrum (e.g. Cu Kα). Also, the electrons can lose energy, contributing to the continuous background radiation (bremsstrahlung). When working with powdered samples, an image of diffraction is possible because the crystal are oriented to different position in order to create a constructive interference [8].
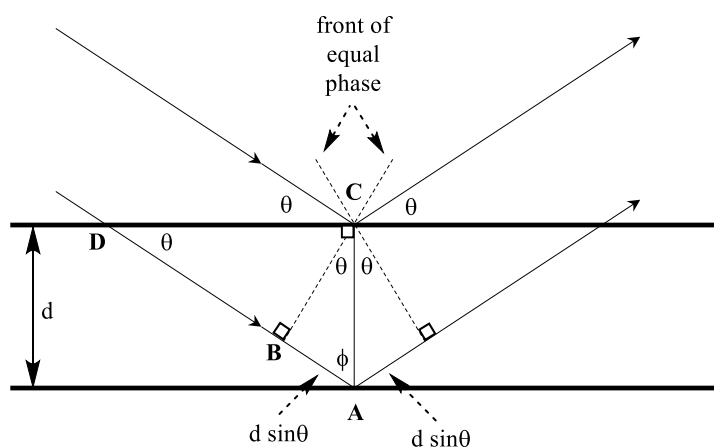
Figure 2.13 – Schematic representation of the diffraction phenomenon

Experimental

XRD diffraction patterns were acquired in the range 2θ=10-80 degrees using an X'PertPro PANalytical instrument. The source of X-rays is a Cu Kα (1.54 Å) with a Ni filter, calibrated against a Si standard. The software X'pert HighScore was used for the data treatment: first, data were corrected by the determination and subtraction of the background; successively, peaks were automatically determined by the Search Peak function. Finally, Search and Match was executed in order to assign each signal to the references in the Library. Determination of the Au and AuPd signals was carried out by direct comparison with ICCD cards (Appendix I).

2.3.3.7 Thermogravimetric Analysis (TGA)

Thermal methods of investigation may be defined as experimental methods for characterising a system (element, compound or mixture) by measuring changes in physic-chemical properties at elevated temperatures as a function of increasing temperature. In thermogravimetric analysis (TGA), changes are measured as function of increasing temperature. The basic instrumental requirements for thermogravimetric analysis are a precision balance and a furnace that is programmed for a linear rise of temperature with time.

TGA is commonly used to determine selected characteristics of materials that exhibit either mass loss or gain. Common application of TGA are 1) materials characterisation through analysis of characteristic

decomposition patterns, 2) study of degradation mechanisms and reaction kinetics, 3) determination of organic content in a sample and 4) determination of inorganic content in a sample.

TGA relies on a high degree of precision in three measurements: mass change, temperature and temperature change. Therefore, the basic instrumental requirements for TGA are precision balance with a pan loaded with the sample and a programmable furnace. The furnace can be programmed either for a constant heating rate, or for heating to acquire a constant mass loss with time.

Experimental

Thermogravimetric analysis was carried out using a Perkin Elmer TGA 4000 with autosampler, under air flow (50 mL/min) in the range of temperature 30-900 °C with a constant heating of 5 °C/min.

Bibliography

1. N. Dimitratos, J. A. Lopez-Sanchez, D. Morgan, A. Carley, L. Prati and G. J. Hutchings, *Catalysis Today*, **2007**, *122*, 317-324.

2. J. A. Lopez-Sanchez, N. Dimitratos, P. Miedziak, E. Ntainjua, J. K. Edwards, D. Morgan, A. F. Carley, R. Tiruvalam, C. J. Kiely and G. J. Hutchings, *Physical Chemistry Chemical Physics: PCCP*, **2008**, *10*, 1921-1930.

3. X. Ke, X. Zhang, J. Zhao, S. Sarina, J. Barry and H. Zhu, *Green Chemistry*, **2013**, *15*, 236-244.

4. G. D. Christian, *Analytical Chemistry,* Wiley and Sons, **1994**.

5. A. Rouessac and F. Rouessac, *Chemical Analysis: Modern Instrumentation Mehods and Techniques*, Wiley and Sons, **2007**.

6. A. Villa, N. Dimitratos, C. E. Chan-Thaw, C. Hammond, G. M. Veith, D. Wang, M. Manzoli, L. Prati and G. J. Hutchings, *Chemical Society Reviews*, **2016**, *45*, 4953-4994.

7. M. Mihaylov, H. Knözinger, K. Hadjiivanov and B. C. Gates, *Chemie Ingenieur Technik*, **2007**, *79*, 795-806.

8. J. W. Niemantsverdriet, *Spectroscopy in Catalysis - an Introduction*, Wiley-VCH, **2007**, pp. 180-184.

9. J. F. Watts and J. Wolstenholme, *An Introduction to Surface Analysis by XPS and AES*, Wiley-VCH, **2003**.

10. B. Fultz and J. Howe, *Transmission Electron Microscopy and Diffractometry of Materials*, Springer, **2013**.

Chapter 3

A Modified Sol-Immobilisation Method For The Synthesis Of Monometallic And Bimetallic Catalysts

3.1 Introduction

Sol-immobilisation [1-7] is a quick synthetic method which allows the preparation of supported nanoparticle catalysts by the formation of a metallic sol (i.e., a dispersion of solid particles in a continuous liquid medium) followed by the deposition of the nanoparticles onto a support material [8-10].

Very briefly, the method [3] consists of the reduction of metal precursor(s) dispersed in water by a strong reducing agent (usually sodium borohydride, $NaBH_4$) in presence of a stabilising polymer (usually polyvinyl alcohol, PVA or polyvinylpyrrolidone, PVP). The use of the stabilising agent (generally polymers and/or surfactants) is crucial for the stability of the generated sol, since it prevents aggregation and coalescence of the colloidal nanoparticles. In the case of PVA and PVP, which are macromolecules, this is achieved by steric hindrance [11]. Figure 3.1 displays the most used stabilising agents.
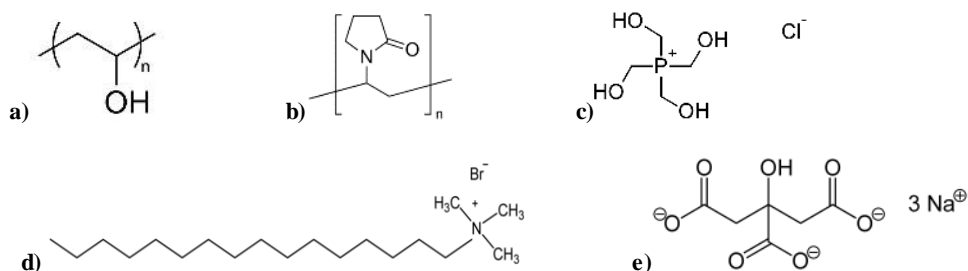
Figure 3.1 - Different stabilising agents normally employed in sol syntheses a) PVA b) PVP, c) THPC, d) CTAB, e) Sodium Citrate

Both the presence of stabilising agents and the isoelectric point (pH-dependent) of the support can affect the nanoparticles' deposition process [10, 12-14]. Moreover, as previously reported [14-19], the presence of stabilisers can be detrimental for the catalytic activity, as can block the active sites on the catalyst surface, although sometimes their presence is useful and required, providing an anchoring point for further functionalisation on the nanoparticles surface [20, 21]. However, for catalytic applications, the supported catalysts prepared by colloidal methods were often treated at high temperature [22], exposed to UV light under ozone [23, 24] or washed in appropriate conditions [15, 17, 19, 25, 26] in order to remove the stabiliser and to make the catalyst more active. Each of these treatments must be carefully selected on the basis of the nature of both the stabiliser and support. Of course these methodologies can be effective in terms of stabiliser removal but, might also cause sintering and changes in the nanoparticles morphology [27, 28]. In this scenario, it would be desirable to develop a new sol-immobilisation route completely avoiding the use of stabilisers. It is true that other synthetic routes are available for preparing catalysts without any polymer coating, such as, e.g., deposition-precipitation or wet impregnation, but a colloidal method presents several advantages in terms of reduced complexity since the nanoparticles formation is not influenced by the support [14].

Deraedt *et al.* [29] previously reported that it is possible to prepare stable (> 1 month) metallic gold colloids without the addition of stabilising agent. They obtained a 3 nm gold nanoparticles colloid by using a stoichiometric excess of $NaBH_4$ (1:10 equivalents per Au atoms) to reduce the gold precursor ($HAuCl_4$). The explanation for this success lies in the stabilisation of the Au^0 cores by a strong covalent Au-H and/or $Au-BH_4$ bond [25] and the presence of Cl^- ions in the surroundings. The unsupported colloids were successfully employed for the reduction of 4-nitrophenol to 4-nitroaniline.

Given the successful stability of the as-prepared colloids, the natural step would be to immobilise them onto a supporting material to obtain heterogeneous catalysts similar to the ones prepared by the traditional sol-immobilisation method, an investigation which to date was not reported in the open literature.

Aim of the Chapter

This chapter focuses on the synthesis and characterisation of TiO_2 supported sol-immobilised monometallic gold and bimetallic gold-palladium nanoparticle catalysts prepared by traditional (i.e., using the stabilising agents PVA and PVP) and modified sol-immobilisation methods, where the stabilising agent was omitted. The as-prepared catalysts were tested for different oxidation reactions both in gas (low temperature CO oxidation) and liquid phase (glycerol and benzyl alcohol oxidation) in order to compare their activity in terms of conversion and selectivity. The aim of the work is to understand the influence of the polymer presence on the catalysts surface and whether and how this can affect the catalytic properties of the material during the different reactions.

Low temperature CO oxidation was the first test reaction to prove the success of the new synthesis and the hypothesis about inactivity of traditional sol-immobilised (monometallic) catalysts due to the polymer presence. This reaction was selected because the gas phase ensures the polymer is not washed away during reaction and it is sensitive to nanoparticles dimension. Following this, the same samples were tested and compared for liquid-phase glycerol oxidation in basic conditions. Finally, the success of the synthesis of bimetallic samples was tested by using the catalysts for solvent-free benzyl alcohol oxidation reaction.

3.2 Catalyst Testing

3.2.1 Monometallic samples

Two monometallic catalysts 1% wt Au/TiO_2 were prepared *via* 1) traditional sol-immobilisation method using PVA as stabilising agent and 2) stabiliser-free route where the polymer was omitted. The traditional synthetic procedure involves the preparation of a colloidal solution by reduction of the Au precursor $HAuCl_4$ with $NaBH_4$ in presence of stabilising polymer, followed by the deposition on TiO_2, as described in Chapter 2.

3.2.1.1 CO oxidation

The monometallic 1% wt Au/TiO_2 catalysts prepared by traditional and stabiliser-free sol immobilisation method (Au/TiO_2-PVA and Au/TiO_2-SF respectively) were tested for low-temperature CO oxidation. This was selected as a test reaction to verify the success of the modified synthesis method and to gain an indication of whether small nanoparticles were synthesised [30-32].

CO oxidation (Scheme 3.1) at ambient and sub ambient temperatures has been widely studied due to its fundamental scientific interest and technological importance: it is a highly toxic gas, which should be either captured or converted to CO_2 before being released in the atmosphere [33-36].

$$CO + \frac{1}{2}O_2 \rightarrow CO_2 \quad \Delta H = -283 \; kJ/mol \quad \text{(Scheme 3.1)}$$
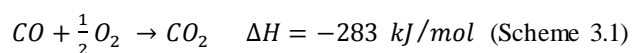
Among catalysts, gold nanoparticles supported on oxides were proven to be very active for CO oxidation at sub ambient temperatures [14,31,32,37]. Investigation of the factors which determine the catalytic activity showed that besides nanoparticle size, the nature of the support and the length of perimeter interface between Au/support are also key factors for the CO oxidation [30], meaning that synthetic routes play a fundamental role. Among the most used methods for preparing active catalysts are co-precipitation and deposition-precipitation. The Au nanoparticles prepared by deposition-precipitation method, for example, have been shown to be extremely active and this has been ascribed to the formation of hemispherical metal particles sized ca. 3 nm strongly attached to the support. Catalysts prepared by other methods, for example impregnation, that lead to the formation of larger (ca. 10 nm) spherical particles exhibiting poorly defined interaction with the support, were shown to be not as active [30].

Comotti *et al.* [14] showed that it is possible to obtain active catalysts also by sol-immobilisation even if their performance is affected by the presence of polymer: its removal by calcination was proven to be effective but the heat treatment conditions needs to be carefully selected in order to avoid nanoparticle sintering with consequent loss in activity.

The dried only 1% wt Au/TiO_2 samples prepared SF and PVA and the corresponding samples calcined at 500 °C for 3 h were compared in terms of CO conversion at 25 °C (Figure 3.2). Calcination at this temperature was necessary in order to ensure polymer removal on the traditional sample, as shown in the thermogravimetric analysis (TGA) in Figure 3.3; the stabiliser-free sample was treated at the same temperature for comparison. Comparing the activity of the dried samples (bold lines) with their calcined counterparts (dashed lines), it is clear that calcination improves catalytic activity in a more pronounced way for the traditional sample than for the stabiliser-free, with CO conversion reaching 45 % for the former. This might be due either to the calcination modifying the nanoparticle/support interface and/or removing the polymer from the surface.
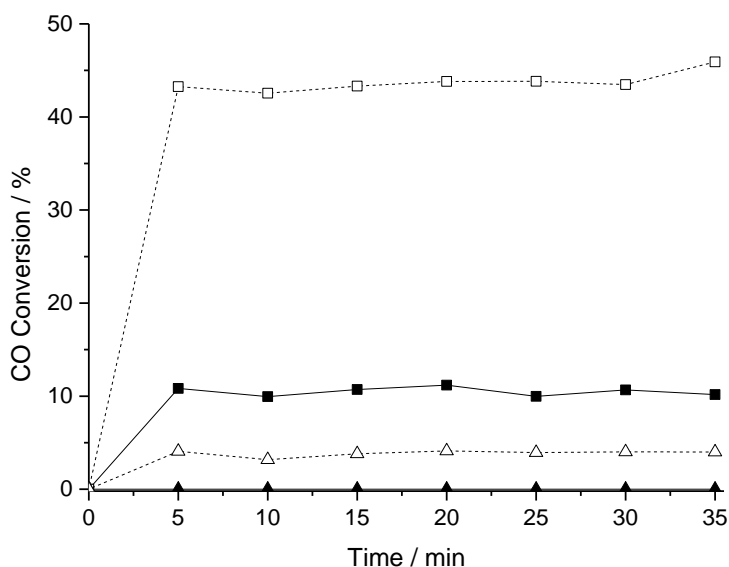
Figure 3.2 - Comparison of the catalytic activity for the 1% wt Au/TiO_2 samples prepared SF and PVA dried and calcined. *Legend*: ▲ SF ■ PVA; Bold line - dried catalyst, dashed line and hollow symbol – calcined 500 °C. *Reaction conditions*: catalyst 0.05 g, 25 °C, CO (1000 ppm in air) 25 mL/min, GHSV =24 000 h^{-1}
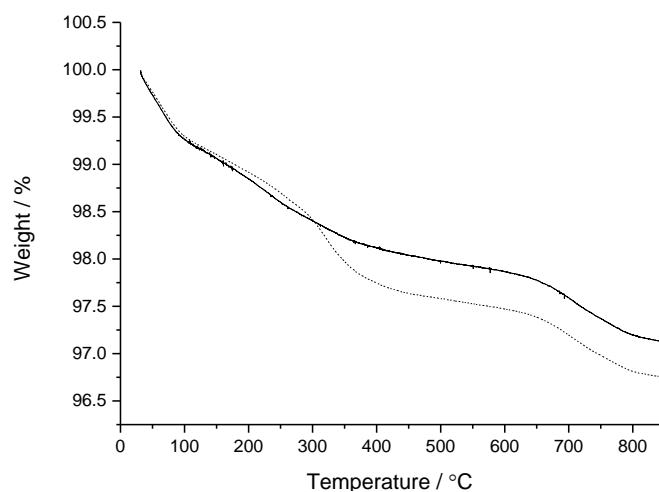
Figure 3.3 - Thermogravimetric analysis for the 1% wt Au/TiO_2 catalysts prepared PVA (dotted line) and SF (bold line)

TGA performed on both the catalysts prepared PVA and SF (Figure 3.3) shows a weight loss for both catalysts with increasing temperature. Taking into account that the SF sample is polymer-free, the mass loss observed for this should be related mainly to the moisture removal, whereas the more pronounced weight drop for the PVA catalyst might indicate the removal of the polymer.

When comparing the dried 1% wt Au/TiO_2-PVA and the 1% wt Au/TiO_2-SF samples, surprisingly the traditional sample shows better activity than the stabiliser-free: in this case, the opposite behaviour could be expected, since the former is expected to have the surface obstructed by the polymer [7, 14, 15]. The origin of the inactivity of the stabiliser-free catalyst might be related to two factors:

a. the presence of chloride residues from the gold precursor;

b. bigger nanoparticle size.

a) Chloride residues

Chloride is known to be a poison for the catalytic active site [38]. The mechanism of interference with the active site depends on the model for the active site that is considered, as reported by Kung *et al.* [39]. For example, in the reaction mechanism proposed in Figure 3.4 the chloride is believed to displace the hydroxyl from the Au cation [38, 40], interfering with the CO adsorption.

It has been demonstrated that the presence of hydroxyl is fundamental for the CO oxidation [41,42]. In the model displayed in Figure 3.4 the reaction proceeds by insertion of an adsorbed CO into an Au-OH bond to form a hydroxycarbonyl, subsequent oxidation to a bicarbonate, which is then decarboxylated to Au-OH and CO_2. It is also proposed that O_2 is dissociatively adsorbed on Au [39].
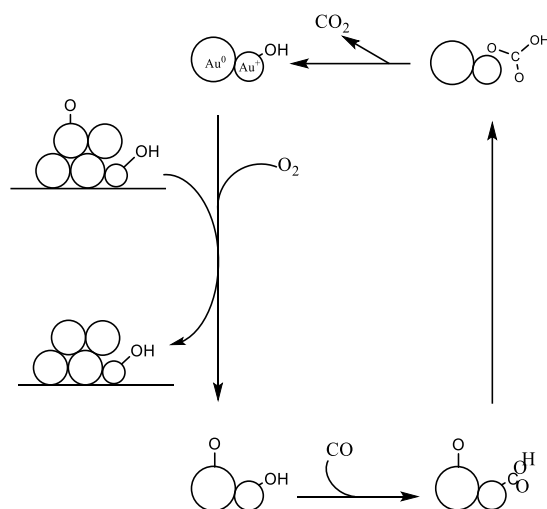
Figure 3.4 - Mechanism of CO oxidation on Au catalyst (reproduced from ref. [39])

Evidence of the involvement of the hydroxyl group in the CO oxidation was given by the observation that water is able to regenerate a deactivated catalyst [40]. The origin of the deactivation has been suggested to be related to the formation of carbonate or bicarbonate species. In particular, Haruta [43] demonstrated that at temperatures below 200 K, when carbonate species are present at the interface Au/TiO_2, the reaction takes place only at step, edge and corner sites on the Au particles. Conversely, at temperatures between 200-300 K, the amount of carbonate species at the interface decreases, and the reaction proceeds at the perimeter interface with an activation energy of nearly zero. These observations agree with the model proposed in Figure 3.4 and further confirm the importance of presence of moisture.

b) Nanoparticles size

TEM results displayed in Figures 3.5 and 3.6, show that the mean nanoparticle size and size distribution appear to be slightly larger with a broader distribution for the 1% wt Au/TiO_2-SF sample, a small difference which might have a great influence on the catalytic performance in such structure-sensitive reaction.
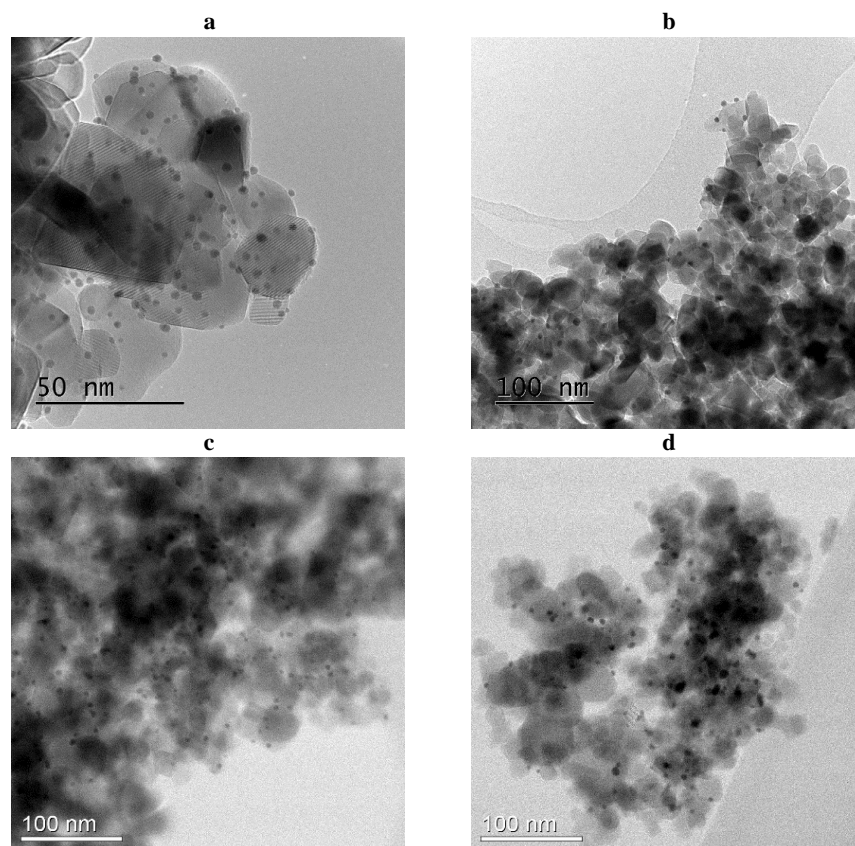
Figure 3.5 – Representative BF-TEM micrographs of the 1% wt Au/TiO_2 catalysts PVA and SF.
a, c TEM images of 1% wt Au/TiO_2 prepared *via* PVA dried (a) and calcined at 500 °C (c);
b, d TEM images of 1% wt Au/TiO_2 prepared *via* SF dried (b) and calcined at 500 °C (d).

Comparison of the particle size distributions in Figure 3.6 shows that materials prepared with polymer addition tend to have a narrower particle size distribution and lower mean particle size (2.7 ± 0.6 nm) than the stabiliser free sample (5.4 ± 1.6 nm), as expected, since the nanoparticles growth was not controlled.

Calcination at 500 °C leads to an increase in the nanoparticles size for the traditional sample, still with a narrow size distribution. Surprisingly, the opposite effect is observed for the stabiliser-free sample, where the mean size decreases, yet with a broad distribution. The formation of smaller nanoparticles (2-3 nm), which could suggest an Ostwald's ripening mechanism of particle sintering, together with the removal of the chloride residues with calcination, might be at the origin of the small increase in the catalytic activity during CO oxidation observed for this sample. The presence of small nanoparticles and the increased surface availability

after calcination (i.e., polymer burnt) might explain the increased activity of the traditional sample. Also, in

both cases, calcination might have improved the nanoparticle/support interaction, that as aforementioned has

been demonstrated to be very important to achieve enhanced activity for CO oxidation reaction [30].
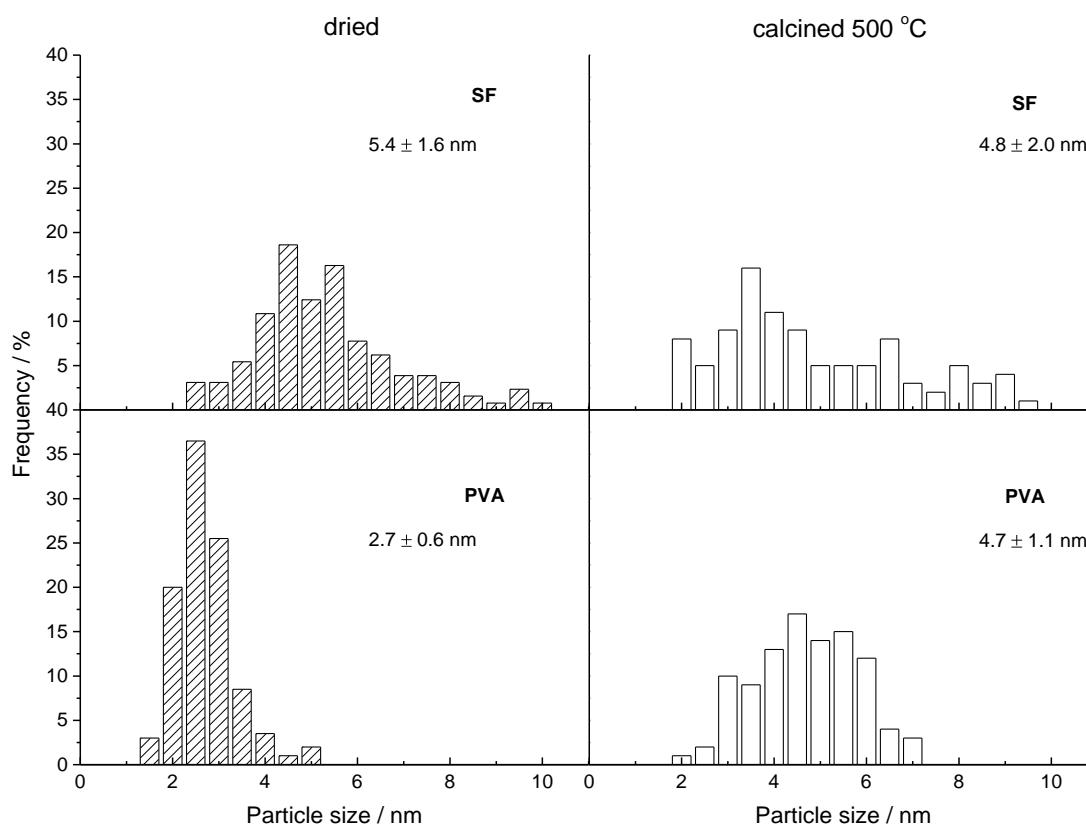
Figure 3.6 - Particle size distributions derived from bright field TEM images of more than 100 Au nanoparticles from the dried only Au/TiO$_2$-SF and Au/TiO$_2$-PVA samples and the correspondent calcined at 500 °C.

3.2.1.2 Glycerol oxidation

Despite the inactivity towards CO oxidation, the stabiliser-free and the PVA catalysts were tested for liquid

phase glycerol oxidation in basic conditions. The catalytic activity of a third catalyst prepared using PVP as

stabilising polymer was also evaluated. The activity of the three samples was compared in terms of conversion

and selectivity to main products, as displayed in Figure 3.7.
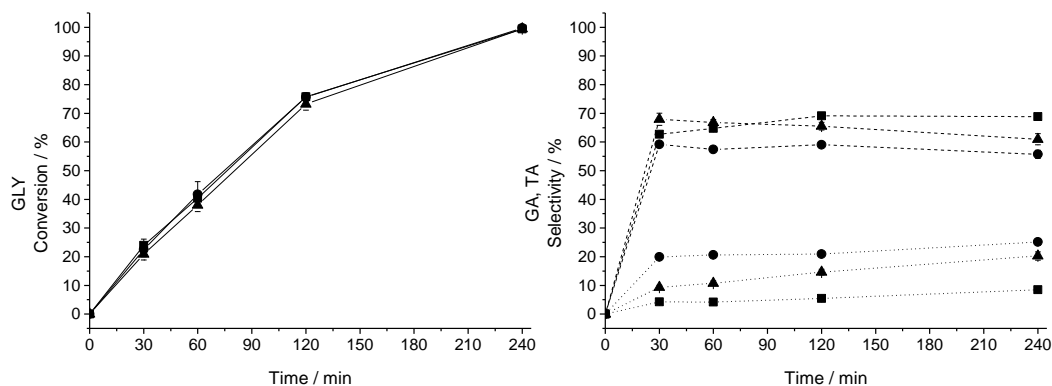
Figure 3.7 - Comparison of the glycerol oxidation activity for sol-immobilised monometallic 1% wt Au/TiO$_2$ catalysts prepared either stabilizer free, SF (●), or in the presence of PVA (▲) or PVP (■) ligands. Reaction conditions: 110 mg catalyst, 3 bar O$_2$, 60 °C, 1200 rpm, Gly/Au=500. *Legend*: dotted lines - tartronate (TA); dashed lines -glycerate (GA).

Comparison of the particle size distributions, displayed in Figure 3.8, shows that materials prepared with polymer addition tend to have a narrower particle size distribution and lower mean particle size (PVA: 2.7 ± 0.6 nm; PVP: 3.5 ± 1 nm) than the stabilizer free sample (5.4 ± 1.6 nm). Nonetheless, the results suggest that the catalyst prepared using the SF route performs in a very similar manner to its analogues prepared with PVA or PVP, as shown by the glycerol oxidation results shown in Figure 3.7. This might be due to the increased accessibility of the reactants in the absence of polymer counterbalanced by the size increase.
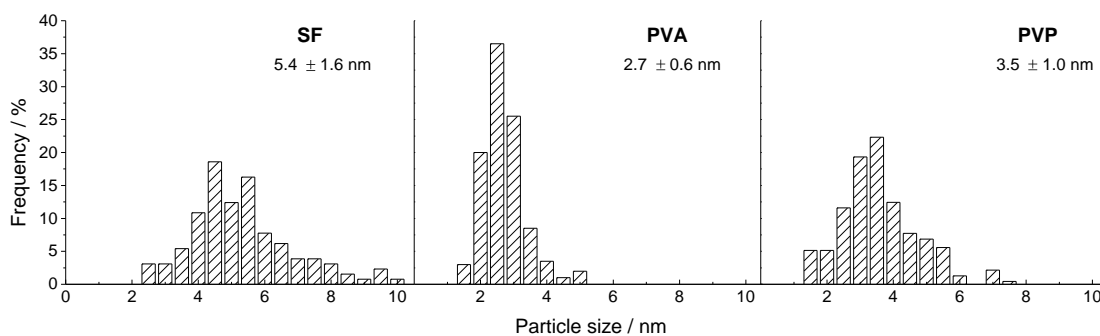
Figure 3.8 – Particle size distributions derived from bright field TEM images of 100 Au particles prepared SF, PVA and PVP.

However, the SF catalyst appears to be more selective to tartronate (TA) than the traditional samples synthesized by PVA and PVP, which are more selective to glycerate (GA). This observation will be discussed in more detail in Chapter 4, with a more complete discussion of this reaction and additional experiments. The

success of the synthesis and the performance of the catalyst in liquid phase reaction encouraged the synthesis of bimetallic AuPd catalysts using the same method. The resulting materials were tested for benzyl alcohol oxidation and later, as presented in Chapter 4, for glycerol oxidation in basic conditions.

3.2.2 Bimetallic samples

Two bimetallic catalysts 1% wt AuPd/TiO$_2$ were prepared *via* the traditional and the stabiliser-free sol-immobilisation method, as described in Chapter 2, in a similar way reported for the synthesis of the monometallic samples.

3.2.2.1 *Benzyl alcohol oxidation*

Dried only bimetallic 1% wt AuPd/TiO$_2$ samples prepared by traditional sol-immobilisation method using PVA as stabiliser polymer (1% wt AuPd/TiO$_2$-PVA), and by the modified method with no stabiliser addition (1% wt AuPd/TiO$_2$-SF) were compared in terms of activity and selectivity for solvent-free benzyl alcohol oxidation reaction. Similarly to CO oxidation, this well-known reaction [1-4, 44-48] (Scheme 3.2), was chosen as a quick test to evaluate the performances of bimetallic catalysts.
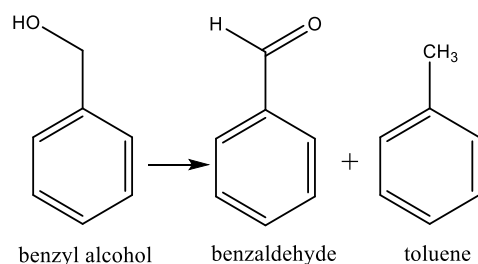
Scheme 3.2 - Reaction scheme of benzyl alcohol oxidation

Figure 3.9 shows that the PVA and SF variants of the AuPd/TiO$_2$ catalysts had very similar reaction profiles in terms of benzyl alcohol conversion and selectivity towards benzaldehyde and toluene. This might indicate that the samples are very similar in composition and morphology despite the absence of the stabiliser. Also, the presence of PVA seems not to affect the activity (and selectivity) for this reaction, as was observed in the monometallic case for glycerol oxidation.

TEM and XPS analysis (Figure 3.10 and Table 3.1) confirmed that the absence of the stabiliser does not have a great influence on the catalyst features in terms of particles size and oxidation state of metals.
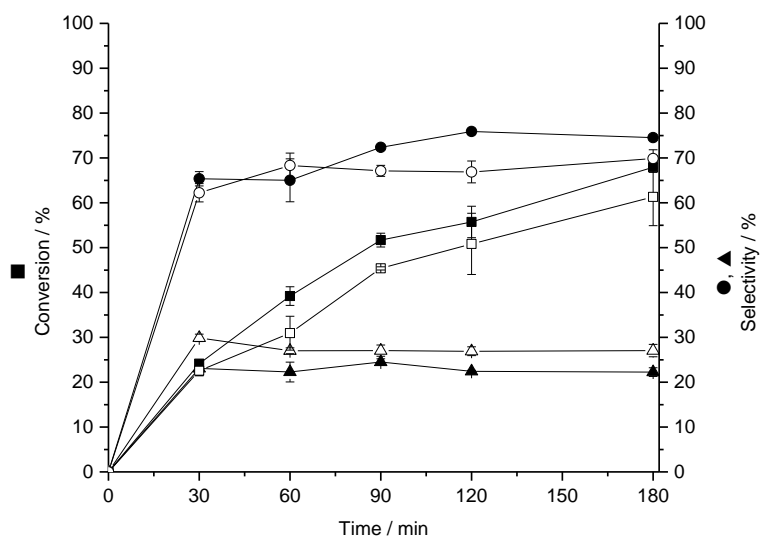
Figure 3.9 – Comparison of PVA and SF 1% wt AuPd/TiO$_2$ catalysts for the solvent-free oxidation of benzyl alcohol. *Reaction conditions*: 20 mg catalyst, BnOH/metals= 28000 (mol), 120 °C, 1 bar O$_2$, 1000 rpm. Filled symbols: PVA, hollow symbols: SF. ■, □ benzyl alcohol conversion; ●,○- benzaldehyde selectivity; ▲,△- toluene selectivity.
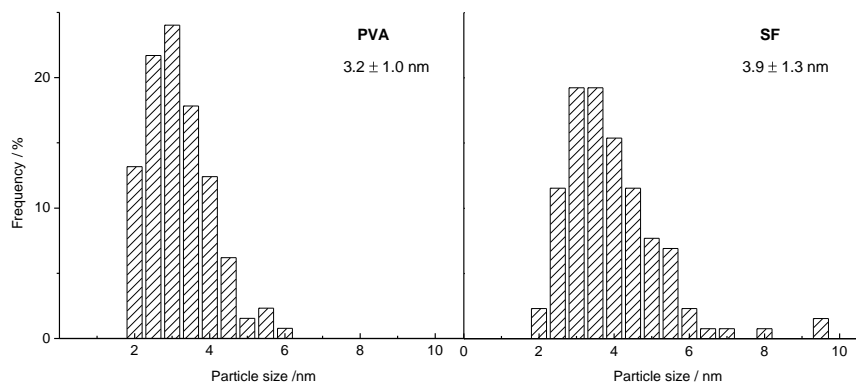
Figure 3.10 – Particle size distributions derived from bright field TEM images of 100 AuPd particles prepared SF and PVA

Analysis of the particle size distributions shows a minimum difference in dimensions between the two catalysts (PVA: 3.2 ± 1 nm; SF: 3.9 ± 1.3 nm). In addition, the size distribution for the SF sample appears to be narrower than in the monometallic case, indicating that the alloy might have a beneficial effect in terms of size control.

XPS results on the same catalysts reported in Table 3.1 indicated a similar Au : Pd surface ratio in all samples, with the Pd being present in the metallic state as confirmed by its binding energy (335.0 - 335.5 eV).

Table 3.1 – Summary of physical characteristics determined by XPS and TEM analysis of monometallic Au and bimetallic AuPd sol-immobilised catalysts supported on TiO$_2$ prepared SF and PVA.

Catalys	Stabilizer Identity	Mean Particle Size (nm)	Au 4f binding energy (eV)	Pd 3d binding energy (eV)	Au:Pd atomic ratio
1% wt AuPd / TiO$_2$	SF	3.9	84.0	335.0	1.5
	PVA	3.0	84.0	335.5	1.4

3.3 Catalyst Characterisation

3.3.1 UV-Vis of Au and AuPd colloidal solutions

UV-Vis analysis was performed on colloidal gold and gold-palladium solutions 30 minutes after reduction by NaBH$_4$, in order to prove the reduction of metals effectively took place. In particular, for gold, the position and shape of plasmonic peak can give an indication on size and shape of nanoparticles, e.g. smaller nanoparticles typically show a blue-shifted signal and nanorods show double signals corresponding to axial and longitudinal resonance [49, 50]. This information though can be misinterpreted since factors such as pH, aggregation of nanoparticles and the dielectric environment can have an effect on the electron resonance and consequently on the peak shape and position [51, 52].

The UV-Vis spectra of colloidal Au and AuPd solutions prepared SF and with PVA and PVP are shown in Figure 3.11. As expected, the formation of metallic gold is evidenced by the presence of the plasmonic peak: spherical gold nanoparticles of size 10-20 nm usually show a plasmonic peak located at 520 nm [12, 53, 54], but as aforementioned, the position depends on many parameters [12, 51, 52, 55-57]. In this case, the blue shift of the peak at 504 nm for all the samples could be related to the formation nanoparticles below this size, while the broader shape for the PVA and PVP samples might be due to the polymer presence modifying the dielectric environment or decreasing nanoparticles size [58].

Regarding the AuPd solutions, as previously reported [59], the presence of Pd in 1:1 mole ratio suppresses the surface plasmon of the gold structures, therefore it is expected to see no plasmonic signal for these colloids, even if the reduction took place. The absence of the plasmon peak of Au is an evidence that a bimetallic particle has been formed.
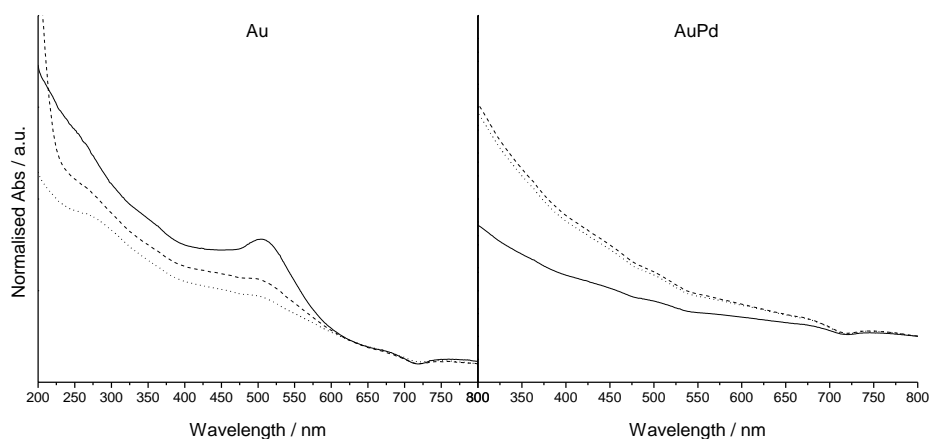
Figure 3.11 - UV-vis spectra of colloidal gold solutions. *Legend*: solid SF; dotted PVA; dashed PVP

3.3.2 Diffuse reflectance UV-Vis of the TiO$_2$-supported Au nanoparticles

The TiO$_2$-supported gold and gold-palladium catalysts were qualitatively analysed by diffuse reflectance UV-Vis (DR-UV-Vis) in order to obtain more information on the final material. DR UV-Vis spectra of the monometallic catalysts prepared stabiliser free, PVA and PVP and the support (bare TiO$_2$, P25) are shown in Figure 3.12.
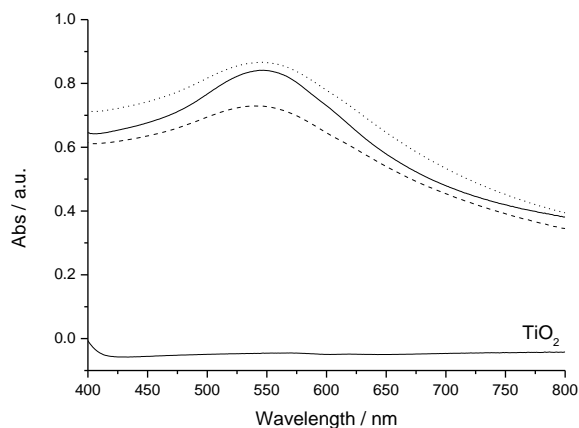
Figure 3.12 - Diffuse Reflectance UV-Vis spectra of 1% wt Au/TiO$_2$ samples prepared SF (solid), PVA (dotted), PVP (dashed), and bare TiO$_2$

Supporting the nanoparticles leads to a red shift of the plasmonic peak (around 545 nm for all the samples), which might be correlated either to the growth of nanoparticles or to the interaction with the support leading to a change in nanoparticles shape and symmetry [12, 60]. The Au/TiO$_2$-SF sample appears to have the sharpest peak, while the PVP and PVA samples show broader peak which again might be due to the presence of the stabilising agent interacting in a different way with the support.

Heat treatment such as calcination in air and reduction in H$_2$ flow both at 500 °C further influences nanoparticles size and interaction with the support for all the three catalysts, as it can be evaluated from the position and shape of the plasmonic peak in Figure 3.13. The heat treatment on the monometallic catalyst prepared stabiliser-free causes a modification in the plasmonic peak position, which shifts from 545 nm of the dried sample to 555 nm for reduced and 566 nm for calcined. Both heat treated samples show broader peak, which might indicate an increase in the nanoparticles size or modification of the interaction with the support. The same effects can be observed also for the catalysts prepared by PVA and PVP, suggesting a similar behaviour for the nanoparticles prepared with the stabiliser addition.
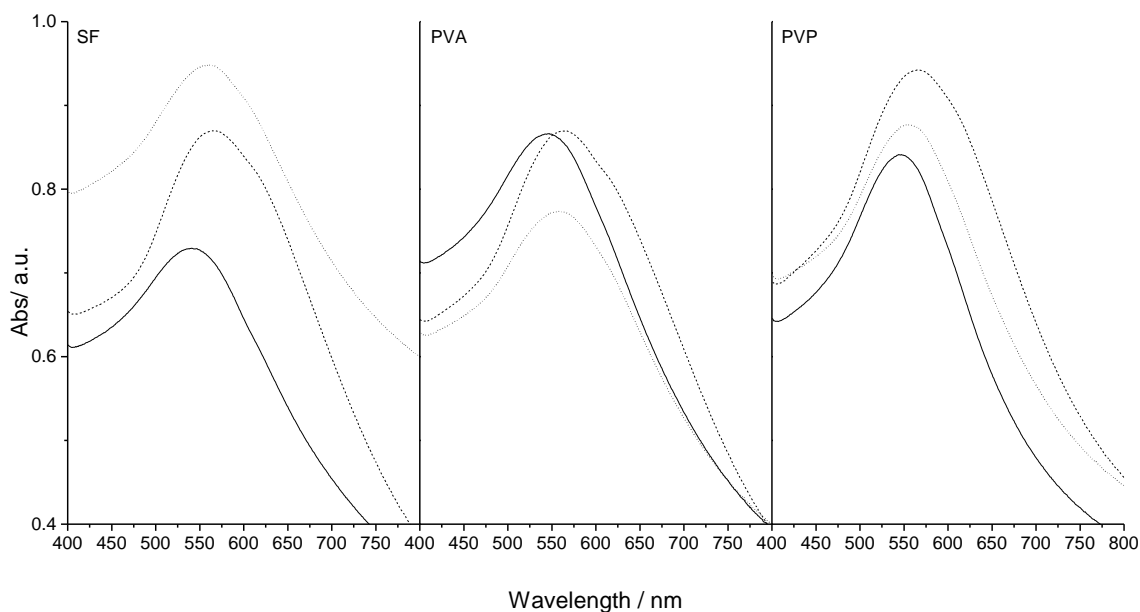
Figure 3.13 - Diffuse Reflectance UV-Vis spectra of 1% wt Au/TiO$_2$ prepared SF, PVA and PVP dried (solid lines), calcined (dashed lines), reduced (dotted lines)

3.3.3   XRD of 1% wt Au/TiO$_2$ and 1% wt AuPd/TiO$_2$

X-ray diffraction analysis was performed on monometallic and bimetallic samples prepared stabiliser-free, PVA and PVP in order to observe any gold and palladium diffraction signals. The diffraction patterns of the monometallic 1% wt Au/TiO$_2$ samples prepared SF, PVA and PVP are shown in Figure 3.14. The successful formation of crystalline gold nanoparticles can be identified by the presence of a reflection signal at $2\theta \approx 44°$, corresponding to the diffraction on the (200) plane (ICCD 00-004-0784, see Appendix I). The intensity of this signal is very low due to both the low amount of gold on the TiO$_2$ support and to the very small particle size (≤ 5 nm); moreover, the reflection at $2\theta \approx 44°$ is not the most intense, but is the only observable on these materials. Indeed, the most intense reflection signal for the gold should be visible at $2\theta \approx 38°$ but is overlapping with the anatase-TiO$_2$ reflections of planes (004) and (112) at a similar angles ($2\theta \approx 37.8°$ and $2\theta \approx 38.6°$) (ICCD 00-021-1272, see Appendix I). Similar patterns are obtained for the bimetallic samples prepared SF, PVA and PVP, displayed in Figure 3.15. As in the monometallic case, also for the bimetallic catalysts the diffraction signals for gold-palladium nanoparticles present very low intensity which makes their location difficult. In this case, a signal can be identified at $2\theta \approx 45°$, correspondent to the reflection of AuPd (200) planes (ICCD 01-072-5376, see Appendix I).
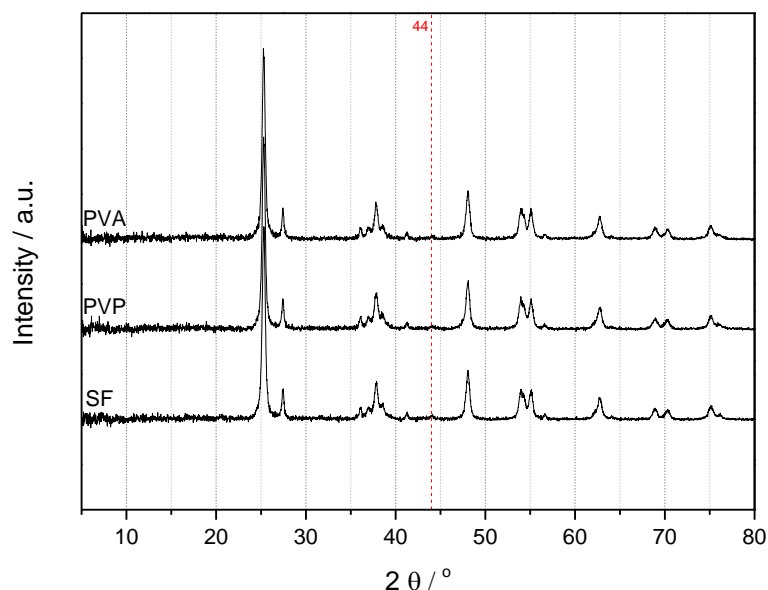
Figure 3.14 - XRD pattern for 1% wt Au/TiO$_2$ samples prepared SF, PVP, PVA
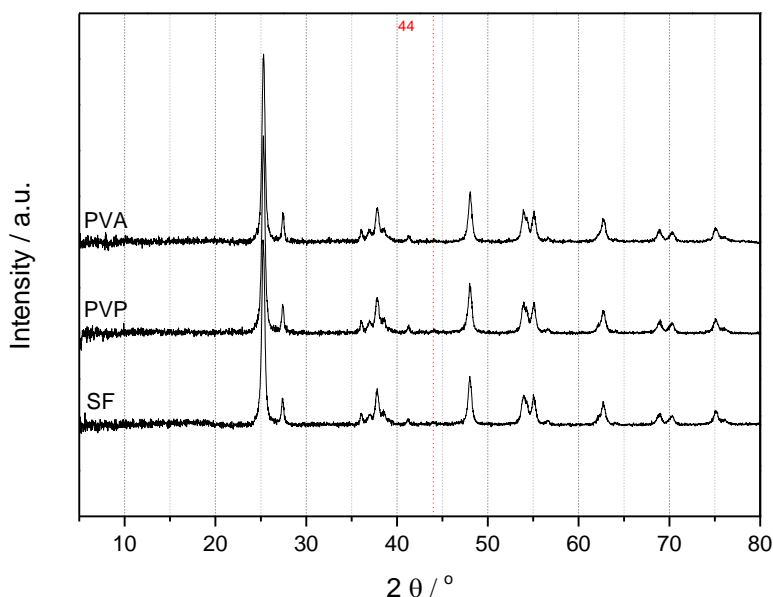
Figure 3.15 - XRD pattern for 1% wt AuPd/TiO$_2$ samples prepared SF, PVP, PVA

3.3.4 CO-DRIFTS of 1% wt Au/TiO$_2$ and 1% wt AuPd/TiO$_2$

CO-DRIFTS analysis was performed for each mono and bimetallic catalyst prepared in the three variants SF, PVA and PVP in order to investigate the modification of the catalyst surface sites and how the presence of the polymer affects them, before and after heat treatment. Calcination and reduction on the monometallic catalysts synthesized SF, PVA and PVP was necessary in order to investigate the origin of the inactivity of the samples towards CO oxidation; in particular, to confirm that it is not related to the presence of species blocking the active sites. For all the spectra presented in this Section, a list of signals and band assignment can be found in Table I in the Appendix I of this Thesis.

Figure 3.16 shows the CO-DRIFTS spectra of the Au/TiO$_2$ sample prepared SF in its versions dried only, calcined and reduced. Only the calcined sample shows a weak adsorption peak at 2095 cm^{-1}, correspondent to linear CO adsorption [61]. This is consistent with the weak activity observed for this sample during CO oxidation and can be due to the presence of small nanoparticles after calcination, as previously shown in TEM size distribution. No CO adsorption was detected onto other surfaces, which might be related to larger nanoparticle

size [31]. All the samples present bands in the region 1700-1000 cm^{-1} which can be assigned to the carboxylate or bicarbonate species [32, 62, 63] on TiO_2.
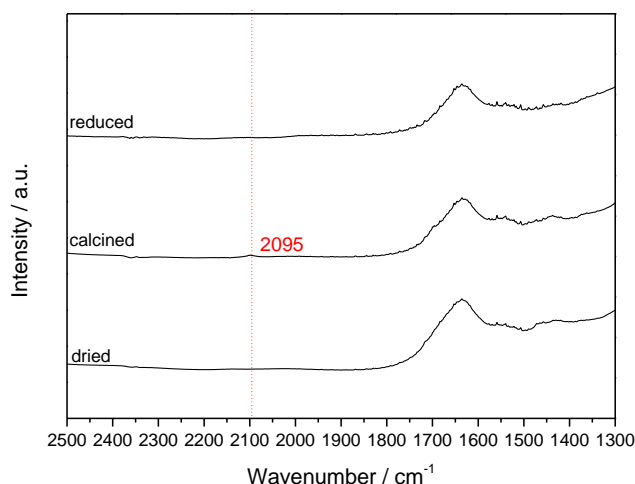
Figure 3.16 - CO-DRIFTS spectra of 1% wt Au/TiO_2 catalyst prepared SF dried, calcined and reduced

Figure 3.17 shows the spectra for the monometallic sample prepared in presence of PVA dried, calcined and reduced. The dried sample is the only one that shows a small but clear peak at 2110 cm^{-1}, which can be attributed to the CO adsorbed linearly. The absence of any signal for the calcined sample might be due to the fact that the fraction of 2-3 nm nanoparticles (responsible of the CO adsorption) is too small to generate a signal in the DRIFTS but at the same time is enough to promote CO oxidation, as experimentally observed. This explanation would be consistent with the size distribution reported in Figure 3.6. In the case of the reduced sample, it is possible that nanoparticles size is too large to adsorb CO and to promote CO oxidation.

Again, all the samples present bands in the region 1700-1000 cm^{-1} which can be assigned to carboxylate or bicarbonate species on TiO_2. It is worth to notice here that the peaks in the region around 1540 cm^{-1} and 1440 cm^{-1}, with the latter being attributed to free carbonate [63], have a slightly different shape when the samples have undergone heat treatment, which can be explained by the modification of the TiO_2 surface.
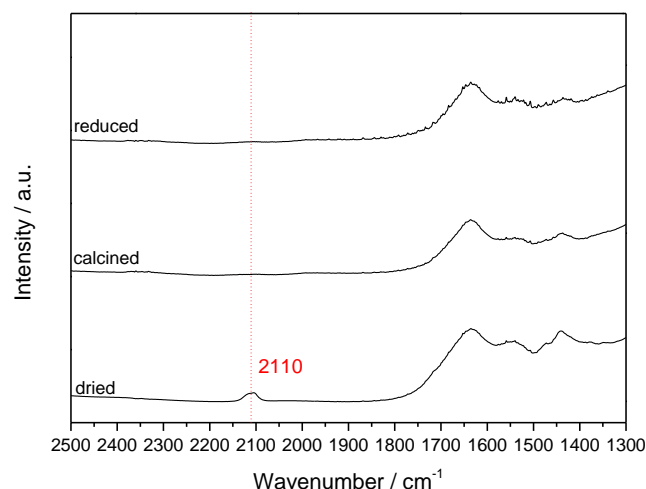
Figure 3.17 - CO-DRIFTS spectra of 1% wt Au/TiO$_2$ catalyst prepared PVA dried, calcined and reduced

Figure 3.18 displays the spectra for the samples prepared in presence of PVP. In this case, none of the samples show a CO adsorption peak. This might be due either to the presence of the polymer completely blocking the access to the catalyst's surface or to the larger nanoparticles size. Calcined and reduced samples are expected to be PVP-free, as shown by thermogravimetric analysis reported in Figure 3.19, therefore the reason of the non-adsorption of CO should be ascribed to the bigger nanoparticle size. The region 1700-1000 cm^{-1} shows bands correspondent to carboxylate or bicarbonate species on TiO$_2$ for all the samples.
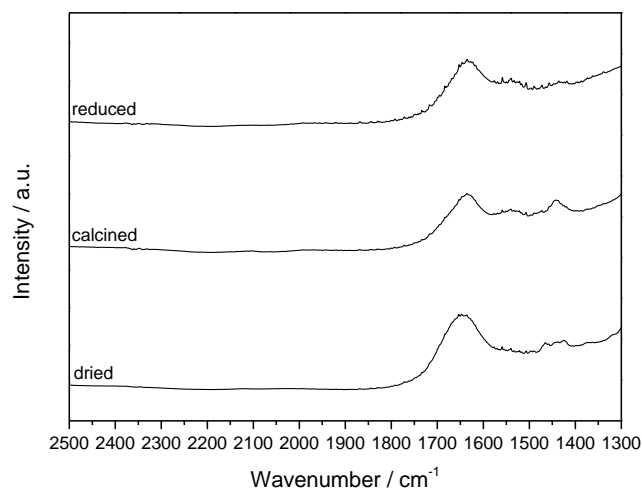
Figure 3.18 - CO-DRIFTS spectra of 1% wt Au/TiO$_2$ catalyst prepared PVP dried, calcined and reduced
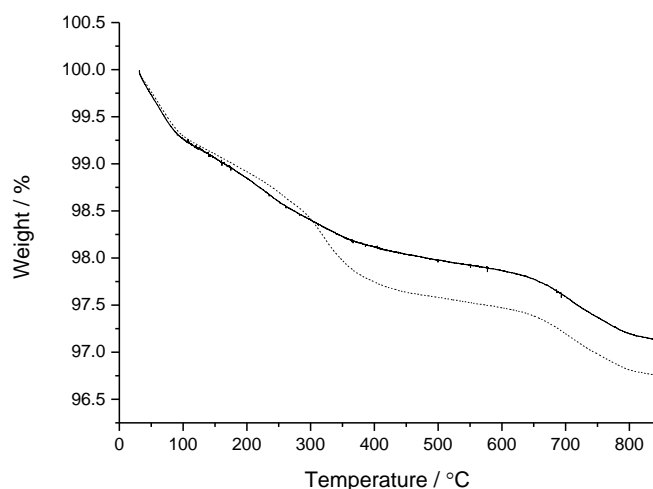
Figure 3.19 – Thermogravimetric analysis for 1% wt Au/TiO$_2$ synthesized PVP (dotted line) and SF (bold line)

CO-DRIFTS analysis was performed also for bimetallic samples. Figure 3.20 shows the DRIFTS spectra of the bimetallic sample prepared SF dried, calcined and reduced. The bimetallic samples also show peaks in the region 2200-2000 cm^{-1}. The dried sample presents two merged peaks at 2080 cm^{-1} and 2053 cm^{-1} respectively, which can be assigned to the linear adsorption of CO on Pd (edge or corner) [61]. The region corresponding to bridged or three fold CO adsorption on Pd or AuPd (2000-1800 cm^{-1}) [61, 64] shows two signals at 1983 cm^{-1} and 1943 cm^{-1} respectively. Heat treatment leads to an increase in the nanoparticles size and this might be at the origin of the disappearance of CO adsorption signals.
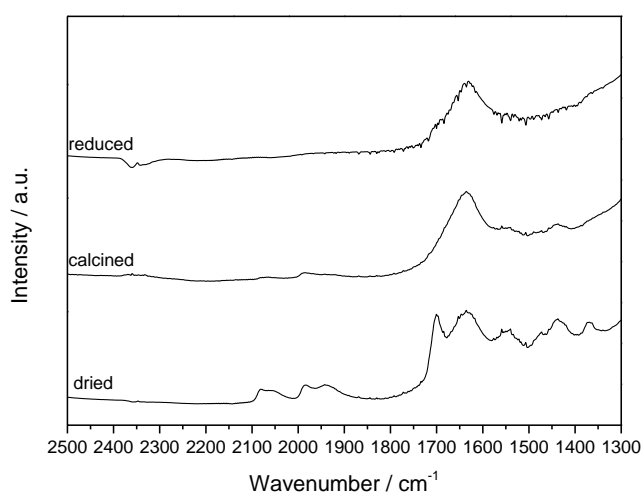
Figure 3.20 - CO-DRIFTS spectra of 1% wt AuPd/TiO$_2$ catalyst prepared SF dried, calcined and reduced

The CO-DRIFTS spectra for the bimetallic samples synthesized with PVA are shown in Figure 3.21. Similarly to the SF catalyst, this sample shows two merged peaks in the region between 2108 cm^{-1} and 2014 cm^{-1} correspondent to the linear CO adsorption. Heat treatment at 500 °C causes an increase in the nanoparticles size and consequently a weaker CO adsorption, but it is still possible to observe clear peaks for the reduced sample at 2055 cm^{-1} and 1934 cm^{-1}.

The CO-DRIFTS spectra for the bimetallic samples synthesized with PVP are shown in Figure 3.22. In this case, the spectrum of the dried catalyst shows more defined peaks in the linear and bridging region (2058 cm^{-1} and 1932 cm^{-1} respectively) [36, 65] when compared with the SF and PVP ones. Similarly to the previous cases, the heat treatment modifies the surface so the signals for these samples are different.
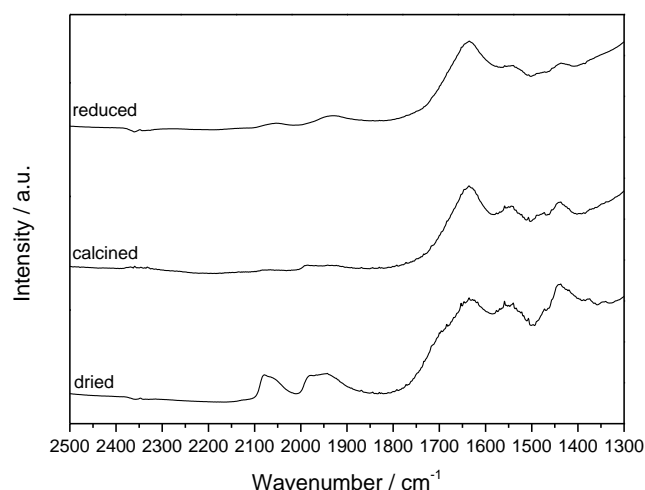
Figure 3.21 -CO-DRIFTS spectra of 1% wt AuPd/TiO$_2$ catalyst prepared PVA dried, calcined and reduced
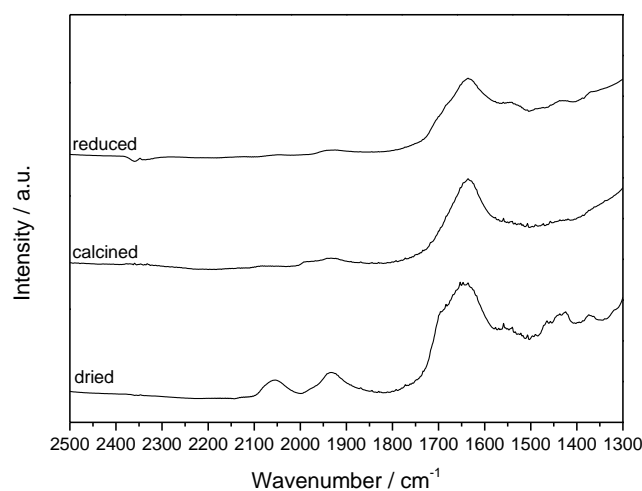
Figure 3.22 - CO-DRIFTS spectra of 1% wt AuPd/TiO$_2$ catalyst prepared PVP dried, calcined and reduced

An interesting comparison as shown in Figure 3.23 can be done on the dried samples synthesized by the three different methods. The SF and PVA samples both present very similar signals in the region 2200-1800 cm^{-1} correspondent to linear and bridged CO adsorption on Pd, suggesting that the active sites are not heavily affected by the polymer presence. This is not true for the PVP sample, for which only two peaks appear, shifted to lower wavenumbers. This might indicate that the polymer is strongly influencing the interaction with the CO by modifying the access to catalytic sites. It is worth to mention here that the fingerprint region (1750-1250 cm^{-1}) contains information regarding the interaction of carbonate and hydroxycarbonyl species with TiO_2. The difference in the signals shape for the three samples might be related to the different TiO_2 surface coverage with stabilising agent. Although not possible during the PhD work, it would be worth to study more accurately the signals in this region, since they might contain more useful information on the polymer-TiO_2 interaction.
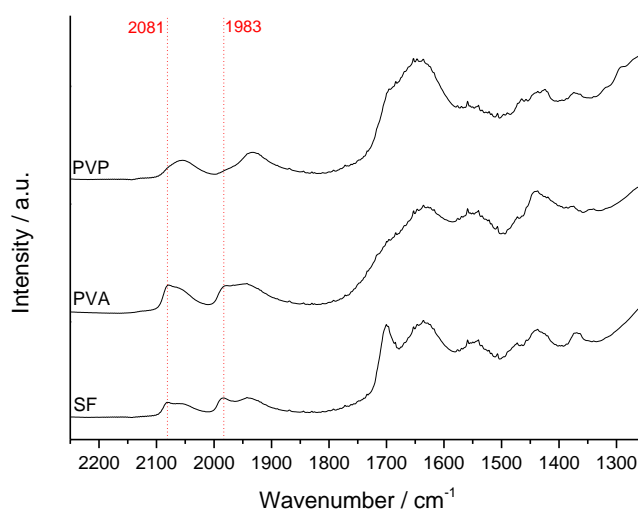
Figure 3.23 - CO-DRIFTS spectra of 1% wt AuPd/TiO_2 dried catalyst prepared SF, PVA and PVP

3.3.5   X-Ray photoelectron spectroscopy

X-ray photoelectron spectroscopy (XPS) (Table 3.2 and Figures 3.24-3.25) was carried out on mono and bimetallic samples prepared in the three variants and confirmed the similarity of the sol-immobilised materials produced with and without the addition of polymer stabilizers. The binding energy of the Au (84.2-83.9 eV) indicates the presence of metallic Au in all of the monometallic samples as expected [66], as shown in Figure

3.24. Analysis of the bimetallic catalysts indicated a similar Au : Pd surface ratio in all samples, with the Pd being present in the metallic state as indicated by its binding energy (335.0 - 335.5 eV).
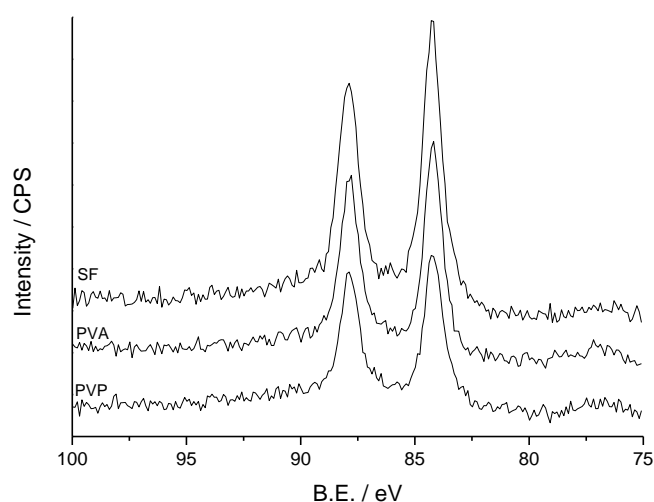
Figure 3.24 – Au4f XPS signals for 1% wt Au/TiO$_2$ prepared SF, PVA, PVP

Table 3.2 – Summary of physical characteristics determined by XPS and TEM analysis of monometallic 1% wt Au and bimetallic 1% wt AuPd sol-immobilised catalysts supported on TiO$_2$ prepared either under stabilizer free (SF) conditions, or in the presence of PVA or PVP ligands.

Catalyst	Stabilizer Identity	Mean Particle Size (nm)	Au 4f binding energy (eV)	Pd 3d binding energy (eV)	Au:Pd atomic ratio
1% wt Au / TiO$_2$	SF	5.4	84.2	-	-
	PVA	2.7	84.2	-	-
	PVP	3.5	84.2	-	-
1% wt AuPd / TiO$_2$	SF	3.9	84.0	335.0	1.5
	PVA	3.0	84.0	335.5	1.4
	PVP	3.2	83.9	335.4	1.4
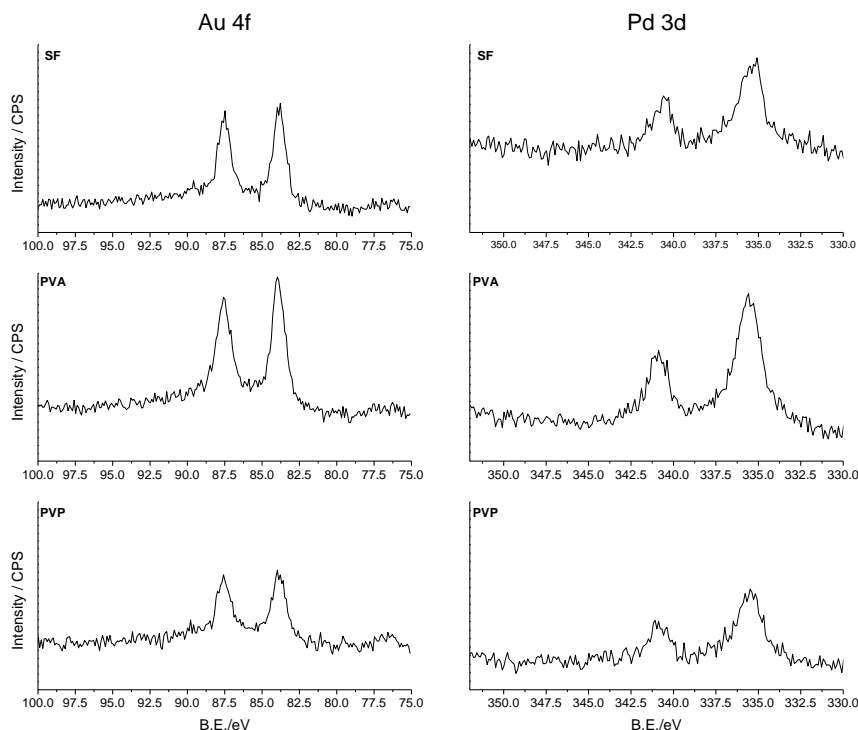
Figure 3.25 – Au4f and Pd3d XPS signals for 1% wt AuPd/TiO$_2$ prepared SF, PVA and PVP

3.4 Conclusion

In conclusion, it has been shown that by using a sol-immobilisation stabiliser-free (SF) method is possible to synthesize Au and AuPd supported catalysts of similar morphology and composition to the materials prepared *via* the traditional synthesis, as confirmed by TEM and XPS analysis. The size of the nanoparticles synthesized SF resulted to be slightly bigger in the case of Au, but more similar in the bimetallic case.

The catalysts' activity were evaluated and compared with the counterparts prepared *via* traditional sol-immobilisation method for gas-phase CO oxidation, solvent-free benzyl alcohol and glycerol oxidation reactions.

The monometallic catalyst prepared *via* the SF route surprisingly did not show any activity for the CO oxidation, conversely to what observed for the traditional sample prepared with PVA and calcined at 500 °C. It was also observed that calcination at 500 °C slightly improved the activity. Two hypotheses were made in order to explain this results: the presence of chloride residues on the SF dried catalyst or the size of the

nanoparticles, which decreased after calcination, and/or the modification of the interface Au/TiO$_2$. However, it was not possible to discriminate between the effects.

Studies on the catalytic oxidation of glycerol revealed that the monometallic catalyst prepared SF behaves very similar to the analogous samples prepared PVA and PVP in terms of activity, yet showing different selectivities, likely related to a different mechanism occurring at the surface because of the presence of the stabilising polymer. Bimetallic catalyst prepared SF showed very similar behaviour to the PVA synthesized catalysts for solvent-free benzyl alcohol oxidation, suggesting that the absence of the stabiliser has not a great effect in the bimetallic case. The results obtained for the reactions run in the liquid phase also suggested that the nanoparticles size is not a crucial factor.

The main advantage of the sol-immobilisation method is the control on the size and shape of nanoparticles that can be achieved prior to the deposition onto the support. These experiments showed how the complication introduced by the presence of the stabilising agent during a sol-immobilisation can be overcome by simply omitting its addition, at least for the preparation of low metal loaded catalysts, using TiO$_2$ as support. However, the preparation of catalysts with higher metal loading, different metals and different support will need further investigation. Control of the size and shape of colloidal nanoparticles without the addition of polymer stabilisers (e.g., by electrostatic stabilisation) will also be a challenging topic in the future development of this synthetic method. Therefore, these preliminary results offer new bases for the design of novel catalysts and/or synthetic routes.

Bibliography

1.   N. Dimitratos, J. A. Lopez-Sanchez, D. Morgan, A. Carley, L. Prati and G. J. Hutchings, *Catalysis Today*, **2007**, *122*, 317-324.

2.   N. Dimitratos, J. A. Lopez-Sanchez, D. Morgan, A. F. Carley, R. Tiruvalam, C. J. Kiely, D. Bethell and G. J. Hutchings, *Physical Chemistry Chemical Physics: PCCP*, **2009**, *11*, 5142-5153.

3.   J. A. Lopez-Sanchez, N. Dimitratos, P. Miedziak, E. Ntainjua, J. K. Edwards, D. Morgan, A. F. Carley, R. Tiruvalam, C. J. Kiely and G. J. Hutchings, *Physical Chemistry Chemical Physics: PCCP*, **2008**, *10*, 1921-1930.

4.   P. Miedziak, M. Sankar, N. Dimitratos, J. A. Lopez-Sanchez, A. F. Carley, D. W. Knight, S. H. Taylor, C. J. Kiely and G. J. Hutchings, *Catalysis Today*, **2011**, *164*, 315-319.

5.   V. Peneau, Q. He, G. Shaw, S. A. Kondrat, T. E. Davies, P. Miedziak, M. Forde, N. Dimitratos, C. J. Kiely and G. J. Hutchings, *Physical Chemistry Chemical Physics: PCCP*, **2013**, *15*, 10636-10644.

6.   R. Su, R. Tiruvalam, A. J. Logsdail, Q. He, C. A. Downing, M. T. Jensen, N. Dimitratos, L. Kesavan, P. P. Wells, R. Bechstein, H. H. Jensen, S. Wendt, C. R. A. Catlow, C. J. Kiely, G. J. Hutchings and F. Besenbacher, *ACS Nano*, **2014**, *8*, 3490-3497.

7.   A. Villa, D. Wang, D. S. Su and L. Prati, *ChemCatChem*, **2009**, *1*, 510-514.

8.   J.-D. Grunwaldt, C. Kiener, C. Wogerbauer and A. Baiker, *Journal of Catalysis*, **1999**, *181*, 223-232.

9.   F. Porta, L. Prati, M. Rossi, S. Coluccia and G. Martra, *Catalysis Today*, **2000**, *61*, 165-172.

10.   L. Prati and G. Martra, *Gold Bulletin*, **1999**, *32*, 96-101.

11.   Y. Xia, Y. Xiong, B. Lim and S. E. Skrabalak, *Angewandte Chemie*, **2009**, *48*, 60-103.

12.   A. Villa, N. Dimitratos, C. E. Chan-Thaw, C. Hammond, G. M. Veith, D. Wang, M. Manzoli, L. Prati and G. J. Hutchings, *Chemical Society Reviews*, **2016**, *45*, 4953-4994.

13.   L. Prati and A. Villa, *Catalysts*, **2011**, *2*, 24-37.

14.   M. Comotti, W.-C. Li, B. Spliethoff and F. Schuth, *Journal of the American Chemical Society*, **2006**, *128*, 917-924.

15.   J. A. Lopez-Sanchez, N. Dimitratos, C. Hammond, G. L. Brett, L. Kesavan, S. White, P. Miedziak, R. Tiruvalam, R. L. Jenkins, A. F. Carley, D. Knight, C. J. Kiely and G. J. Hutchings, *Nature Chemistry*, **2011**, *3*, 551-556.

16.   A. Villa, D. Wang, G. M. Veith, F. Vindigni and L. Prati, *Catalysis Science & Technology*, **2013**, *3*, 3036.

17.   M. Luo, Y. Hong, W. Yao, C. Huang, Q. Xu and Q. Wu, *Journal of Material Chemistry A*, **2015**, *3*, 2770-2775.

18.   S. Campisi, M. Schiavoni, C. Chan-Thaw and A. Villa, *Catalysts*, **2016**, *6*, 185.

19.   D. Li, C. Wang, D. Tripkovic, S. Sun, N. M. Markovic and V. R. Stamenkovic, *ACS Catalysis*, **2012**, *2*, 1358-1362.

20.   M. C. Daniel and D. Astruc, *Chemical Reviews*, **2004**, *104*, 293-346.

21.   R. Mout, D. F. Moyano, S. Rana and V. M. Rotello, *Chemical Society Reviews*, **2012**, *41*, 2539-2544.

22.   H. Ziaei-Azad and N. Semagina, *Applied Catalysis A: General*, **2014**, *482*, 327-335.

23.   L. Menard, F. Xu, R. Nuzzo and J. Yang, *Journal of Catalysis*, **2006**, *243*, 64-73.

24.   C. Aliaga, J. Y. Park, Y. Yamada, H. S. Lee, C.-K. Tsung, P. Yang and G. A. Somorjai, *Journal of Physical Chemistry C*, **2009**, *113*, 6150-6155.

25.   S. M. Ansar, F. S. Ameer, W. Hu, S. Zou, C. U. Pittman, Jr. and D. Zhang, *Nano letters*, **2013**, *13*, 1226-1229.

26.   L. Liu, S. Ouyang and J. Ye, *Angewandte Chemie International Edition*, **2013**, *52*, 6689-6693.

27.   H. Yin, Z. Ma and M. Chi, *Catalysis Letters*, **2010**, *136*, 209-221.

28.   H. Yin, C. Wang, H. Zhu, S. H. Overbury, S. Sun and S. Dai, *Chemical Communications*, **2008**, *0*, 4357-4359.

29.   C. Deraedt, L. Salmon, S. Gatard, R. Ciganda, R. Hernandez, J. Ruiz and D. Astruc, *Chemical Communications*, **2014**, *50*, 14194-14196.

30.   M. Haruta, *Journal of New Materials for Electrochemical Systems*, **2004**, *7*, 163-172.

31.   F. Boccuzzi, A. Chiorino, M. Manzoli, P. Lu, T. Akita, S. Ichikawa and M. Haruta, *Journal of Catalysis*, **2001**, *202*, 256-267.

32.   F. Boccuzzi, S. Tsubota and M. Haruta, *Journal of Electron Spectroscopy and Related Phenomena*, **1993**, *64/65*, 241-250.

33.   I. H. Kim, H. O. Seo, E. J. Park, S. W. Han and Y. D. Kim, *Scientific Reports*, **2017**, *7*, 40497.

34.   F. Mariño, C. Descorme and D. Duprez, *Applied Catalysis B: Environmental*, **2004**, *54*, 59-66.

35.   M. E. Grass, Y. Zhang, D. R. Butcher, J. Y. Park, Y. Li, H. Bluhm, K. M. Bratlie, T. Zhang and G. A. Somorjai, *Angewandte Chemie*, **2008**, *47*, 8893-8896.

36.   J. Xu, T. White, P. Li, C. He, C. Yu, Y. Weikang and Y.-F. Han, *Journal of the American Chemical Society*, **2010**, *132*, 10398-10406.

37.   M. Haruta, S. Tsubota, T. Kobayashi, H. Kageyama, M. Genet and B. Delmon, *Journal of Catalysis*, **1993**, *144*, 175-192.

38.   H. Oh, J. H. Yang, C. K. Costello, Y. M. Wang, S. R. Bare, H. H. Kung and M. C. Kung, *Journal of Catalysis*, **2002**, *210*, 375-386.

39.   H. H. Kung, M. C. Kung and C. K. Costello, *Journal of Catalysis*, **2003**, *216*, 425-432.

40.   C. K. Costello, M. C. Kung, H. Oh, Y. Wang and H. H. Kung, *Applied Catalysis A: General*, **2002**, *232*, 159-168.

41.   W. Ketchie, Y. Fang, M. Wong, M. Murayama and R. Davis, *Journal of Catalysis*, **2007**, *250*, 94-101.

42.   W. C. Ketchie, M. Murayama and R. J. Davis, *Topics in Catalysis*, **2007**, *44*, 307-317.

43.   M. Haruta, *CATTECH*, **2002**, *6*, 102-103.

44.   E. H. Cao, M. Sankar, E. Nowicka, Q. He, M. Morad, P. J. Miedziak, S. H. Taylor, D. W. Knight, D. Bethell, C. J. Kiely, A. Gavriilidis and G. J. Hutchings, *Catalysis Today*, **2013**, *203*, 146-152.

45.   V. R. Choudhary, P. A. Chaudhari and V. S. Narkhede, *Catalysis Communications*, **2003**, *4*, 171-175.

46.   P. Weerachawanasak, G. J. Hutchings, J. K. Edwards, S. A. Kondrat, P. J. Miedziak, P. Prasertham and J. Panpranot, *Catalysis Today*, **2015**, *250*, 218-225.

47.   M. Sankar, E. Nowicka, R. Tiruvalam, Q. He, S. H. Taylor, C. J. Kiely, D. Bethell, D. W. Knight and G. J. Hutchings, *Chemistry - A European Journal*, **2011**, *17*, 6524-6532.

48.   J. Pritchard, M. Piccinini, R. Tiruvalam, Q. He, N. Dimitratos, J. A. Lopez-Sanchez, D. J. Morgan, A. F. Carley, J. K. Edwards, C. J. Kiely and G. J. Hutchings, *Catalysis Science & Technology*, **2013**, *3*, 308-317.

49.   M. El-Sayed, *Accounts of Chemical Research*, **2001**, *34*, 257-264.

50.   X. Huang and M. A. El-Sayed, *Journal of Advanced Research*, **2010**, *1*, 13-28.

51.   K. L. Kelly, E. Coronado and G. C. Schatz, *Journal of Physical Chemistry B*, **2003**, *107*, 668-677.

52.   S. Sarina, S. Bai, Y. Huang, C. Chen, J. Jia, E. Jaatinen, G. A. Ayoko, Z. Bao and H. Zhu, *Green Chemistry*, **2014**, *16*, 331-341.

53.   S. Link and M. El-Sayed, *Int. Reviews in Physiscal Chemistry*, **2000**, *19*, 409-453.

54.   S. Jelveh and D. B. Chithrani, *Cancers*, **2011**, *3*, 1081-1110.

55.   C.-F. Chen and S. Gwo, *Journal of the American Chemical Society*, **2007**, *130*, 824-826.

56.   Y. C. Yen, J. A. Chen, S. Ou, Y. S. Chen and K. J. Lin, *Scientific Reports*, **2017**, *7*, 42524.

57.   X. Huang, I. H. El-Sayed, W. Qian and M. A. El Sayed, *Journal of the American Chemical Society*, **2006**, *128*, 2115-2120.

58.   T. Huang and L. Qi, *Jornal of Physical Chemistry C*, **2009**, *113*, 13636-13642.

59.   M.-L. Wu, D.-H. Chen and T.-C. Huang, *Langmuir: The ACS Journal Of Surfaces And Colloids*, **2001**, *17*, 3877-3883.

60.   X. Ke, X. Zhang, J. Zhao, S. Sarina, J. Barry and H. Zhu, *Green Chemistry*, **2013**, *15*, 236-244.

61.   J. H. Carter, S. Althahban, E. Nowicka, S. J. Freakley, D. J. Morgan, P. M. Shah, S. Golunski, C. J. Kiely and G. J. Hutchings, *ACS Catalysis*, **2016**, *6*, 6623-6633.

62.   B. Schumacher, V. Plazk, M. Kinne and R. J. Behm, *Catalysis Letters*, **2003**, *89*, 109-114.

63.   M. A. Bollinger and M. A. Vannice, *Applied Catalysis B: Environmental*, **1995**, *8*, 417-443.

64.   F. Cárdenas-Lizana, S. Gómez-Quero, A. Hugon, L. Delannoy, C. Louis and M. A. Keane, *Journal of Catalysis*, **2009**, *262*, 235-243.

65.   K. Duan, Z. Liu, J. Li, L. Yuan, H. Hu and S. I. Woo, *Catalysis Communications*, **2014**, *57*, 19-22.

66.   A. Zwijnenburg, A. Goossens, W. G. Sloof, M. W. J. Crajé, A. M. van der Kraan, L. Jos de Jongh, M. Makkee and J. A. Moulijn, *Journal of Physical Chemistry B*, **2002**, *106*, 9853-9862.

Chapter 4

A Study on the Catalytic Performance of the Mono and Bimetallic Catalysts Synthesized by a Modified Sol-Immobilisation for Glycerol Oxidation in Basic Conditions

4.1 Introduction

Due to the rapid depletion of fossil fuel resources, the search for new chemical feedstocks and the development of new processes for the production of fine chemicals and fuels has become essential[1]. Biomass represents a large source of renewable feedstocks, which can be converted to fine chemicals and fuels: its major components are carbohydrates (75%), lignin (20%) and the remaining fractions are fats, oils, proteins, terpenes and waxes[2]. The fatty and oily fraction of biomass (triglycerides) can currently be used for biodiesel production, as an alternative to fossil fuels[2-5]. The production of biofuels involves transesterification (usually with methanol) catalysed by acid or base, according to Scheme 4.1.
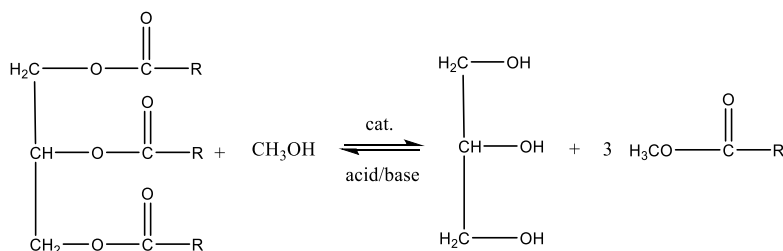
Scheme 4.1 Transesterification process with methanol

In the transesterification process, the fatty acids (triglycerides) are treated with an alcohol (usually methanol or ethanol) to give fatty acid esters and glycerol as a by-product [1,3,5,6]. The glycerol obtained by this process is cheap and biorenewable but highly impure: it typically contains a mixture of water, alcohol, catalyst residue, free fatty acids, unreacted glycerides and a variety of organic materials depending on the biodiesel process [5]. Refinement to high purity, usually by means of vacuum distillation followed by fractional distillation, is rather expensive. Yet, the high degree of functionalisation in glycerol makes it interesting from an industrial perspective as a starting material for more valuable C_3 products [1,6]. Processes such as selective oxidation, dehydration, hydrogenolysis, hydrogenation, etherification and esterification would lead to a wide range of potential products [2,3] (Scheme 4.2).
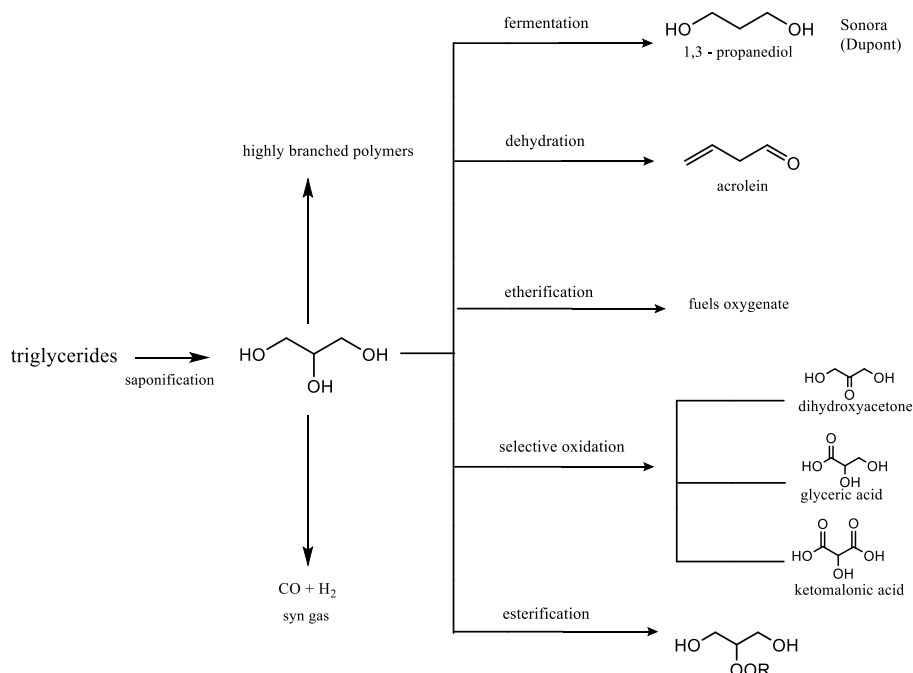
Scheme 4.2 Main reaction pathways for the transformation of glycerol to commodity chemicals and fuels [2]

Some of these processes are already commercialised, such as the esterification and the reforming. The former leads to monoacyl and diacyl esters, which are employed as emulsifiers, plasticisers and solvents that find applications in the food and cosmetics industry. The latter leads to the production of syngas, used in the synthesis of methanol in a process known as glycerol-to-methanol (GTM) [1].

Other processes for glycerol valorisation are not yet commercialised but are under intensive investigation. Catalytic routes could be developed for the conversion of glycerol to valuable intermediates, however, due to the high degree of functionalisation already within the molecule, selective catalytic oxidation is challenging. For example, a wide range of fine chemicals of pharmaceutical interest such as dihydroxyacetone (DHA), tartronic and mesoxalic acid [1] can be obtained by oxidation processes. Scheme 4.3 [2] illustrates the potential products which can be obtained from the selective oxidation of glycerol. Alternative schemes can be found in literature [1,5-11].
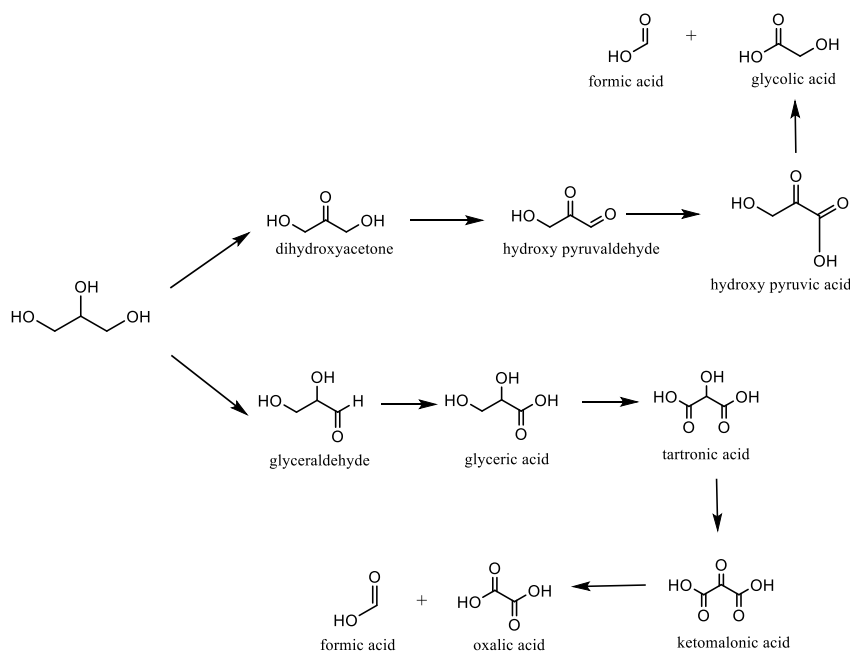
Scheme 4.3 Scheme of glycerol oxidation reaction in basic conditions [2]

Supported metal nanoparticles have been shown to be extremely active and selective for oxidations of organic alcohols such as glycerol and benzyl alcohol [9,12-14]. Metals such as gold, platinum or palladium have previously been shown to be active for oxidation reactions [15-17], with the gold being very promising as it has

been shown to be less prone to deactivation in presence of O_2; it was also shown to be more selective towards the oxidation of primary alcohols to aldehydes [15,16]. Besides the nature of the metal, the experimental conditions play a fundamental role in determining the activity and directing the selectivity to the desired products: for example, gold has been shown to be active for glycerol oxidation in basic environments [10,15,18,19]; when alloyed with Pt or Pd it can also be active in base-free conditions [9,13]. Also the support material is of primary importance in addressing the activity and selectivity for this reaction [20]. Basic conditions are necessary since it is believed that the oxidation process starts with the deprotonation of the alcohol to give the alkoxide that is rapidly converted to glyceraldehyde by the initial oxidation step [15,16,18,21,22], Scheme 4.4.
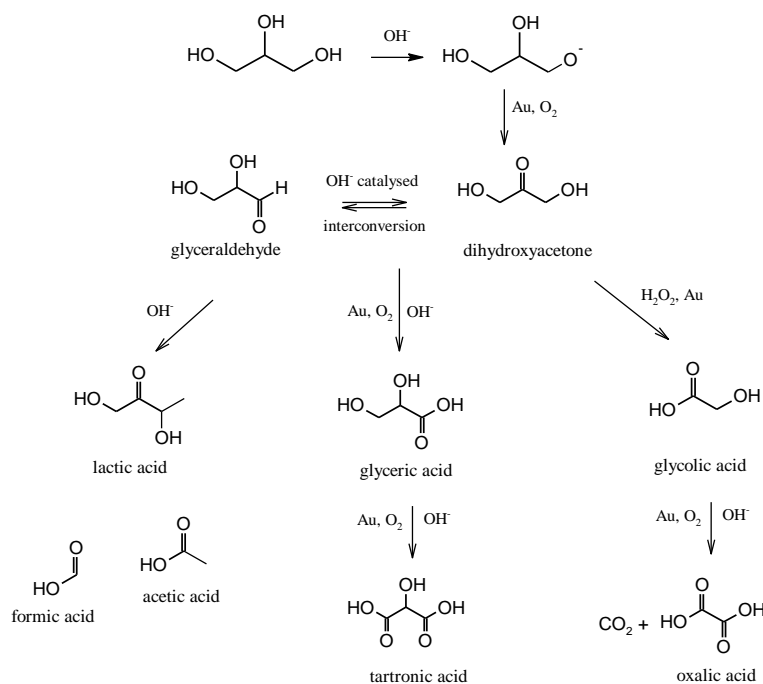
Scheme 4.4 – Proposed reaction pathway over supported Au catalysts in presence of a strong base [21]

Aim of the Chapter

This chapter presents a study of glycerol oxidation in a basic environment using mono and bimetallic catalysts prepared by the sol-immobilisation method presented in Chapter 3. Their catalytic performance will be compared in terms of conversion and selectivity to main products. The aim of the chapter is to analyse the different catalytic activity of the materials depending on polymer presence and to study how it can affect the performance both in terms of conversion and selectivity.

4.2 Catalyst Testing

Supported (1% wt) Au and AuPd nanoparticles on TiO_2 were prepared by sol-immobilisation *via* the traditional route using PVA and PVP as polymer stabilisers and the modified route without any stabiliser addition (stabiliser-free). The resultant materials were named PVA, PVP and SF respectively, as explained in Chapter 3. The catalysts were tested for glycerol oxidation in basic conditions and compared in terms of conversion and selectivity towards main products, tartronate and glycerate. The testing was performed using 10 mL of a glycerol solution in presence of NaOH (0.3 M glycerol, with NaOH/glycerol=2) at 60 °C under 3 bar of oxygen and 110 mg of catalyst, as described in Chapter 2.

4.2.1 Glycerol oxidation in basic conditions using Au and AuPd catalysts supported on TiO_2

Glycerol oxidation was studied in the presence of base for the monometallic stabiliser-free 1% wt Au/TiO_2 material and the counterpart catalysts that use either PVA or PVP as a polymer stabiliser. Figure 4.1, already displayed in Chapter 3, shows the conversion and selectivity profile to major products for the three catalysts.

Figure 4.1 - Comparison of the glycerol oxidation activity for 1% wt Au/TiO_2 catalysts prepared SF, PVA and PVP. *Reaction conditions*: glycerol 0.6 M, NaOH 1.2 M, 110 mg catalyst, 3 bar O_2, 60 °C, 1200 rpm, Gly/Au=500, total volume 10 mL. *Legend*: SF (●), PVA (▲), PVP (■); dotted lines - tartronate (TA) selectivity; dashed lines -glycerate (GA) selectivity.

Complete glycerol conversion was achieved after 4 h for all the three catalyst variants (PVA, PVP and SF), with similar conversion *versus* time-on-line profiles. The main products obtained were glycerate (GA) and tartronate (TA) with a combined selectivity typically above 70%. The remaining 30% comprised minor

products such as oxalate (OXA), lactate (LA), glycolate (GLY), formate (FA), pyruvate (PA) and acetate (ACA), displayed in Figure 4.2. Overall, the product distribution was broadly similar for all three catalysts. During the course of the reaction, the selectivity towards GA and TA remained constant for all three catalysts tested, indicating that they were relatively stable to further oxidation under the reaction conditions employed in the presence of glycerol. This also suggests that GA and TA are both produced as primary oxidation products and that TA is not predominantly generated *via* a consecutive oxidation pathway.

A comparison of the activity of the samples synthesized with and without polymeric stabilising ligands showed no significant difference in conversion, implying that polymer stabilisers are not necessary to produce highly active catalysts. Comparing the selectivity towards the major products, a 10-15% difference in the selectivity towards TA and GA was observed between the SF and the PVA/PVP stabilized catalysts. The selectivity at *iso-conversion* throughout the reaction towards TA followed the order SF > PVA > PVP, while the opposite trend was observed for selectivity towards GA. This suggests that the nature and presence of the polymer can alter reaction selectivity either through particle size effects or by partial ligand coverage of the active surface of the nanoparticles.

A comparison of the selectivity towards minor products for all the three monometallic catalysts, displayed in Figure 4.2, further evidences the influence of the presence and nature of the polymer. Indeed, the catalysts prepared by polymer addition showed higher selectivity towards lactate (LA); the highest value observed in the case of PVP suggests that its production is also dependent on the nature of the polymer. Conversely, the major product observed for the SF catalyst was the acetate (ACA). These results suggest that the SF surface is less selective to C_3 products, indicating a different oxidation mechanism for this catalyst due to the absence of the stabiliser or to the nanoparticles size resulting from the absence of polymer in the preparation. Indeed, previous studies on glycerol oxidation [11, 20, 23] found that larger nanoparticle size was related to an increase in the selectivity towards C_3 products (such as glycerate), while others [17] observed the same results with smaller (but of specific size) nanoparticles. Therefore, there is not a general consensus about the size influence on the selectivity [1, 21]. However, all the studies agreed that smaller nanoparticle size is related to higher catalytic

activity [11, 15] and to a higher selectivity towards C_2 products. This was proven [21] to be favoured by the *in-situ* formation of H_2O_2, that promotes C-C oxidative cleavage [19, 21].

Figure 4.2 – Time on line selectivity profile to minor oxidation products for the monometallic catalysts synthesized SF, PVA and PVP. *Legend*: ■ Oxalate (OXA) ▲ Lactate (LA) ○ Glycolate (GLYA) ● Pyruvate (PA) ▼ Formate (FA) ✕ Acetate (ACA)

Results of the TEM analysis performed on the three catalysts are displayed in Figures 4.3-4.4, while Figure 4.5 shows the aberration corrected scanning transmission electron microscopy (AC-STEM) analysis performed on the SF sample. Comparison of the particle size distributions for the three catalysts displayed in Figures 4.3 showed that materials prepared with polymer addition tend to have a narrower particle size distribution and lower mean particle size (PVA: 2.7 ± 0.6 nm; PVP: 3.5 ± 1 nm) than the stabilizer free sample (5.4 ± 1.6 nm). AC-STEM analysis did not reveal any distinctive feature for this sample. These results suggest that the difference in the nanoparticles size cannot justify the difference in the selectivity towards TA and GA observed for the three samples, therefore the influence of the presence and nature of the polymer stabiliser [23] must be taken into consideration.

Figure 4.3 - Particle size distributions derived from bright field TEM images of more than 100 monometallic Au particles prepared stabilizer free, or with PVA and PVP ligands present

Figure 4.4 – Representative BF-TEM micrographs of the monometallic 1% wt Au/TiO$_2$ catalysts prepared *via* (a) SF, (b) PVA and (c) PVP methods.
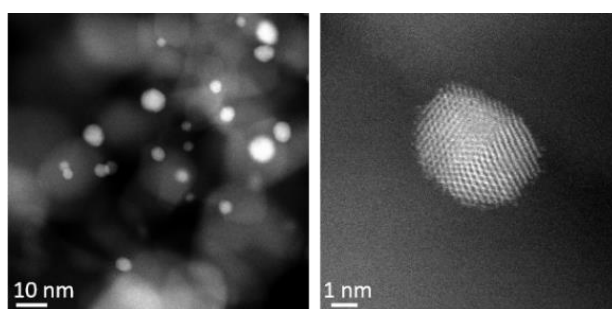
Figure 4.5 – Representative high angle annular dark field (HAADF) STEM images of 1% wt Au/TiO$_2$-SF.

Bimetallic 1% wt AuPd/TiO$_2$ sol-immobilised materials were also tested for the same reaction and the results are displayed in Figure 4.6. Again, all three catalyst variants (PVA, PVP and SF) showed similar

reaction profiles in terms of glycerol conversion indicating that the presence of a polymer during the preparation of the catalyst is not required to achieve high catalytic activity. A comparison of these results with the results obtained with the monometallic samples evidences how the presence of the Pd alloyed with gold enhances the catalytic activity, as previously observed by other studies [24, 25], with full conversion being reached after 2 h of reaction. On the other hand, comparison with monometallic Pd/TiO_2 catalysts was rather difficult since very few information could be found in the literature, perhaps because it is known that these catalysts are prone to deactivation and enhance the over-oxidation of substrates with the formation of carbon oxides [26, 27], especially when compared to the analogous supported on carbon [references]. A further element of complication for comparison with literature is given by the use of different reactors and reaction conditions. The most complete information was found in the work of Namdeo *et al.* [28], who investigated the role of different supports for monometallic Pd catalysts employed for glycerol oxidation. In their study, they compared the activity of Pd nanoparticles supported onto SiO_2, Al_2O_3, activated carbon and TiO_2. This last was the only one synthesized by an impregnation-reduction method, whereas the others are commercial catalysts. TEM analysis evidenced that all the samples supported on oxides showed very similar particle size distribution (around 22 nm), whereas 9 nm was the size of Pd nanoparticles supported on activated carbon. The Pd/TiO_2 was the least active of the set of catalysts, not even reaching 100% conversion throughout the reaction time (400 minutes), conversely to the activated carbon and Al_2O_3 supported samples. More interestingly, in terms of selectivity, the carbon-supported catalyst showed the highest to C_3 products, whereas the oxide supports enhanced the over-oxidation to C_2 and C_1 products (oxalic and formic acids). According to the XPS results, the authors proposed that this results should be rationalised in terms of difference in the oxidation state of Pd depending on the support (i.e., metal support-interaction), with the hypothesis of a charge transfer from the support to the metal in the case of TiO_2 and SiO_2 that might interfere with the adsorption of hydroxide ions and therefore with the oxidation pathway.

In a work reported by Sankar *et al.* [26] are mentioned, without further insight, the results obtained using a Pd/TiO_2 catalyst prepared by sol-immobilisation method. Also in this case, the selectivity to C_2 (oxalate) was rather high, especially when compared to analogous supported on activated carbon. On the other hand,

conversely to the previous work, this latter did not show a complete glycerol oxidation after 4 hours experiment.

Also in this case, comparison with the present results is rather difficult, due to the conditions being different.
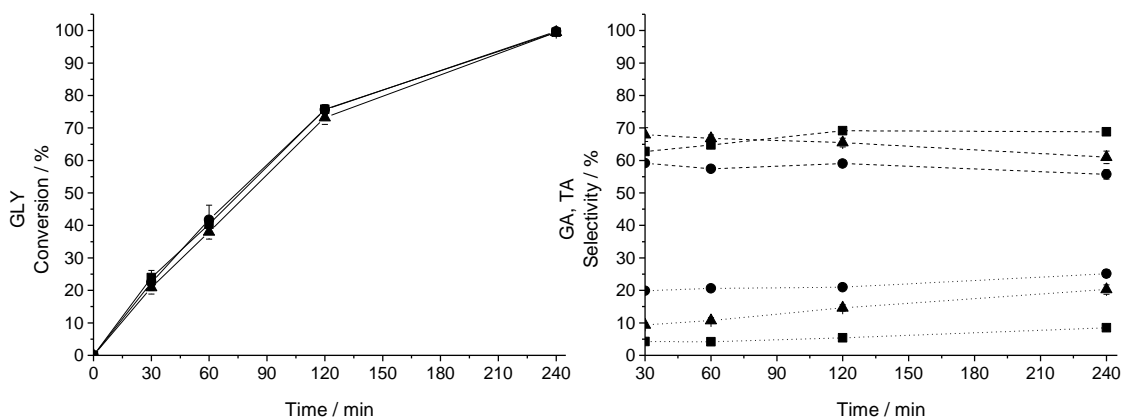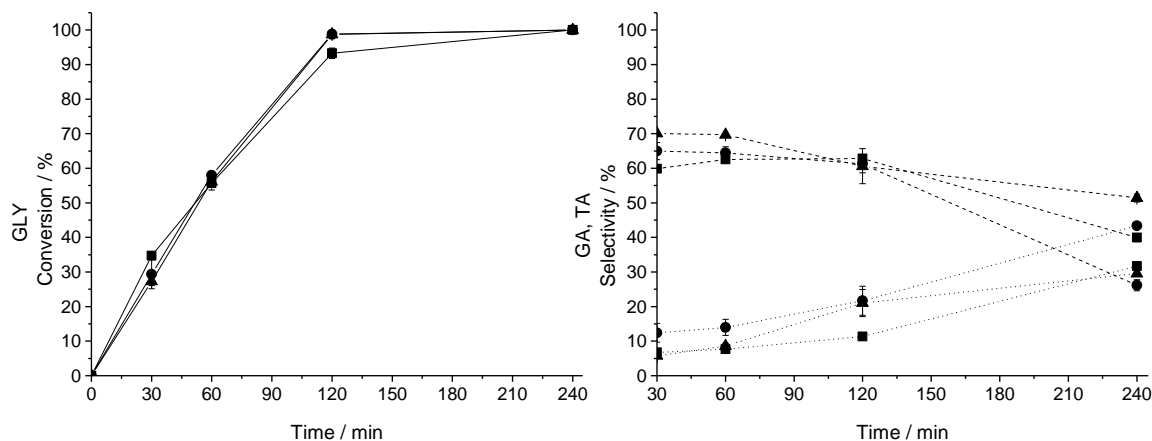

Figure 4.6 - Comparison of the glycerol oxidation activity for 1% wt AuPd/TiO$_2$ catalysts prepared stabiliser-free, PVA and PVP. *Reaction conditions*: glycerol 0.6 M, NaOH 1.2 M, 110 mg catalyst, 3 bar O$_2$, 60 °C, 1200 rpm, Gly/Au=500, total volume 10 mL. *Legend*: SF (●), PVA (▲), PVP (■); dotted lines - tartronate (TA) selectivity; dashed lines -glycerate (GA) selectivity.

The trends in selectivity toward main products were not as pronounced as those observed for the corresponding monometallic Au catalysts at short reaction times. At reaction times exceeding 120 min, GA selectivity decreased with a concurrent increase in TA selectivity, meaning that when glycerol was no longer available in the reaction mixture, further GA oxidation to TA occurred. A similar study, where 1% wt AuPd/C catalysts[25] were used, showed this behaviour before the total glycerol conversion, with GA selectivity being fairly stable after complete depletion of glycerol. This indicates that also the support and preparation method play a fundamental role in determining the selectivity of the reaction.

The selectivity towards minor products for the three catalysts is displayed in Figure 4.7. Conversely to the monometallic case, the bimetallic catalyst synthesized SF showed higher selectivity to LA, similarly to the samples prepared with the polymer. A comparison of product distribution at *iso-conversion* throughout all the reaction time evidences a difference in the oxidation mechanism for all the three catalysts: the SF catalyst showed a constant and marked increase in the selectivity to C$_2$ products OXA and ACA compared to the other

catalysts, again suggesting a different oxidation mechanism on this surface. Interestingly, the PVP sample showed the highest selectivity to LA analogously to the monometallic catalyst.
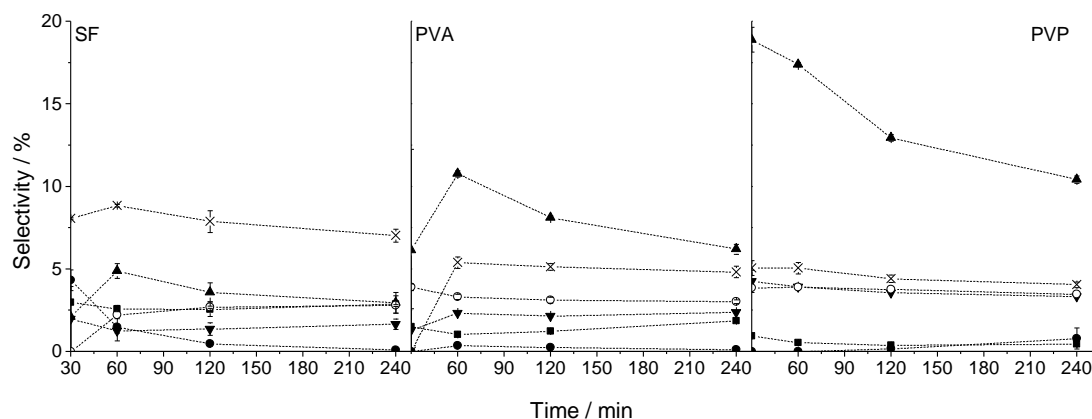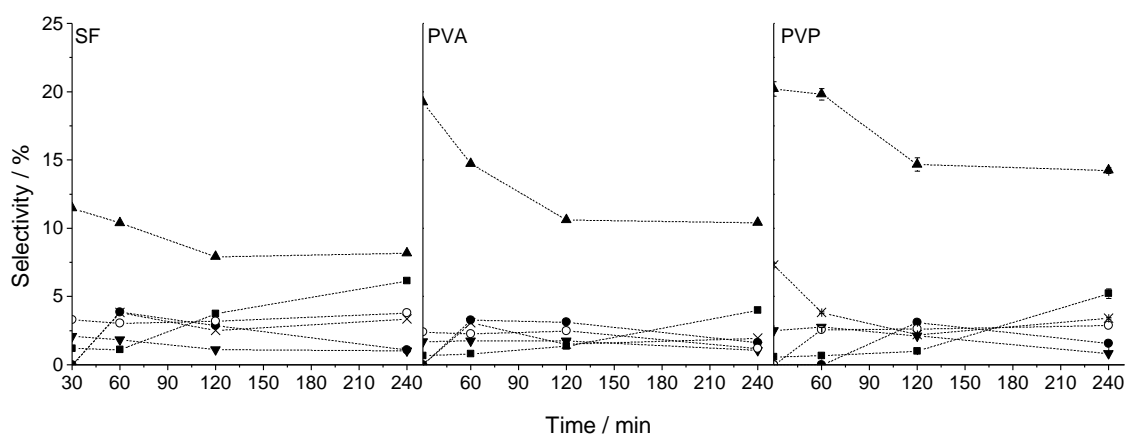

Figure 4.7 – Time on line selectivity profile to minor oxidation products for the bimetallic catalysts synthesized SF, PVA and PVP. *Legend*: ■ Oxalate (OXA) ▲ Lactate (LA) ○ Glycolate (GLYA) ● Pyruvate (PA) ▼ Formate (FA) x Acetate (ACA)

These results suggest that the preparation of AuPd catalysts without the addition of stabilisers obtains materials with similar catalytic performance to those prepared in the presence of PVA or PVP for the selective oxidation of glycerol, as already mentioned in Chapter 3. A deeper analysis on the product selectivity at *iso-conversion* though evidences the presence of different oxidation pathways for the catalyst prepared SF, analogously to what observed in the monometallic case.

In order to exclude any morphological or structural difference of the catalysts prepared *via* the three methods, they were analysed by TEM and AC-STEM, as displayed in Figures 4.8 - 4.10. Similar to the monometallic catalysts, the materials prepared with polymer addition tend to have a narrower particle size distribution and lower mean particle size (PVA: 3.2 ± 1 nm; PVP: 3.0 ± 1.2 nm) than the stabilizer free sample (3.9 ± 1.3 nm). The results did not show any significant variations in metal particle morphology or metal support interaction compared to catalysts prepared with PVA and PVP polymers as reported in previous studies [29]. For the SF catalyst, the nanoparticles were determined to be bimetallic as expected, as confirmed by X-ray energy dispersive spectroscopy (X-EDS) (Figure 4.10).
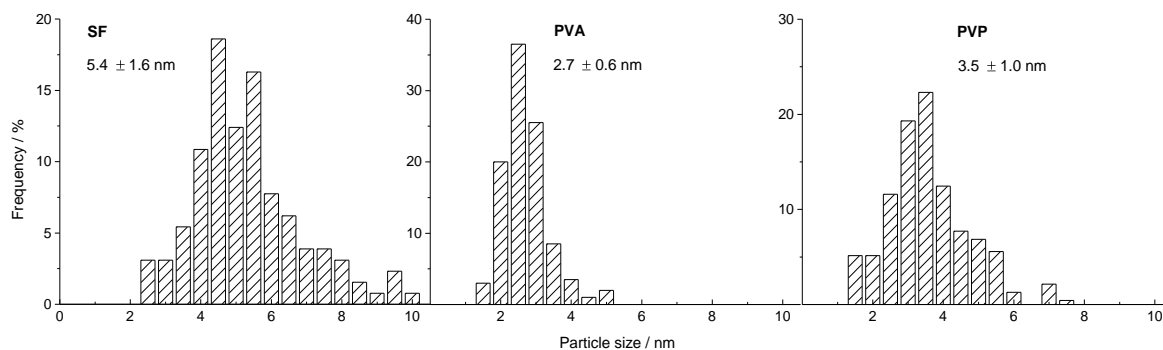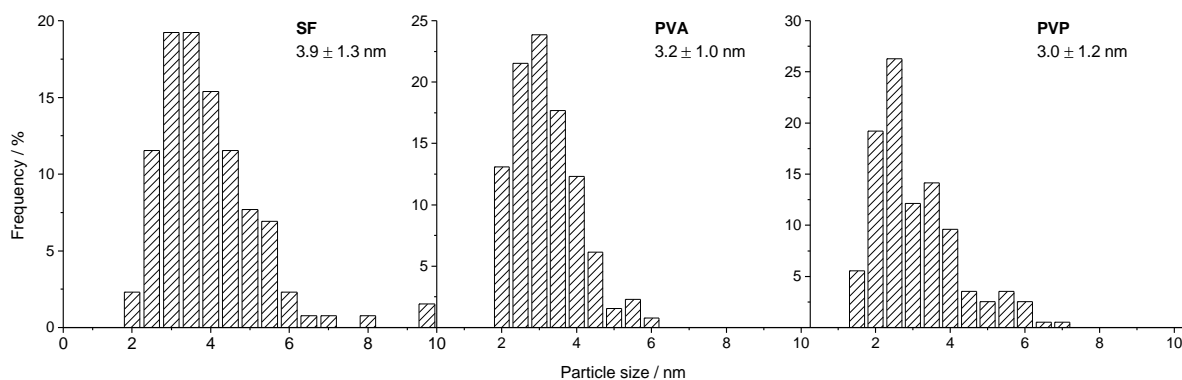
Figure 4.8 – Particle size distributions derived from bright field TEM images of more than 100 AuPd particles prepared either stabilizer free, or with PVA and PVP ligands present.
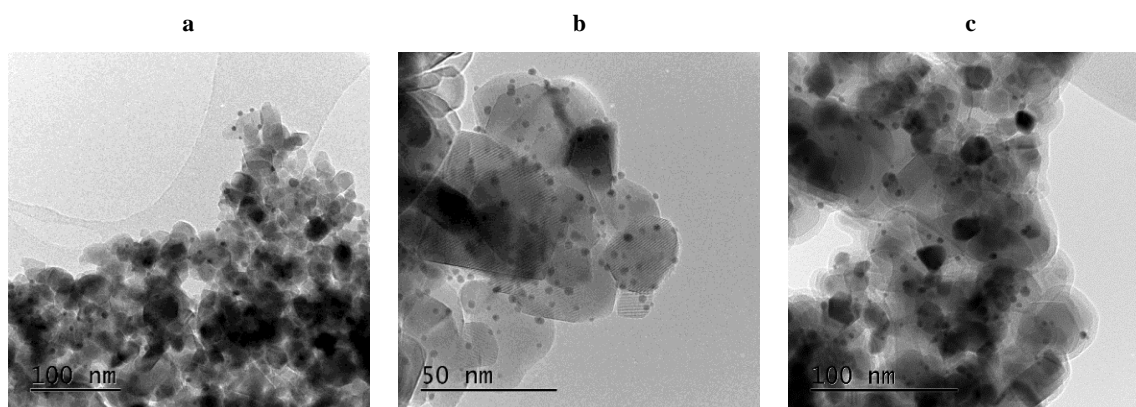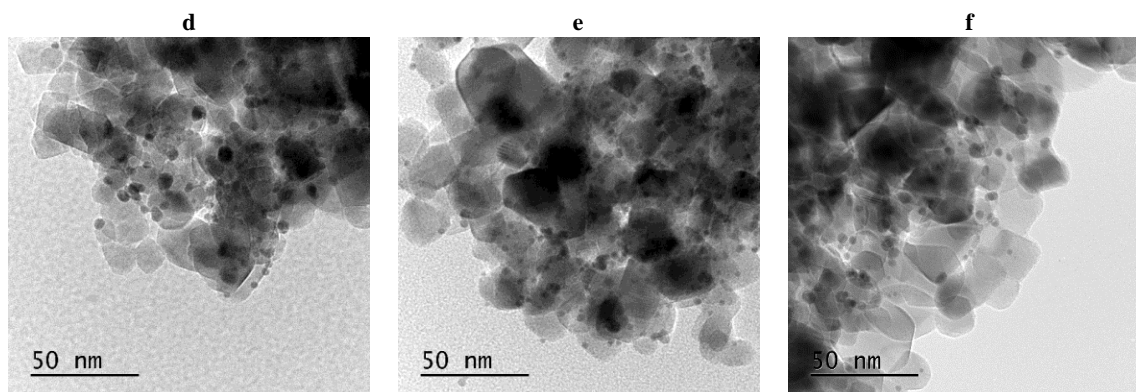

Figure 4.9– Representative BF-TEM micrographs of the bimetallic 1% wt AuPd/TiO$_2$ catalysts prepared via (d) SF, (e) PVA and (f) PVP.
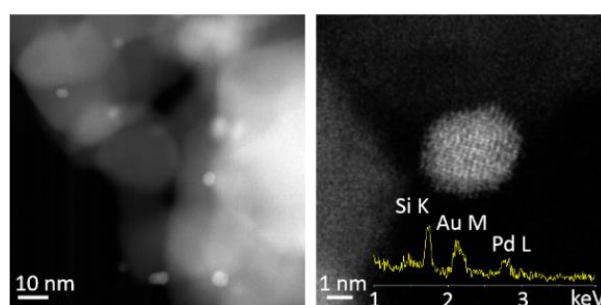
Figure 4.10 – Representative high angle annular dark field (HAADF) STEM images of 1% wt AuPd/TiO$_2$-SF. The inset shows the corresponding X-ray energy dispersive spectrum (XEDS) obtained from the particle imaged, indicating that it is a bimetallic alloy. The Si K signal is an artefact arising from internal fluorescence of the detector

The results obtained for the monometallic and bimetallic materials suggest that the catalysts prepared *via* the SF method behave in a very similar way in terms of glycerol conversion to the analogues prepared *via*

PVA/PVP method. On the other hand, it seems that they are able to promote oxidation *via* a different pathway. This is evidenced by the marked difference in selectivity toward main products TA and GA at *iso-conversion* throughout the reaction time, particularly pronounced in the monometallic case, and in the difference in the selectivity toward minor products. Also, the nature of the polymer seems to have an effect on the selectivity, as evinced from the different values observed for the catalysts prepared PVP and PVA.

The aim of the next section is to analyse the origin of the alternative oxidation pathway. Two hypotheses will be taken into account: 1) different adsorption of glycerol on the surface 2) the formation of H_2O_2 depending on the presence/nature of stabiliser.

4.2.2 Mechanistic study and further clarification of the stabilisers role

The present section gathers a series of experiments performed on the mono and bimetallic catalysts prepared SF and PVA/PVP in order to clarify the role of the stabiliser during the glycerol oxidation reaction and how this is affecting the catalytic properties of the materials.

4.2.2.1 *Glyceric acid oxidation: insight on the glycerol oxidation reaction mechanism*

According to the proposed reaction schemes (e.g., Scheme 4.1 and 4.2), TA should be obtained *via* secondary oxidation of glycerate. In order to investigate the reaction mechanism, experiments using GA as starting material were performed on the monometallic SF and on the bimetallic SF and PVA catalysts. It was assumed, based on the glycerol oxidation experiments, that the monometallic PVA and the mono and bimetallic PVP catalysts give very similar results. The tests were run in presence of base and under the same conditions used for glycerol oxidation. The aims of this experiment were: 1) to obtain more information on the adsorption mechanism and the consequent oxidation pathway as a function of the stabilising agent present on the surface and 2) to investigate whether the observed TA is a primary product.

Figure 4.11 presents the GA conversion profile and the relative selectivity to products as a function of time for the monometallic sample prepared SF. This experiments shows that GA oxidation was much slower (Table 4.1) than glycerol oxidation using the same catalyst: indeed, after 4 hours reaction glycerol conversion reached 100% (Figure 4.1), whereas GA conversion stopped at 30 % (Figure 4.11). This might indicate that the relative

stability of GA and TA during the glycerol oxidation reaction is due either to lower relative reaction rates or to competitive adsorption of glycerol and GA. In a similar experiment performed by Ketchie *et al.* [21] it was proposed that the lower reaction rate observed for GA oxidation is due to the difficulty in generating the alkoxide, which represents the starting point of the oxidation process (Scheme 4.2). The deprotonation of the alcohol group of the GA is indeed disfavoured because of the presence of the carboxylic group.

Regarding the product distribution, the major product appears to be the TA. Glycolate (GLYA) is also produced at higher amounts from the beginning, but undergoes rapid conversion to oxalate (OXA) and CO_2 throughout the reaction time; according to Scheme 4.2. Small amounts of formate (FA) were also detected.

Table 4.1 – Reaction rates ($[M]/g_{cat}$·h) calculated for the glycerol (GLY) and glyceric acid (GA) oxidation reactions

Catalyst	Rate of substrate depletion / $[M]/g_{cat}$·h	
	GA	GLY
Au/TiO$_2$-SF	$1.8 \cdot 10^{-1}$	$5.7 \cdot 10^{-1}$
AuPd/TiO$_2$-PVA	$1.6 \cdot 10^{-1}$	$5.4 \cdot 10^{-1}$
AuPd/TiO$_2$-SF	$2.5 \cdot 10^{-1}$	$4.8 \cdot 10^{-1}$
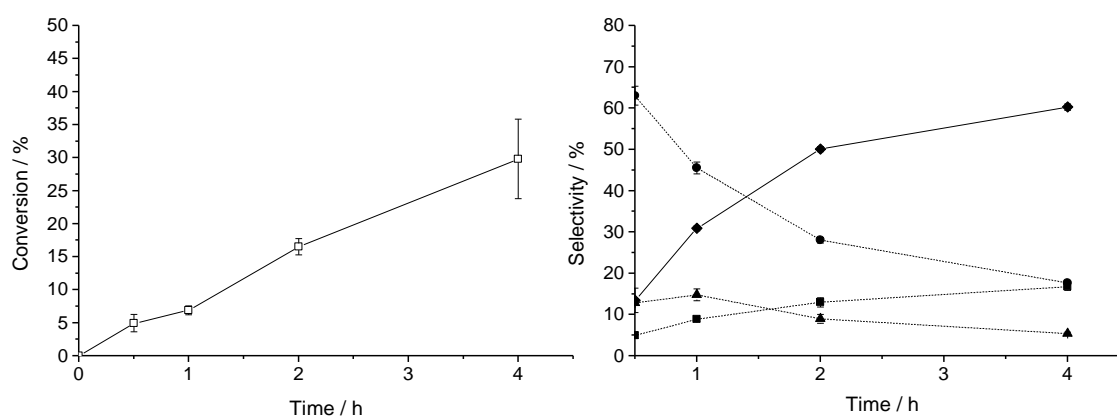
Figure 4.11 – Glyceric acid oxidation conversion and selectivity profile for the 1% wt Au/TiO$_2$-SF catalyst. *Reaction conditions*: 110 mg catalyst, 60 °C, 3 bar O$_2$, 1200 rpm, GA/metal(s) = 500:1(mol), NaOH/GA = 2:1 (mol), total volume 10 mL. *Legend*: □ GA ◆ TA (bold line); ● Glycolate (GLYA) ■ Oxalate (OXA) ▲ Formate (FA) (dotted lines)

Similar trends, even though less pronounced, can be observed in the case of the bimetallic catalysts prepared SF and PVA displayed in Figures 4.12 and 4.13 respectively. The bimetallic samples showed higher reaction

rates than the monometallic SF (Figure 4.11), reaching 45% and 30% GA conversion for respectively the SF and PVA catalysts after 4 hours reaction. These results are consistent with the results observed during glycerol oxidation (Figure 4.6), where further GA oxidation did clearly occur when 100% glycerol conversion was reached, with the 1% wt AuPd/TiO$_2$-SF catalyst having a higher GA oxidation activity than the 1% wt AuPd/TiO$_2$-PVA variant.
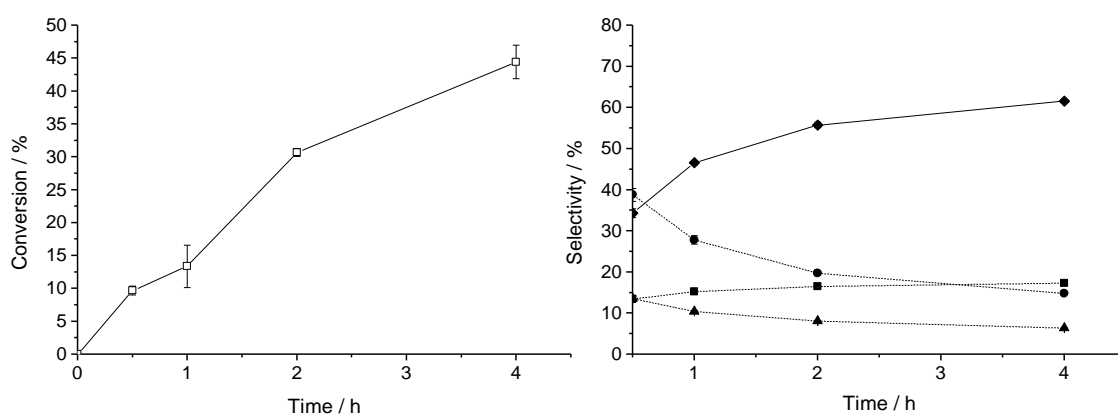
Figure 4.12 – Glyceric acid oxidation conversion and selectivity profile for 1% wt AuPd/TiO$_2$-SF catalyst. *Reaction conditions*: 110 mg catalyst, 60 °C, 3 bar O$_2$, 1200 rpm, GA/metal(s) = 500:1(mol), NaOH/GA = 2:1 (mol), total volume 10 mL. *Legend*: □ GA ◆ TA (bold line); ● Glycolate (GLYA) ■ Oxalate (OXA) ▲ Formate (FA) (dotted lines)
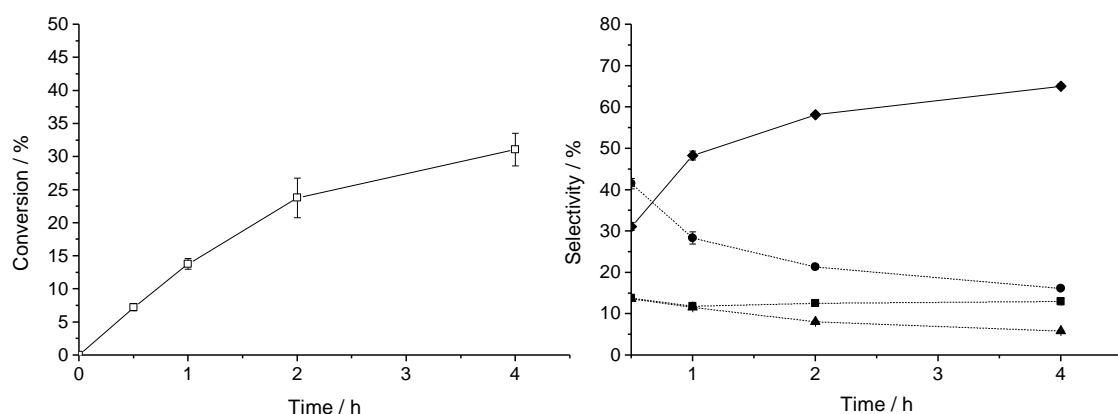
Figure 4.13 – Glyceric acid oxidation conversion and selectivity profile for 1% wt AuPd/TiO$_2$-PVA catalyst. *Reaction conditions*: 110 mg catalyst, 60 °C, 3 bar O$_2$, 1200 rpm, GA/metal(s) = 500:1(mol), NaOH/GA = 2:1 (mol), total volume 10 mL. *Legend*: □ GA ◆ TA (bold line); ● Glycolate (GLYA) ■ Oxalate (OXA) ▲ Formate (FA) (dotted lines)

Again, for both the SF and PVA samples, the oxidation products and relative profiles are the same as observed in the monometallic case, with TA being the major product followed by GLYA, OXA and FA. It seems that the oxidation happens faster on the stabiliser-free surface, in accordance with the results obtained during glycerol oxidation. This suggests a different mechanism happening on these surfaces. Evidence of this is displayed in Figure 4.14, where are reported the selectivity *versus* conversion plots at *iso-conversion* for the bimetallic SF and PVA catalysts.
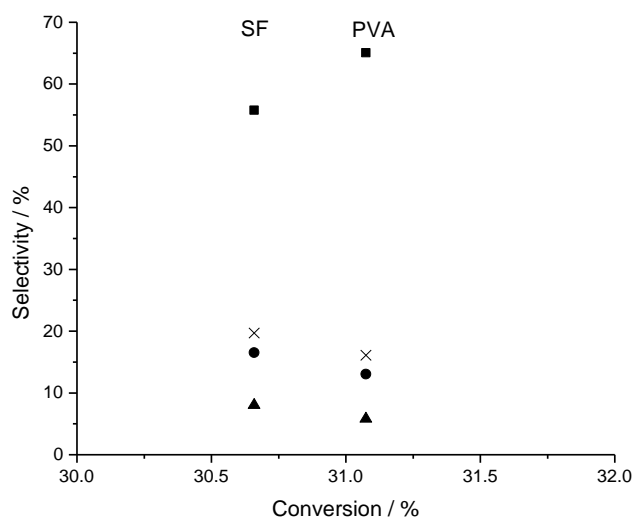
Figure 4.14 – Selectivity vs conversion plot for the GA oxidation using 1% wt AuPd/TiO$_2$ catalysts prepared SF and PVA. *Legend*: ■ Tartronate (TA) ✕ Glycolate (GLYA) ● Oxalate (OXA) ▲ Formate (FA).

These results clearly suggest that at *iso-conversion*, SF surfaces enhance the formation of GLYA. This might be related to the formation of H$_2$O$_2$, although this would be in contrast with the findings of Ketchie *et al.* [9] on similar catalysts: they indeed observed that the presence of Pd decreases the formation of H$_2$O$_2$; nonetheless, the extent of this process might be related to the presence of the stabiliser. However, another pathway accounting of faster O$_2$ dissociation cannot be excluded. The selectivity to TA appears to be higher on PVA catalyst, according to the hypothesis of a different oxidation mechanism. Indeed, on these surface the oxidation process appears to happen slower (23.5% conversion is reached after 2 hours reaction, Table 4.2) but is more selective towards TA, which would be in accordance with the hypothesis of different mechanism occurring on the two surfaces. In the long term though, the oxidation mechanism, either through the presence

of H_2O_2 or a faster O_2 dissociation rate, would lead to higher selectivity towards TA on the SF materials, since GA oxidation is favoured.

It is observed that the GA is mainly converted to TA, but, comparing the oxidation rates of glycerol and GA to the TA selectivity (or yield) reported in Table 4.2, the latter cannot be an exclusive product from GA oxidation during glycerol oxidation. Most of the literature reports the TA as a secondary oxidation product from the GA, but the results obtained in this experiment, together with those obtained from glycerol oxidation, suggest the primary nature of TA. Evidence of this was also reported in a reaction modelling study by Demirel-Gulen *et al*. [7] using gold catalysts. Moreover, it is clear from glycerol oxidation experiments that the GA conversion to TA only starts when the glycerol has been consumed, at least on bimetallic samples (Figure 4.7). Nonetheless, it is possible that a small fraction of GA is converted to TA during the reaction, and this would justify the slight decrease in selectivity to GA throughout the reaction time. This would be in accordance with the present findings, and would explain the difference in the selectivity to TA observed when SF catalysts are used (faster GA conversion to TA).

In summary, the following conclusions can be drawn from this experiment:

- TA is primary product;

- GA oxidation seems to occur faster on SF surfaces, perhaps due to higher H_2O_2 formation or to a faster O_2 dissociation.

Table 4.2– Selectivity % and yield % of TA after 2 hours GA oxidation for the 1% wt Au/TiO_2 and $AuPd/TiO_2$ samples

Sample	Conversion / %	TA Selectivity / %	TA Yield / %
Au/TiO_2-SF	16.5	50	8
$AuPd/TiO_2$-SF	30	56	17
$AuPd/TiO_2$-PVA	23.5	58	14

4.2.2.2   Glycerol oxidation short reaction time study

To further investigate the reaction mechanism, the same samples were used for experiments at very short reaction times. Figures 4.15 and 4.16 show the glycerol conversion and the corresponding selectivity to main products TA and GA as a function of time for all the three catalysts tested.

The results obtained for the 1% wt Au/TiO$_2$ catalyst prepared SF (Figure 4.15) show that both TA and GA are produced at the very beginning of the oxidation reaction. After 5 minutes of reaction, the selectivity towards TA reaches 28%, and is kept fairly stable throughout all the experiment time. Interestingly, the selectivity to GA seems to decrease with increase in conversion, according to the results obtained in previous GA oxidation experiments (Figure 4.11) and likely due to the formation of H$_2$O$_2$ on this surfaces as previously discussed in Section 4.2.1.
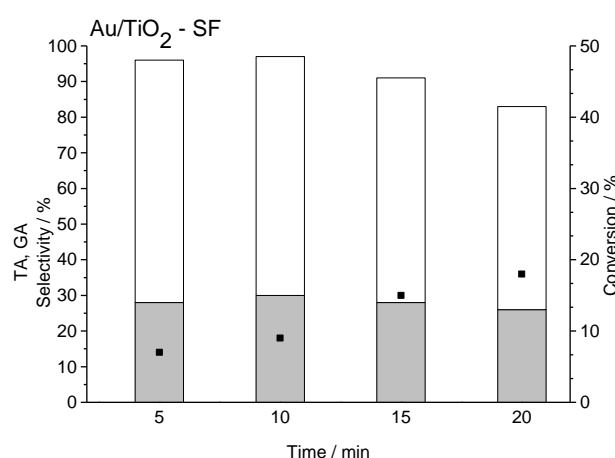
Figure 4.15 – Glycerol oxidation on 1% wt Au/TiO$_2$ prepared SF. *Reaction conditions*: 110 mg catalyst, 60 °C, 3 bar O$_2$, 1200 rpm, GA/metal(s) = 500:1(mol), NaOH/GA=2:1 (mol), total volume 10 mL. *Legend*: ■ TA, □ GA, ▪ Glycerol

Results for the bimetallic samples prepared SF and PVA are displayed in Figure 4.16. Comparing the results at *iso-conversion* after 10 minutes of reaction, it is possible to observe that the selectivity to TA is almost the double for the SF sample compared to the PVA sample, again suggesting a different oxidation mechanism that seems to favour the oxidation pathway to TA as a primary product. A further evidence of different oxidation mechanism happening on the two surfaces is given by the GA/TA selectivity ratios at *iso-conversion*, as reported in Table 4.3. Indeed, if the mechanism was the same, it should be expected the same ratio values for all the catalysts.

The results obtained from these experiments using mono and bimetallic catalysts suggest that the absence of the polymer seems to affect the glycerol oxidation mechanism and can drive the selectivity to TA at very early stages of the reaction. This might be related either to an increased production of H$_2$O$_2$ or to a faster O$_2$

dissociation on SF surfaces, promoting a faster oxidative pathways which lead to an increase in the TA selectivity. The second hypothesis of a different adsorption mechanism which is capable of directly oxidising the glycerol to TA is discussed in more detail in the following paragraph.
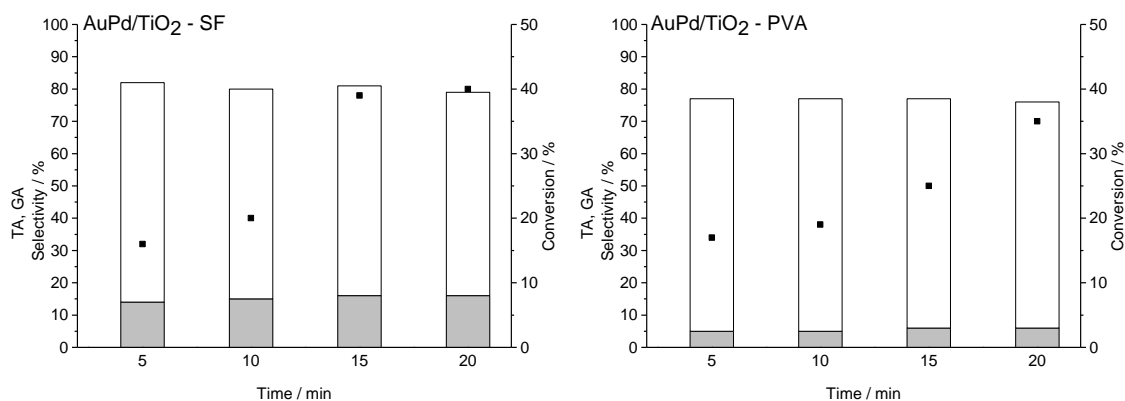
Figure 4.16 - Glycerol oxidation on 1% wt AuPd/TiO$_2$ prepared SF and PVA. *Reaction conditions*: 110 mg catalyst, 60 °C, 3 bar O$_2$, 1200 rpm, GA/metal(s) = 500:1(mol), NaOH/GA = 2:1 (mol), total volume 10 mL. *Legend*: ■ TA, □ GA, ■ Glycerol

Table 4.3 - GA/TA ratio at *iso-conversion* for the mono and bimetallic catalysts prepared SF and PVA

Catalyst	Time / min	Conversion / %	GA/TA
Au/TiO$_2$-SF	10	9	2
AuPd/TiO$_2$-SF	10	20	4
AuPd/TiO$_2$-PVA	10	19	14

4.2.2.3 A study on the polymer effect during glycerol oxidation

To analyse the effect of the two stabilising polymers used in the syntheses (PVA and PVP), they were added in various amounts during a glycerol oxidation experiments using the 1% wt Au/TiO$_2$-SF catalyst. The aim of the study was to obtain more information about the influence of the two different polymers during the reaction on a bare surface (i.e., competition for the active sites or blocking access to active sites) and if and how they affect the conversion rate and drive the selectivity.

Figure 4.17 shows the comparison of catalytic activity after 1 and 4 hours reaction for the 1% wt Au/TiO$_2$ catalysts prepared SF and PVA (the two "extreme" situations, far left and far right in the graph respectively),

with the SF sample in presence of aliquots of PVA (0.1 g/10 mL) correspondent to selected PVA/Au mass ratios (0.3, 0.65 and 1.3 respectively). After 1 hour reaction, the presence of PVA during the reaction reduces the glycerol conversion by about 10% with respect to the two extremes. The extent to which the PVA is affecting the conversion seems to be quite independent from its amount, with values being around 30% in all three cases. The selectivity to GA and TA are similar for the three experiments, suggesting that the polymer amount does not influence the mechanism but only the oxidation rate. This is in accordance with the findings of Villa and co-workers [30], who showed that monometallic sol-immobilised catalysts synthesized in the presence of lower amounts of PVA were more active during glycerol oxidation, but no marked difference in the selectivity in dependence of the polymer amount was observed. They concluded that the PVA at certain amount (i.e., when Au>PVA) has a beneficial effect on the catalytic performance since it might create a sort of porous structure on the metal surface that facilitates the glycerol adsorption. This would also be in accordance with the results after four hour reactions, where the conversion could not reach 100%, with values decreasing with the increase in the amount of stabiliser, and with the sample PVA/Au =0.3 being the more active of the set of three. This trend might be due either to the competitive adsorption of PVA on active sites (since the PVA presents –OH functionalities), or to restricted access for glycerol to catalytic active sites.
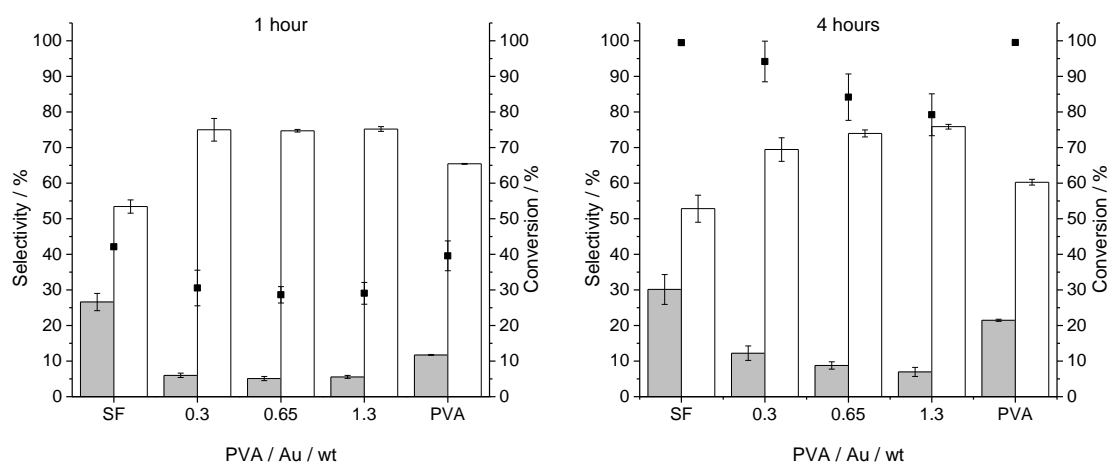
Figure 4.17 - Glycerol conversion and selectivity after 1 hour and 4 hours reaction for the 1% wt Au/TiO$_2$-SF in presence of different aliquots of PVA, compared with the 1% wt Au/TiO$_2$–SF and 1% wt Au/TiO$_2$-PVA. *Reaction conditions*: 110 mg catalyst, 60 °C, 3 bar O$_2$, 1200 rpm, GA/metal=500:1(mol), NaOH/GA = 2:1 (mol), total volume 10 mL. *Legend*: ■ TA, □ GA, ■ Glycerol

In Figure 4.18 are reported the results for analogous experiments carried out using different amounts of PVP, after 1 hour and 4 hours reaction. Again, the results are compared to the two "extreme" cases, i.e. when using Au/TiO_2 – SF and Au/TiO_2 – PVP, shown in the far left and right of the graph respectively. In this case, the PVP seems not to have a large effect on the conversion after 1 hour, reaching ~ 40% for all the samples. Conversely, it does have a marked effect on the selectivity, with values for TA and GA very similar to those obtained when the Au/TiO_2 – PVP catalyst was used: the presence of the stabilising agent seems to drive the selectivity to GA rather than to TA. This can be explained with the PVP covering the nanoparticle and blocking the surface, favouring the oxidation of glycerol to GA. The same trend is observed after 4 hours reaction: by contrast with the PVA addition case, the PVP does not have any effect on the conversion. Also, selectivity towards TA and GA seems to be fairly stable over time and despite the stabiliser amount added, suggesting that either the PVP is not competing with glycerol for the active sites on the catalyst, or its presence is suppressing the formation of H_2O_2, necessary to oxidise the GA as discussed in previous sections. Conversely to what observed in the PVA case, these results suggest that PVP does not completely block the access to the active sites, so it is still possible for the glycerol to be oxidised completely after 4 hours, but only one pathway is possible.
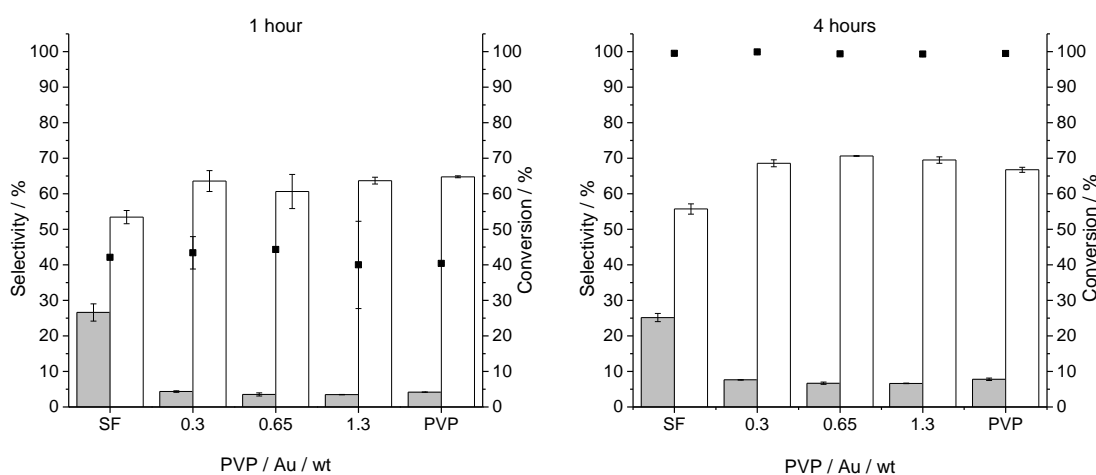
Figure 4.18 - Glycerol conversion and selectivity after 1 hour and 4 hours reaction for the 1% wt Au/TiO_2-SF in presence of different aliquots of PVP, compared with the 1% wt Au/TiO_2–SF and 1% wt Au/TiO_2-PVP. *Reaction conditions*: 110 mg catalyst, 60 °C, 3 bar O_2, 1200 rpm, GA/metal=500:1(mol), NaOH/GA=2:1 (mol), total volume 10 mL. *Legend:* ■ TA, ☐ GA, ■ Glycerol.

On the basis of the results obtained from all the experiments gathered in the above sections, a new reaction mechanism, displayed in Scheme 4.5, is proposed for the catalysts used in the present study. The mechanism accounts for the primary nature of the TA and GA, and for the over-oxidation of the latter due to the presence of the H_2O_2 or of the faster rate of O_2 dissociation. The former is also responsible of the C-C cleavage of the molecules, leading to higher selectivity to C_2 products.
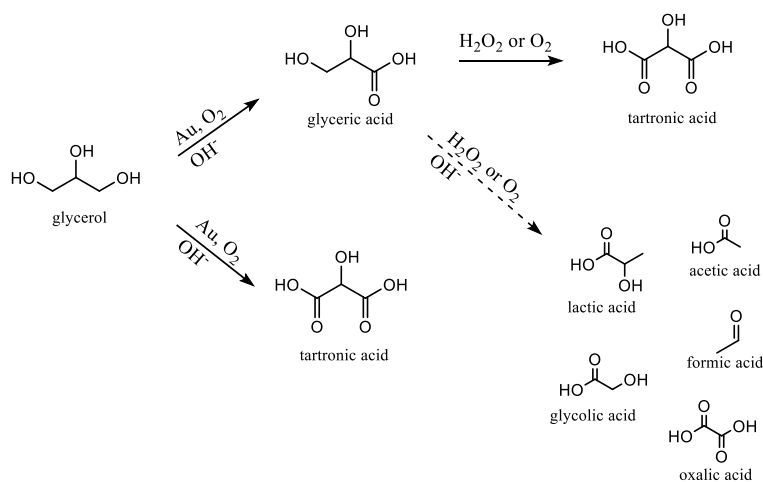
Scheme 4.5 – Proposed reaction mechanism for glycerol oxidation on mono and bimetallic catalysts prepared SF, PVA and PVP

4.2.3   Reusability of catalysts

In order to assess the stability of the catalysts prepared *via* the stabiliser-free route and the traditional method, reusability studies for the glycerol oxidation were carried out on both mono and bimetallic samples. Full description of experimental conditions is reported in Chapter 2. Figures 4.19 and 4.20 compare the results in terms of activity and selectivity between the original (filled symbols) and the 1st cycle reused (hollow symbols) mono and bimetallic catalysts.

The results showed that the catalysts prepared by PVP are stable to reuse within the experimental error throughout the reaction time. In contrast, monometallic catalyst prepared with PVA, which is known to be prone to removal from the metal surface in aqueous solution at elevated temperatures [31], showed a decrease in conversion after 3 hours of around 6%, and the SF sample around 10% . For the bimetallic catalysts the degree of deactivation seems to be less pronounced.
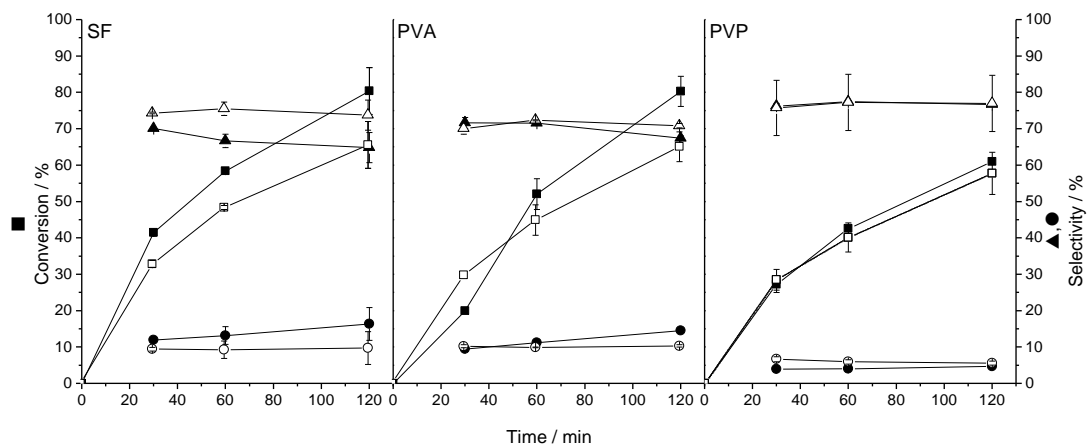
Figure 4.19 – Reusability experiments for monometallic catalysts. *Reaction conditions*: 55 mg catalyst, 60 °C, 3 bar O_2, 1200 rpm, GA/metal(s) = 500:1(mol), NaOH/GA=2:1 (mol), total volume 10 mL. *Legend*: ■ Glycerol ▲ Glycerate (GA) ● Tartronate (TA). Filled symbols: original, hollow symbols: 1st cycle reuse
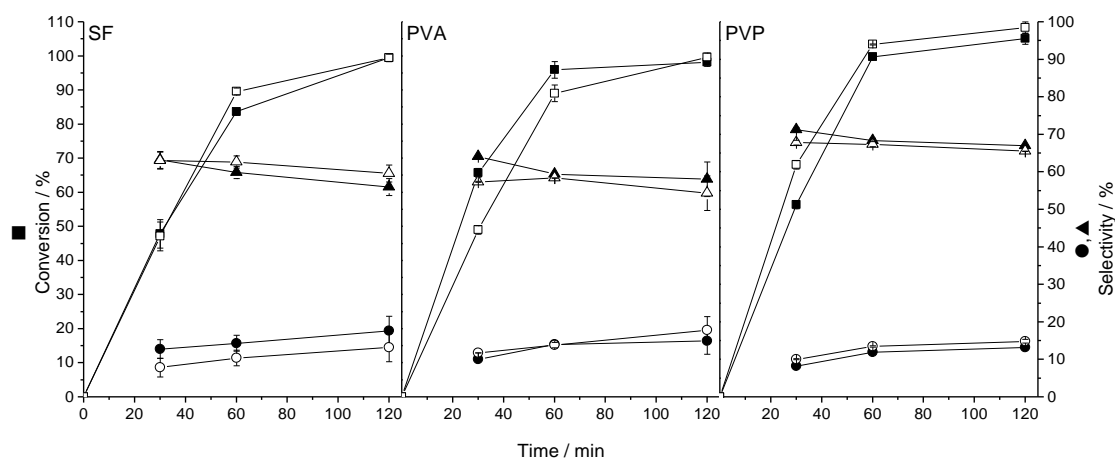
Figure 4.20 – Reusability experiments for bimetallic catalysts. *Reaction conditions*: 55 mg catalyst, 60 °C, 3 bar O_2, 1200 rpm, GA/metal(s) = 500:1(mol), NaOH/GA=2:1 (mol), total volume 10 mL. *Legend*: ■ Glycerol ▲ Glycerate (GA) ● Tartronate (TA). Filled symbols: original, hollow symbols: 1st cycle reuse

In order to evaluate the origin of the deactivation, MP-AES analysis was carried out on the reaction effluents to exclude any leaching of metal during the reaction. The results for all the six catalysts are reported in Table 4.4, revealing the good stability of the bimetallic catalysts. Surprisingly, among the monometallic samples, the SF showed the lowest leaching value. However, considering the highest degree of deactivation observed for

this sample, it can be concluded that these results do not correlate with the observed catalytic behaviour and that the absence of stabiliser does not enhance the leaching of metal.

Therefore, TEM analysis was carried out on the used catalysts in order to estimate any changes in the morphology of the nanoparticles that can be responsible of the deactivation. Particle size resulted to increase for both the mono and bimetallic catalysts, as displayed in Figures 4.21-4.22 and in Table 4.5, excepted for the monometallic SF catalyst, perhaps due to an Ostwald's ripening mechanism. Metal content determined by ICP analysis did not show any metal leaching, according to the results reported in Table 4.4. From the TEM micrographies (Figure 4.23) it is possible to appreciate the non-homogeneous dispersion of the nanoparticles after reaction, independently from the stabiliser absence, and the presence of nanoparticle aggregation, especially distinguishable in the case of the bimetallic catalyst.

Table 4.4– Metal leaching detected in the solution after glycerol oxidation reaction determined by MP-AES

Catalyst	Stabiliser	Metal concentration in solution after reaction mg/L	
		Au	Pd
	SF	0.03	-
1% wt Au/TiO$_2$	PVA	0.15	-
	PVP	0.12	-
	SF	<0	<0
1% wt AuPd/TiO$_2$	PVA	<0	<0
	PVP	<0	<0

Table 4.5 - Comparison of nanoparticles size for the mono and bimetallic catalysts before and after glycerol oxidation

Catalyst		Nanoparticle size / nm	
		Before reaction	After reaction
	SF	5.4 ± 1.6	4.5 ± 1.4
Au	PVA	2.7 ± 0.6	4.5 ± 1.6
	PVP	3.5 ± 1.0	3.9 ± 1.0
	SF	3.9 ± 1.3	4.9 ± 1.3
AuPd	PVA	3.2 ± 1.0	4.2 ± 1.6
	PVP	3.0 ± 1.2	5.1 ± 1.4
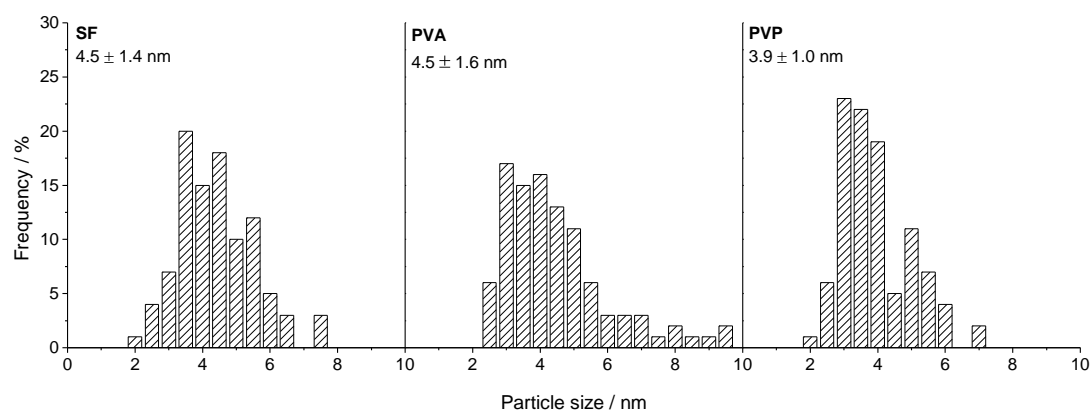
Figure 4.21 - Particle size distribution for the monometallic catalysts prepared SF, PVA and PVP after 1st use for glycerol oxidation
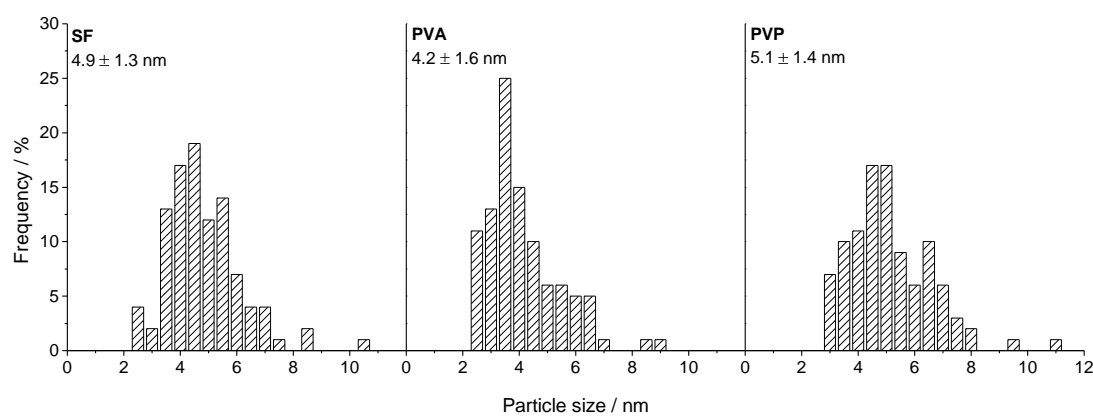
Figure 4.22 - Particle size distribution for the bimetallic catalysts prepared SF, PVA and PVP after 1st use for glycerol oxidation
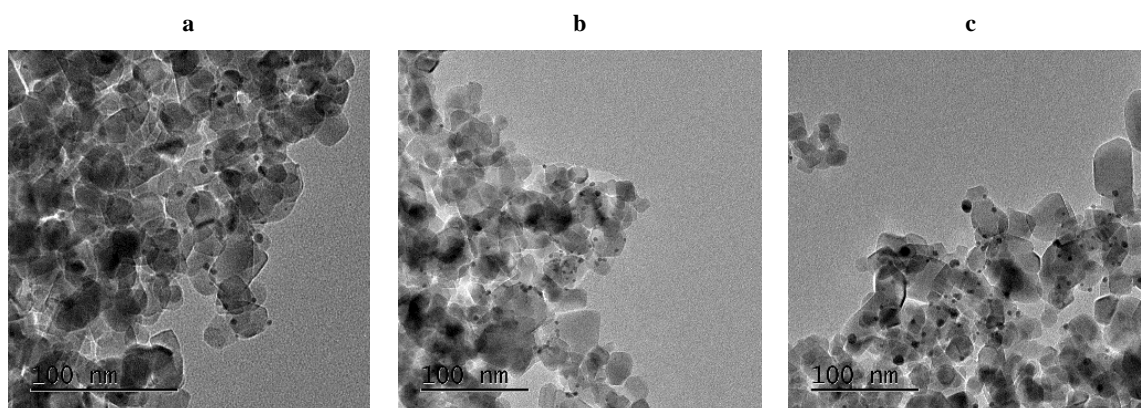
Figure 4.23 (a-c) - TEM micrographies for the monometallic catalysts prepared PVA (a) PVP (b) and SF (c).
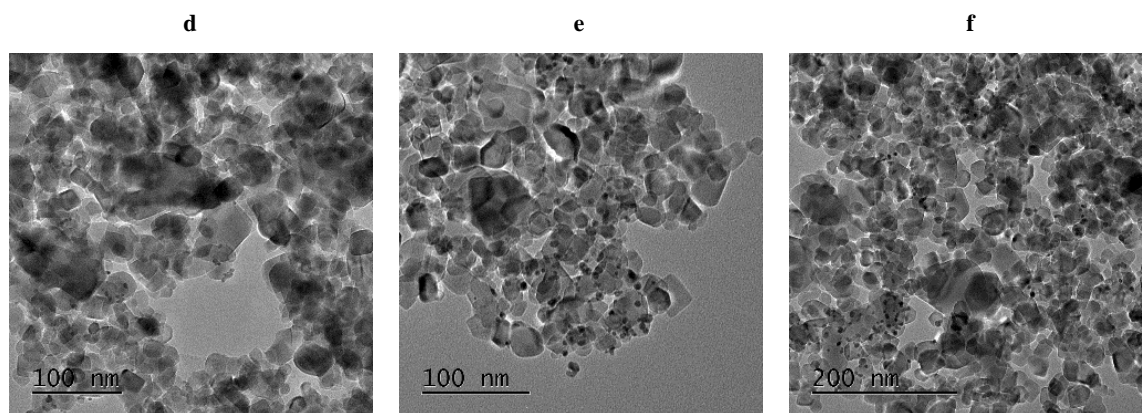
Figure 4.23 (d-f) - TEM micrographies for the bimetallic catalysts prepared PVA (d) PVP (e) and SF (f).

Since the catalyst deactivation can be due to the strong adsorption of reaction products on the surfaces [20], CO-DRIFTS analysis was performed on the mono and bimetallic used catalysts in order to see any modification on the catalytic active site after reaction. The results, compared with the fresh catalysts, are displayed in Figures 4.24 and 4.25.

Monometallic fresh catalysts did not exhibit any signal in the region around 2100 cm^{-1}, excepted the sample prepared by PVA addition that showed a signal at 2110 cm^{-1}, correspondent to CO linear adsorption. The reason of this could be related to the nanoparticles dimension, as previously discussed in Chapter 3. Conversely, all the bimetallic catalysts showed signals in the region 2200-2000 cm^{-1}, corresponding to linear CO adsorption on the edge or corner of Pd [32], and in the 2000-1800 cm^{-1}, correspondent to bridged or three-fold CO adsorption on Pd or AuPd [33], as previously discussed in Chapter 3. After use for glycerol oxidation, the signal of the monometallic catalyst prepared by PVA disappeared, and this can be related to the increase in the nanoparticle size or to the presence of adsorbed species, e.g., reaction products; the effect of Na^+ or OH^- ions cannot be excluded. The same reasons can be used to explain the modification of the peak shape and position observable for the bimetallic catalysts. This is clearly visible for the PVP catalyst, suggesting for this catalyst a heavier site modification. Interestingly, though, this is not affecting the catalytic activity, as previously shown in Figure 4.18. Therefore, was not possible to find a correlation between these results and the observed catalytic behaviour.
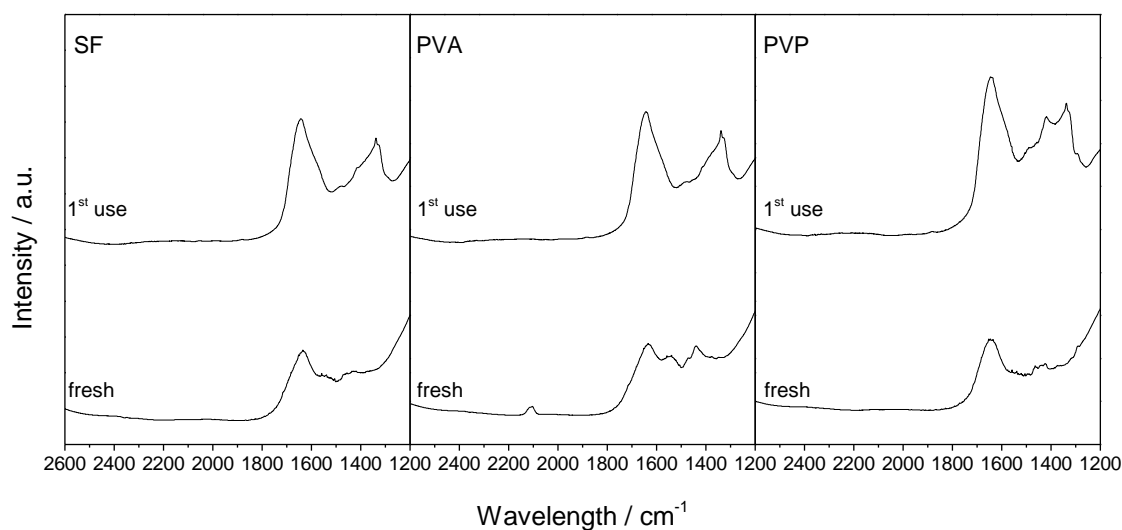
Figure 4.24 – CO-DRIFTS spectra for the monometallic catalyst before and after glycerol oxidation
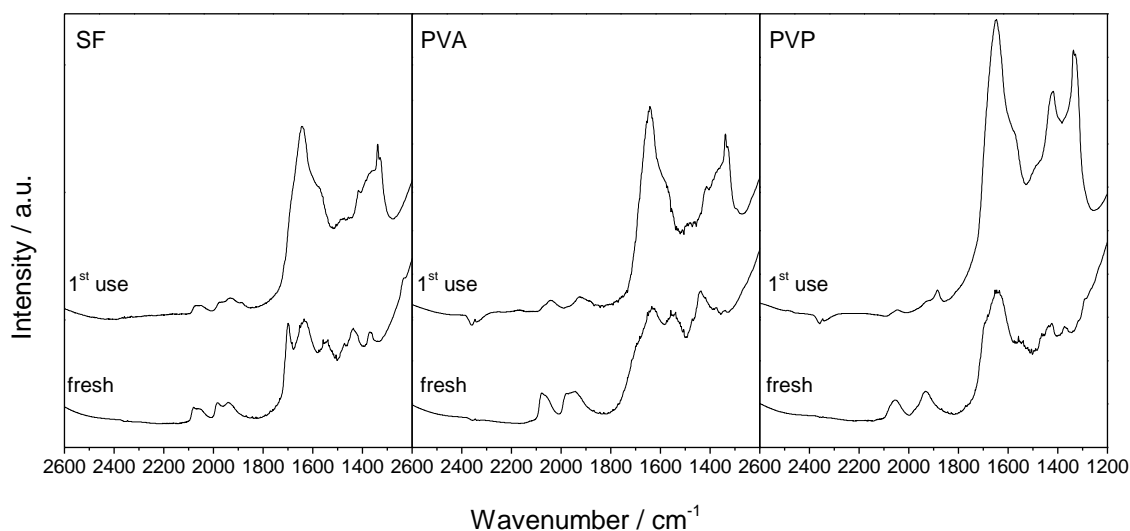
Figure 4.25 – CO-DRIFTS spectra for the bimetallic catalyst before and after glycerol oxidation

The analysis of the fingerprint region is a very complicated matter, and limited information is found in the literature. Nonetheless, it is possible to analyse the differences in this region to gain some information that might be useful to understand the adsorption modes in dependence of the presence and nature of the polymer, even though the discussion is pure speculative. As briefly mentioned in Chapter 3, the fingerprint region might contain useful information about the interaction of the CO with the TiO_2 [34-36], strongly dependent to the presence of polymer, as evinced from the spectra comparison of the catalysts prepared by the three methods.

Interestingly, both the monometallic and bimetallic catalysts prepared SF and PVA, show a very similar signal shape after being used. Prior to use though, the observed signals were different. This might suggest that the interaction of CO with the TiO_2 is the same, or, in other words, that the surfaces are similar after reaction. This can be related to a partial removal of the PVA from the surface [37], or indicate that the possible reaction residues are adsorbed in the same way on both the surfaces, producing very similar interaction signals for both the catalysts. On the other hand, the samples prepared by PVP addition showed very different shape of signals in the fingerprint region, suggesting a different interaction of CO with the TiO_2 when compared to the SF and PVA catalysts. Again, this might be related to the modification of TiO_2 following the adsorption of reaction species.

4.3 Conclusion

This Chapter investigated the catalytic response of the monometallic and bimetallic catalysts prepared by sol-immobilisation *via* SF, PVA and PVP and rationalised the results on the basis of the presence and nature of the polymer. A series of experiments were performed in order to deeply investigate the reaction mechanism and the polymer influence on the catalytic activity. On the basis of the results obtained, the following conclusions can be drawn:

1. On monometallic and bimetallic catalysts, the glycerol oxidation rate was independent on the stabiliser presence and nature;

2. On monometallic catalysts, selectivity to GA followed the trend PVP>PVA>SF, the opposite trend was observed for the selectivity to TA. A similar trend could not be observed for the bimetallic catalysts.

3. Experiments performed using GA as starting material suggested a different oxidation mechanism occurring on the SF and PVA surfaces. As evidenced by experiments using the bimetallic catalysts, GA oxidation appears to happen faster on the SF surfaces. At *iso-conversion*, the higher selectivity to GLYA observed for these catalysts might be related to a higher production of H_2O_2, which is believed to enhance GA oxidation (to TA), or to a faster O_2 dissociation. However, TA cannot be generated only *via* this process.

4. Short time glycerol oxidation experiments, performed using mono and bimetallic catalysts prepared SF and PVA, evidenced the formation of TA since the very beginning both on PVA and SF surfaces, the latter being more selective to it, as observed in the 4 hours testing. This suggests that TA is a primary oxidation product, independently from the presence of the polymer.

5. Polymer addition studies on SF catalysts evidenced that the PVA influences both the selectivity and the conversion, with a more marked effect on this latter in dependence of the amount. Conversely, PVP addition influenced the selectivity but not the conversion, independently from the amount. Both these results suggest a different oxidation mechanism in presence of polymer. There was no possibility to discriminate whether the polymer presence and nature influences the adsorption of glycerol on the surfaces, i.e. enhancing adsorption modes that favour the selectivity to GA rather than to TA or vice versa.

Bibliography

1.   B. Katryniok, H. Kimura, E. Skrzynska, J. S. Girardon, P. Fongarland, M. Capron, R. Ducoulombier, N. Mimura, S. Paul and F. Dumeignil, *Green Chemistry*, **2011**, *13*, 1960-1979.

2.   A. Villa, N. Dimitratos, C. E. Chan-Thaw, C. Hammond, L. Prati and G. J. Hutchings, *Accounts of Chemical Research*, **2015**, *48*, 1403-1412.

3.   A. Behr, J. Eilting, K. Irawadi, J. Leschinski and F. Lindner, *Green Chem.*, 2008, 10, 13-30.

4.   G. W. Huber and A. Corma, *Angewandte Chemie Int. Ed.*, **2007**, *46*, 7184-7201.

5.   C. H. C. Zhou, J. N. Beltramini, Y. X. Fan and G. Q. M. Lu, *Chemical Society Reviews*, **2008**, *37*, 527-549.

6.   S. Demirel, K. Lehnert, M. Lucas and P. Claus, *Applied Catalysis B: Environmental*, **2007**, *70*, 637-643.

7.   S. Demirel, M. Lucas, J. Wärnå, T. Salmi, D. Murzin and P. Claus, *Topics in Catalysis*, **2007**, *44*, 299-305.

8.   S. Gil, M. Marchena, L. Sánchez-Silva, A. Romero, P. Sánchez and J. L. Valverde, *Chemical Engineering Journal*, **2011**, *178*, 423-435.

9.   W. Ketchie, M. Murayama and R. Davis, *Journal of Catalysis*, **2007**, *250*, 264-273.

10.   N. Dimitratos, A. Villa, L. Prati, C. Hammond, C. E. Chan-Thaw, J. Cookson and P. T. Bishop, *Applied Catalysis A: General*, **2016**, *514*, 267-275.

11.   N. Dimitratos, J. A. Lopez-Sanchez, D. Lennon, F. Porta, L. Prati and A. Villa, *Catalysis Letters*, **2006**, *108*, 147-153.

12.   D. I. Enache, J. K. Edwards, P. Landon, B. Solsona-Espriu, A. F. Carley, A. A. Herzing, M. Watanabe, C. J. Kiely, D. W. Knight and G. J. Hutchings, *Science*, **2006**, *311*, 362-365.

13.   N. Dimitratos, J. A. Lopez-Sanchez, J. M. Anthonykutty, G. Brett, A. F. Carley, R. C. Tiruvalam, A. A. Herzing, C. J. Kiely, D. W. Knight and G. J. Hutchings, *Physical Chemistry Chemical Physics: PCCP*, **2009**, *11*, 4952-4961.

14.   V. Peneau, Q. He, G. Shaw, S. A. Kondrat, T. E. Davies, P. Miedziak, M. Forde, N. Dimitratos, C. J. Kiely and G. J. Hutchings, *Physical Chemistry Chemical Physics: PCCP*, **2013**, *15*, 10636-10644.

15.   S. Carrettin, P. McMorn, P. Johnston, K. Griffin, C. J. Kiely and G. J. Hutchings, *Physical Chemistry Chemical Physics: PCCP*, **2003**, *5*, 1329-1336.

16. F. Porta and L. Prati, *Journal of Catalysis*, **2004**, *224*, 397-403.

17. S. Demirel-Gülen, M. Lucas and P. Claus, *Catalysis Today*, **2005**, *102-103*, 166-172.

18. S. Carrettin, P. McMorn, P. Johnston, K. Griffin and G. J. Hutchings, *Chemical Communications*, **2002**, *0*, 696-697.

19. W. Ketchie, Y. Fang, M. Wong, M. Murayama and R. Davis, *Journal of Catalysis*, **2007**, *250*, 94-101.

20. L. Prati, A. Villa, C. E. Chan-Thaw, R. Arrigo, D. Wang and D. S. Su, *Faraday Discussions*, **2011**, *152*, 353-365.

21. W. C. Ketchie, M. Murayama and R. J. Davis, *Topics in Catalysis*, **2007**, *44*, 307-317.

22. S. Carrettin, P. McMorn, P. Johnston, K. Griffin, C. J. Kiely, G. A. Attard and G. J. Hutchings, *Topics in Catalysis*, **2004**, *27*, 131-136.

23. N. Dimitratos, A. Villa, C. L. Bianchi, L. Prati and M. Makkee, *Applied Catalysis A: General*, **2006**, *311*, 185-192.

24. A. Villa, C. Campione and L. Prati, *Catalysis Letters*, **2007**, *115*, 133-136.

25. C. L. Bianchi, P. Canton, N. Dimitratos, F. Porta and L. Prati, *Catalysis Today*, **2005**, *102-103*, 203-212.

26. M. Sankar, N. Dimitratos, D. W. Knight, A. F. Carley, R. Tiruvalam, C. J. Kiely, D. Thomas and G. J. Hutchings, *ChemSusChem*, **2009**, *2*, 1145-1151.

27. C. H. Zhou, J. N. Beltramini, Y. X. Fan and G. Q. Lu, *Chemical Society Reviews*, **2008**, *37*, 527-549.

28. A. Namdeo, S. M. Mahajani and A. K. Suresh, *Journal of Molecular Catalysis A: Chemical*, **2016**, *421*, 45-56.

29. N. Dimitratos, J. A. Lopez-Sanchez, D. Morgan, A. F. Carley, R. Tiruvalam, C. J. Kiely, D. Bethell and G. J. Hutchings, *Physical Chemistry Chemical Physics: PCCP*, **2009**, *11*, 5142-5153.

30. A. Villa, D. Wang, G. M. Veith, F. Vindigni and L. Prati, *Catalysis Science & Technology*, **2013**, *3*, 3036-3041.

31. D. I. Enache, J. K. Edwards, P. Landon, B. Solsona-Espriu, A. F. Carley, A. A. Herzing, M. Watanabe, C. J. Kiely, D. Knight and G. J. Hutchings, *Science*, **2006**, *311*, 362-365.

32. J. H. Carter, S. Althahban, E. Nowicka, S. J. Freakley, D. J. Morgan, P. M. Shah, S. Golunski, C. J. Kiely and G. J. Hutchings, *ACS Catalysis*, **2016**, *6*, 6623-6633.

33.   F. Cárdenas-Lizana, S. Gómez-Quero, A. Hugon, L. Delannoy, C. Louis and M. A. Keane, *Journal of Catalysis*, **2009**, *262*, 235-243.

34.   M. A. Bollinger and M. A. Vannice, *Applied Catalysis B: Environmental*, **1995**, *8*, 417-443.

35.   B. Schumacher, V. Plazk, M. Kinne and R. J. Behm, *Catalysis Letters*, **2003**, *89*, 109-114.

36.   F. Boccuzzi, S. Tsubota and M. Haruta, *Journal of Electron Spectroscopy and Related Phenomena*, **1993**, *64/65*, 241-250.

37.   J. A. Lopez-Sanchez, N. Dimitratos, C. Hammond, G. L. Brett, L. Kesavan, S. White, P. Miedziak, R. Tiruvalam, R. L. Jenkins, A. F. Carley, D. Knight, C. J. Kiely and G. J. Hutchings, *Nature Chemistry*, **2011**, *3*, 551-556.

Chapter 5

Plasmonic Photocatalysis for Glycerol Oxidation Using Mono and Bimetallic Sol-Immobilised Catalysts

5.1 Introduction

The possibility to use the inexhaustible, abundant and clean energy of the sun to promote chemical reactions is a great incentive in the development of photocatalysts. For this reason, photocatalysis is expected to play an increasingly important role in tackling the challenges of the 21st century, such as depletion of (fossil) energy resources, environmental pollution and global warming [1]. The investigation in the photocatalysis field started with the observation that some materials, belonging to the class of semiconductors, were able to accelerate the degradation of organic compounds under illumination. As extensively explained in Section 1.3, Chapter 1, upon illumination at specific frequency determined by the band gap between the valence band and the conduction band of the material, electron-hole pairs (charge carriers) are generated, and migrate on the particle surface where they can promote reduction and oxidation reactions. However, the process in a traditional photocatalyst, such as e.g., titania (TiO_2), is very inefficient since the charge carriers lifetime is not long

enough, and most often the energy is dissipated through their recombination, as displayed in Figure 1.7 (Chapter 1). Moreover, the generation of charge carriers requires frequencies in the UV range (representing only the 4% of sunlight) because of the big band gap.

Given these drawbacks, a new photocatalytic perspective can be provided by the use of materials able to harvest the visible portion of the light through their localised surface plasmon resonance (LSPR) response. As explained in Chapter 1, the plasmon is defined as the collective oscillation of the free electrons of the nanoparticle, in phase with the incident radiation [2, 3]. This oscillation causes the excitation of the electrons at very high energy levels, and the subsequent relaxation process is accompanied by energy redistribution which can lead to local heating and to injection of high energy electrons to e.g., adsorbate's orbitals. Most importantly, the LSPR properties of the nanoparticles can be tuned by size and shape modification, as well as the surroundings (dielectric constant). The fact that some nanoparticles (e.g., Au, Cu, Ag) show this effect in the visible range makes them of fundamental interest for a wide range of applications, including spectroscopy and medicine [4, 5 6, 7].

Regarding the photocatalytic applications, since some of these nanoparticles are already employed as "thermal" photocatalysts, the interest is on the possibility of enhancing their activity or tuning the selectivity by the LSPR effects. However, the intrinsic catalytic activity of each metal is fundamental in determining the selectivity [8]. Various plasmonic nanostructures, including of different shape [9, 10], composition [11-15] and morphology [16], have been successfully employed for quasi-homogeneous and heterogeneous catalytic applications, including oxidation, reductions and coupling reactions. Exhaustive reviews can be found, e.g., in references [17, 18]. Oxidation of alcohols and polyols has been widely investigated by a number of authors [15, 19-21]. Effect of parameters such as nature of the support, wavelength and intensity of the radiation have also been reported in a number of studies. For example, Ke *et al.* [22, 23] synthesised a series of Au nanoparticles deposited onto different materials (TiO_2, CeO_2, ZrO_2, Al_2O_3 and zeolite Y) and evaluated their catalytic activity for various reduction reactions, showing the superior performances of the Au/CeO_2 catalyst and demonstrating the dependency of the plasmonic effect on the intensity and wavelength of the radiation.

Amongst the noble metals, Ag nanoparticles [24, 25] were also employed for a number of reactions. Transition metal nanoparticles such as Cu, also show LSPR properties in the visible range, and have been employed as either monometallic catalyst or alloyed with other metals; however, the major challenge is to keep them in the metallic state, since the high electronic instability leads to rapid oxidation. It has been reported that irradiation with visible light ($\lambda > 450$ nm) of AuCu alloy nanoparticles supported on TiO_2 (P25) is beneficial for keeping the Cu in the metallic state, and these catalysts were employed for the oxidation of 2-propanol, showing superior activity when compared to the monometallic catalysts [26]. Stabilisation has also been reported by Guo *et al.* [27] by depositing Cu nanoparticles onto graphene, whose delocalised electrons can move freely and can improve the chemical stability of Cu nanoparticles.

Recently, Sarina *et al.* [28] showed the potential photocatalytic applications of non-plasmonic transition metal nanoparticles such as Pd, Pt, Ir, Rh, already used in a wide number of reactions. Such nanoparticles show different behaviour under illumination, and this effect has to be ascribed to the combination of the optical properties of the free (LSPR) and the bound electrons.

The versatility shown by plasmonic nanoparticles can be used to design catalysts with specific features. For example, it is possible to prepare catalysts with appropriate distance between the nanoparticles which give rise to multiple resonances (hot spots) with a characteristic resonance frequency that falls at longer wavelengths than the resonance showed by isolated nanoparticles [29, 30].

Aim of the Chapter

This chapter presents the study of the plasmonic photocatalytic oxidation of glycerol in neutral conditions performed using Au and AuPd nanoparticles-based catalysts. The plasmonic response of these materials is compared to their "thermal" activity. Parameters such as metal loading, nature and presence of stabilising agent, support, irradiation wavelength and reaction time were also investigated. The experimental set up was designed as a part of the research partnership with the Max Net Energy partners in Mulheim an der Ruhr (Germany).

5.2 Catalyst Testing

Glycerol oxidation in neutral conditions was investigated as a model oxidation reaction using plasmonic photocatalysis. This reaction has been well studied in the literature and is linked to the previous work done during the PhD and was recently reported as a reaction that can be enhanced by visible light absorption using Au nanoparticles [21] by our Max Net partners working in the Max Planck Institute (MPI) für Kohlenforschung in Mülheim an der Ruhr (Germany). The reaction conditions as well as the reactor were modelled on previous experiments reported in reference [21]. Preliminary tests of the reaction system were carried out using a 7.5% wt Au/TiO$_2$ synthesized in Germany by the authors of reference [22] by deposition-precipitation method, to ensure the reproducibility of the results, as will be further explained.

In the present work, the catalytic systems investigated were:

- a series of Au/TiO$_2$ catalysts at different wt% Au loading (nominal wt % 1, 3, 5, 7) prepared by sol-immobilisation method using PVA as stabiliser polymer and the counterparts prepared stabiliser-free;

- a series of 1% wt AuPd/TiO$_2$ at different Au:Pd molar ratio.

Further testing was carried out using other catalysts in order to investigate the support effect, the stabilising polymer effect and the calcination effect. The aim of all the experiments was to observe any difference in the catalytic activity under dark conditions and visible light illumination, and, if possible, to identify the existence of any differences in oxidation mechanism depending on the illumination conditions.

5.2.1   Glycerol oxidation

Glycerol oxidation in a neutral environment was performed under dark and illuminated conditions. The neutral environment is necessary because the reactions in basic environment (see Chapter 4) are faster, suggesting that the "thermal" process could dominate compared to the photocatalytic process. The reactor was designed and manufactured specifically for this process, as explained in Chapter 2. The design was planned according to the reactor used at the MPI in Germany, for the same catalytic testing. The main differences to the original reactor were: 1) the total volume of 30 mL instead of 10 mL; 2) PTFE liner instead of glass; 3) no direct temperature control inside the reaction mixture.

The initial photocatalytic glycerol oxidation tests using this set-up were unsuccessful, despite modifying parameters such as the catalyst composition and its loading in the reactor, volume and concentration of the solution. It became clear that the absence of any enhancement was due to the reactor set up rather than to the reaction conditions. At a later stage it was decided to use a glass liner in order to reduce the total volume from 30 mL to 15 mL. The new liner was a common glass vial, cut to the appropriate size, and prior to each experiment it was wrapped with aluminium foil to ensure both thermal contact and light reflection inside the reaction mixture. Also a Teflon ring was prepared in order to fit the vial inside the reactor, as illustrated in Figure 5.1, and temperature recalibrated accordingly.

Figure 5.1 – Reactor's volume modification

Preliminary studies of the response of the new reactor set up and the reproducibility were performed using a 7.5% wt Au/TiO_2 catalyst from the MPI prepared by deposition-precipitation (DP), known to be active. The reaction conditions were slightly different from those reported in [21]: in the original set-up, indeed, the experiments were performed using an autoclave of 10 mL total volume and batch conditions (static O_2). Other conditions were kept the same, i.e., 5 mg catalyst, 5 mL of 0.05 M glycerol solution, 90 °C, 5 hours total reaction time.

Testing under illuminated conditions was carried out using a 300 W Xe source equipped with a 420 nm wavelength cut-off filter (unless otherwise stated), to ensure the radiation was not exciting TiO_2 levels [31-34], and with an IR water filter, to ensure a minimum heating effect. The results are displayed in Figure 5.2. The results showed that illumination has a beneficial effect on the glycerol conversion reaching 35% *versus* the 15% observed under dark conditions. The carbon mass balance (CMB), calculated taking into account only

the products detected by HPLC analysis as explained in Chapter 2, was good in both cases (≥ 90%), with the lower value for the illuminated sample due to the higher carbon dioxide (CO_2) production. CO_2 was only qualitatively detected, and the missing material in the mass balance assigned to it.
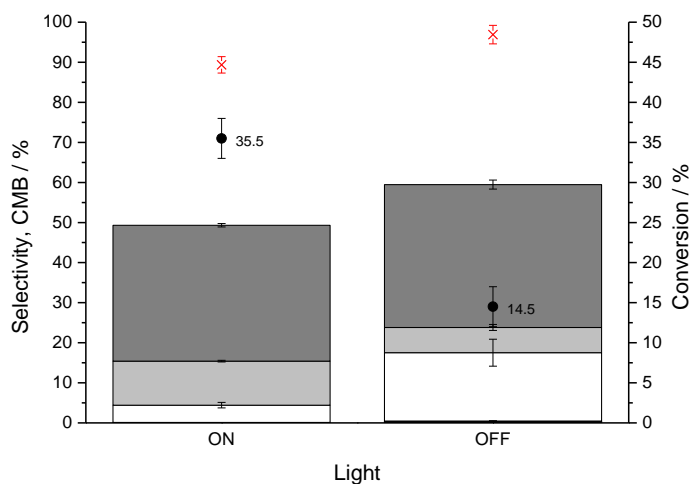
Figure 5.2 - 7.5% wt Au/TiO$_2$-DP (MPI). *Testing conditions*: 5 mL glycerol 0.05 M, 5 mg catalyst, 90 °C, 3h, Gly/Au = 130, 5 hours. *Legend*: ● glycerol conversion ■ pyruvic acid (PA) □ glyceric acid (GA) ▨ glycolic acid (GLYA) ■ dihydroxyacetone (DHA) x Carbon Mass Balance (CMB); missing material to be assigned to CO_2

The lower CMB observed for the illuminated samples has been suggested, by the authors of the original study, to be linked to a higher H_2O_2 production under these conditions [35, 36], which favours the over-oxidation of products to CO_2. The production of H_2O_2 on Au nanoparticles has been documented also in dark conditions [37-40]. For example, in their studies on alcohol oxidation in basic conditions, Davis *et al.* [37, 41] demonstrated, with the support of experiments using labelled reactants and density functional theory (DFT) calculations, that molecular O_2 is not directly involved in the reaction (i.e., is not incorporated in the products), but its role is to act as a scavenger of electrons accumulated on the metal surface following the adsorption of the alcohol, regenerating the hydroxide ions consumed in the reaction to form the reactive alkoxide intermediate, and closing the catalytic cycle. The mechanism proposed accounts of the reduction of O_2 with water to obtain peroxide and hydrogen peroxide, according to the following sequence (where * indicates a catalytic site):

$$O_2{}^* + H_2O^* \rightarrow OOH^* + HO^*$$

$$OOH^* + H_2O^* \rightarrow H_2O_2{}^* + HO^*$$

$$HO^*+e^- \rightarrow HO^- + {}^*$$
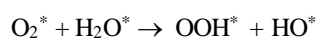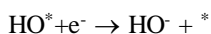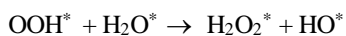
The mechanism proposed in the literature [20, 42-45] for the formation of H_2O_2 in plasmonic catalysts under illumination accounts of the injection of the excited "hot" electrons into the TiO_2 conduction band (Figure 1.13, Chapter 1), in a reverse process with respect of that a supported Au/TiO_2 catalyst is irradiated by the UV light [36, 46, 47]. The O_2 adsorbed on the TiO_2 surface is subsequently reduced to superoxide radicals and then converted to H_2O_2, according to the process reported for the classic TiO_2 photocatalytic mechanism [35, 36, 48]. The well-known H_2O_2-mediated cleavage process [39, 49, 50] has been suggested to be responsible for the conversion of GA to glycolic acid (GLYA) and dihydroxyacetone (DHA).

A comparison of these results with the results obtained in Germany reported in reference [21] and reported in Figure 1.14 (Chapter 1) showed that the experiment is reproducible. It must be pointed out that the difference in the selectivity and conversion values should be ascribed to the difference in the experimental set up and in the use of a different batch of catalyst. Taking into account these factors, the response to illumination was consistent with previous reports.

Preliminary testing was also carried out on a 5% wt Au/TiO_2 prepared by sol-immobilisation (traditional method with PVA), in order to investigate whether the preparation method was crucial for catalytic activity. As in the previous case, this sample was originally tested in Mulheim and proven to be active. The results of the catalytic testing run in Mulheim and in Cardiff are displayed in Figure 5.3. The difference in the results observed for the two tests should be ascribed to the difference in the set-up, as previously mentioned. The fact that the GLYA was not observed under dark conditions for the catalyst tested in Cardiff might be due to the very low conversion value. Nonetheless, it is important to point out that despite these differences, the catalytic response was very similar for the two set-up: indeed, the improvement in the conversion observed under illumination is around 16-17% in both the systems. Therefore, it can be concluded that the experimental conditions (especially the total volume, which influences the extent to which the light can penetrate into the solution) play a fundamental role in determining the catalytic response.

When comparing these results with the results obtained with the 7.5% wt Au/TiO_2 - DP catalyst (Figure 5.2), as expected, it was observed a decrease in the conversion values accordingly to the lower metal loading. However, the very similar product distribution suggests a similar reaction pathway for the two catalysts, indicating that the preparation method does not to affect the catalytic performances in terms of selectivity. This is also confirmed when comparing the results with the reactions obtained with a similar catalyst (5% wt Au/TiO_2) prepared by DP displayed in Figure 1.14 (Chapter 1). Similarly to the 7.5 % wt Au/TiO_2 - DP catalyst, also in this case the CMB was lower under illumination conditions, with a higher production of GLYA and CO_2 likely related to a higher amount of H_2O_2 as previously discussed.
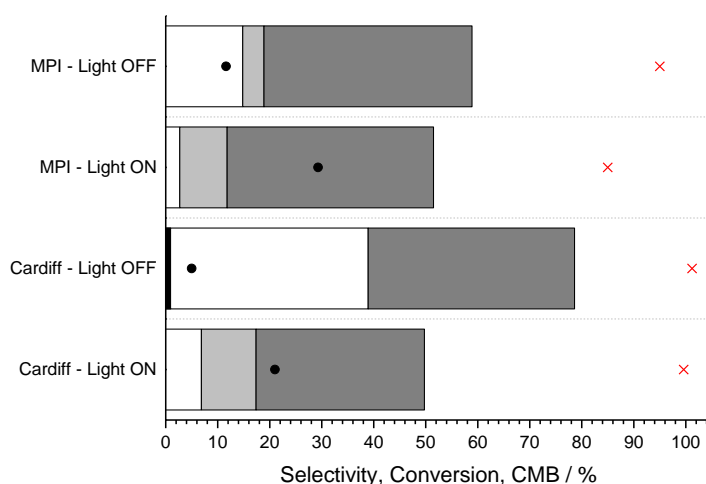
Figure 5.3 - 5% wt Au/TiO_2-PVA tested at the MPI in Mülheim and in Cardiff. *Testing conditions*: 5 mL glycerol 0.05 M, 5 mg catalyst, 90 °C, 3 h, Gly/Au = 130, 5 hours. *Legend*:● glycerol conversion ■ pyruvic acid (PA) □ glyceric acid (GA) ■ glycolic acid (GLYA) ■ dihydroxyacetone (DHA) x Carbon Mass Balance (CMB); missing material to be assigned to CO_2

The preliminary test determined that the reactor and chosen conditions would allow the study of light and dark photocatalytic reactions, and further testing was performed to screen different catalysts, decreasing the total reaction time from 5 hours to 3 hours. At this stage of the work, the interest was focused on the difference in the catalytic response under dark and illumination conditions, rather than on their performance in terms of activity.

5.2.2   Catalyst screening: the Au/TiO$_2$–PVA series

A series of 1, 3, 5, 7 % wt Au/TiO$_2$ catalyst (nominal wt %) was prepared by a previously reported sol-immobilisation method using PVA as stabilising agent as described in Chapter 2, and tested for glycerol oxidation under dark and illuminated conditions.

The experiments were carried out using 5 mg of catalyst and 5 mL of glycerol 0.05 M, meaning that the substrate/catalyst ratio changed for each experiment (Gly/Au respectively 984, 330, 200, 140). The catalytic testing between catalysts was comparable since the nanoparticles, independently from the metal loading, showed regular shape and dispersion on the support as well as very similar size distribution, averaging 2.8 $\pm$ 0.7 nm for all the samples (Figure 5.4 and 5.5).
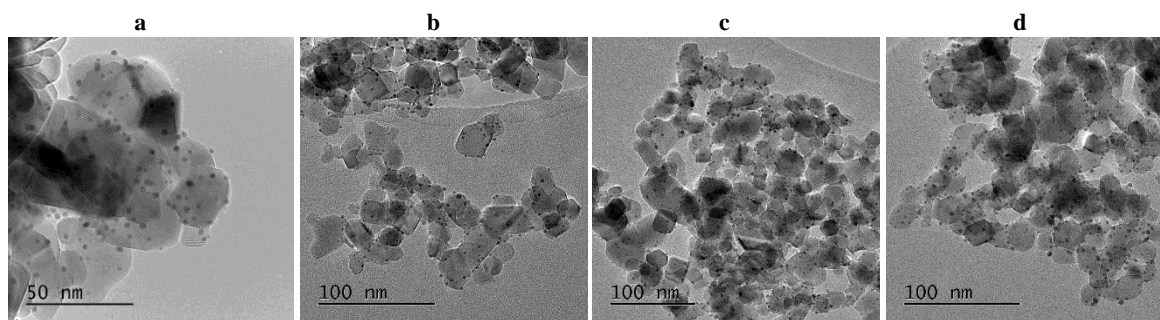
Figure 5.4 - Representative TEM images for the Au/TiO$_2$–PVA series (wt %): (a) 1% (b) 3% (c) 5% (d) 7%
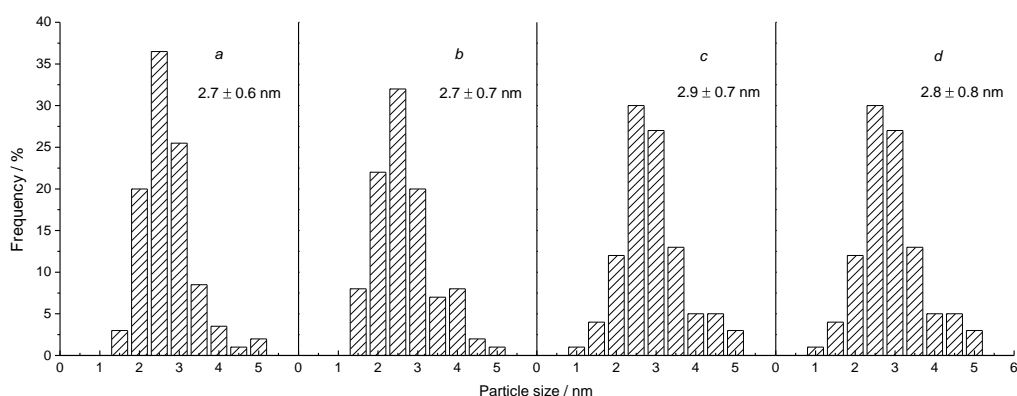
Figure 5.5 - Nanoparticle size distribution for the 1, 3, 5, 7% (*a, b, c, d* respectively) wt Au/TiO$_2$ catalysts calculated by counting 100 nanoparticles from TEM images

Figure 5.6 displays the results of the catalytic testing for the 1-7% wt Au/TiO_2 – PVA catalysts in terms of conversion, selectivity and carbon mass balance, carried out under dark and illumination conditions. As expected, conversion values after 3 hours testing were lower when compared to the 5 hours experiments, yet this reaction time allowed to observe a difference in the catalyst performance under illumination. For all the samples, independent of the gold loading, an enhancement in the conversion under illumination was observed. The 3-7% wt Au/TiO_2 samples showed were very similar behaviour under dark and illumination conditions, with conversion values around 10% in the former case and around 5% in the latter. The 1% wt sample, as expected, showed the lower conversion. Under dark conditions, the 3%, 5% and 7% wt catalysts showed the formation of a small fraction of pyruvic acid (PA), which was never detected in reactions under illumination. This might indicate a different oxidation pathway occurring under the two conditions. Another feature common to all the samples is the production of CO_2, except for the 1% wt sample in dark, perhaps due to its very low conversion.
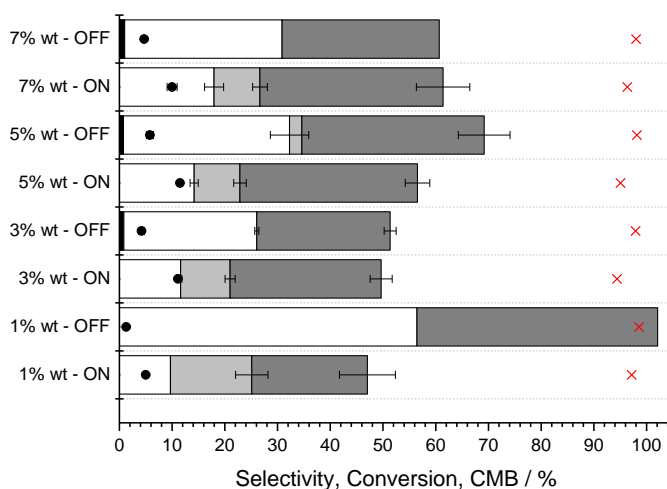
Figure 5.6 – Catalytic activity of 1, 3, 5, 7% wt Au/TiO_2–PVA. *Testing conditions*: 5 mL glycerol 0.05 M, 5 mg catalyst, 90 °C, 3 h, (1%) Gly/Au = 984 (3%) Gly/Au = 330 (5%) Gly/Au = 200 (7%) Gly/Au = 140, 3 hours. *Legend*:● glycerol conversion ■ pyruvic acid (PA) □ glyceric acid (GA) ■ glycolic acid (GLYA) ■ dihydroxyacetone (DHA) x Carbon Mass Balance (CMB); missing material to be assigned to CO_2.

All the samples showed a similar product distribution, with selectivity predominantly to GA, GLYA and DHA. GLYA was mainly detected for the reactions run under illumination, suggesting a higher production of

H_2O_2 [39, 49, 50] under these conditions, as previously discussed for the preliminary testing. However, the detection of a small quantity of GLYA for the 5% wt catalyst under dark conditions might suggest that the H_2O_2 production is conversion-dependent rather than related to a different mechanism. Indeed, the GLYA was never observed at lower conversion (i.e., dark conditions) values. Nonetheless, the existence of a different oxidation pathway cannot be excluded, since the GLYA was detected under illumination conditions even if the conversion was low (5%) such as in the case of the 1% wt catalyst.

Further examination of the results obtained at *iso-conversion* for the 5% wt catalyst (Figure 5.7) showed a similar product distribution under dark and illumination conditions, so that GA, GLYA, DHA were detected in both cases, but with different selectivity values. For example, the selectivity to GLYA appeared to be slightly higher for the illuminated catalyst, in accordance with the previous discussion of a possible enhanced production of H_2O_2 under illumination conditions. Conversely, the selectivity to GA and DHA is higher under dark conditions, which can be explained considering a slower rate of H_2O_2 production. This, together with the detection of a small quantity of PA, further suggests the existence of a different oxidation pathway for the two conditions.
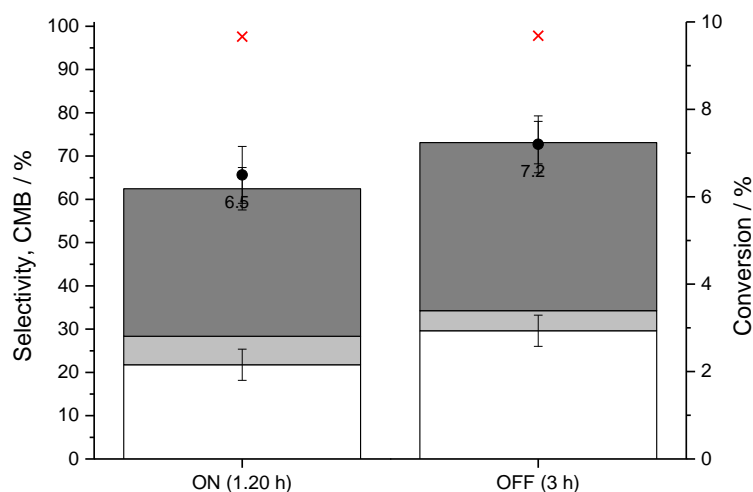
Figure 5.7 - *Iso-conversion* 5% wt Au/TiO_2–PVA. *Testing conditions*: 5 mL glycerol 0.05 M, 5 mg catalyst, 90 °C, Gly/Au=200, 3 hours. *Legend*:● glycerol conversion ■ pyruvic acid (PA) □ glyceric acid (GA) ▨ glycolic acid (GLYA) ▨ dihydroxyacetone (DHA) x Carbon Mass Balance (CMB); missing material to be assigned to CO_2

In order to better visualise the trend of the catalytic response for the 1-7% wt series, the values were plotted (Figure 5.8) *versus* the actual Au loading, determined by ICP analysis and reported in Table 5.1. The small difference in the performance of the 3-7% wt catalysts can be explained taking into consideration the real metal content. This was always lower than the nominal value, indicating an incomplete metal deposition, with the highest discrepancy at higher loading, so that the gold content was very similar for the 5% and 7% wt catalysts.
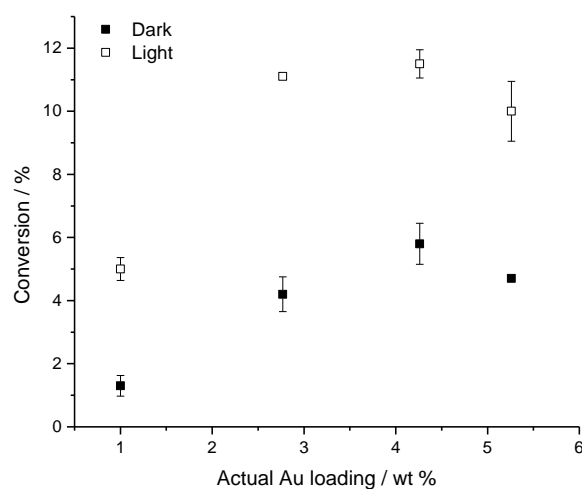
Figure 5.8 - Conversion under illumination and dark conditions for the 1-7% Au/TiO$_2$-PVA series

Table 5.1 Real metal amount determined by ICP for the 1-7% wt Au/TiO$_2$-PVA series.

Metal amount (wt %) determined by ICP		
Catalyts	**Au nominal wt%**	**Au real wt%**
Au/TiO$_2$-PVA	1	0.99
	3	2.77
	5	4.26
	7	5.26

Figure 5.9 displays the UV-Vis spectra of the 1-7% wt catalysts. As already described in Chapter 3, the position and the shape of the plasmonic peak of nanoparticles is influenced by several parameters, especially when there is an interaction with the support [12, 23, 51, 52]. All the catalysts showed a similar plasmonic peak shape at similar wavelength (around 540 nm), which is expected for regular nanoparticles shape observed by TEM. As expected, higher metal loading showed higher absorption values [17]. Since the preparation method involves the use of the PVA polymer as stabilising agent, which is known to be detrimental for catalytic and

photocatalytic applications [53-58], it was decided to calcine the samples in order to see any beneficial effect on the catalytic performances. The 3% and the 5% wt Au/TiO_2 catalysts were calcined at 500 °C in static air for 3 hours and tested under the same conditions in order to study the effect of calcination on the catalytic performance (Figure 5.10). These conditions are expected to be effective for the polymer removal from TGA analysis previously carried out on the 1% wt Au/TiO_2-PVA catalyst (Chapter 3, Figure 3.3).
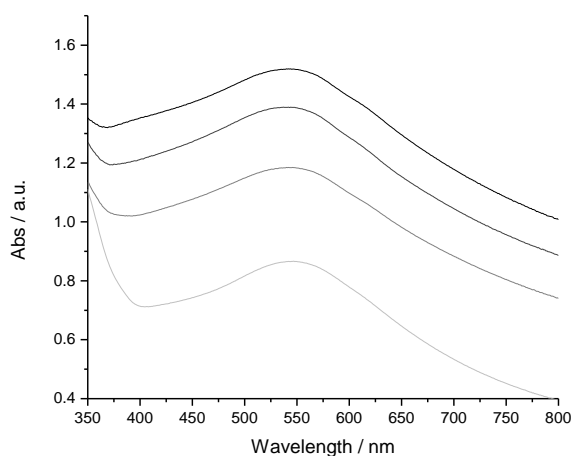
Figure 5.9 - UV-Vis diffuse reflectance spectra for the 1-7% wt Au/TiO_2–PVA samples.

Legend: —1% — 3% — 5% — 7%
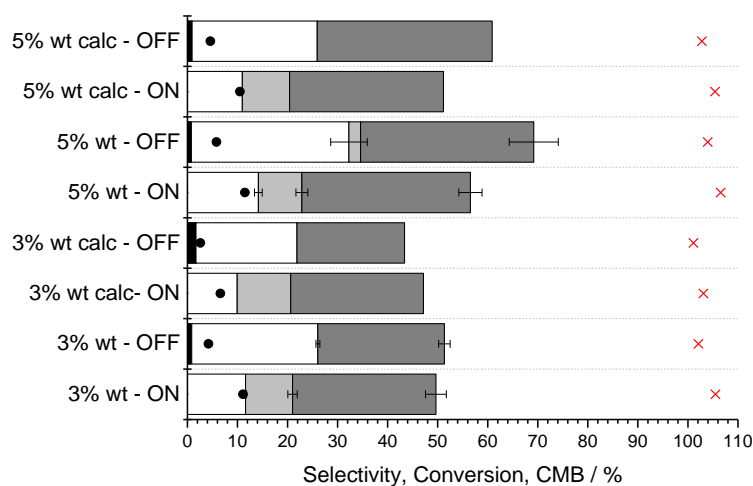
Figure 5.10 - Calcination effect on the 3% and 5% wt Au/TiO_2–PVA catalysts, compared to the dried counterparts. *Testing conditions*: 5 mL glycerol 0.05 M, 5 mg catalyst, 90 °C, Gly/Au = 330 and 200 respectively, 3 hours. *Legend*:● glycerol conversion ■ pyruvic acid (PA) □ glyceric acid (GA) ▨ glycolic acid (GLYA) ▨ dihydroxyacetone (DHA) x Carbon Mass Balance (CMB); missing material to be assigned to CO_2

As displayed in Figure 5.10, the heat treatment did not result in an improvement in the performance of the catalysts with respect to the dried counterparts. In the case of the 3% wt catalyst the performance was diminished, with conversion values almost half of the original under both conditions. For the 5% wt sample, performances were similar to the dried counterpart.

The changes in the catalytic behaviour are understandable if it is considered the consequence of heat treatments to remove polymers can be nanoparticle growth, as shown in the size distribution derived from TEM micrographies (Figure 5.11). Calcination, as expected, increases the mean nanoparticles size for both the samples (6.5 nm and 6.7 nm for the 3% wt and 5% wt respectively, *versus* 2.7 nm and 2.9 nm measured for the dried counterparts, Figure 5.5) and broadens the size distribution.
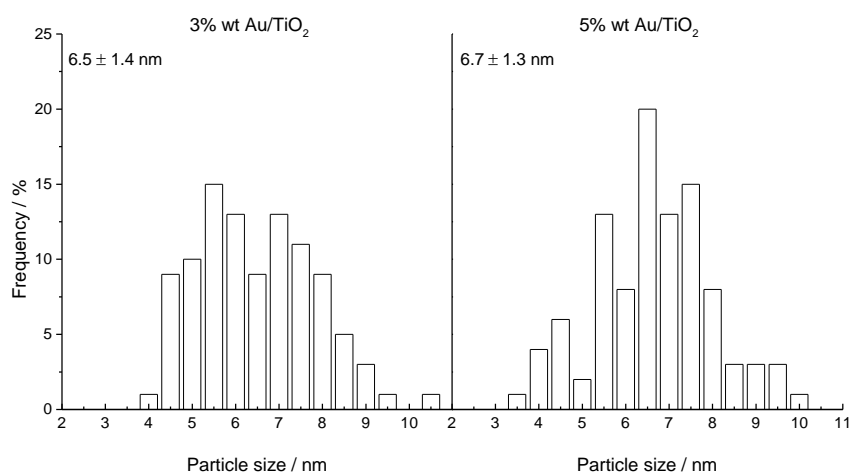
Figure 5.11 - Particle size distribution of the calcined 3% wt and 5% wt Au/TiO$_2$–PVA catalysts derived from counting 100 nanoparticles from TEM images

Assuming a total polymer removal from the catalyst surface, it can be speculated from these results that the PVA seems not to have a significant effect on the catalytic activity, e.g. by blocking the access to active sites and driving the selectivity, since the oxidation reaction leaded to a product distribution similar to the one obtained using the dried counterparts. This conclusion however cannot be completely verified since the effect of calcination and the consequent alteration of the nanoparticle/support interface must be taken into account. Indeed, as demonstrated by Majima and co-workers [59], the reduction and oxidation reactions induced by the

LSPR occur on TiO_2 surface in proximity (few tens of nm) of gold nanoparticles, indicating that the interface nanoparticle/support plays a fundamental role in the catalytic response.

5.2.3 Investigation of a representative sample: 3% wt Au/TiO₂-PVA

The following paragraphs are focused on a series of different experiments carried out using the 3% wt Au/TiO_2 catalyst in order to investigate how the plasmonic response is affected by the conditions (i.e., wavelength, illumination time, support, stabilising agent).

5.2.3.1 Testing under illumination at different wavelengths

The 3% wt Au/TiO_2-PVA catalyst was selected to further investigate the catalytic response under illumination. The sample was tested under illumination at different wavelengths by including cut off filters, in order to prove the effective dependence of the catalytic activity on the LSPR effect. Different wavelengths were selected by using filters, as displayed in Figure 5.12. The figure reports the position of the cut-off filter wavelengths compared to the position of the plasmon resonance peak of the 3% wt Au/TiO_2 catalyst and bare TiO_2. As the filtered light approaches the resonance wavelength (in this case around 550 nm), this should affect the catalytic activity of the illuminated sample, since the LSPR cannot occur in an efficient way (or not happen at all) [11, 22, 23, 45, 60, 61].
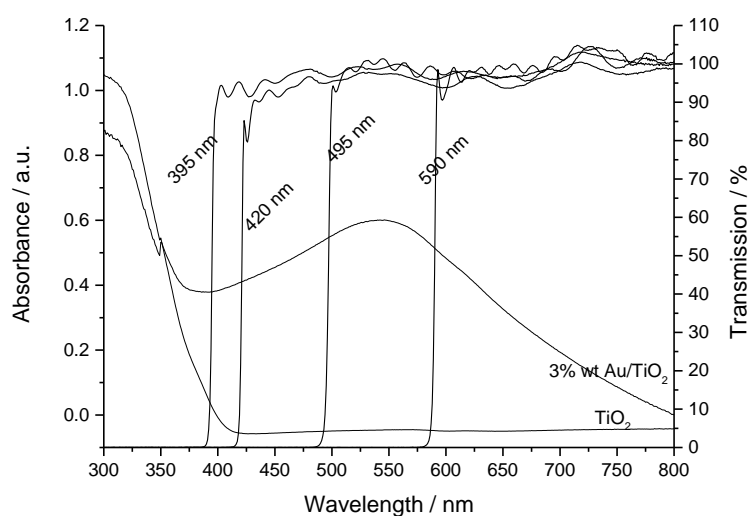
Figure 5.12 - Cut-off filters wavelengths position with respect to 3% wt Au/TiO_2 and bare TiO_2 spectra

Therefore, it is expected to observe a decrease in the catalytic activity by using the 495 nm and 590 nm cut off filters, with conversion values more similar to those obtained under dark conditions. The catalytic response for these experiments are displayed in Figure 5.13. The figure displays the conversion and selectivity values obtained for the reactions carried out using different illumination conditions, as described earlier. A test using full spectrum illumination, where no cut-off filters were used apart from the IR, was also performed in order to see the effect of shorter wavelengths (UV), which are expected to excite the TiO_2 [31, 32, 36, 62]: the catalyst under this condition showed a full glycerol conversion (mineralisation) to CO_2, due to over-oxidation [31, 35, 63-69].
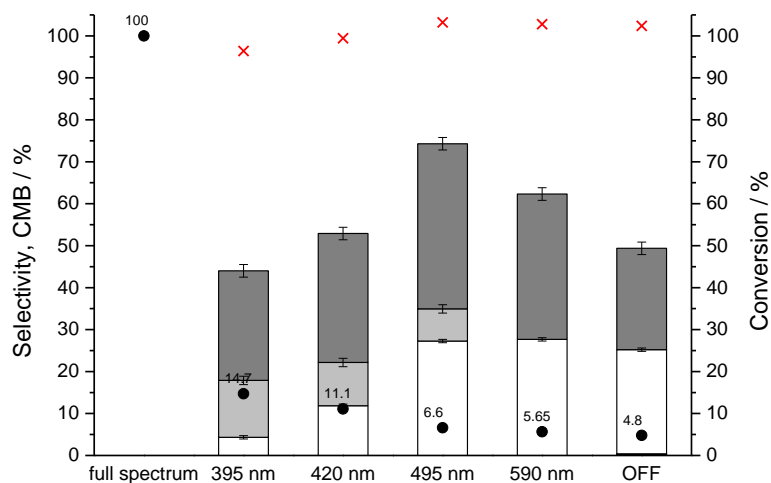
Figure 5.13 - 3% wt Au/TiO₂ tested under different wavelength irradiation. *Testing conditions*: 5 mL glycerol 0.05 M, 5 mg catalyst, 90 °C, Gly/Au = 330, 3 hours. *Legend*:● glycerol conversion ■ pyruvic acid (PA) □ glyceric acid (GA) ▨ glycolic acid (GLYA) ■ dihydroxyacetone (DHA) x Carbon Mass Balance (CMB); missing material to be assigned to CO_2

When the 395, 420, 495 and 590 nm wavelength cut-off filters were used, the catalytic activity decreased with the increase in the wavelengths cut-off, according with what expected with the cut off filters position relative to the plasmon absorption from Figure 5.12. When the catalyst was illuminated with a radiation of wavelengths higher than 395 nm, it showed the highest conversion, since these frequencies are able to excite a little also the TiO_2 [62] (see Figure 5.12). Conversely, when the sample was irradiated with wavelengths higher than 420, 495 and 590 nm, the catalytic activity decreased, until reaching conversion values very similar to the ones obtained under dark conditions when the 590 nm filter was used (wavelengths out of the range of the

plasmon resonance). These experiments confirmed that the catalytic activity under illumination is driven by the excitement of the plasmon rather than a thermal mechanism.

5.2.3.2 Time on line

The 3% wt Au/TiO_2 – PVA catalyst was also tested for a time-on-line study under illumination, in order to observe the catalytic response as a function of time. Direct sampling was not possible due to the batch system used, therefore multiple experiments were run and stopped at selected times (after 45, 90, 120, 180 and 300 minutes). The results are reported in Figure 5.14. As expected, the conversion increases linearly with time of illumination, reaching 20% after 5 hours. Higher conversion values correspond to lower CMB, in accordance with an increased C-C cleavage proportional to the time of illumination. The products detected were GA and DHA throughout all the analysed exposure times, whereas GLYA was not detected at low conversion (< 5%), as observed in previous testing. In a similar experiment carried out during 24 h, Dodekatos *et al.*[21] noticed that the higher production of CO_2 due to over-oxidation observed at a long reaction times makes the batch reactor not suitable for long run experiments.
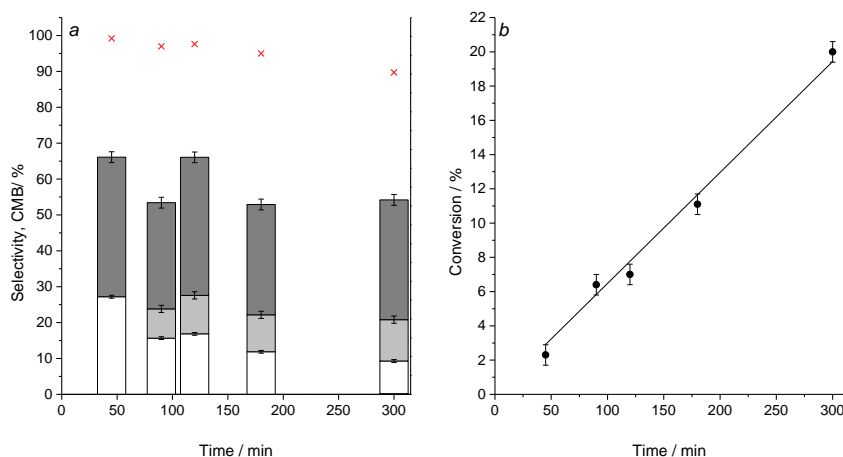
Figure 5.14 – Selectivity % (*a*) and Conversion % (*b*) plots for time on line testing on 3% wt Au/TiO_2 under illumination. *Testing conditions*: 5 mL glycerol 0.05 M, 5 mg catalyst, 90 °C, Gly/Au = 330. *Legend*: ● glycerol conversion ■ pyruvic acid (PA) □ glyceric acid (GA) ▨ glycolic acid (GLYA) ▧ dihydroxyacetone (DHA) X Carbon Mass Balance (CMB); missing material to be assigned to CO_2

5.2.3.3   Different support materials

In order to study the effect of the support, a 3% wt Au/CeO_2 catalyst was prepared by impregnation-reduction method as described in Chapter 2 and tested for plasmonic glycerol oxidation under the same conditions of the TiO_2-supported materials. Cerium (IV) oxide was selected as a support since previous studies of plasmonic nanoparticles supported on it showed very promising results for reduction [22, 23] and oxidation [19, 20] reactions. As well as the TiO_2, also the CeO_2 is a semiconductor with a band gap of 3.2 eV, and presents similar advantages in terms of stability, non-toxicity, low-cost [70, 71]. Moreover, due to its redox nature (Ce^{4+}/Ce^{3+}), may support the charge carrier transfer to the catalyst surface and give rise to oxygen vacancies [72, 73] that can prolong the charge carriers lifetime, making this oxide very interesting for photocatalytic applications [71, 74-77].

Similarly to the catalyst prepared by sol-immobilisation, also the 3% wt Au/CeO_2 sample showed a plasmonic peak at about 540 nm, as displayed in the UV-Vis spectrum in Figure 5.15, indicating the presence of gold nanoparticles [78, 79]. The real metal loading, determined by ICP analysis on the solution after catalyst digestion in aqua regia, was 2.56 % wt, indicating that a complete gold deposition was not achieved.
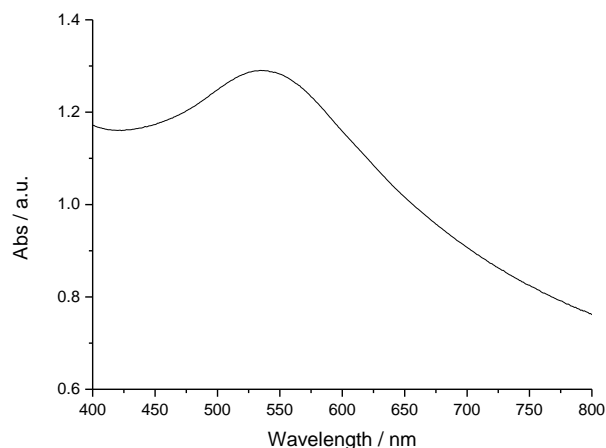
Figure 5.15 - UV-Vis diffuse reflectance spectra for the 3% wt Au/CeO_2 sample

The catalyst was tested for glycerol oxidation under the same conditions earlier reported. The results, compared with the results obtained using the 3% wt Au/TiO_2 – PVA catalyst, are displayed in Figure 5.16. Conversion values were very similar for both the catalysts under illumination and dark conditions, but the

selectivity to $\geq C_2$ products was significantly lower for the CeO_2-supported catalyst, with CO_2 being the major product. Moreover, no glyceric acid was detected and oxalic acid was produced instead of pyruvic acid, indicating a different or a faster oxidation mechanism on the CeO_2 surface. Kominami *et al.* [78,79] showed that 1% wt Au/CeO_2 catalyst was very effective in the photocatalytic stoichiometric mineralisation of organic compounds such as acetic, oxalic and formic acid under illumination ($\lambda \geq 520$ nm). They found that unsupported Au nanoparticles do not show any photocatalytic activity under the same conditions, leading to the conclusion that the support plays a fundamental role. Basing on Kowalska *et al.* studies [43], they proposed that its activity depends on the ease of injection of the photogenerated electrons into the conduction band of the support. However, in contrast with these findings, the 3% wt Au/CeO_2 catalyst was found to be slightly active also under dark conditions. This might be due to the higher gold loading respect to the samples reported in the literature.
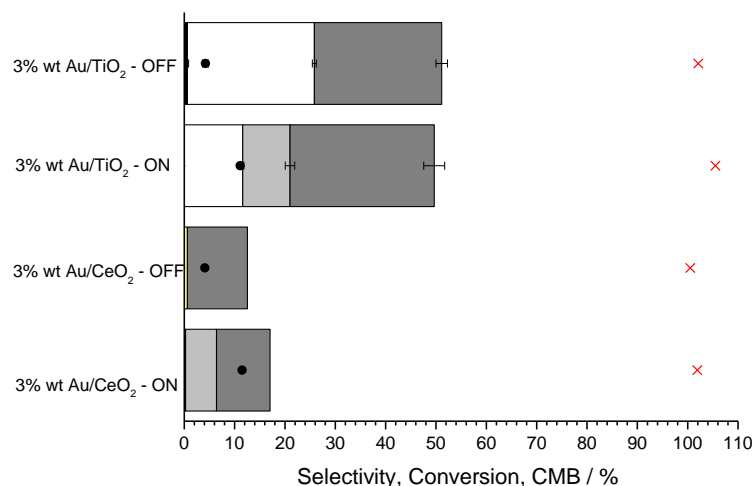
Figure 5.16 – Comparison of the catalytic activity of the 3% wt Au/TiO_2 and 3% wt Au/CeO_2 under dark and illumination conditions. *Testing conditions*: 5 mL glycerol 0.05 M, 5 mg catalyst, 90 °C, Gly/Au = 330, 3 hours. *Legend*: ● glycerol conversion ■ pyruvic acid (PA) ■ oxalic acid (OXA) □ glyceric acid (GA) ■ glycolic acid (GLYA) ■ dihydroxyacetone (DHA) x Carbon Mass Balance (CMB); missing material to be assigned to CO_2

In order to prove that the catalytic activity is plasmonic-dependent, the catalyst was tested under irradiation conditions at higher wavelengths (> 590 nm, Figure 5.17) in an experiment similar to the one carried out using the TiO_2-supported catalyst. Once again, the results obtained using light of wavelengths higher than the

resonance wavelength are comparable to the results obtained in the dark (Figure 5.16), confirming the plasmonic dependency of the catalytic activity and also demonstrating that the nature of the support is still important in determining the reaction pathways.
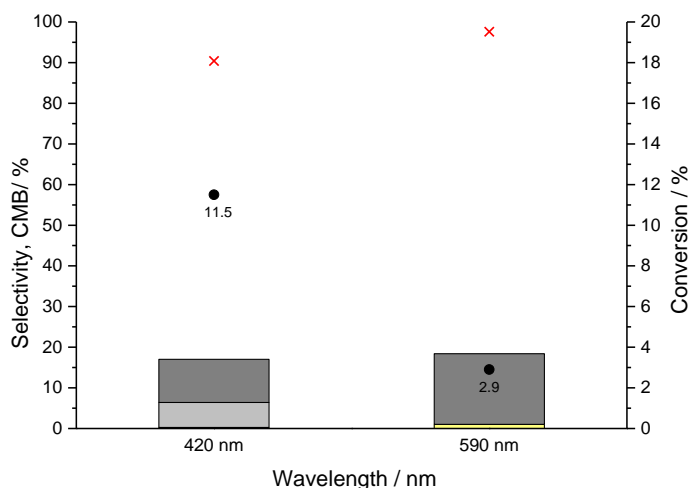
Figure 5.17 – Plasmonic response of 3% wt Au/CeO_2 under different illumination wavelengths during glycerol oxidation experiment. *Testing conditions*: 5 mL glycerol 0.05 M, 5 mg catalyst, 90 °C, Gly/Au = 330, 3 hours. *Legend*: ● glycerol conversion ■ pyruvic acid (PA) ■ oxalic acid (OXA) ■ glycolic acid (GLYA) ■ dihydroxyacetone (DHA) X Carbon Mass Balance (CMB); missing material to be assigned to CO_2

5.2.3.4 Investigating the role of the stabiliser

Since a large part of the presented thesis work was focused in the synthesis and characterisation of supported-nanoparticle catalysts prepared by sol-immobilisation, the natural step was to investigate the properties of similar catalysts prepared *via* sol-immobilisation using either a different stabilising agent or no stabiliser at all.

5.2.3.4.1 Different stabilising agent - PVP

A 3% wt Au/TiO_2 catalyst (nominal weight) was synthesized by sol-immobilisation using PVP as stabilising polymer. The aim was to observe any difference in the catalytic response of the catalyst when compared to the analogue synthesized by PVA addition. Figure 5.18 shows the results for the 3% wt Au/TiO_2 – PVP catalyst tested under illumination and dark conditions compared with the analogue synthesized by PVA.

The product selectivity is similar to the one obtained with the analogue prepared by PVA, with GA, GLYA and DHA being the main products. However, the sample differs from these in terms of conversion: indeed, it appears to be much lower even under illumination conditions. This can be explained taking into account the difference in the polymer stabilisers: the polymer presence might be detrimental for the photocatalytic activity [57, 80], and the PVP is known to bind more strongly to the nanoparticles surface, which might lead to a decrease in the activity by interfering with the plasmonic resonance [81]. For this reason, the catalyst was calcined at 500 °C for 3 hours in static air to burn the polymer off. The calcination conditions should be sufficient to achieve a complete polymer removal from the surface, as observed from TGA analysis carried out on a 1% wt Au/TiO$_2$-PVP catalyst displayed in Figure 3.19, Chapter 3.
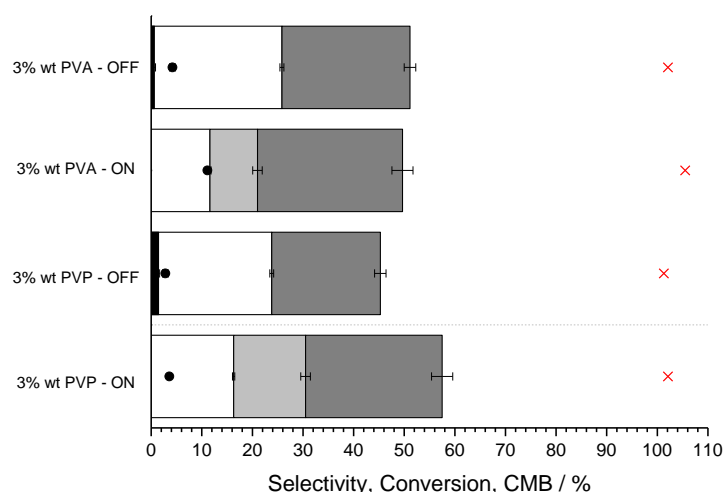
Figure 5.18 – Catalytic test on 3% wt Au/TiO$_2$-PVA and PVP. *Testing conditions*: 5 mL glycerol 0.05 M, 5 mg catalyst, 90 °C, Gly/Au=330, 3 hours. *Legend*:● glycerol conversion ■ pyruvic acid (PA) □ glyceric acid (GA) ■ glycolic acid (GLYA) ■ dihydroxyacetone (DHA) x Carbon Mass Balance (CMB); missing material to be assigned to CO$_2$

The catalytic results of the calcined sample are displayed in Figure 5.19: calcination improved the activity of the catalyst both under dark and illumination conditions. The higher enhancement observed when the sample was illuminated suggests that the polymer presence has a heavier influence on the plasmonic effects rather than on the mechanisms that control the "thermal" process: indeed, the results are quite similar under dark conditions, although the influence of the size and of the nanoparticle/support interface in this case cannot be

excluded (Figure 5.20). Interestingly, calcination of the analogue catalyst prepared by PVA did not show the same improvement in the catalytic response (Figure 5.10). This further confirms the influence of polymer strongly depends on its nature. In the case of PVP, it seems clear that its removal by calcination has a beneficial effect on the catalytic activity. Therefore, when selecting synthesis methodologies for catalytic applications, and in particular when working with sol-immobilised catalysts, it is important considering the nature of the stabilising agent. If removal is needed, it is important to carefully select and optimise the calcination conditions in order to find the best compromise between polymer removal and size increase, in order to achieve the best results.
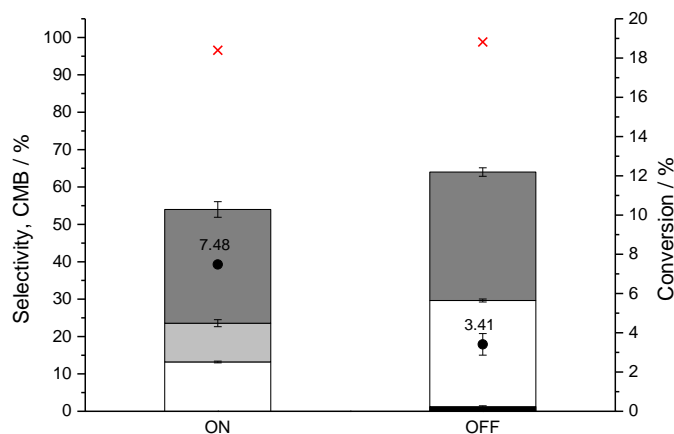
Figure 5.19 – Catalytic testing on 3% wt Au/TiO$_2$ -PVP calcined at 500 ^{o}C. *Testing conditions*: 5 mL glycerol 0.05 M, 5 mg catalyst, 90 ^{o}C, Gly/Au=330, 3 hours. *Legend*:● glycerol conversion ■ pyruvic acid (PA) □ glyceric acid (GA) ▨ glycolic acid (GLYA) ▨ dihydroxyacetone (DHA) x Carbon Mass Balance (CMB); missing material to be assigned to CO$_2$

Figure 5.20 – Particle size distribution of the 3% wt Au/TiO$_2$ – PVP catalyst dried and calcined derived from counting 100 nanoparticles

5.2.3.4.2 Stabiliser-free catalysts

An analogous series of catalysts (nominal 1, 3, 5, 7 % wt Au/TiO$_2$) prepared stabiliser-free were also tested in the same conditions as the PVA series. The aim was to see if and how the stabiliser absence influences the catalytic performance, i.e. by improving the catalytic activity and/or promoting a different product distribution, in a comparative study similar to the one presented in Chapter 4 for glycerol oxidation in basic conditions. Surprisingly, all the dried catalysts prepared by the stabiliser-free method were totally inactive in their dried only version, excepted the 7% wt, that showed a little activity under illumination conditions, as displayed in Figure 5.21.
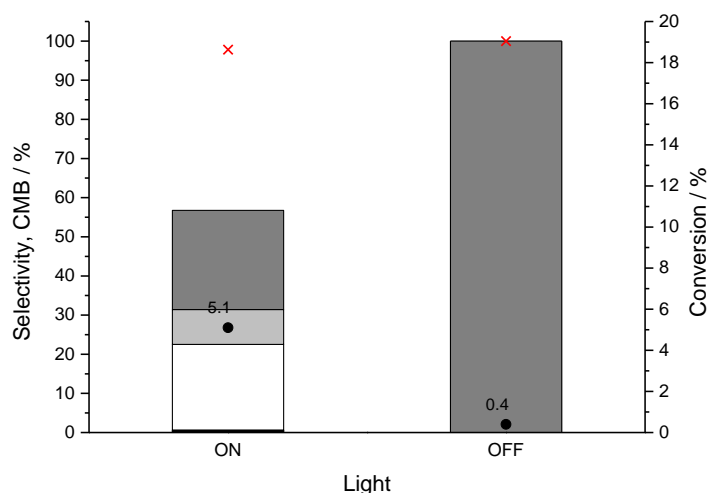
Figure 5.21 – Catalytic testing on 7% wt Au/TiO$_2$-SF. *Testing conditions*: 5 mL glycerol 0.05 M, 5 mg catalyst, 90 °C, Gly/Au=140, 3 hours. *Legend*: ● glycerol conversion ■ pyruvic acid (PA) □ glyceric acid (GA) ▨ glycolic acid (GLYA) ■ dihydroxyacetone (DHA) x Carbon Mass Balance (CMB); missing material to be assigned to CO$_2$

When comparing these results with the previous obtained with the analogous catalyst prepared by PVA (Figure 5.6), it is interesting to notice how the absence of the stabiliser leads to a less active catalyst under dark conditions, but when illuminated, its activity is switched on. This seems to suggest a pure dependence of the catalytic activity on the plasmonic resonance. For all the catalysts in the series, the real gold amount was determined by ICP after sample digestion in aqua regia, and the results are reported in Table 5.2. The analysis was necessary in order to make sure that the SF catalysts were comparable to the PVA counterparts in terms of metal loading, and more importantly, that their activity was not related to an unsuccessful metal deposition.

As displayed in Table 5.2, it was not possible achieving a complete metal deposition, but the series is fully comparable to the analogue synthesized by PVA (Table 5.1), showing very similar metal loadings. This further suggests that the absence of the stabiliser does not affect the metal deposition on the support, according with previous findings presented in Chapters 3 and 4.

Table 5.2 - Real metal amount determined by ICP for the 1-7% wt Au/TiO_2-SF series.

Metal amount (wt %) determined by ICP		
Catalyst	Au nominal wt%	Au Real wt%
	1	0.99
	3	2.81
Au/TiO₂-SF	5	4.44
	7	5.83

Diffuse reflectance UV-Vis analysis carried out on the 1-5% wt Au/TiO_2–SF catalysts displayed in Figure 5.22 showed that all the samples present an absorption band corresponding to the plasmonic resonance, with values increasing with metal loading. The shape and position of the plasmonic resonance peaks are different for the three catalysts, with broader profile for the 3% and 5% wt samples and a red shift of the associated wavelengths. Also, both the signals of the 3% and 5% wt catalysts show a shoulder at higher wavelengths (more evident for the 5% wt sample) which might indicate a non-uniform resonance frequency, correspondent to a non-uniform particle size distribution [22,51,52,82]. It was previously shown (Chapter 4) that 1% wt Au/TiO_2 catalyst prepared *via* stabiliser-free sol-immobilisation method is active in the liquid phase oxidation of glycerol in basic conditions, despite the slightly larger nanoparticle size. Therefore, a similar catalytic behaviour should be expected also in this case.

TEM analysis carried out on the 1-7% wt Au/TiO_2-SF catalysts confirmed a broader size distribution and larger particle size at higher loadings, as shown in Figures 5.23 and 5.24. As displayed in the representative micrographs of the 1-7% wt catalysts, increasing the metal amount during the synthesis when no stabilising agent is added led to the formation of bigger nanoparticles of a different size range, which also resulted in a non-homogeneously dispersion onto the TiO_2 (Figure 5.23 b-d). Interestingly, looking at the size distribution

displayed in Figure 5.24, the 7% wt catalyst still showed a broad nanoparticle size distribution, but with a lower mean size. This might partially explain the weak activity observed for this sample (Figure 5.21).
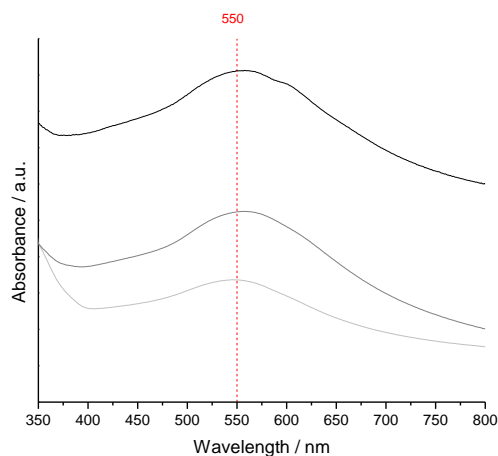
Figure 5.22 - UV-Vis diffuse reflectance spectra for the Au/TiO$_2$–SF samples different Au loading (wt %).

Legend: ▬1% ▬ 3% ▬ 5%
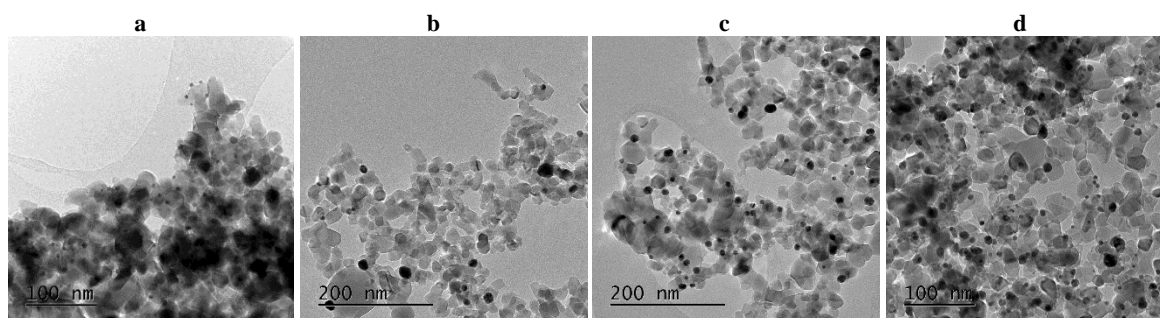
Figure 5.23 - Representative TEM images for the 1% wt Au/TiO$_2$–SF series: (a) 1% wt (b) 3% wt (c) 5% wt (d) 7% wt
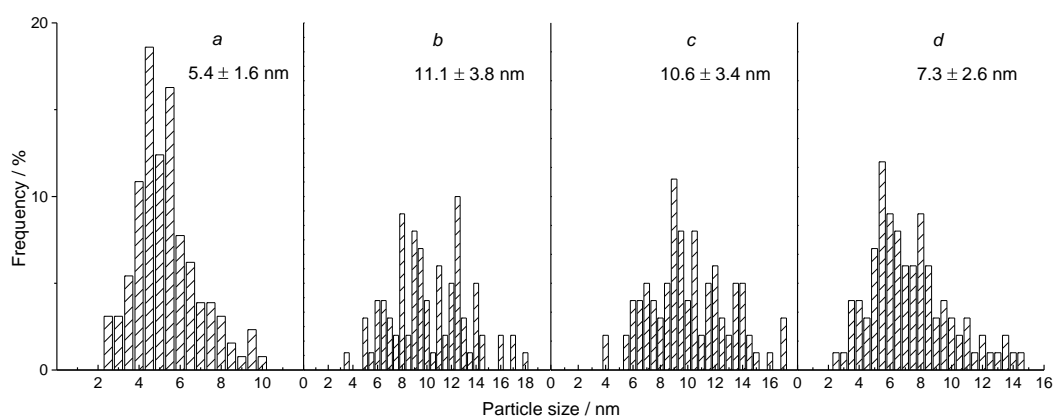
Figure 5.24 - Nanoparticle size distribution for the 1, 3, 5, 7% wt (*a, b, c, d* respectively) Au/TiO$_2$–SF catalysts derived from TEM images

The calcination effect on the 3% and 5% wt catalysts was also investigated in order to compare the performances with the analogues obtained for the catalysts synthesized by PVA (Figure 5.10). As in the PVA case, the 3% and 5% wt samples were calcined at 500 °C in static air for 3 hours and tested under the usual conditions. The results are displayed in Figure 5.25. Surprisingly, calcined samples were more active than the dried counterparts, conversely to what was observed in the PVA case. Calcination, as expected, increased the nanoparticles size, as displayed in in Figure 5.26. From these findings, it can be concluded that the catalytic activity for the stabiliser-free samples, despite their larger particle size and size distribution, can be enhanced by calcination. The effect of the calcination in this case might result in a modification of the support/nanoparticle interface [59] which is beneficial for the catalytic response under these reaction conditions.

Taking into account the negligible difference in the nanoparticles size between the dried and calcined samples (Figure 5.24 and Figure 5.26), and that the plasmonic effect is expected to be more effective for bigger nanoparticles (generation of more intense plasmonic response) [17, 83], it can be concluded that the nanoparticle size, although crucial, cannot be the main factor determining the catalytic activity.
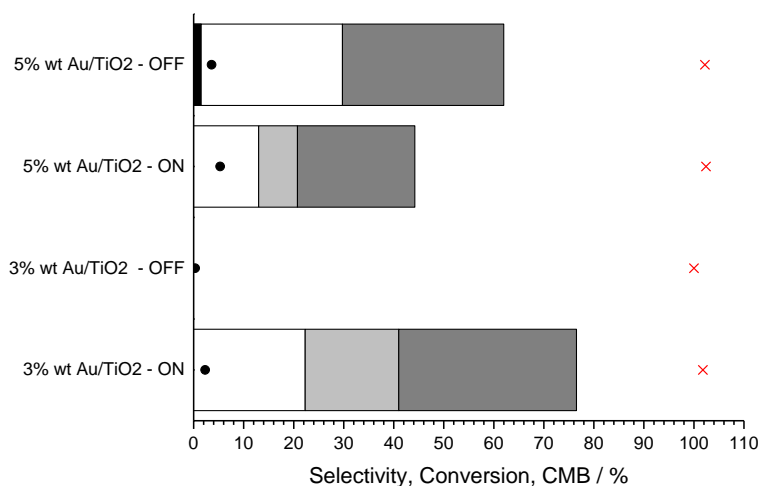
Figure 5.25 - Calcination effect on the activity of the 3% wt and 5% wt Au/TiO$_2$–SF catalysts. *Testing conditions*: 5 mL glycerol 0.05 M, 5 mg catalyst, 90 °C, Gly/Au = 330 and 200, 3 hours. *Legend*:● glycerol conversion ■ pyruvic acid (PA) □ glyceric acid (GA) ■ glycolic acid (GLYA) ■ dihydroxyacetone (DHA) x Carbon Mass Balance (CMB); missing material to be assigned to CO$_2$
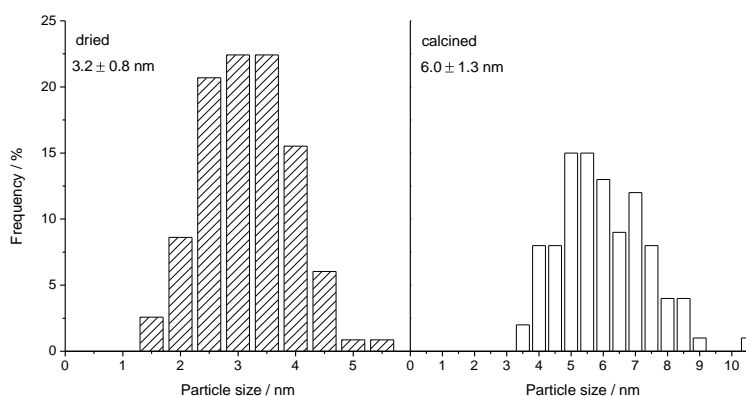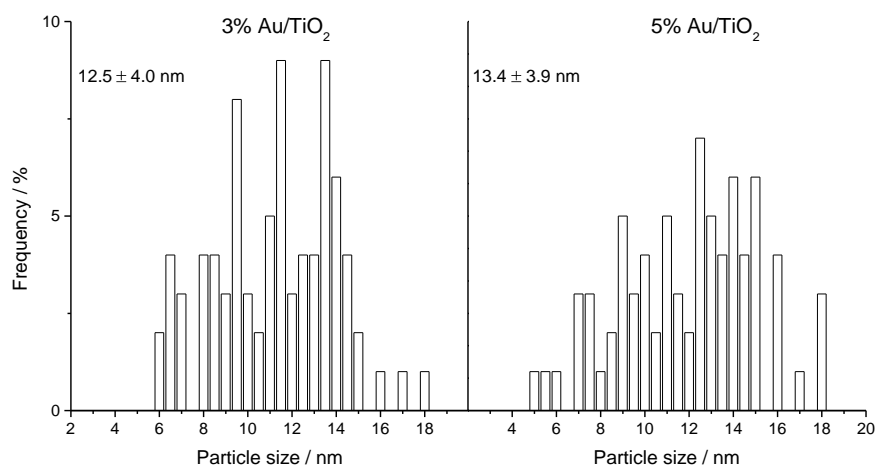
Figure 5.26 - Nanoparticle size distribution for the 3 and 5% wt Au/TiO$_2$ – SF catalysts calcined at 500 °C

In summary, the stabiliser-free catalysts showed a plasmonic response that could catalyse the oxidation of glycerol. The absence of the stabiliser is therefore not crucial for obtaining active catalysts, according to the results presented in Chapters 3 and 4. Nonetheless, in this case, given the higher nanoparticle size and broader size distribution, additional heat treatment was required for obtaining active catalysts, likely because its influence on the nanoparticle/support interface. Therefore, when working with stabiliser-free materials it would be important to balance the synergistic effect of all the parameters that influence the catalytic performances, i.e., nanoparticle size and interaction with the support.

5.2.4 A study on bimetallic catalysts

A series of bimetallic 1% wt AuPd/TiO$_2$ with different Au:Pd molar ratio, prepared by sol-immobilisation using PVA as stabilising agent were also tested for plasmonic glycerol oxidation. A complete description of the synthesis procedure is reported in Chapter 2.

Bimetallic AuPd catalysts were proven to be active for "thermal" glycerol oxidation under base-free conditions [84]. In Chapter 4, 1% wt AuPd/TiO$_2$ catalysts (Au:Pd = 1:1 mol) were successfully employed for the oxidation of glycerol in basic conditions. For the plasmonic glycerol oxidation experiment, the catalysts were prepared both Pd rich and Au rich, in order to study the influence of the Pd on the plasmonic response, in a

similar approach to the one reported by Sarina *et al.*[11, 12]. The two metals are well known to be miscible in a wide range of compositions, forming AuPd alloy nanoparticles [85-87]. Table 5.3 reports the catalyst series ordered in increasing Au content and with the correspondent molar fraction determined from the nominal content (moles) and the real, determined by ICP analysis.

It is known that the presence of Pd suppresses the gold plasmon [88], yet the catalysts absorb in the visible region, as displayed in Figure 5.27. Of all the samples, only the Au9Pd1 catalyst showed a clear plasmonic peak at about 550 nm, as expected from its higher gold loading. This effect might be due to the formation of gold-rich nanoparticles, already observed in AuPd alloys [89, 90].

TEM analysis performed on selected samples and displayed in Figure 5.28 did not reveal any structural difference in dependence of the Au/Pd ratio. The nanoparticles appear to be generally spherical and well dispersed on the support. The size distribution derived from counting 100 nanoparticles showed similar dimensions included between 2.6 and 3.3 nm, suggesting that the metal ratio is not an issue for the morphology. Nonetheless, the technique did not allow to determine any difference in the nanoparticle composition.

Table 5.3 – 1% wt AuPd/TiO$_2$ series prepared *via* sol-immobilisation method with PVA

	Catalyst	Theoretical χ Au/(Au+Pd)	Real χ Au/(Au+Pd)[*]
Au<Pd	**Au1Pd9**	0.10	0.17
	Au1Pd4	0.20	0.21
	Au1Pd3	0.25	0.29
	Au1Pd2	0.33	0.38
	Au1Pd1	0.50	0.44
Au>Pd	**Au1.5Pd1**	0.60	0.49
	Au2Pd1	0.67	0.56
	Au3Pd1	0.75	0.66
	Au5Pd1	0.83	0.76
	Au9Pd1	0.90	0.90

[*] as determined by ICP analysis on the digested catalyst
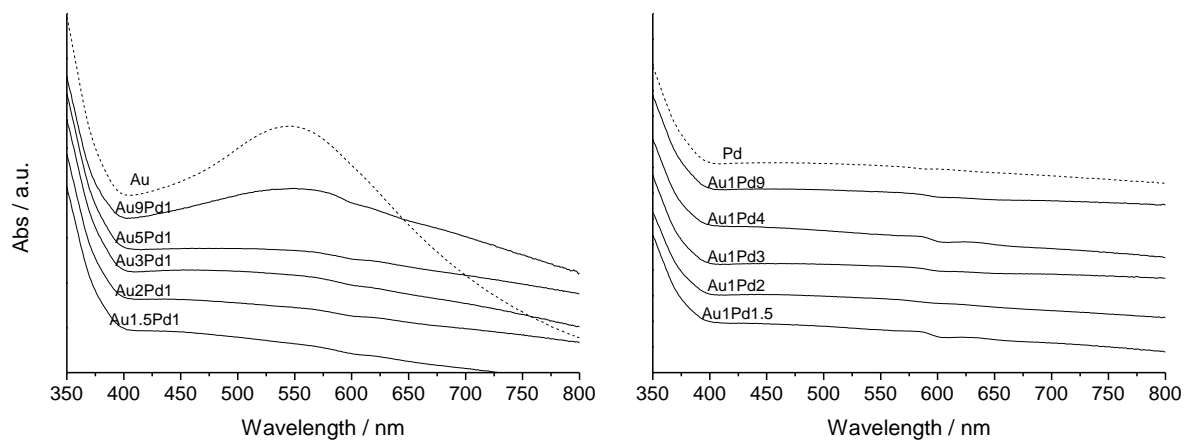
Figure 5.27 - Diffuse Reflectance UV-Vis of 1% wt AuPd/TiO$_2$ catalysts Au rich and Pd rich, compared with the spectra of pure 1% wt Au/TiO$_2$ and 1% wt Pd/TiO$_2$.
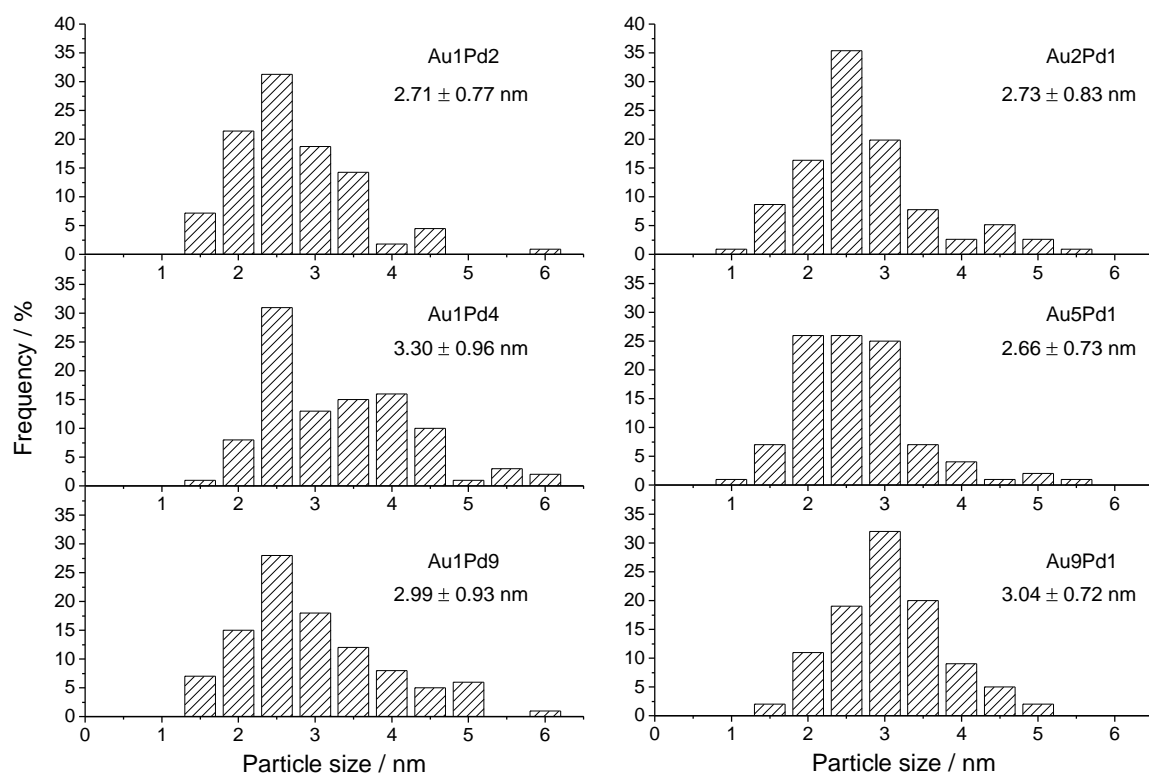
Figure 5.28 – Particle size distribution for 1% wt AuPd/TiO$_2$ selected catalysts

Sarina *et al.*[11, 12] studied the performance of bimetallic 3% wt AuPd catalysts supported on ZrO_2 for a wide series of plasmonic enhanced reactions including Suzuki-Myiaura coupling, benzyl alcohol oxidation, dehydrogenation of organic alcohols. They proposed that the origin of the activity of the bimetallic catalysts is related to the formation of the alloy and to its electronic heterogeneity [91], meaning the electrons can flow across the Au and Pd interface until the electron chemical potential equalizes throughout the alloy nanoparticle [11]. Since the nanoparticles are able to absorb in the visible, when illuminated, the additional energised electrons are also transported, enhancing the catalytic activity [11, 12].

Figure 5.29 reports the results in terms of conversion under illumination and dark conditions *versus* the gold molar fraction for the 1% wt $AuPd/TiO_2$ series. In principle, it is possible to observe two different trends for the catalysts, depending on the gold and palladium content. The trend changes around the region Au1Pd1, in a sort of volcano-shape plot previously reported in the literature [86, 92] for similar catalysts. The Pd-rich catalysts, as expected [90, 93, 94], are more active also under dark conditions, reaching 10% conversion, but they do not show a great enhancement in the activity when illuminated. It is interesting to notice how the Pd presence seems to be beneficial to the catalytic activity only at certain amount (i.e, Au1Pd2).

Conversely, the gold-rich catalysts were less active under dark conditions, but when illuminated they showed a higher conversion enhancement, likely due to the higher gold content. This behaviour is more similar to the one already observed for the pure 1% wt Au/TiO_2 presented in the previous section.
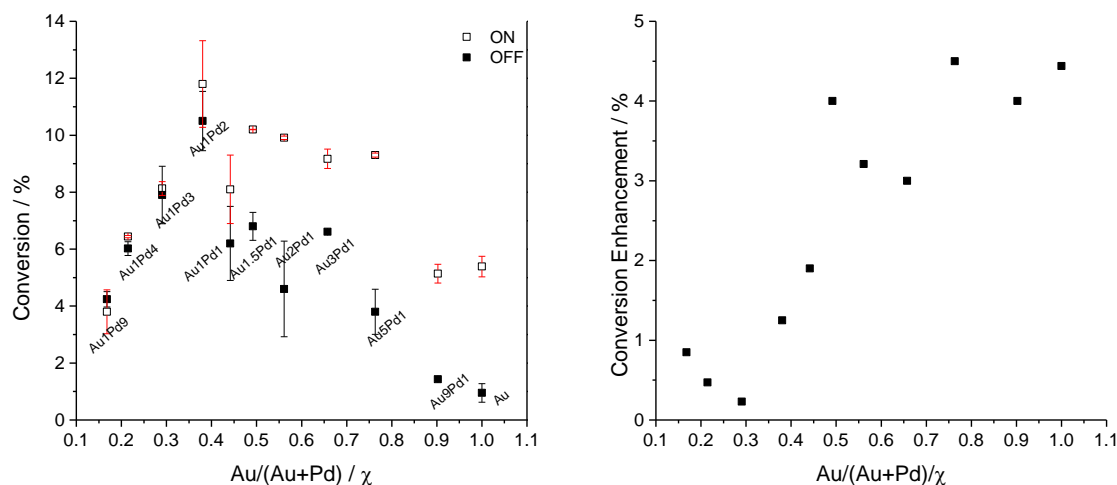
Figure 5.29 - Catalytic performance of $AuPd/TiO_2$ series under dark and illumination conditions

Since AuPd nanoparticles were previously shown to be more active than Au in the synthesis of H_2O_2 [92, 95, 96], the low CMB observed for these reactions (Figure 5.30) should be ascribed to its formation under the reaction conditions. However, Ketchie *et al.* [97] reported that glycerol oxidation in basic conditions using AuPd/C catalysts resulted in an enhanced selectivity towards $\geq C_2$ products, meaning that the Pd presence reduces the production of H_2O_2 respect to the monometallic Au catalysts. In this case, it is possible that both the neutral reaction conditions and the support play a fundamental role in determining the production of H_2O_2.

Figure 5.30 also displays the selectivity to major products. Small amounts of tartronic acid and glyceraldehyde (not shown) were qualitatively detected for all the catalysts, indicating a different oxidation mechanism when Pd is present, respect to monometallic Au catalysts.
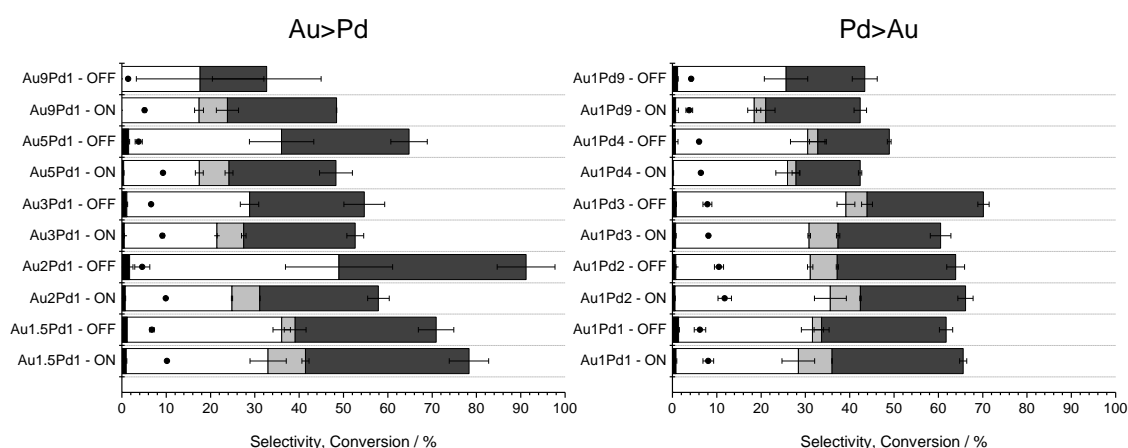
Figure 5.30 – Conversion and selectivity values for the AuPd series under dark and illumination conditions. *Testing conditions*: 5 mL glycerol 0.05 M, 5 mg catalyst, 90 °C, 3 hours. *Legend*: ● glycerol ■ pyruvic acid (PA) □ glyceric acid (GA) ■ glycolic acid (GLYA) ■ dihydroxyacetone (DHA); missing material to be assigned to CO_2

Taking into consideration the experimental errors, bigger at lower conversion values, once again is possible to observe as a general trend that there is higher selectivity to products $\geq C_2$ under dark conditions, even though the difference is not as marked as in the monometallic case. This is in accordance with the aforementioned H_2O_2 enhanced production when Pd is present.

It seems that at higher Au loadings (Au>1.5, Figure 5.30) under dark conditions, the formation of glycolic acid is not favoured. This is in accordance with previous experimental observations on the monometallic 1% wt Au/TiO$_2$ catalyst (Figure 5.6). As previously discussed, this should be related to a different reaction mechanism

under illumination conditions, related to an enhanced H_2O_2 production. Conversely, when the Pd-rich catalysts were used, glycolic acid was present under both conditions for all the catalysts excluding the Au1Pd9 and the AuPd1.5, for undetermined reasons.

Nonetheless, the existence of a different mechanism under illumination also for these samples seems to be confirmed by the different selectivity values at *iso-conversion*: for example, comparing the selectivity of the Au1Pd4 and Au1Pd3 catalysts under dark and illumination, the lower selectivity to GA and to $\geq C_2$ products for the catalysts under illumination indicates a different reaction mechanism in a similar way of what previously observed for monometallic catalysts, which might be related to a higher production of H_2O_2 in a similar way of what observed for the monometallic catalyst.

In summary, it has been shown that plasmonic response can be expected and be effective also when using bimetallic catalysts. The influence of the Pd is remarkable in terms of conversion and selectivity when compared to monometallic catalysts, however its effect tends to predominate at higher Pd content (Pd>Au), resulting in the suppression of the LSPR effect. Conversely, when Au>Pd, the catalysts show higher sensitivity to illumination conditions, even though the conversion values are lower (Figure 5.29).

5.3 Conclusion

It has been shown for the first time that Au and AuPd sol-immobilised nanoparticles can be effective catalysts for the oxidation of glycerol under neutral and plasmonic conditions. In general, an enhancement in conversion was observed under illumination, and this was found to be influenced by several parameters.

In the monometallic case the effect was found to be dependent on the metal loading, as expected, and on the presence and nature of the stabilising agent; catalysts prepared without the stabiliser addition showed bigger nanoparticle size and a broader size distribution: calcination though was found to be effective for obtaining more active catalysts, perhaps due to the modification of the nanoparticle/surface interface. Calcination was also found to be effective to enhance the catalytic activity of the samples prepared using PVP as a stabilising agent, indicating that the choice of this latter has to be carefully selected in order to observe a satisfactory catalytic response. On the other hand, heat treatment on catalysts prepared by PVA did not show any improvement on these materials.

In the bimetallic case, the response of the catalysts under illumination conditions was found to be higher at higher Au loading, according to the expected plasmonic enhancement, and suggesting that the composition of the alloy plays a fundamental role in the photocatalytic response. Therefore, the optimisation of the catalyst should be addressed to find the best compromise between "thermal" activity and photocatalytic response.

It can be therefore concluded that the preparation method is not a limiting factor for obtaining active catalysts. However, in order to better understand the photocatalytic mechanism involved in such structures, would be required more investigation in order to clarify:

- the role of the stabilising agent and how it can affect the LSPR;

- the role of the support and in particular the importance of its interface with the nanoparticles;

- the role of the alloy and the effect of its composition.

Bibliography

1. P. Wang, B. Huang, Y. Dai and M. H. Whangbo, *Physical Chemistry Chemical Physics: PCCP*, **2012**, *14*, 9813-9825.

2. X. Zhang, Y. L. Chen, R. S. Liu and D. P. Tsai, *Reports on Progress in Physics. Physical Society*, **2013**, *76*, 046401 (41pp).

3. C. Clavero, *Nature Photonics*, **2014**, *8*, 95-103.

4. T. Huang and L. Qi, *Journal of Physical Chemistry C*, **2009**, *113*, 13636-13642.

5. J. Anker and R. Van Duyne, *Nature Materials*, **2008**, *7*, 442-453.

6. X. Huang, I. H. El-Sayed, W. Qian and M. A. El Sayed, *Journal of the American Chemical Society*, **2006**, *128*, 2115-2120.

7. X. Huang and M. A. El-Sayed, *Journal of Advanced Research*, **2010**, *1*, 13-28.

8. X. Zhang, X. Li, D. Zhang, N. Q. Su, W. Yang, H. O. Everitt and J. Liu, *Nature Communications*, **2017**, *8*, 14542.

9. X. Huang, Y. Li, Y. Chen, H. Zhou, X. Duan and Y. Huang, *Angewandte Chemie*, **2013**, *52*, 6063-6067.

10. R. He, Y. C. Wang, X. Wang, Z. Wang, G. Liu, W. Zhou, L. Wen, Q. Li, X. Wang, X. Chen, J. Zeng and J. G. Hou, *Nature Communications*, **2014**, *5*, 4327.

11. S. Sarina, H. Zhu, E. Jaatinen, Q. Xiao, H. Liu, J. Jia, C. Chen and J. Zhao, *Journal of the American Chemical Society*, **2013**, *135*, 5793-5801.

12. S. Sarina, S. Bai, Y. Huang, C. Chen, J. Jia, E. Jaatinen, G. A. Ayoko, Z. Bao and H. Zhu, *Green Chemistry*, **2014**, *16*, 331-341.

13. Q. Xiao, S. Sarina, E. R. Waclawik, J. Jia, J. Chang, J. D. Riches, H. Wu, Z. Zheng and H. Zhu, *ACS Catalysis*, **2016**, *6*, 1744-1753.

14. F. Wang, C. Li, H. Chen, R. Jiang, L. D. Sun, Q. Li, J. Wang, J. C. Yu and C. H. Yan, *Journal of the American Chemical Society*, **2013**, *135*, 5588-5601.

15. S. Schünemann, G. Dodekatos and H. Tüysüz, *Chemistry of Materials*, **2015**, *27*, 7743-7750.

16. H. Huang, L. Zhang, Z. Lv, R. Long, C. Zhang, Y. Lin, K. Wei, C. Wang, L. Chen, Z. Y. Li, Q. Zhang, Y. Luo and Y. Xiong, *Journal of the American Chemical Society*, **2016**, *138*, 6822-6828.

17. C. Wang and D. Astruc, *Chemical Society Reviews*, **2014**, *43*, 7188-7216.

18. S. Sarina, E. R. Waclawik and H. Zhu, *Green Chemistry*, **2013**, *15*, 1814-8133.

19. A. Tanaka, K. Hashimoto and H. Kominami, *Journal of the American Chemical Society*, **2012**, *134*, 14526-14533.

20.   D. Tsukamoto, Y. Shiraishi, Y. Sugano, S. Ichikawa, S. Tanaka and T. Hirai, *Journal of the American Chemical Society*, **2012**, *134*, 6309-6315.

21.   G. Dodekatos and H. Tüysüz, *Catalysis Science & Technology*, **2016**, *6*, 7307-7315.

22.   X. Ke, S. Sarina, J. Zhao, X. Zhang, J. Chang and H. Zhu, *Chemical Communications*, **2012**, *48*, 3509-3511.

23.   X. Ke, X. Zhang, J. Zhao, S. Sarina, J. Barry and H. Zhu, *Green Chemistry.*, **2013**, *15*, 236-244.

24.   P. Christopher, H. Xin and S. Linic, *Nature Chemistry*, **2011**, *3*, 467-472.

25.   K. Awazu and T. Watanabe, *Journal of the American Chemical Society*, **2008**, *130*, 1676-1680.

26.   Y. Sugano, Y. Shiraishi, D. Tsukamoto, Satoshi Ichikawa, S. Tanaka and T. Hirai, *Angewandte Chemie International Edition*, **2013**, *52*, 5295-5299.

27.   X. Guo, C. Hao, G. Jin, H. Y. Zhu and X. Y. Guo, *Angewandte Chemie*, **2014**, *53*, 1973-1977.

28.   S. Sarina, H. Y. Zhu, Q. Xiao, E. Jaatinen, J. Jia, Y. Huang, Z. Zheng and H. Wu, *Angewandte Chemie*, **2014**, *53*, 2935-2940.

29.   S. Linic, U. Aslam, C. Boerigter and M. Morabito, *Nature Materials*, **2015**, *14*, 567-576.

30.   S. J. Tan, M. J. Campolongo, D. Luo and W. Cheng, *Nature Nanotechnology*, **2011**, *6*, 268-276.

31.   A. Fujishima, T. N. Rao and D. Tryk, *Journal of Photochemistry and Photobiology C: Photochemistry Reviews*, **2000**, *1*, 1-21.

32.   A. Fujishima, X. Zhang and D. Tryk, *Surface Science Reports*, **2008**, *63*, 515-582.

33.   L. G. Devi and R. Kavitha, *Applied Catalysis B: Environmental*, **2013**, *140-141*, 559-587.

34.   L. Liu, S. Ouyang and J. Ye, *Angewandte Chemie*, **2013**, *52*, 6689-6693.

35.   M. Hoffmann and W. Bahnemann, *Chemical Reviews*, **1995**, *95*, 69-96.

36.   J. Schneider, M. Matsuoka, M. Takeuchi, J. Zhang, Y. Horiuchi, M. Anpo and D. W. Bahnemann, *Chemical Reviews*, **2014**, *114*, 9919-9986.

37.   B. N. Zope, D. D. Hibbitts, M. Neurock and R. J. Davis, *Science*, **2010**, *330*, 74-78.

38.   W. Ketchie, Y. Fang, M. Wong, M. Murayama and R. Davis, *Journal of Catalysis*, **2007**, *250*, 94-101.

39.   W. C. Ketchie, M. Murayama and R. J. Davis, *Topics in Catalysis*, **2007**, *44*, 307-317.

40.   M. Comotti, C. Della Pina, E. Falletta and M. Rossi, *Advanced Synthesis & Catalysis*, **2006**, *348*, 313-316.

41.   M. S. Ide and R. J. Davis, *Accounts of Chemical Research*, **2014**, *47*, 825-833.

42.   Y. Tian and T. Tatsuma, *Journal of the American Chemical Society*, **2005**, *127*, 7632-7637.

43.   E. Kowalska, O. O. Mahaney, R. Abe and B. Ohtani, *Physical Chemistry Chemical Physics: PCCP*, **2010**, *12*, 2344-2355.

44.   A. Furube, L. Du, K. Hara, R. Katoh and M. Tachiya, *Journal of the American Chemical Society*, **2007**, *129*, 14852-14853.

45. C. Gomes Silva, R. Juarez, T. Marino, R. Molinari and H. Garcia, *Physical Chemistry Chemical Physics: PCCP*, **2011**, *13*, 886-910.

46. H. Zhang, G. Chen and D. W. Bahnemann, *Journal of Materials Chemistry*, **2009**, *19*, 5089.

47. V. Subramanian and P. V. Kamat, *Journal of the American Chemical Society*, **2004**, *126*, 4943-4950.

48. V. Diesen and M. Jonsson, *The Journal of Physical Chemistry C*, **2014**, *118*, 10083-10087.

49. L. Prati, A. Villa, C. E. Chan-Thaw, R. Arrigo, D. Wang and D. S. Su, *Faraday Discussions*, **2011**, *152*, 353-365.

50. L. Prati, P. Spontoni and A. Gaiassi, *Topics in Catalysis*, **2009**, *52*, 288-296.

51. A. Villa, N. Dimitratos, C. E. Chan-Thaw, C. Hammond, G. M. Veith, D. Wang, M. Manzoli, L. Prati and G. J. Hutchings, *Chemical Society Reviews*, **2016**, *45*, 4953-4994.

52. K. L. Kelly, E. Coronado and G. C. Schatz, *Journal of Physical Chemistry B*, **2003**, *107*, 668-677.

53. J. A. Lopez-Sanchez, N. Dimitratos, C. Hammond, G. L. Brett, L. Kesavan, S. White, P. Miedziak, R. Tiruvalam, R. L. Jenkins, A. F. Carley, D. Knight, C. J. Kiely and G. J. Hutchings, *Nature Chemistry*, **2011**, *3*, 551-556.

54. A. Villa, D. Wang, G. M. Veith, F. Vindigni and L. Prati, *Catalysis Science & Technology*, **2013**, *3*, 3036-3041.

55. M. Luo, Y. Hong, W. Yao, C. Huang, Q. Xu and Q. Wu, *Journal of Materials Chemistry A*, **2015**, *3*, 2770-2775.

56. M. Comotti, W.-C. Li, B. Spliethoff and F. Schuth, *Journal of the American Chemical Society*, **2006**, *128*, 917-924.

57. S. Campisi, M. Schiavoni, C. Chan-Thaw and A. Villa, *Catalysts*, **2016**, *6*, 185.

58. C. A. Stowell and B. A. Korgel, *Nano letters*, **2005**, *5*, 1203-1207.

59. T. Tachikawa, T. Yonezawa and T. Majima, *ACS Nano*, **2013**, *7*, 263-275.

60. Z. Liu, W. Hou, P. Pavaskar, M. Aykol and S. B. Cronin, *Nano Letters*, **2011**, *11*, 1111-1116.

61. Y. Zhang, Q. Xiao, Y. Bao, Y. Zhang, S. Bottle, S. Sarina, B. Zhaorigetu and H. Zhu, *The Journal of Physical Chemistry C*, **2014**, *118*, 19062-19069.

62. A. Ibhadon and P. Fitzpatrick, *Catalysts*, **2013**, *3*, 189-218.

63. J. Schwitzgebel, J. G. Ekerdt, H. Gerischer and A. Heller, *Journal of Physical Chemistry,* **1995**, *99*, 5633-5638.

64. T. Minabe, D. A. Tyrk, P. Sawunyama, Y. Kikuchi, K. Hashimoto and A. Fujishima, *Journal of Photochemistry and Photobiology A: Chemistry*, **2000**, *137*, 53-62.

65. W. Bahnemann, M. Muneer and M. M. Haque, *Catalysis Today*, **2007**, *124*, 133-148.

66. M. A. Fox and M. T. Dulay, *Chemical Reviews*, **1993**, *93*, 341-357.

67. E. R. Carraway, A. J. Hoffman and M. R. Hoffmann, *Environmental Science & Technology*, **1994**, *28*, 786-793.

68.   A. J. Hoffman, E. R. Carraway and M. R. Hoffmann, *Environmental Science & Technology*, **1994**, *28*, 776-785.

69.   C. Kormann, D. W. Bahnemann and M. R. Hoffmann, *Environmental Science & Technology*, **1988**, *22*, 798-806.

70.   D. Yin, F. Zhao, L. Zhang, X. Zhang, Y. Liu, T. Zhang, C. Wu, D. Chen and Z. Chen, *RSC Advances*, **2016**, *6*, 103795-103802.

71.   A. D. Liyanage, S. D. Perera, K. Tan, Y. Chabal and K. J. Balkus, *ACS Catalysis*, **2014**, *4*, 577-584.

72.   B. Choudhury, P. Chetri and A. Choudhury, *RSC Advances*, **2014**, *4*, 4663-4671.

73.   X. Liu, K. Zhou, L. Wang, B. Wang and Y. Li, *Journal of the American Chemical Society*, **2009**, *131*, 3140-3141.

74.   N. Sabari Arul, D. Mangalaraj, P. C. Chen, N. Ponpandian and C. Viswanathan, *Materials Letters*, **2011**, *65*, 3320-3322.

75.   M. a. D. Hernández-Alonso, A. B. Hungría, A. Martínez-Arias, M. Fernández-García, J. M. Coronado, J. C. Conesa and J. Soria, *Applied Catalysis B: Environmental*, **2004**, *50*, 167-175.

76.   F. Chen, Y. Cao and D. Jia, *Applied Surface Science*, **2011**, *257*, 9226-9231.

77.   T. Feng, X. Wang and G. Feng, *Materials Letters*, **2013**, *100*, 36-39.

78.   H. Kominami, A. Tanaka and K. Hashimoto, *Applied Catalysis A: General*, **2011**, *397*, 121-126.

79.   H. Kominami, A. Tanaka and K. Hashimoto, *Chemical Communications*, **2010**, *46*, 1287-1289.

80.   L. Liu, S. Ouyang and J. Ye, *Angewandte Chemie International Edition*, **2013**, *52*, 6689-6693.

81.   S. K. Ghosh, S. Nath, S. Kundu, K. Esumi and T. Pal, *The Journal of Physical Chemistry B*, **2004**, *108*, 13963-13971.

82.   C.-F. Chen and S. Gwo, *Journal of the American Chemical Society*, **2007**, *130*, 824-826.

83.   K. Yamada, K. Miyajima and F. Mafune, *Journal of Physical Chemistry C*, **2007**, *111*, 11246-11251.

84.   G. L. Brett, Q. He, C. Hammond, P. J. Miedziak, N. Dimitratos, M. Sankar, A. A. Herzing, M. Conte, J. A. Lopez-Sanchez, C. J. Kiely, D. W. Knight, S. H. Taylor and G. J. Hutchings, *Angewandte Chemie*, **2011**, *50*, 10136-10139.

85.   M. Chen, D. Kumar, Y. Cheol-Woo and D. W. Goodman, *Science*, **2005**, *310*, 291-293.

86.   T. A. Silva, E. Teixeira-Neto, N. Lopez and L. M. Rossi, *Scientific Reports*, **2014**, *4*, 5766.

87.   A. M. Venezia, V. La Parola, V. Nicolì and G. Deganello, *Journal of Catalysis*, **2002**, *212*, 56-62.

88.   M.-L. Wu, D.-H. Chen and T.-C. Huang, *Langmuir: the ACS Journal of Surfaces and Colloids*, **2001**, *17*, 3877-3883.

89.   A. Villa, N. Dimitratos, C. E. Chan-Thaw, C. Hammond, L. Prati and G. J. Hutchings, *Accounts of Chemical Research*, **2015**, *48*, 1403-1412.

90.   G. J. Hutchings, *Chemical Communications,* **2007**, *0*, 1148-1164.

91. H. A. E. Hagelin-Weaver, J. F. Weaver, G. B. Hoflund and G. N. Salaita, *Journal of Alloys and Compounds*, **2005**, *393*, 93-99.

92. B. Solsona, J. K. Edwards, P. Landon, A. F. Carley, A. A. Herzing, C. J. Kiely and G. J. Hutchings, *Chemistry of Materials*, **2006**, *18*, 2689-2695.

93. N. Dimitratos, J. A. Lopez-Sanchez, J. M. Anthonykutty, G. Brett, A. F. Carley, R. C. Tiruvalam, A. A. Herzing, C. J. Kiely, D. W. Knight and G. J. Hutchings, *Physical Chemistry Chemical Physics: PCCP*, **2009**, *11*, 4952-4961.

94. N. Dimitratos, J. A. Lopez-Sanchez and G. J. Hutchings, *Topics in Catalysis*, **2009**, *52*, 258-268.

95. J. K. Edwards, B. Solsona, P. Landon, A. F. Carley, A. Herzing, M. Watanabe, C. J. Kiely and G. J. Hutchings, *Journal of Materials Chemistry*, **2005**, *15*, 4595.

96. J. Edwards, B. Solsona, P. Landon, A. Carley, A. Herzing, C. Kiely and G. Hutchings, *Journal of Catalysis*, **2005**, *236*, 69-79.

97. W. Ketchie, M. Murayama and R. Davis, *Journal of Catalysis*, **2007**, *250*, 264-273.

Chapter 6

Conclusion and Future Work

The aims of this Thesis were to investigate the catalytic properties of supported monometallic and bimetallic catalysts prepared by a modified sol-immobilisation method (without any stabiliser addition). This method is of particular interest for the preparation of supported nanoparticles thanks to its relative simplicity and versatility. The generation of a colloidal nanoparticle dispersion prior to immobilisation on a support is very advantageous since in principle it allows control on the size and shape of the nanoparticles before immobilisation. The activity of the catalysts were investigated in oxidation reactions in the gas phase (CO oxidation) and in the liquid phase (solvent-free benzyl alcohol oxidation and glycerol oxidation). The plasmonic response of these catalysts was also studied and the materails were applied for the visible-light photocatalytic oxidation of glycerol. The following conclusions can be made from the investigations reported in this thesis.

6.1 Chapter 3

The aim of Chapter 3 was to show that the stabiliser-free sol-immobilisation method is feasible for the preparation of 1% wt Au and AuPd catalysts supported on TiO_2. TEM and XPS analysis showed that the catalysts presented very similar morphology and composition with respect to the materials prepared *via* the traditional sol-immobilisation. However, unexpectedly, the dried-only monometallic SF catalysts were not active for the gas-phase oxidation of CO; it was observed that calcination at 500 °C slightly improved the

activity. It was speculated that the reason of this catalytic behaviour lies in the presence of chloride residues on the SF dried catalyst or on a nanoparticles size effect. However, while was possible to see an effective reduction in the size of the nanoparticles after calcination, the possible presence of the chloride could not be confirmed. It would be useful to perform analysis such as TGA-MS on the SF sample, since this analysis was not possible during the timescale of this work. In contrast, the same catalyst was found to be active for the liquid phase glycerol oxidation, suggesting that the preparation method might be an issue only for structure-sensitive reactions such as CO. Bimetallic samples were tested for the benzyl alcohol oxidation and also in this case the results were found to be fully comparable with the results obtained with the traditional catalyst.

Future work

It has been shown that is possible to prepare active nanoparticles by the sol-immobilisation method avoiding the use of stabilising agents. Further investigation is required in order to gain more control on the nanoparticle size and shape when using this innovative methodology, in order to prepare "naked" catalysts (supported or unsupported) that do not present the major drawbacks related to the stabiliser presence. For example, it would be interesting to investigate additional parameters that could affect the colloid generation and stability, such as e.g., concentration and nature of the precursor(s) and reductant, temperature, addition of salts or other species that might induce an electrostatic stabilisation. Investigation on the synthesis of other catalysts based on non-noble metal nanoparticles would be also desirable, as well as the deposition onto different supports (e.g., carbon).

6.2 Chapter 4

The aim of Chapter 4 was to investigate in more detail the activity and selectivity of the mono and bimetallic sol-immobilised catalysts for the oxidation of glycerol under basic conditions. The catalysts showed very similar activity. However, the selectivity towards main products glycerate (GA) and tartronate (TA) changed according to the presence and nature of the polymer. This was especially true for the monometallic samples, where the selectivity to GA was found to follow the trend PVP>PVA>SF, and the opposite trend was observed for TA. Therefore, it was concluded that different surfaces promote different oxidation mechanisms, and this

result was supported by experimental results obtained using GA as starting material. On the basis of previous studies reported in the literature, it was postulated the production of H_2O_2 on Au/TiO_2 catalysts, which is correlated to a higher selectivity to C_2 products (in particular glycolate) and which might be responsible of further oxidation of GA to TA, enhanced on SF surfaces. However, it was evident from the results both on glycerol oxidation and glyceric acid oxidation, and supported by short reaction time studies on glycerol oxidation, that this cannot be produced only *via* a consecutive oxidation pathway as reported in the literature, but must be a primary product. In this respect, it would be interesting to understand whether the selectivity to TA can be tuned by the presence and nature of the polymer, and further spectroscopic investigation is planned in the future.

Future work

In order to give an answer to these problems, it would be useful to study the catalyst surface with chemisorption experiments using either probe molecules (such as NH_3, CO) or the glycerol itself, coupled with high resolution spectroscopic analysis (e.g., FT-IR, Raman). As discussed both in Chapters 3 and 4, the information gathered in the fingerprint region might be very useful for better understanding the surface covering and the mode of adsorption, but the extreme convolution of these signals makes the data treatment quite hard.

6.3 Chapter 5

Finally, the aim of Chapter 5 was to investigate the plasmonic response of a series of mono Au and bimetallic AuPd materials prepared *via* the sol-immobilisation method(s). The monometallic catalysts were synthesized at different metal loadings (1-7 nominal wt %) *via* the traditional and SF method. The effect of the polymer stabiliser and of the support was also investigated. The oxidation of glycerol under neutral conditions was chosen as a test reaction. It was found that sol-immobilised catalysts can be successfully employed also for plasmonic photocatalytic applications: an enhancement in the glycerol conversion was observed under illumination with visible light, and the effect was confirmed to be plasmonic since experiments with different cut-off filters were performed. However, the catalytic response was found to be very sensitive to different parameters such as metal loading, nanoparticles size, nature of the polymer stabiliser, interaction

nanoparticle/support. Also in this conditions, it was concluded that the production of H_2O_2, expected to be enhanced under illumination as shown in previous studies, enhances the conversion but drives the selectivity to C_2 (glycolic acid) and C_1 products (CO_2).

Bimetallic AuPd/TiO$_2$ catalysts (1% wt) with different Au:Pd ratio were also tested under the same conditions and the results showed an increase in the plasmonic response with the increase of gold content, suggesting the composition of the alloy plays a fundamental role in the photocatalytic response.

Future work

Basing on the outcomes of the study developed in Chapter 5, further investigation will be needed in order to clarify the following points.

- **The role of the stabilising agent and how it can affect the LSPR**. It has been showed that stabilisation seems to be required for this reaction in order to obtain a good catalytic response. However, the nature of the stabiliser plays a fundamental role, because it can interfere with the excited electrons limiting the plasmonic effect. Therefore, when working with the sol-immobilisation method for the preparation of catalysts active for plasmonic photocatalytic applications, the role of the stabiliser should be taken into account. To further pursue this hypothesis, investigation of other ligands or polymers would be helpful for identifying the best compromise between stability and activity. This results to be embedded in the future work proposed for Chapter 3.

- **The role of the support and in particular the importance of its interface with the nanoparticles.** As it has been shown, the monometallic SF catalysts were not active for this reaction (excepted the 7% wt, which showed a weak activity under illumination), although they present plasmonic resonance. This was surprising, since similar catalysts were found to be as active as the traditional ones for the glycerol oxidation under basic conditions. Calcination though was proven to be beneficial for the activity. It was speculated therefore that the nanoparticles size and the interaction with the support play a fundamental role. Future work based on investigation on the nanoparticles size and on different supports will be required (again, this point should be considered embedded in the future work proposed for Chapter 3).

- **The role of the alloy and the effect of its composition**. As it has been shown, the bimetallic catalysts were found to show a plasmonic response, which increased with the increase of the Au content. However, data suggest that the catalytic response is at a maximum at selected Au:Pd ratio (volcano shape). This suggests that further investigation should be addressed to find the best compromise between "thermal" activity and photocatalytic response of such catalysts. In addition, higher metal loading should be taken into consideration in order to enhance the catalytic response, as well as the presence of other metals such as e.g., Pt, Cu, Ag.

- **The reactor and reaction conditions.** They were found to be of paramount importance for a successful catalytic response, therefore reaction conditions such as e.g., use of a continuous flow reactor, adjustment of the volume of solution and amount of catalyst should be object of a deeper investigation in order to optimise the process.

- **H_2O_2 production control**. It has been shown that the major drawback of these nanostructures is the formation of H_2O_2 which promotes the formation of C_2 and C_1 products at the expensed of more valuable C_3 products (DHA). Further investigation in order to understand the reaction mechanism would be desirable since it could provide solutions to limit the H_2O_2 production and therefore the consequent over-oxidation of the products.

Appendix I

Table I – CO-DRIFTS bands and assignment (Section 3.3.4, Chapter 3)

Wavenumber / cm^{-1}	CO band assignment	Figure	Reference
Region 2000-1800	Pd, bridged or three fold	3.20-3.22	[1, 2]
Region 1700-1000	TiO$_2$, carboxylate or bicarbonate	[all]	[3-5]
Region 1540-1440	free carbonate	[all]	[4]
2108, 2014	Pd, linear (edge or corner)	3.21	[1]
2110	Au, linear	3.17	[1]
2095	Au, linear	3.16	[1]
2080, 2053	Pd, linear (edge or corner)	3.20	[1]
2058, 1932	Pd, linear and bridged	3.22	[6, 7]
1983, 1943	Au or AuPd, bridged or three fold	3.20	[1, 2]

References

1. J. H. Carter, S. Althahban, E. Nowicka, S. J. Freakley, D. J. Morgan, P. M. Shah, S. Golunski, C. J. Kiely and G. J. Hutchings, *ACS Catalysis*, **2016**, *6*, 6623-6633.

2. F. Cárdenas-Lizana, S. Gómez-Quero, A. Hugon, L. Delannoy, C. Louis and M. A. Keane, *Journal of Catalysis*, **2009**, *262*, 235-243.

3. B. Schumacher, V. Plazk, M. Kinne and R. J. Behm, *Catalysis Letters*, **2003**, *89*, 109-114.

4. M. A. Bollinger and M. A. Vannice, *Applied Catalysis B: Environmental*, **1995**, *8*, 417-443.

5. F. Boccuzzi, S. Tsubota and M. Haruta, *Journal of Electron Spectroscopy and Related Phenomena*, **1993**, *64/65*, 241-250.

6. K. Duan, Z. Liu, J. Li, L. Yuan, H. Hu and S. I. Woo, *Catalysis Communications*, **2014**, *57*, 19-22.

7. J. Xu, T. White, P. Li, C. He, C. Yu, Y. Weikang and Y.-F. Han, *Journal of the American Chemical Society*, **2010**, *132*, 10398-10406.

Appendix I

Name and formula

Reference code: 00-004-0784

Mineral name: Gold, syn
Compound name: Gold

Empirical formula: Au
Chemical formula: Au

Crystallographic parameters

Crystal system: Cubic
Space group: Fm-3m
Space group number: 225

a (Å):   4.0786
b (Å):   4.0786
c (Å):   4.0786
Alpha (°):   90.0000
Beta (°):   90.0000
Gamma (°):   90.0000

Calculated density (g/cm^3):   19.30
Measured density (g/cm^3):   19.30
Volume of cell (10^6 pm^3):   67.85
Z: 4.00

RIR: -

Subfiles and quality

Subfiles: Alloy, metal or intermetalic
Common Phase
Educational pattern
Forensic
Inorganic
Mineral
NBS pattern
Quality: Star (S)

Comments

Color: Yellow metallic
ANX: N
Creation Date: 9/1/1954
Modification Date: 1/1/1970
ANX: N
Analysis: Spectrographic analysis (%): Si 0.001, Ca 0.001, Ag 0.001(?). Color: Yellow metallic. Melting Point: 1334.6-1336.2 K. Opaque Optical Data: Opaque mineral optical data on specimen from unspecified locality: RR2Re=71.6, Disp.=16, VHN100=53-58, Color values=.384, .391, 72.7, Ref.: IMA Commission on Ore Microscopy QDF. Sample Source or Locality: Sample purified at NBS, Gaithersburg, Maryland, USA and is about 99.997% Au. Temperature of Data Collection: Pattern taken at 299 K. Unit Cell Data Source: Powder Diffraction.

Appendix I

File: 00-002-0321

User: CARDIFF UNIVERSITY

References

Primary reference: Swanson, Tatge., *Natl. Bur. Stand. (U. S.), Circ. 539*, **I**, 33, (1953)
Optical data: Winchell., *Elements of Optical Mineralogy*, 17

Peak list

No.	h	k	l	d [Å]	2Theta[deg]	I [%]
1	1	1	1	2.35500	38.185	100.0
2	2	0	0	2.03900	44.393	52.0
3	2	2	0	1.44200	64.578	32.0
4	3	1	1	1.23000	77.549	36.0
5	2	2	2	1.17740	81.724	12.0
6	4	0	0	1.01960	98.137	6.0
7	3	3	1	0.93580	110.802	23.0
8	4	2	0	0.91200	115.264	22.0
9	4	2	2	0.83250	135.423	23.0

Stick Pattern

Appendix I

Name and formula

Reference code:	00-021-1272
Mineral name:	Anatase, syn
Compound name:	Titanium Oxide
PDF index name:	Titanium Oxide
Empirical formula:	O_2Ti
Chemical formula:	TiO_2

Crystallographic parameters

Crystal system:	Tetragonal
Space group:	I41/amd
Space group number:	141
a (Å):	3.7852
b (Å):	3.7852
c (Å):	9.5139
Alpha (°):	90.0000
Beta (°):	90.0000
Gamma (°):	90.0000
Calculated density (g/cm^3):	3.89
Volume of cell (10^6 pm^3):	136.31
Z:	4.00
RIR:	3.30

Subfiles and quality

Subfiles:	Alloy, metal or intermetalic
	Common Phase
	Educational pattern
	Excipient
	Forensic
	Inorganic
	Mineral
	NBS pattern
	Pharmaceutical
	Pigment/Dye
Quality:	Star (S)

Comments

Color:	Colorless
Creation Date:	1/1/1970
Modification Date:	1/1/1970
Additional Patterns:	See PDF 01-071-1166. Validated by calculated pattern
Color:	Colorless. Anatase and another polymorph, brookite (orthorhombic), are converted to rutile (tetragonal) by heating above 700 C. Pattern reviewed by Holzer, J., McCarthy, G., North Dakota State Univ, Fargo, North Dakota, USA, ICDD Grant-in-Aid (1990). Agrees well with experimental and calculated patterns
Sample Source or Locality:	Sample obtained from National Lead Co., South Amboy, New Jersey, USA
Temperature of Data Collection:	Pattern taken at 298 K

Appendix I

Source of Unit Cell Data: Powder Diffraction.

References

Primary reference: **7**, 82, (1969)

Peak list

No.	h	k	l	d [Å]	2Theta[deg]	I [%]
1	1	0	1	3.52000	25.281	100.0
2	1	0	3	2.43100	36.947	10.0
3	0	0	4	2.37800	37.801	20.0
4	1	1	2	2.33200	38.576	10.0
5	2	0	0	1.89200	48.050	35.0
6	1	0	5	1.69990	53.891	20.0
7	2	1	1	1.66650	55.062	20.0
8	2	1	3	1.49300	62.121	4.0
9	2	0	4	1.48080	62.690	14.0
10	1	1	6	1.36410	68.762	6.0
11	2	2	0	1.33780	70.311	6.0
12	1	0	7	1.27950	74.031	2.0
13	2	1	5	1.26490	75.032	10.0
14	3	0	1	1.25090	76.020	4.0
15	0	0	8	1.18940	80.727	2.0
16	3	0	3	1.17250	82.139	2.0
17	2	2	4	1.16640	82.662	6.0
18	3	1	2	1.16080	83.149	4.0
19	2	1	7	1.06000	93.221	2.0
20	3	0	5	1.05170	94.182	4.0
21	3	2	1	1.04360	95.143	4.0
22	1	0	9	1.01820	98.319	2.0
23	2	0	8	1.00700	99.804	2.0
24	3	2	3	0.99670	101.221	2.0
25	3	1	6	0.95550	107.448	4.0
26	4	0	0	0.94640	108.963	4.0
27	3	0	7	0.92460	112.841	2.0
28	3	2	5	0.91920	113.861	2.0
29	4	1	1	0.91380	114.909	2.0
30	2	1	9	0.89660	118.439	4.0
31	2	2	8	0.88900	120.104	2.0
32	4	1	3	0.88190	121.725	2.0
33	4	0	4	0.87930	122.336	2.0
34	4	2	0	0.84640	131.036	2.0
35	3	2	7	0.83080	135.998	2.0
36	4	1	5	0.82680	137.391	4.0
37	3	0	9	0.81020	143.888	2.0
38	4	2	4	0.79740	150.039	4.0
39	0	0	12	0.79280	152.634	2.0

Stick Pattern

Appendix I

Intensity [%]

Ref. Pattern: Titanium Oxide, 00-021-1272

Position [º2Theta] (Copper (Cu))
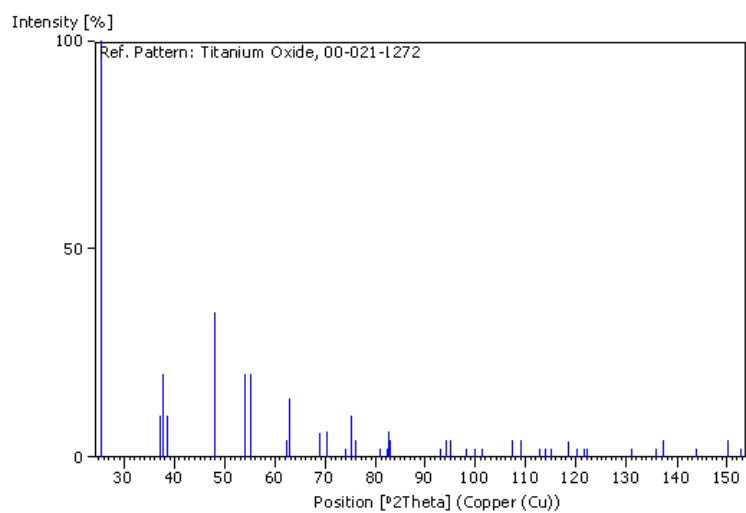
Appendix I

Name and formula

Reference code: 01-072-5376

Compound name: Gold Palladium
PDF index name: Gold Palladium

Empirical formula: AuPd
Chemical formula: AuPd

Crystallographic parameters

Crystal system: Cubic
Space group: Fm-3m
Space group number: 225

a (Å):   3.9800
b (Å):   3.9800
c (Å):   3.9800
Alpha (°):   90.0000
Beta (°):   90.0000
Gamma (°):   90.0000

Volume of cell (10^6 pm^3):   63.04
Z: 2.00

RIR: 20.85

Subfiles and quality

Subfiles: Alloy, metal or intermetalic
       ICSD Pattern
       Inorganic
Quality: Indexed (I)

Comments

ANX: N
ICSD collection code: 58571
Creation Date: 9/1/2006
Modification Date: 9/1/2011
ANX: N
Analysis: Au1 Pd1
Formula from original source: Au Pd
ICSD Collection Code: 58571
Minor Warning: No e.s.d reported/abstracted on the cell dimension. No R factors reported/abstracted
Wyckoff Sequence: a(FM3-M)
Unit Cell Data Source: Powder Diffraction.

References

Primary reference: *Calculated from ICSD using POWD-12++*
Structure: Krishna Rao, K.V., Iyengar, L., Venudhar, Y.C., *J. Less-Common Met.*, **58**, P55, (1978)

Peak list

Appendix I

No.	h	k	l	d [Å]	2Theta[deg]	I [%]
1	1	1	1	2.29780	39.173	100.0
2	2	0	0	1.99000	45.547	45.6
3	2	2	0	1.40710	66.383	23.4
4	3	1	1	1.20000	79.870	23.6
5	2	2	2	1.14890	84.206	6.5
6	4	0	0	0.99500	101.460	2.9
7	3	3	1	0.91310	115.047	9.0
8	4	2	0	0.89000	119.881	8.6
9	4	2	2	0.81240	142.948	7.5

Stick Pattern
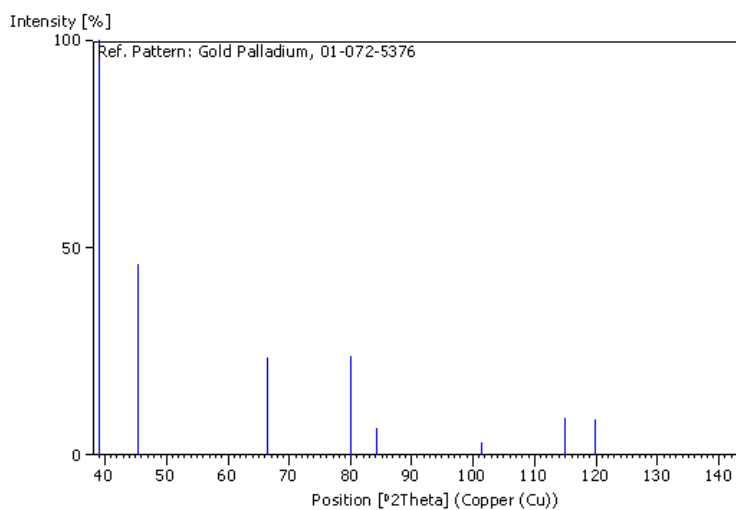
Intensity [%]

Ref. Pattern: Gold Palladium, 01-072-5376

Position [°2Theta] (Copper (Cu))

Appendix I

Name and formula

Reference code: 00-021-1276

Mineral name: Rutile, syn
Compound name: Titanium Oxide
Common name: titania
PDF index name: Titanium Oxide

Empirical formula: O_2Ti
Chemical formula: TiO_2

Crystallographic parameters

Crystal system: Tetragonal
Space group: P42/mnm
Space group number: 136

a (Å):   4.5933
b (Å):   4.5933
c (Å):   2.9592
Alpha (°):   90.0000
Beta (°):   90.0000
Gamma (°):   90.0000

Calculated density (g/cm^3):   4.25
Measured density (g/cm^3):   4.23
Volume of cell (10^6 pm^3):   62.43
Z: 2.00

RIR: 3.40

Subfiles and quality

Subfiles: Alloy, metal or intermetalic
                    Common Phase
                    Educational pattern
                    Excipient
                    Forensic
                    Inorganic
                    Mineral
                    NBS pattern
                    Pharmaceutical
                    Pigment/Dye
Quality: Star (S)

Comments

Color: White
Creation Date: 1/1/1970
Modification Date: 1/1/1970
Additional Patterns: Validated by calculated pattern
Analysis: No impurity over 0.001%
Color: White. Pattern reviewed by Syvinski, W., McCarthy, G., North Dakota State Univ, Fargo,
                    North Dakota, USA, ICDD Grant-in-Aid (1990). Agrees well with experimental and
                    calculated patterns. Two other polymorphs, anatase (tetragonal) and brookite

Appendix I

Optical Data Specimen location: (orthorhombic), converted to rutile on heating above 700 C. Additional weak reflections
Reflectance: (indicated by brackets) were observed. Naturally occurring material may be reddish brown
                                   Optical data on specimen from Dana`s System of Mineralogy, 7th Ed., I 555
                                   Opaque mineral optical data on specimen from Sweden: R3R%=20.3, Disp.=Std. Sample
                                   Source or Locality: Sample obtained from National Lead Co., South Amboy, New Jersey,
                                   USA. Temperature of Data Collection: Pattern taken at 298 K. Vickers Hardness Number:
                                   VHN100=1132-1187. Source of Unit Cell Data: Powder Diffraction.

References

Primary reference: **7**, 83, (1969)
Optical data: **I**, 575

Peak list

No.	h	k	l	d [Å]	2Theta[deg]	I [%]
1	1	1	0	3.24700	27.447	100.0
2	1	0	1	2.48700	36.086	50.0
3	2	0	0	2.29700	39.188	8.0
4	1	1	1	2.18800	41.226	25.0
5	2	1	0	2.05400	44.052	10.0
6	2	1	1	1.68740	54.323	60.0
7	2	2	0	1.62370	56.642	20.0
8	0	0	2	1.47970	62.742	10.0
9	3	1	0	1.45280	64.040	10.0
10	2	2	1	1.42430	65.480	2.0
11	3	0	1	1.35980	69.010	20.0
12	1	1	2	1.34650	69.790	12.0
13	3	1	1	1.30410	72.410	2.0
14	3	2	0	1.27390	74.411	1.0
15	2	0	2	1.24410	76.510	4.0
16	2	1	2	1.20060	79.822	2.0
17	3	2	1	1.17020	82.335	6.0
18	4	0	0	1.14830	84.260	4.0
19	4	1	0	1.11430	87.464	2.0
20	2	2	2	1.09360	89.557	8.0
21	3	3	0	1.08270	90.708	4.0
22	4	1	1	1.04250	95.275	6.0
23	3	1	2	1.03640	96.017	6.0
24	4	2	0	1.02710	97.177	4.0
25	3	3	1	1.01670	98.514	1.0
26	4	2	1	0.97030	105.099	2.0
27	1	0	3	0.96440	106.019	2.0
28	1	1	3	0.94380	109.406	2.0
29	4	0	2	0.90720	116.227	4.0
30	5	1	0	0.90090	117.527	4.0
31	2	1	3	0.88920	120.059	8.0
32	4	3	1	0.87740	122.788	8.0
33	3	3	2	0.87380	123.660	8.0
34	4	2	2	0.84370	131.847	6.0
35	3	0	3	0.82920	136.549	8.0
36	5	2	1	0.81960	140.052	12.0
37	4	4	0	0.81200	143.116	2.0
38	5	3	0	0.78770	155.870	2.0

Stick Pattern

Appendix I